Newcastle University

Faculty of Science, Agriculture and Engineering

School of Engineering

Ground-based synthetic aperture radar (GBSAR) interferometry for deformation monitoring

Zheng Wang

Thesis submitted for the degree of

Doctor of Philosophy

2018

Abstract

Ground-based synthetic aperture radar (GBSAR), together with interferometry, represents a powerful tool for deformation monitoring. GBSAR has inherent flexibility, allowing data to be collected with adjustable temporal resolutions through either continuous or discontinuous mode. The goal of this research is to develop a framework to effectively utilise GBSAR for deformation monitoring in both modes, with the emphasis on accuracy, robustness, and real-time capability.

To achieve this goal, advanced Interferometric SAR (InSAR) processing algorithms have been proposed to address existing issues in conventional interferometry for GBSAR deformation monitoring. The proposed interferometric algorithms include a new non-local method for the accurate estimation of coherence and interferometric phase, a new approach to selecting coherent pixels with the aim of maximising the density of selected pixels and optimizing the reliability of time series analysis, and a rigorous model for the correction of atmospheric and repositioning errors.

On the basis of these algorithms, two complete interferometric processing chains have been developed: one for continuous and the other for discontinuous GBSAR deformation monitoring. The continuous chain is able to process infinite incoming images in real time and extract the evolution of surface movements through temporally coherent pixels. The discontinuous chain integrates additional automatic coregistration of images and correction of repositioning errors between different campaigns.

Successful deformation monitoring applications have been completed, including three continuous (a dune, a bridge, and a coastal cliff) and one discontinuous (a hillside), which have demonstrated the feasibility and effectiveness of the presented algorithms and chains for high-accuracy GBSAR interferometric measurement. Significant deformation signals were detected from the three continuous applications and no deformation from the discontinuous. The achieved results are justified quantitatively via a defined precision indicator for the time series estimation and validated qualitatively via a priori knowledge of these observing sites.

Acknowledgements

I would like to express my greatest gratitude to my supervisors, Professor Jon Mills and Professor Zhenhong Li, for their invaluable guidance, advice and support throughout my PhD. Their kindness and patience were truly appreciated.

I would like to thank the China Scholarship Council (CSC) and Newcastle University for funding my PhD program over the past three years. Also, I would like to thank The Great Britain-China Educational Trust (GBCET) and The Henry Lester Trust for their financial support/awards during my thesis pending time.

I am deeply grateful to Mr. Martin Robertson and Mr. James Goodyear for their technical support. Thank you to Professor Andy Hooper for providing the free and open-source InSAR package StaMPS and Dr. Mi Jiang for the FaSHPS package. I would also like to acknowledge all the past and present members of NEOLab and Geodesy groups, particularly Jiajun, Chen, Maria, Wen, Jiaxing, Yasir, Ahmed, Aun, Chris, Chuang, Hui, Zhenhai, Sichun, Anxi, Jing, La, Yang, Lifu, etc. Thanks for their knowledge sharing and discussion, and for making life much easier, fun and colourful. I am always grateful to my friends, Qingyuan, Tianhui, Kuo, Xiaodong, Xilin, Qian, Lin, Bill, etc, in Newcastle and Nottingham. They always kindly give the support when I need.

Last, but never least, I would like to thank my parents and parents-in-law for their endless love and support throughout my life. I am also indebted to my beautiful wife, Anqi Yao, for her taking care, support and understanding over the past eight years, for making me delicious food, for always standing by my side without doubt, for companying me all the time and filling every day of my life.

Thank you all.

Contents

List of Publications

Wang, Z., Li, Z., Mills, J., 2018. A new non-local method for ground-based sar deformation monitoring. *IEEE Journal of Selected Topics in Applied Earth Observations and Remote Sensing* 11(10), 3769-3781.

Wang, Z., Li, Z., Mills, J., 2018. A new approach to selecting coherent pixels for ground-based SAR deformation monitoring. *ISPRS Journal of Photogrammetry and Remote Sensing* 144, 412-422.

Wang, Z., Li, Z., Liu Y., Peng J., Long S., and Mills, J., A novel processing chain for real-time ground-based SAR (RT-GBSAR) deformation monitoring, *Manuscript submitted to IEEE Transactions on Geoscience and Remote Sensing on 31st January, 2019 for publication*.

Wang, Z., Li, Z., Mills, J., Modelling of instrument repositioning errors in discontinuous Multi-Campaign Ground-Based SAR (MC-GBSAR) deformation monitoring, *Manuscript submitted to ISPRS Journal of Photogrammetry and Remote Sensing on 5th May 2019 for publication*.

Wang, Z., Li, Z., Mills, J., Modelling and correction of atmospheric phase screen in ground-based SAR interferometry, *Manuscript submitted to International Journal of Applied Earth Observation and Geoinformation on 26th May 2019 for publication*.

List of Figures

List of Tables

List of Abbreviations

1D	One-Dimensional
2D	Two-Dimensional
2D FFT	Two-Dimensional Fast Fourier Transform
3D	Three-Dimensional
ADI	Amplitude Dispersion Index
APS	Atmospheric Phase Screen
ATS	Airborne Laser Scanning/Scanner
CLT	Central Limit Theorem
CR	Corner Reflector
DEM	Digital Elevation Model
D-InSAR	Differential Synthetic Aperture Radar Interferometry
DS	Distributed Scatterer
FaSHPS	Fast SHP Selection
FMCW	Frequency Modulated Continuous Wave
GBSAR	Ground-Based Synthetic Aperture Radar
GNSS	Global Navigation Satellite Systems
GPRI	Gamma Portable Radar Interferometer
GPS	Global Positioning System
IEEE	Institute of Electrical and Electronic Engineers
InSAR	Synthetic Aperture Radar Interferometry
IRLS	Iteratively Reweighted Least Squares
LOS	Line-of-Sight
MCF	Minimum Cost Flow
MC-GBSAR	Multi-Campaign Ground-Based Synthetic Aperture Radar

MIAS	Multi-temporal Interferometry based on Amplitude Similarity
MIMO	Multiple-Input Multiple-Output
MMAE	Multiple Model Adaptive Estimation
PCP	Partially Coherent Pixel
PPP	Precise Point Positioning
PS	Persistent Scatterer
PSC	Persistent Scatterer Candidate
PSI	Persistent ScattererInterferometry
PTK	Post-Processing Kinematic
RAM	Random-Access Memory
RAR	Real Aperture Radar
RMS	Root Mean Square
RT-GBSAR	Real Time Ground-Based Synthetic Aperture Radar
RTK	Real Time Kinematic
SAR	Synthetic Aperture Radar
SBAS	Small Baseline Subset
SCR	Signal-to-Clutter Ratio
SHP	Statistically Homogeneous Pixel
SLC	Single-Look Complex
SNR	Signal-to-Noise Ratio
StaMPS	Stanford Method for Persistent Scatterers
TLS	Terrestrial Laser Scanning/Scanner

Chapter 1. Introduction

1.1 Research background

Natural hazards have been normal occurrences around the world. Large events are infrequent but catastrophic, while most hazards are of moderate size and common occurrence (e.g. Park, 2013; Paton, 2008). Landslides behave as the movement of a mass of rock, earth or debris down a slope (Cruden, 1991) and represent typical hazardous natural phenomena of moderate size, often leading to significant human and economic losses (UNISDR, 2015, 2017). They are commonly triggered by earthquakes, heavy rainfalls, volcanic processes, ground subsidence, natural erosion, hydrogeological processes, human activities, or any combination of these factors (e.g. Clague and Stead, 2012; Haque et al., 2016; Lin and Wang, 2018). For 27 European countries over the period 1995 – 2014, a total of 1370 deaths and 784 injuries, along with the economic loss of approximately 4.7 billion Euros per year, were reported resulting from 476 landslides (Haque et al., 2016). In China, 1,911 non-seismically triggered landslides from 1950 to 2016 were recorded in the Fatal Landslide Event Inventory, which resulted in a total of 28,139 deaths during that period (Lin and Wang, 2018). The direct economic losses caused by fatal landslide events ranged from 4 million to 1,255 million RMB per year from 2000 to 2016, averaging about 313 million RMB per year. In the United States, landslides cause in excess of $1 billion in damages and 25 to 50 deaths per annum (Coalition, 2007). It is reported that most landslide fatalities are from rock fall, debris-flows, or volcanic debris flows (Rice, 2014). Globally, they cause billions of dollars in damages and thousands of deaths and injuries per annum (Coalition, 2007). In comparison to elsewhere in the world, the United Kingdom presents a low risk environment (Gibson et al., 2013) with small scale failures and low fatality rates (Pennington et al., 2015). However, in recent years, the periods September 2012 – March 2013, November 2013 – March 2014, and November 2015 – March 2016 experienced precipitous increase of landslides at both the coast and inland due to intensive rainfalls (BGS Landslides Team, 2018), and these events had significant impacts on infrastructure and people (Pennington et al., 2015). Beyond risk communication and public awareness campaigns, landslide risk can be mitigated by proactive strategies such as (i) structural slope-stabilization measures to reduce the probability of the occurrence of landslides and the vulnerability of the elements, and (ii) non-structural measures, e.g. early warning systems calling for actions in risky areas to reduce the hazard consequences, and measures to pool and transfer the risks (e.g. Calvello, 2017; Nadim and Lacasse, 2008). Landslide monitoring is the key to implement

proactive strategies. Firstly, ground movements can be detected through monitoring and the spatio-temporal variability can be analysed on the basis of the detected movements and numerical simulation, which plays an important role in understanding maintenance and remedial slope-stabilization measures (e.g. Calvello, 2017; Nadim and Lacasse, 2008; Scaioni, 2015). The monitoring, especially in real-time or near-real-time, of slope movements ensures the efficient generation of risk maps, which is the fundamental basis of early warning and rapid decision-making for countermeasures or evacuation (e.g. Nadim and Lacasse, 2008; Rödelsperger, 2011; Van Westen, 2013).

Apart from landslides, the effective monitoring of structural deformation for dams, levees, embankments, and other flood control structures that are subject to external loads has a critical role in detecting abnormal behaviour that may threaten the safety of the structure and implementing maintenance and remedial measures (Schroedel, 2002). Deformation monitoring (also referred to as deformation survey) is defined as the systematic measurement and tracking of the alteration in the shape or dimensions of an object as a result of external forces (Settles et al., 2008). In terms of landslide monitoring methods, they are classified into four broad categories: geotechnical, geodetic, geophysical and remote sensing (Settles et al., 2008). Except geophysical methods which usually measure direct geophysical parameters (e.g., direct current geoelectric, microseismic emission, earth strain) (Settles et al., 2008), the other three basically belong to the concept of deformation monitoring. Regarding structural deformation monitoring, Schroedel (2002) differentiated the surveying with reference from relative replacement observations, and the point-based surveying from the network-based. Despite the diversified categorization, geohazard monitoring and structural deformation surveying utilize similar sensors or technologies that are introduced as follows.

(1) In-situ sensors, such as tiltmeters (or inclinometers), extensometers, and piezometers, represent the most common geotechnical technologies (Scaioni, 2015).

A tiltmeter is a sensitive inclinometer that is usually installed either on the ground or in structures and used to measure very small inclination angles from the vertical level (Dunnicliff and Green, 1993). The measurement of changing inclinations with a tiltmeter can provide valuable data on the mechanics and activity of the instability (Settles et al., 2008).

An extensometer is a device that allows the continuous measurement of changes in the

length of an object or over convex surfaces with a rapid response rate (Brimacombe et al., 1991). In practice, extensometers installed in boreholes can measure the extension along the borehole axis by means of rods or wires and measure the distance between any two specific points within the borehole (Corominas et al., 2000). The extensometer is simple and low-cost and has been one of the most commonly employed tools for landslide early warning systems (Fujisawa et al., 2007).

A piezometer is a device capable of measuring groundwater pressures. Monitoring of groundwater conditions can provide important quantitative information on the slope and structure stability (e.g. Schroedel, 2002; Settles et al., 2008).

This class of sensors or technologies are usually sensitive, precise and capable of subsurface measurement (e.g. Scaioni, 2015; Settles et al., 2008). The disadvantages are, however, multifold: (i) the deployment of such in-situ sensors requires physical access to the observing site/object, which is hazardous in some cases, and (ii) their point-based measurement is generally not sufficient for analyzing a landslide behaviour (Scaioni, 2015).

(2) The common geodetic surveying techniques or technologies include conventional levelling, total stations, and the Global Navigation Satellite Systems (GNSS) especially the Global Positioning System (GPS).

Levelling is a conventional, simple, and precise surveying means to measure and transfer the height difference between specific points or networks (Berry, 1976), which has been widely used in cartography and in structural monitoring (Clancy, 2013). It is particularly suitable for monitoring ground subsidence and uplift (Bitelli et al., 2000).

A total station is an surveying instrument that integrates an electronic distance meter for distance measurement and an electronic theodolite for horizontal and vertical angle measurement (Kavanagh et al., 1996). With the measured distance and angles, a total station can determine the coordinates of an unknown point relative to a known coordinate. Currently, a state-of-the-art total station instrument, e.g. a Leica Nova MS60 instrument (https://leica-geosystems.com/en-gb/products/total-stations/multistation/leica-nova-ms60), can automatically pick up and repeat the measurement of a set of targets. Modern total stations are capable of measuring angles to 0.5'', along with the distance measurement accuracy at the level of millimetres over a distance up to 1,500 metres (Settles et al., 2008).

Together with the necessary in-situ retroreflectors, total stations can be used in the continuous assessment of unstable slopes and structures (e.g. Schroedel, 2002; Settles et al., 2008).

GPS is a global navigation satellite system that enables a GPS receiver to determine its geolocation and time information if four or more GPS satellites are in the view of the receiver (Djuknic and Richton, 2001). GPS surveying is combined with multiple techniques, such as static GPS, real time kinematic (RTK) or post-processing kinematic (PTK) GPS (Nickitopoulou et al., 2006), and precise point positioning (PPP) (e.g. Zumberge et al. 1997; Li et al., 2014). With necessary correction of relevant errors, the static GPS can achieve an accuracy of up to a few millimetres (Nickitopoulou et al., 2006), RTK and PTK a few centimetres (e.g. Berber et al., 2012; Nickitopoulou et al., 2006), and PPP several centimetres (e.g. Cai et al., 2015; Li et al., 2015). Continuous GPS observations are valuable data in long-term monitoring campaigns (e.g. Ching et al., 2011; Jin and Luo, 2009; Sagiya et al., 2000) and high-frequency GPS is able to monitor fast-changing scenarios (e.g. Yi et al., 2013; Yue and Lay, 2011). Thus, GPS has been widely used in geohazard monitoring (e.g., landslides (e.g. Benoit et al., 2015; Wang, 2011), volcanic eruptions (e.g. Lagios et al., 2013; Larson et al., 2010), and crustal deformation (e.g. Borghi et al., 2009; Vigny et al., 2011)) and structural monitoring (e.g., bridges (Yi et al., 2013), dams (e.g. Barzaghi et al., 2018; Kalkan, 2014), and buildings (e.g. Casciati and Fuggini, 2011; Jones and Rose, 2015)).

Geodetic technologies have been widely used in geohazard monitoring. Their main weaknesses in deformation monitoring are (i) the requirement of some form of site access, such as the installation of total station retroreflectors or GPS receivers, and (ii) the point-based nature of the resultant survey.

(3) Unlike the conventional geotechnical and geodetic techniques, remote sensing represents a non-contact surveying technology of capturing, processing and analyzing imagery from sensors mounted on terrestrial, aerial and spaceborne platforms (e.g. Chen et al., 2016; Settles et al., 2008). Remote sensing techniques can provide surface-based and dense measurements (Settles et al., 2008). Generally speaking, space imagery supplies wider swath while ground-based imagery provides better spatial resolution and accuracy (Delacourt et al., 2007). This class mainly includes photogrammetry, laser scanning, and synthetic aperture radar (SAR) interferometry (InSAR) (Settles et al., 2008).

Photogrammetry is a conventional remote sensing technology of extracting the exact positions of surface points from photographs (McGlone, 2013). In modern photogrammetry, photographs are mostly taken by digital cameras with prime lenses (Mikhail et al., 2001), also a few by zoom-lens cameras (e.g. Wang et al., 2017; Zheng et al., 2015). Photogrammetric measurement of deformation can be achieved through surface-point tracking or comparing multiple-temporal dense surfaces (Scaioni et al., 2015). Photogrammetric solutions are usually low-cost with high degrees of automation (e.g. Lucieer et al., 2014; Scaioni, 2015). The measurement accuracy depends on the platforms and the ground sampling distance, and the typical accuracy of close-range (generally less than 1,000 feet) photogrammetry in slope and structural monitoring applications ranges from centimetres to a few decimetres (e.g. Delacourt et al., 2007; Lucieer et al., 2014; Peppa et al., 2019; Scaioni et al., 2015). Limitations are (i) the requirement of illumination, thus, only applicable during day time, and (ii) conventionally the deployment of ground control points (James et al., 2017).

Laser scanning is a technology that enables the rapid generation of a dense surface point cloud (Marshall and Stutz, 2004). Particularly, terrestrial laser scanning (TLS) and airborne laser scanning (ATS) have been widely used for deformation monitoring and change detection (e.g. Abellán et al., 2014; Mukupa et al., 2017). Deformation can be detected through the comparison of multiple-temporal point clouds or surface models (Barbarella et al., 2015). Compared to photogrammetry and the aforementioned point-based approaches, TLS and ATS systems usually require more up-front financial investment (Peppa et al., 2019). The typical TLS accuracy of the coordinates in the medium-to-long range (a few hundred metres to a few kilometres) varies from millimetres to centimetres (Mukupa et al., 2017), which may not be sufficient for the monitoring of millimetric displacement (Scaioni, 2015).

InSAR is the fundamental technique that is able to detect surface deformation and generate a digital elevation model (DEM) of an observed area by exploiting phase change between SAR acquisitions (Hanssen, 2001). InSAR was initiated with the development of related SAR satellites. Spaceborne InSAR has been extensively adopted in different deformation monitoring applications, such as landslides (e.g. Calvello, 2017; Dai et al., 2016), earthquakes (e.g. Fielding et al., 2009; Zhou et al., 2018), volcanoes (Spaans and Hooper, 2016), and ground subsidence and uplift (Ding et al., 2004). Spaceborne InSAR is capable

of detecting millimetric ground displacements over large areas independent of solar illumination (e.g. Delacourt et al., 2007; Zhang et al., 2015). It is cost-effective, especially after the development of Sentinel-1 satellites which provide SAR data free of charge to all data users (Harris and Baumann, 2015). But the revisit period of SAR satellites (e.g. every 12 days for Sentinel-1) constrains flexibility for deformation monitoring tasks (Pipia et al., 2013).

More recently, ground-based synthetic aperture radar (GBSAR) has been developed, which offers users enhanced capabilities in monitoring surface displacements (e.g. Crosetto et al., 2015; Crosetto et al., 2017; Monserrat et al., 2014). Together with InSAR techniques, GBSAR has proven to be a powerful remote sensing tool for deformation monitoring (Caduff et al., 2015; Monserrat et al., 2014; Wujanz et al., 2013). As an active remote sensing technology based on microwave interferometry, GBSAR is independent of solar illumination and can be operated day and night (Scaioni, 2015). In comparison to other ground-based technologies, GBSAR is able to monitor natural and artificial surfaces with areal extents of up to a few square kilometres and offers the measurement of surface displacements towards the sensor with sub-millimetre precision in the ideal case (e.g. Caduff et al., 2015; Monserrat Hernández, 2012). In comparison to spaceborne SAR, GBSAR has inherent advantages in terms of portability and flexibility for data collection (e.g. Caduff et al., 2015; Monserrat et al., 2014). The GBSAR monitoring technique can also be applied to deformation phenomena with a wide range of surface change rates, theoretically ranging from a few millimetres per year up to metres per day (e.g. Monserrat Hernández, 2012; Rödelsperger, 2011). The aforementioned characteristics of GBSAR make it unique and complementary to existing deformation monitoring techniques, thereby possessing potential in the prediction and mitigation of relevant hazards. However, GBSAR is still a relatively new endeavour and requires improvements related to data processing for the exploitation of its ability and potential in deformation monitoring.

It is worth noting that the inherent disadvantages of any InSAR techniques (spaceborne or ground-based InSAR) include (e.g. Caduff et al., 2015; Monserrat et al., 2014): (i) they require coherent data and are therefore not applicable to areas with thick vegetation; and (ii) the deformation measurement is limited to the line-of-sight (LOS) direction, which means that displacements perpendicular to the LOS cannot be measured.

Overall, each technology has its own pros and cons. Given the specific characteristics of

GBSAR and the opportunity that Newcastle University purchased a state-of-the-art MetaSensing FastGBSAR system (Rödelsperger and Meta, 2014) in October 2015, this project focuses on the development, improvement and scientific application of GBSAR interferometry for deformation monitoring.

1.2 Aims and objectives

Due to the inherent flexibility, a typical GBSAR system can be performed in either continuous or discontinuous mode for different scenarios, depending on the rates of change or the practical environment for instrument deployment (e.g. Caduff et al., 2015; Crosetto et al., 2014a; Crosetto et al., 2017; Monserrat et al., 2014).

The continuous operation mode offers a zero-baseline geometry, thus avoiding the effects of hardware related technical issues and leading to the best performances in terms of density, precision, reliability and real-time capability of deformation measurements (e.g. Crosetto et al., 2014a; Tarchi et al., 2005). According to Crosetto et al. (2017), continuous GBSAR represents the most commonly used configuration, which generally aims to achieve the surface evolution of an event or to provide rapid response to an urgent situation. In continuous monitoring, the flexibility and portability of GBSAR systems usually leads to a stack of consecutive acquisitions and offers opportunities for time series analysis. InSAR time series analysis is the advanced form of the differential InSAR technique to identify and quantify ground movements based on multiple interferograms generated from a stack of SAR images (e.g. Ferretti et al., 2001; Hooper et al., 2012; Lanari et al., 2007), which has advantages in terms of temporal resolution and decorrelation mitigation in contrast to the conventional differential InSAR. However, the majority of InSAR time series analysis algorithms were originally developed for spaceborne SAR imagery, and their applicability and performance has not been investigated by real-world GBSAR imagery which has its own unique imaging geometry and signal characteristics (e.g. Caduff et al., 2015; Rödelsperger, 2011). As a result, a special processing strategy for continuous GBSAR deformation monitoring needs to be developed, which has important implications for accurate estimation of surface movements and rapid response to deformation emergencies.

As far as discontinuous GBSAR is concerned, hardware related technical issues, such as repositioning errors due to installation and the difficulties in precise measurement of the GBSAR position and orientation parameters in practice, degrade the high-accuracy

measurement of deformation in a discontinuous campaign. With technical effort on its installation, discontinuous GBSAR is useful for monitoring an event whereby the deformation becomes significant within a relatively long period and the deployment of continuous GBSAR cannot be achieved (Crosetto et al., 2014a). Therefore, to unlock the potential of GBSAR, it is important to resolve these relevant research issues and develop a complete discontinuous GBSAR strategy as a complementary tool to the continuous GBSAR deformation monitoring for all scenarios to which GBSAR is potentially suited.

This research aims to design and develop an optimised processing framework to effectively utilise GBSAR for both continuous and discontinuous deformation monitoring applications. The research will emphasize the performance of InSAR time series analysis algorithms in terms of accuracy, robustness, and real-time capability. Specific objectives of this research are as follows:

1. To evaluate the suitability and, where necessary, make necessary improvements to current fundamental InSAR techniques and advanced time series analysis algorithms for processing GBSAR imagery;
2. To develop a (near-) real-time processing procedure with a high degree of automation for a current FastGBSAR instrument to minimise delay after each data acquisition and to maximise the precision and reliability of the output deformation maps;
3. To develop a discontinuous GBSAR procedure as a complementary module to the continuous pipeline for a complete GBSAR interferometry framework;
4. To establish case studies to prove the feasibility of the developed GBSAR data processing techniques and procedures for a range of deformation monitoring applications to which GBSAR is potentially suited.

It is worth noting that experiments in the thesis have been conducted based on FastGBSAR datasets. Nevertheless, the algorithms proposed are independent of the GBSAR system and could in principle be applied to any GBSAR instrument and similar high-resolution ground-based imaging radar instrument, e.g. the Gamma Portable Radar Interferometer (GPRI) (Werner et al., 2012) and multiple-input multiple-output (MIMO) radars (Tarchi et al., 2013).

1.3 Thesis outline

The thesis comprises seven chapters. The rest is outlined below.

Chapter 2 provides an overview of the concepts of GBSAR (especially FastGBSAR) and the principles of the GBSAR interferometric technique. It also details the methodological steps of the general procedure of GBSAR time series analysis for deformation monitoring. It explains the core process of GBSAR time series analysis, and highlights associated error sources. This chapter establishes the fundamental aspects and the basic workflow of the proposed GBSAR data processing software system. A review of various relevant algorithms, alongside their applications, are also presented.

Chapter 3 proposes an efficient similarity measure to identify pixels with similar amplitude behaviours and presents a comprehensive non-local algorithm based upon this concept for accurate coherence estimation and phase filtering in GBSAR interferometric processing. Experiments are conducted to assess the performance of the proposed algorithm on coherence estimation and phase filtering.

Chapter 4 presents an effective approach to selecting coherent pixels from a network of interferograms, aiming to maximise the density of selected pixels and optimise the reliability of GBSAR time series analysis. Experiments are carried out on two actual FastGBSAR datasets and a deeper analysis is performed by comparing the proposed approach with the selection of coherent pixels using a single pair of GBSAR images, as well as the persistent scatterer selection based on amplitude dispersion index.

Chapter 5 describes the challenges of processing long and consecutive stacking GBSAR acquisitions and presents a complete GBSAR data processing chain for real-time continuous GBSAR deformation monitoring. The challenges in processing continuous GBSAR data have been rigorously resolved in the proposed GBSAR chain. Two continuous monitoring applications are completed in this chapter. The accuracy, reliability of the results are evaluated and the real-time capability of the proposed chain are assessed.

Chapter 6 presents a complete interferometric processing chain for discontinuous GBSAR deformation monitoring. Automatic co-registration of GBSAR data is implemented in this processing procedure. Typical errors in GBSAR interferometry, such as repositioning and atmospheric errors, are investigated and simulated from the fundamental GBSAR observation geometry. A new model is proposed and integrated to this discontinuous processing procedure for the correction of these errors. Experiments on both synthetic and real GBSAR data are conducted, demonstrating the feasibility of the proposed chain.

Chapter 7 brings together the findings and contributions from Chapters 3, 4, 5 and 6 and addresses the advantages, limitations, challenges and opportunities related to the developed GBSAR data processing techniques and procedures for deformation monitoring.

Chapter 2. Principles of GBSAR interferometry

2.1 GBSAR principles

2.1.1 Radar basics

Radar, the acronym for radio detection and ranging (Skolnik, 1962), is an active sensor technology which radiates electromagnetic pulses from an antenna to propagate in space and detects the returning pulses from reflecting objects in its LOS (e.g. Hanssen, 2001; Skolnik, 2008). The range (r) between a target and a radar sensor is determined by measuring the two-way travel time (τ) of the pulse that propagates at the speed of light (c) out to the target and back to the radar, i.e.:

$$r = c\tau/2. \tag{2.1}$$

To designate radar operating frequency bands, a list of letter-band nomenclature has been officially standardized by the IEEE (Institute of Electrical and Electronic Engineers) (IEEE, 2003), as shown in Table 2.1. Radar technology, capabilities, and applications vary considerably with the operating frequency bands (Skolnik, 2008). Generally, it is easier to construct high-power transmitters and large antennas, thus longer-wavelength and higher-frequency bands are easier to achieve. On the other hand, shorter-wavelength signals at lower frequency bands have advantages in measuring accurate range and location due to wider bandwidth, as well as narrower beam antennas at a given physical size antenna.

Table 2.1. IEEE Standard Radar Frequency Letter-Band Nomenclature.

Band Designation	Frequency (GHz)	Wavelength (cm)
HF	0.003 to 0.030	10000 to 1000
VHF	0.030 to 0.300	1000 to 100
UHF	0.300 to 1	100 to 30.0
L band	1 to 2	30.0 to 15.0
S band	2 to 4	15 to 7.5
C band	4 to 8	7.5 to 3.8
X band	8 to 12	3.8 to 2.5
Ku band	12 to 18	2.5 to 1.7
K band	18 to 27	1.7 to 1.1
Ka band	27 to 40	1.1 to 0.75
V band	40 to 75	0.75 to 0.40
W band	75 to 110	0.40 to 0.27
Mm	110 to 300	0.27 to 0.10

Radar represents a broad concept and can be classified into more than ten types by Skolnik (2008) based on the major features. As a specific class of radar systems, imaging radars, such as side-looking (airborne) radar and later SAR, are built with the ability to resolve targets (Soumekh, 1999). This type of radar produces a two-dimensional (2D, i.e. in range and cross-range) image of an observed scene. GBSAR belongs to the high-resolution imaging radar class. GBSAR was originally adapted from spaceborne platforms to terrestrial applications in the late 1990s (e.g. Rudolf et al., 1999; Tarchi et al., 1999b). The last couple of decades have witnessed rapid advancement of GBSAR instrumentation in terms of operating flexibility, data acquisition efficiency, range and azimuth resolutions (Caduff et al., 2015). This section introduces the main features of a typical GBSAR system by making explicit reference to the FastGBSAR system manufactured by the Metasensing Company, The Netherlands. An overview of the FastGBSAR system is given in Figure 2.1.

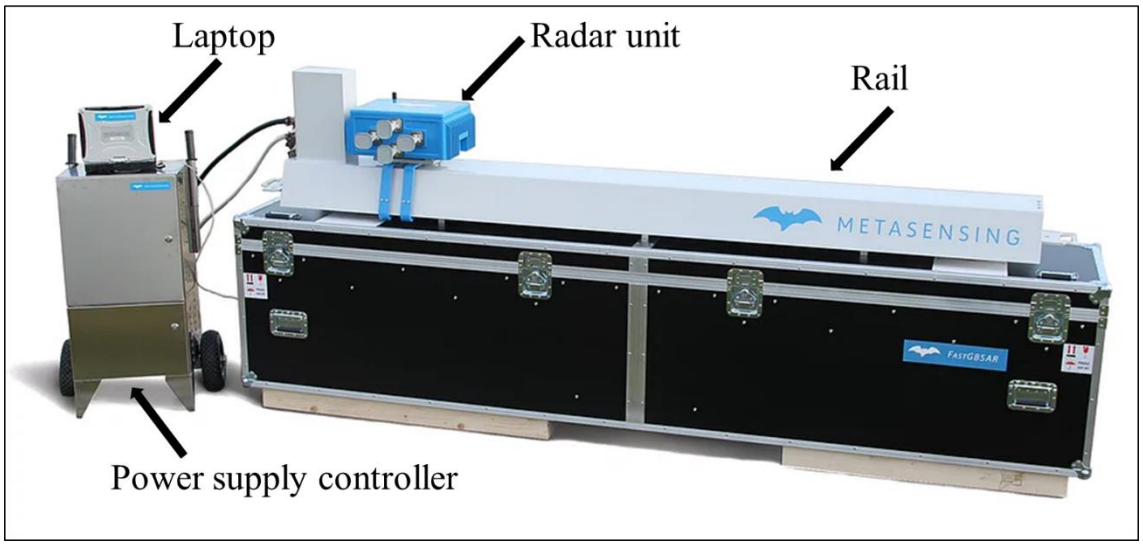

Figure 2.1. Overview of a FastGBSAR instrument. Main hardware components include laptop, power supply controller, radar unit, and rail. The background image (without labels) is courtesy of the Metasensing Company, The Netherlands.

FastGBSAR is the product of the combination of the frequency modulated continuous wave (FMCW) technique and the SAR technique (e.g. Meta et al., 2007; Rödelsperger et al., 2012). The range imaging is achieved by FMCW and the cross-range imaging by SAR.

2.1.2 Range imaging equation

FMCW represents a special technique capable of determining the range with high resolution between the radar and the reflecting targets (Yang, 2017). In the simplest form of a FMCW radar (Melvin and Scheer, 2014), the transmitted signal (or pulse) is increased with a constant

rate, each successive signal thus has a higher frequency than its previous one. The frequency of the transmitted signal is usually linearly modulated and this process continues for a period that is at least several times as long as the two-way propagation time of the furthest target in an observing scene. During this period, the frequency difference between the transmitted and received signal can be measured and converted to the time delay and hence the range. The cycle is then repeated from the starting frequency. The basic principle of FMCW is actually to convert the problem of measuring the time lag to measuring the corresponding frequency difference, because the latter is usually much easier to be measured as it is in audio range (Wolff, 2018). To generate constant power, FMCW radars operate with low transmission power, which leads to their compactness but limits the measuring range to a few kilometres (Meta et al., 2007). In FastGBSAR, the transmitted pulse is linearly modulated (Metasensing, 2015b). The FMCW waveform of FastGBSAR is illustrated in Figure 2.2.

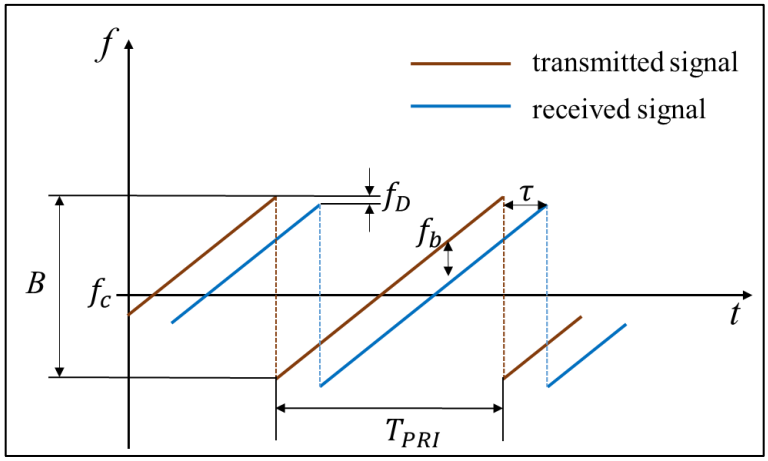

Figure 2.2. FMCW waveform of FastGBSAR.

As shown in Figure 2.2, f_c is the centre frequency of the signal; B the bandwidth; T_{PRI} the pulse repetition interval; and f_D a possible Doppler frequency caused by a moving target. The frequency difference between the transmitted and received signal is termed beat signal or beat frequency (denoted as f_b). The measured beat frequency f_b is the raw data recorded by the FastGBSAR (Metasensing, 2015b). At any time, the beat frequency f_b is proportional to the time delay τ between the transmitted and received signal and therefore proportional to the range r between the radar and the observing target:

$$f_b = \frac{2B}{c\,T_{PRI}} r. \tag{2.2}$$

Therefore, the range can be measured through the observed f_b:

$$r = \frac{c\, f_b\, T_{PRI}}{2B}. \tag{2.3}$$

In terms of the range resolution (δ_r), it means the minimum distance between two targets in the range direction that a radar is able to distinguish and separate to each other. The range resolution depends on the bandwidth B of the transmitted signal:

$$\delta_r = c/2B. \tag{2.4}$$

2.1.3 Cross-range imaging equation

Cross-range direction is also known as azimuth direction, which is perpendicular to the range direction. To determine the 2D position of a target, it requires the angular measurement of the direction between the radar antenna and the target. This is achieved by the directivity (or known as directive gain) of the antenna, which is the ability of the antenna to concentrate the transmitted energy in a particular direction (Wolff, 2018). The transmitted energy for most radar antennas is designed in a one-directional lobe or beam (Wolff, 2018). The beam width of the transmitted signal determines the accuracy of angular measurement and therefore the spatial resolution in the cross-range direction. The beam width is the angular range of a radio antenna pattern (or signal) in which half power (-3 decibels) can be transmitted thus it is usually expressed in degrees (e.g. Edde, 1993; Van Trees, 2004). Cross-range resolution (δ_{cr}), also known as azimuth resolution, is the minimum distance between two targets at the same range that a radar can distinguish and separate to each other. Figure 2.3 illustrates the relationship between the beam width (θ_B) and the cross-range resolution, as well as the range.

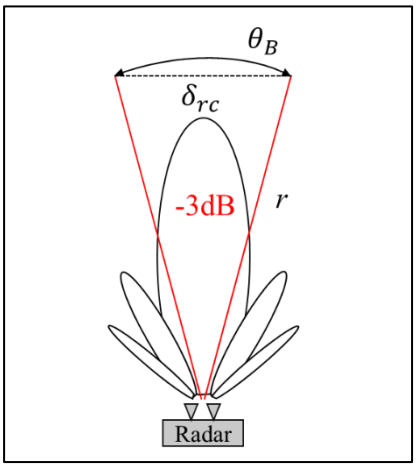

Figure 2.3 The relationship between cross-range resolution and beam width.

As shown in Figure 2.3, the relationship between δ_{cr}, θ_B, and r is:

$$\delta_{cr} \approx r\theta_B. \tag{2.5}$$

Therefore, cross-range resolution can be enhanced by narrowing the antenna beam width (Edde, 1993). It is known that the beam width for the real aperture radar (RAR) is determined by the physical length (L_a) of the antenna in the azimuth direction and the wavelength (λ) of the transmitted signal (Paul, 1997):

$$\theta_B = \frac{\lambda}{L_a}. \tag{2.6}$$

Accordingly, to improve the cross-range resolution, RAR systems need to enlarge the physical size of the antenna. However, there are several practical restrictions: (i) it is almost impractical to construct such long antennas for the long-range space observation with the cross-range resolution better than several hundred metres (Paul, 1997); and (ii) mounting long antennas may be challenging or not cost-effective for airborne platforms. Therefore, SAR techniques were developed with the aim of overcoming the issues and achieving a finer azimuth resolution in airborne and spaceborne radar observation. SAR is usually mounted on a moving platform and uses the motion of the radar to synthesize a large size of the antenna (Skolnik, 2008). Particularly, FastGBSAR creates a synthetic antenna by moving the radar unit along a linear rail (Rödelsperger et al., 2012). A general 2D SAR imaging scenario is illustrated in Figure 2.4.

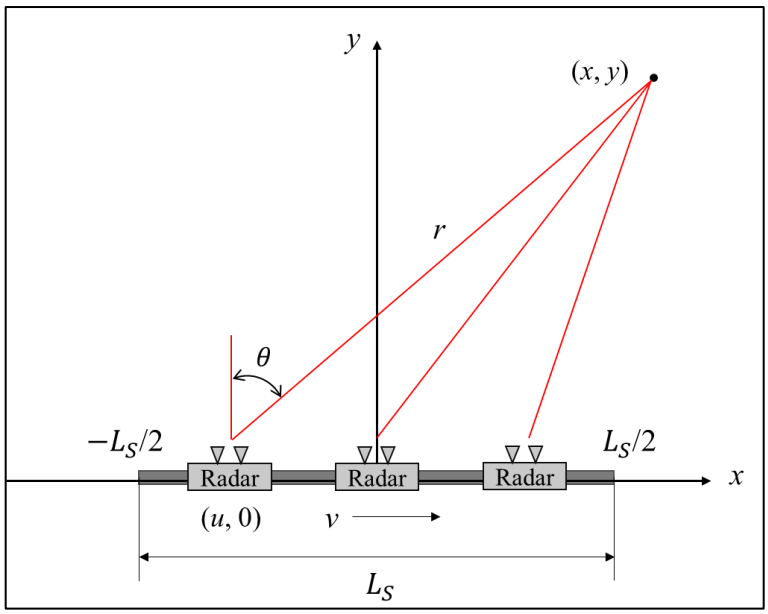

Figure 2.4 SAR geometry for cross-range imaging.

As shown in Figure 2.4, the scenario comprises a SAR system and an arbitrary target located at (*x, y*), where the *x*-axis is parallel to the radar rail and the *y*-axis is perpendicular to the rail

direction. L_S is the length of the radar rail. For one acquisition, the radar unit (with antennas) moves along a linear track between the range $[-L_S/2,\ L_S/2]$ with a constant velocity (v). While the radar unit moves, the antennas continuously transmit and receive signals. That is to say the target is illuminated by the radar from many positions. Assuming the radar is at the position (*u, 0*), the antenna aspect angle (θ) and the range *r* with respect to the target are:

$$\begin{cases} r = \sqrt{(x-u)^2 + y^2}, \\ \theta = \arctan\left(\frac{x-u}{y}\right) = \arcsin\left(\frac{x-u}{r}\right). \end{cases} \tag{2.7}$$

The constant motion of the radar has a range-directional component ($v_r = v\sin(\theta)$, i.e. the velocity that the target approaches or recedes from the sensor), which results in a shift in frequency (f_D) known as the Doppler effect (Paul, 1997):

$$f_D = \frac{2v\sin(\theta)}{\lambda} = \frac{2v}{\lambda}\frac{(x-u)}{r}. \tag{2.8}$$

The azimuth coordinate of the target can thus be determined:

$$x = u + \frac{\lambda r f_D}{2v}. \tag{2.9}$$

During the period that the radar moves along the track, the range between the target and the radar changes. Accordingly, the beat frequency changes with the radar position according to Equation (2.2). The total frequency shift (f_B) is the difference between the frequencies of the two ends of the moving track, which determines the cross-range resolution (Rödelsperger, 2011):

$$\begin{cases} f_B = \frac{2L_S}{\lambda r}, \\ \delta_{cr} = \frac{1}{f_B} = \frac{2L_S}{\lambda r}. \end{cases} \tag{2.10}$$

For FastGBSAR, the history of beat frequency is the raw data that is recorded by the system. However, the beat frequency history of one single target inside the antenna beam contributes to a sample in the recorded raw data (or a pixel in the raw image) therefore is defocused. The time of acquisition of the raw data is termed coherency time (Metasensing, 2015b). To form a 2D image with range and azimuth resolution, FastGBSAR coherently combines the acquired raw data during the coherence time and finally transforms the data into a grid, which is termed focusing (Rödelsperger, 2011).

Combining the range and cross-range imaging, the resolution of a GBSAR image is fixed in range but variable in cross-range. The concept of GBSAR image resolution is illustrated in Figure 2.5.

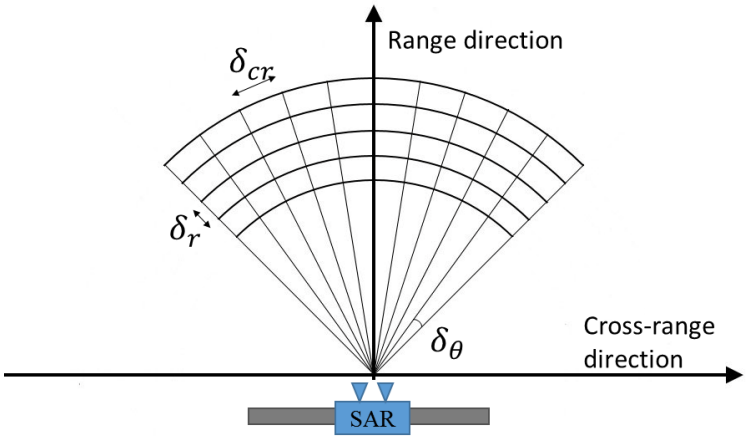

Figure 2.5 GBSAR image resolution.

It is worth mentioning that the SAR technique is not the only strategy to improve the spatial resolution for ground-based imaging radars. As the working range of a ground-based radar is usually limited to a few kilometres, which is much shorter than that of a spaceborne radar, obtaining a high cross-range resolution by increasing the physical aperture of the antenna is feasible for ground-based radars. A representative ground-based RAR system is the GPRI (Werner et al., 2012), the cross-range resolution can reach up to 8 metres at 1 km distance. More recently, the MIMO or MIMO-SAR concept has been demonstrated as a potentially equivalent technique to SAR for ground-based imaging radars and become an active area of research for the next generation of radars (e.g. Tarchi et al., 2013; Zeng et al., 2016). Unlike GBSAR, which moves the antenna for image acquisition, ground-based MIMO radars place and fix a set of antennas on a rail and transmit different waveforms at the same time while acquiring data. They can be superior to conventional GBSAR system in terms of portable size, financial cost, and more attractive acquisition efficiency (possibly at a rate of 25+ frames per second) (Tarchi et al., 2013). However, this technique is still under development (e.g. Aria et al., 2018; Liu et al., 2018; Monserrat et al., 2014). Although the GPRI and MIMO radars utilise different techniques for high-resolution cross-range imaging, they produce 2D radar images in the same form as GBSAR.

2.1.4 GBSAR observation

Like any SAR measurements, GBSAR acquisitions have two types of observable: amplitude and phase (Osmanoğlu et al., 2016). The amplitude is the strength of the back-scattered electromagnetic wave, which provides information on the reflectivity of the illuminated field (Deledalle et al., 2011) and can be used to interpret the observing scene (Monserrat et al., 2014). The phase is related to the round-trip time that the electromagnetic wave travels between the radar and the target, and thus can be exploited to measure the surface topography and displacement (Monserrat et al., 2014). In a GBSAR image, a pair of amplitude and phase observations can be represented as a complex number. For example, the amplitude a and phase ϕ are represented as complex number s:

$$s = ae^{\phi} = a\cos\phi + ja\sin\phi. \tag{2.11}$$

where j is the imaginary unit. The amplitude and phase information of an observing area is stored in the single-look complex (SLC) image, i.e. the focused SAR image.

As mentioned in Section 2.1.3, the GBSAR image geometry is the result of a constant range sampling coupled with a constant angular sampling (Monserrat Hernández, 2012). However, as GBSAR has an oblique viewing geometry, irregular terrain elevation will result in slant-range distortions in the image. Figure 2.6 shows the typical effects of foreshortening, layover, and shadow.

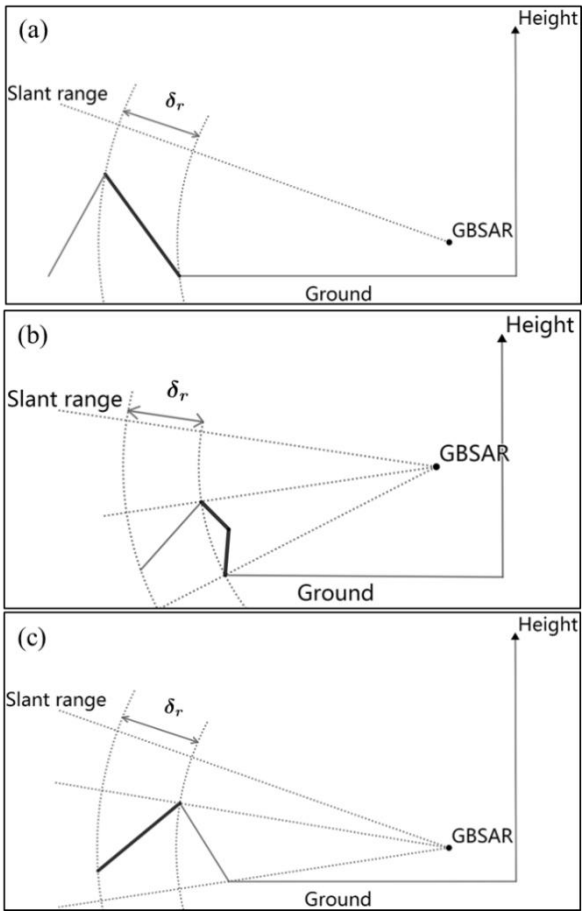

Figure 2.6. Slant-range distortions in GBSAR: (a) foreshortening, (b) layover, and (c) shadow.

Owing to the inherent geometric distortions, interpretation of GBSAR imagery is not as straightforward as in photographic imagery. Figure 2.7 shows a GBSAR amplitude mean image of a farm and the corresponding photographic image of the scene. For the sake of interpretation, the GBSAR amplitude mean image is manually co-registered with the planimetric view of the observing site in Google Earth.

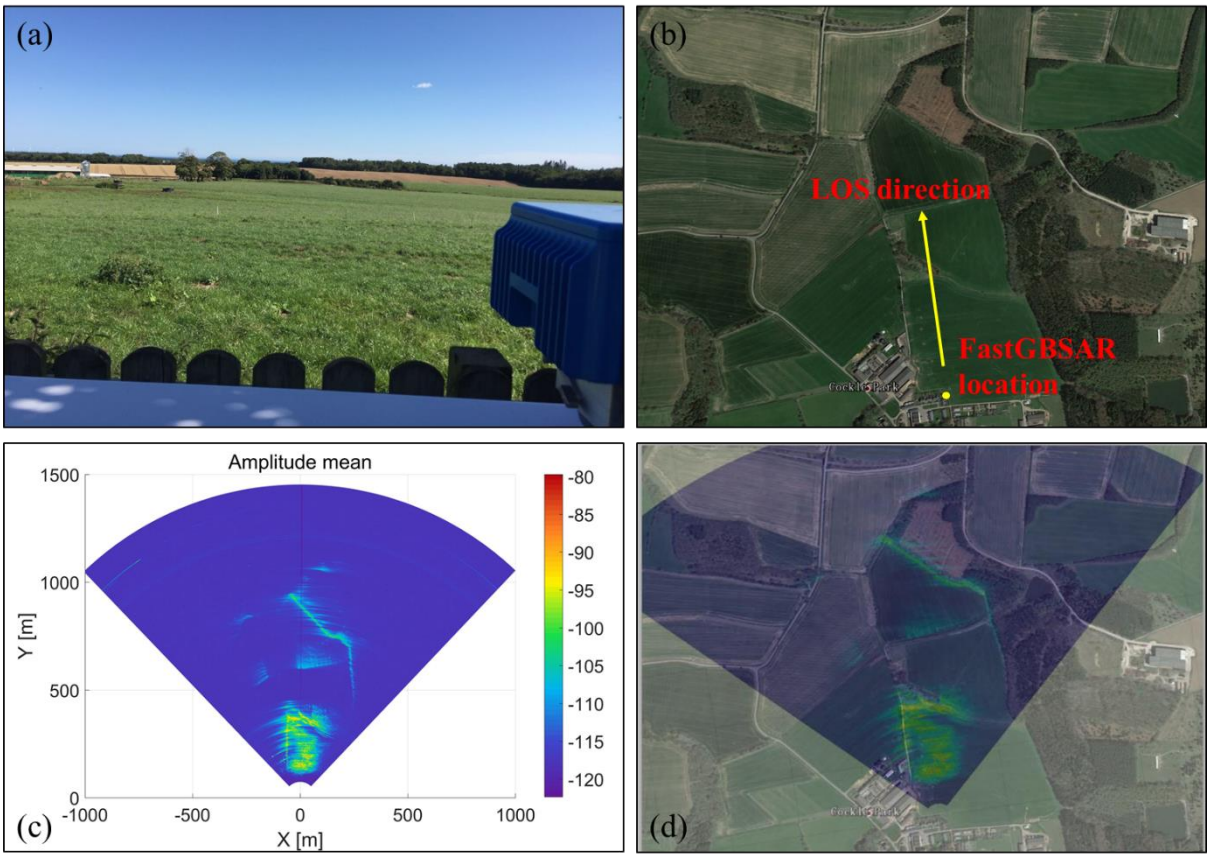

Figure 2.7. GBSAR imagery compared to photographic imagery, acquired at Cockle Park Farm in Morpeth, UK. (a) Overview of the site. (b) The planimetric view of the site from Google Earth. (c) The GBSAR amplitude map (the mean amplitude over a stack of images), coloured in decibels (dB). (d) Approximate alignment and co-registration of the mean amplitude image with the planimetric view of the site in Google Earth.

2.1.5 Relevant coordinate systems

To visualize or georeference GBSAR imagery, several coordinate systems are introduced. Specifically, the object space coordinate system in three dimensions is defined as $O-XYZ$. The GBSAR image local coordinate systems include two planar coordinate systems: $s-r\theta$ (a polar coordinate system) and $s-xy$ (a Cartesian coordinate system, also known as the orthogonal coordinate system). In particular, the x-axis of the Cartesian coordinate system is parallel to the moving rail. In addition, a transition coordinate system $s-xyz$ is also introduced, which can be used to express the position and attitudes of a GBSAR instrument in operation.

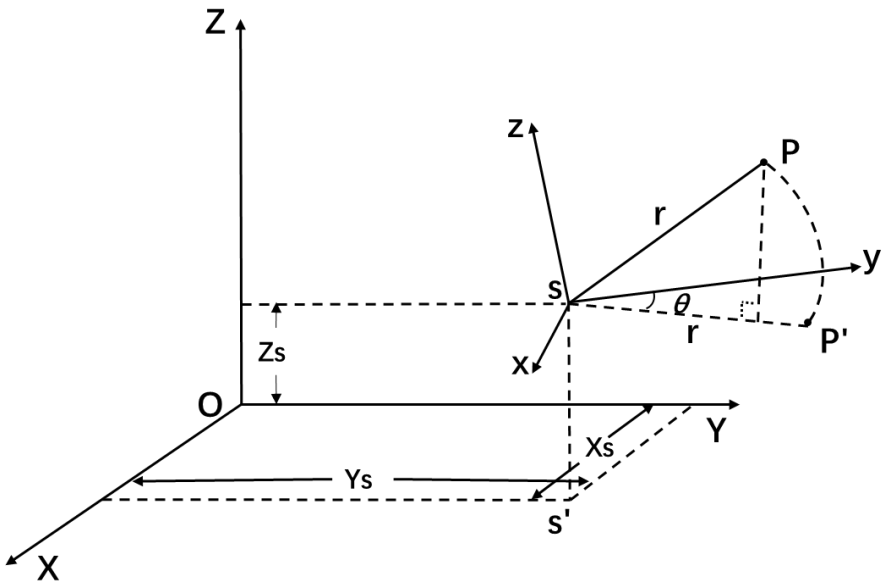

Figure 2. 8. Illustration of GBSAR related coordinates systems.

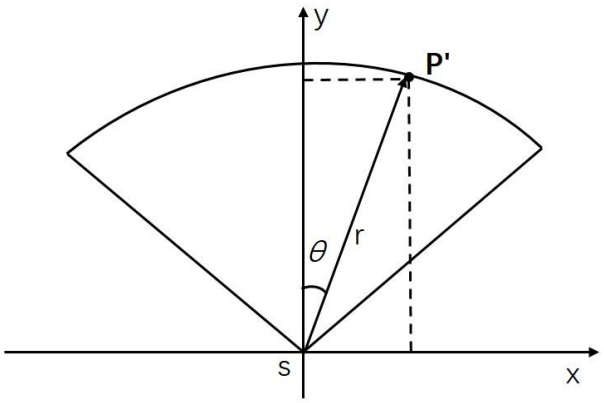

Figure 2.9. Illustration of GBSAR local systems, including the Cartesian coordinate system $s-xy$ and the polar coordinate system $s-r\theta$.

As shown in Figure 2.8, a ground target P is located at $(X,\ Y,\ Z)$ in space and observed by a GBSAR system. The location of P in the GBSAR local coordinate systems is at P' with the polar coordinates of $(r,\ \theta)$ and the Cartesian coordinates of (x, y). The coordinates in the transition coordinate system are (x, y, z). Note that P' is different from the perpendicular projection position of P on the GBSAR image plane. The origin of the GBSAR local coordinate system is denoted as s, of which the object space coordinates are (X_s, Y_s, Z_s). The relations among these coordinate systems are summarized as follows:

$$\begin{cases} x = X - X_s, \\ y = \sqrt{(Y - Y_s)^2 + (Z - Z_s)^2}. \end{cases} \tag{2.12}$$

$$\begin{cases} r = \sqrt{x^2 + y^2}\,, \\ \theta = \text{atan2}(y, x). \end{cases} \tag{2.13}$$

$$\begin{cases} R = r/\delta_r\,, \\ C = (\pi - \theta)/\delta_\theta\,. \end{cases} \tag{2.14}$$

where atan2 is the four-quadrant inverse tangent function; R and C are the row number and the column number, respectively, in the GBSAR image.

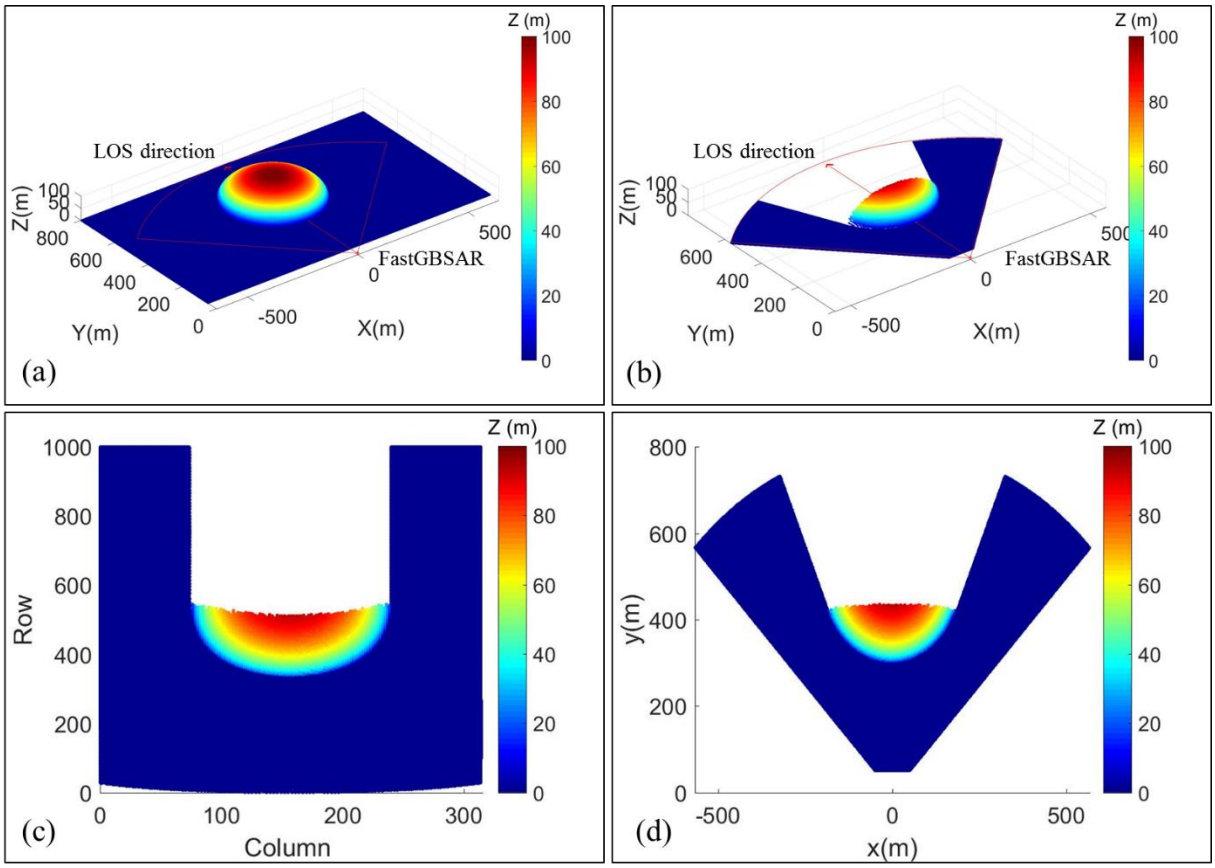

Figure 2.10. Simulation of GBSAR imaging geometry. (a) Overview of the simulation: the DEM is generated in the object space coordinate system with a spatial resolution of 0.5 m in X axis and 0.75 m in Y axis within the range (-640≤X≤640,20≤Y≤800). Elevation for the whole grid is zero, except for the "dome" which is simulated as a hemisphere from an ellipsoid with the mathematical expression:$X^2/200^2+(Y-500)^2/200^2+Z^2/100^2=1$ (Z>0). A FastGBSAR is located at (0, 0, 5), looking at (0, infinity, 5) with an angle of view of 90 degrees. (b) Removal of the non-imaging areas, including the shadow zone that is detected by means of occlusion-test and the outside of the area of interest that is defined as (100≤R≤800,45°≤θ≤135°). (c) The 2D GBSAR occlusion-free map of the synthetic terrain, which is displayed in the planar Cartesian coordinate system. (d) The row and column numbers (i.e. pixel coordinates) with respect to the GBSAR occlusion-free map.

To further explain the transformation of different GBSAR-related coordinate systems, a simulation of a synthetic DEM, together with FastGBSAR geometry, is given in Figure 2.10.

An occlusion-test is performed during the process of projecting the DEM defined in the 3D object space coordinate system to the 2D GBSAR local coordinate systems. Since the simulation focuses only on the geometry, the reflection (namely the radiation part) is not considered.

2.1.6 FastGBSAR specifications

FastGBSAR arguably represents the state-of-the-art GBSAR hardware available globally. The FastGBSAR system can be set up in either RAR or SAR mode (Liu et al., 2015). The spatial resolution for FastGBSAR can be adjusted and the technical specifications with respect to the finest resolution are summarized in Table 2.2.

Table 2.2. Nominal FastGBSAR technical specifications with respect to the finest resolution.

	RAR	**SAR**
Frequency	17.2 GHz (Ku)	17.2 GHz (Ku)
Bandwidth	300 MHz	300 MHz
Maximum working range	4 km	4 km
Range resolution	0.5 m	0.5 m
Rail length	Not required	1.8 m
Azimuth resolution	Not available	4.8 mrad
Repeat interval	0.25 ms	10 s

In FastGBSAR RAR mode, each acquisition can be performed and repeated within a few milliseconds, which makes it ideal for monitoring vibrations of buildings and structures (Placidi et al., 2015). The incapability of azimuth resolution, however, excludes its application to scenarios in which 2D spatial resolution is required. In this research, only FastGBSAR SAR mode is used and FastGBSAR specifically indicates the SAR mode of FastGBSAR.

In addition, the employed FastGBSAR system in this research is the polarimetric version (Metasensing, 2015b). Apart from deformation monitoring, this instrument allows the acquisition of full polarimetric data for retrieving additional information about the observed area, i.e. classification of vegetation. As this research focuses only on deformation monitoring, the potential of FastGBSAR polarization has not been explored and all FastGBSAR data used in this research is vertically polarized.

2.2 GBSAR interferometry

2.2.1 Differential InSAR

InSAR was developed to generate maps of surface deformation or digital elevation, using phase change between SAR acquisitions (Hanssen, 2001). The most common InSAR technique is differential InSAR (D-InSAR) which uses two SAR images, generally referred to as the master and the slave images, to identify and quantify ground movements (e.g. Hu et al., 2014; Osmanoğlu et al., 2016). In D-InSAR processing, an interferogram is formed by interfering two complex images, i.e. it is the product of the pointwise multiplication between the master complex image and the conjugate of the slave image (Hanssen, 2001):

$$\mathrm{s} = s_1 s_2^* = a_1 a_2 e^{j(\phi_1 - \phi_2)}, \tag{2.15}$$

where s_1 and s_2 are the complex backscattered signals of the same target on the master and the slave images, respectively. a_i and ϕ_i are the amplitude and phase of the complex signals s_i $(i = 1, 2)$, respectively. The superscript * denotes the complex conjugate operator and j the imaginary unit. The phase difference between the master and slave SAR images is termed interferometric phase (φ^w) (Prati et al., 2010), which is the superposition of many terms including the change resulted from the surface movement in the LOS direction (φ^{disp}), the topographic effect (φ^{topo}), the variation of atmospheric delays (φ^{atm}), the ambiguous cycles (n) and noise (φ^{noise}). The symbol w represents the wrapping operation of angle in radians $[-\pi,\ \pi]$. The differential interferometric phase for a pair of pixels on the two images with respect to the same target can be written as follows:

$$\varphi^w = w(\phi_1 - \phi_2) = \varphi^{disp} + \varphi^{topo} + \varphi^{atm} + \varphi^{noise} - 2n\pi. \tag{2.16}$$

The parameter of interest in D-InSAR application is the phase contribution φ^{disp}, which is directly related to the change of the ranges r_1 and r_2 from the radar system to the target at two acquisitions:

$$\varphi^{disp} = \frac{-4\pi}{\lambda}(r_2 - r_1) = \frac{-4\pi}{\lambda}\Delta r = \frac{-4\pi}{\lambda} d_{LOS}. \tag{2.17}$$

where Δr is the range change, i.e. the surface displacement in the LOS direction (d_{LOS}). Thus, the aim of D-InSAR is to extract the phase contribution φ^{disp}, together with other components. Once it is done, the surface displacement in the LOS direction for each pixel can be calculated

by:

$$d_{LOS} = \Delta r = (r_2 - r_1) = \varphi^{disp} \frac{\lambda}{(-4\pi)}. \tag{2.18}$$

The LOS displacement d_{LOS} for each pixel is the GBSAR measurement in deformation monitoring. It is worth noting that d_{LOS} is only the projection of the true displacement in the LOS direction, which is shown in Figure 2.11. This one-dimensional (1D) measurement represents the inherent disadvantage of InSAR as mentioned previously.

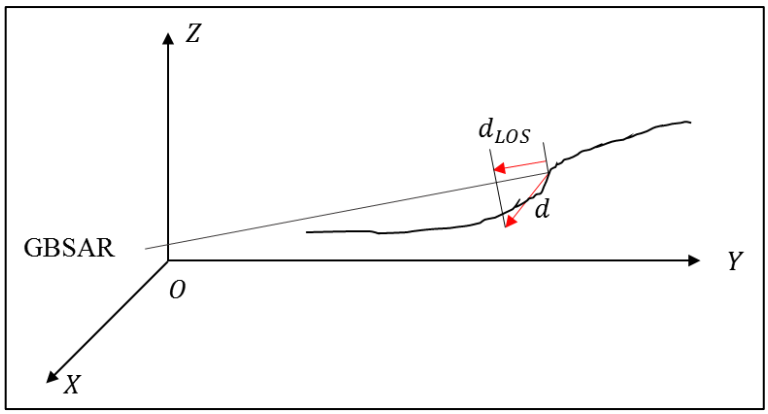

Figure 2.11. The LOS displacement d_{LOS} versus the true displacement d.

To extract the LOS displacement, it requires a complex procedure of D-InSAR processing. Specifically, in Equation (2.16), the interferometric phase φ^w is wrapped into the range $[-\pi,\ \pi]$. The interferometric phase is actually a relative value due to the integer ambiguity n (Osmanoğlu et al., 2016). To obtain the absolute value (i.e. unwrapped phase), the recovery of the ambiguity is required, and the process is known as phase unwrapping (Zebker and Lu, 1998). Figure 2.12 compares the wrapped and unwrapped phase with respect to a time series of displacements. This 1D phase unwrapping concept can be extended to the 2D and 3D scenarios, which are known as 2D and 3D phase unwrapping and further discussed in the next chapter.

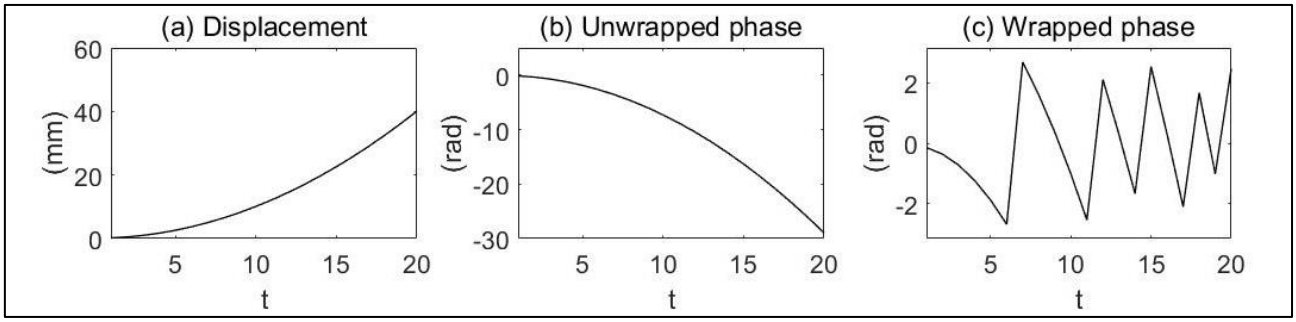

Figure 2.12. The wrapped and unwrapped phase of the same displacements (λ=17.43 mm).

After unwrapping, the unwrapped phase can be written as follows:

$$\varphi = \varphi^{topo} + \varphi^{disp} + \varphi^{atm} + \varphi^{noise}. \tag{2.19}$$

The topographic term φ^{topo} is a function of the perpendicular spatial baseline B and the elevation z along the axes defined by the antenna vertical motion:

$$\varphi^{topo} = \frac{4\pi}{\lambda} r \left(1 - \sqrt{1 - \frac{2zB + B^2}{r^2}} \right), \tag{2.20}$$

where r is the range to the target when the antenna is positioned at z = 0 (Noferini et al., 2007).

Unlike spaceborne SAR, GBSAR data can be acquired continuously and discontinuously (Takahashi et al., 2013). The continuous operation mode offers a zero-baseline geometry, thus the topographic phase component is always zero. In a discontinuous campaign, the topographic contribution resulting from small repositioning errors can be corrected by treating it as a spatially smooth signal (e.g. Crosetto et al., 2014a; Monserrat et al., 2014). Otherwise, the topographic term can be removed with the support of a DEM of the monitoring area and the precise geometry configuration of the radar equipment in the event of a significant spatial baseline. Without loss of generality, there are always at least three other terms that play a role in GBSAR interferometry (Crosetto et al., 2015):

$$\varphi = \varphi^{disp} + \varphi^{atm} + \varphi^{noise}. \tag{2.21}$$

To obtain precise displacement, the atmospheric term φ^{atm}, also known as atmospheric phase screen (APS) in spaceborne SAR, must be properly compensated and removed by means of any suitable technique (Iannini and Guarnieri, 2011). The atmospheric term is caused by the variation of the refractivity at different times. A general and simple model explaining its physical existence is based on the velocity of an electromagnetic wave through the homogeneous troposphere by the refractivity N, which strictly depends on pressure P (in millibars or hectoPascal), temperature T (in Kelvin) and relative humidity H (as a percentage) (Iannini and Guarnieri, 2011; Iglesias et al., 2014b; Pipia et al., 2008):

$$N = N(P, T, H) = N_{\mathrm{dry}} + N_{\mathrm{wet}} = \frac{77.6 \cdot P}{T} + \frac{3.73 \times 10^5 \omega_P}{T^2}, \tag{2.22}$$

where N_{dry} represents a dry or hydrostatic component that is related to the partial pressure of

dry gases, and N_{wet} a wet component that is dependent on the partial pressure of water vapour ω_{P}:

$$\omega_{\mathrm{P}} = 6.11\mathrm{e}^{(19.7\frac{\mathrm{T}-273}{\mathrm{T}})}H. \tag{2.23}$$

Accordingly, the atmospheric phase variation between the master and the slave images is:

$$\varphi^{\mathrm{atm}} = 10^{-6}\frac{4\pi}{\lambda}\Delta N\, r = 10^{-6}\frac{4\pi}{\lambda}[N(P_2, T_2, H_2) - N(P_1, T_1, H_1)]\, r. \tag{2.24}$$

The aforementioned interferometric phase equations hold for every pixel in the interferogram. However, the application of D-InSAR to deformation monitoring encounters problems due to the phase noise term. Not all the observed pixels can be exploited for deformation measurement. A higher noise level means a lower phase quality and a lower capability of this pixel to derive deformation information (Monserrat Hernández, 2012). Filtering techniques are, therefore, applied to increase the signal-to-noise ratio (SNR) of interferograms (e.g. Bioucas-Dias et al., 2008; Deledalle et al., 2011; Goldstein and Werner, 1998). Increasing the SNR leads to better phase statistics and fewer problems at the stage of phase unwrapping (Hanssen, 2001). The final step of D-InSAR processing is the geo-referencing, or geocoding, of the results through transformation of the relevant coordinate systems.

2.2.2 GBSAR time series analysis

The phase noise term in GBSAR interferometry results from variability in scattering from the target and thermal noise (e.g. Baran et al., 2003; Noferini et al., 2007), and the former source is dominant (Monserrat Hernández, 2012). The scattering variability depends on the physical and geometric characteristics of the measured target and its changes over the time elapsed between the master and slave images (Monserrat Hernández, 2012). The scattering variability due to physical and geometric characteristics are known as temporal and geometrical decorrelations, respectively (Hanssen, 2001). Specifically, the temporal decorrelation increases with the time span and the geometrical decorrelation increases with the spatial baseline (i.e. spatial separation) between acquisitions. Interferograms suffering from temporal decorrelations will have limited use for deformation monitoring. The advent of time series analysis has mitigated this limitation (e.g. Berardino et al., 2002; Ferretti et al., 2001). InSAR time series analysis is the advanced form of the differential InSAR technique to identify and quantify ground movements based on multiple interferograms generated from a stack of SAR images (e.g. Ferretti et al., 2001; Hooper

et al., 2012; Lanari et al., 2007). In comparison to D-InSAR, the InSAR time series analysis technique is primarily characterized by exploiting scattering properties of resolution elements and measuring mean velocities and incremental displacements (Hooper et al., 2012).

A number of InSAR time series analysis algorithms have been developed over the last two decades (Osmanoğlu et al., 2016). The majority of these analysis algorithms were originally developed for the purposes of processing spaceborne SAR imagery. These algorithms fall into two broad categories regardless of various derivatives: the first being persistent scatterer (PS) InSAR (PSI) (e.g. Ferretti et al., 2001; Hooper, 2008) which targets pixels with consistent scattering properties in time and viewing geometry, thus making this technique more suitable for artificial surfaces with sufficiently strong back scatterers, and the second being the more general small baseline subset (SBAS) algorithm which uses distributed scatterers and singular value decomposition to connect independent unwrapped interferograms in time (e.g. Berardino et al., 2002; Lanari et al., 2004). PSI techniques are commonly based on a single-master configuration and the main drawback of PSI techniques is the low spatial density of targets behaving coherently over the whole observation span (Perissin and Wang, 2012). By contrast, SBAS approaches construct a network of interferograms with multiple master images and small baselines (Shanker et al., 2011). More recently, methods have been developed that take advantage of both types of scattering (e.g. Blanco-Sanchez et al., 2008; Ferretti et al., 2011; Hooper, 2008; Perissin and Wang, 2012). A review of InSAR time series analysis algorithms can be found in Crosetto et al. (2016) and Osmanoğlu et al. (2016).

2.3 General procedure for GBSAR time series analysis

In spite of many variations, InSAR time series analysis follows a general procedure: generation of a network of interferograms from a stack of SAR images, selection of coherent pixels including persistent and distributed scatterers, phase filtering and unwrapping for coherent pixels, separation of APS from deformation, and geocoding. In the GBSAR case, geocoding may be dispensable, depending on the monitoring target and the purpose of the monitoring. Nevertheless, interpretation or visualisation of GBSAR imagery should be accomplished. Since geocoding or visualisation of GBSAR imagery has been introduced in Section 2.1.5, it will not be discussed again in this chapter.

2.3.1 Generation of interferograms

InSAR deformation monitoring with high accuracy is achieved by exploiting the interferometric phase. To generate an interferogram, any pixel pairs on master and slave images must correspond to the same observed target. In InSAR time series processing, SAR images are usually co-registered and resampled onto the same grid of a selected reference image (i.e. master image) before interferogram generation (Wang et al., 2014). As far as continuous deformation monitoring is concerned, a GBSAR instrument is usually installed on a fixed and stable base during the campaign. Continuous GBSAR acquisitions hold a zero-baseline geometry and they can be regarded as perfectly co-registered. Therefore, the co-registration of SAR images in traditional space-borne InSAR processing can be skipped for zero-baseline GBSAR data. Thus, a GBSAR interferogram can be easily generated from a pair of complex images based on Equation (2.15). In spaceborne SAR processing, multilooking is commonly applied in SBAS algorithms during the generation of interferograms, which aims to improve the SNR of the generated interferogram at the expense of spatial resolution. For the best preservation of spatial resolution, multilooking is not used in most GBSAR interferometric applications (e.g. Caduff et al., 2015; Crosetto et al., 2014a; Iglesias et al., 2015c; Monserrat et al., 2014; Rödelsperger, 2011), while it is used in some polarimetric applications (e.g. Iglesias et al., 2014d; Kang et al., 2009).

The goal of InSAR time series analysis for deformation monitoring is to obtain the displacement time series with respect to a reference acquisition. To this end, a connected network of interferograms must be constructed (Perissin and Wang, 2012). There are two network types: single-master and multiple-master (Perissin and Wang, 2012), of which the choice depends on the particular time series analysis algorithms. Figure 2.13 shows the schematic diagram of different interferogram networks. PSI algorithms often operate a number of interferograms regarding a common master image (Hooper et al., 2012), as illustrated in Figure 2.13(a). The single-master network is formed with the assumption that each slave image is coherent with the master image for pointlike PS targets (Perissin and Wang, 2012). In SBAS algorithms, in order to mitigate the decorrelation issues, a multiple-master network (Figure 2.13(b)) is often adopted (e.g. Berardino et al., 2002; Shanker et al., 2011). Nevertheless, it should be noted that (i) not every PS algorithm adopts the single-master network and (ii) a multiple-master network of interferograms is often but not necessarily redundant. For instance, Rödelsperger (2011) exploited the interferometric phase of PS pixels between time-adjacent acquisitions for the real-

time processing of GBSAR data. The network comprises only sequential interferograms and involves multiple masters. The network is not, however, redundant, which can be seen in Figure 2.13(c).

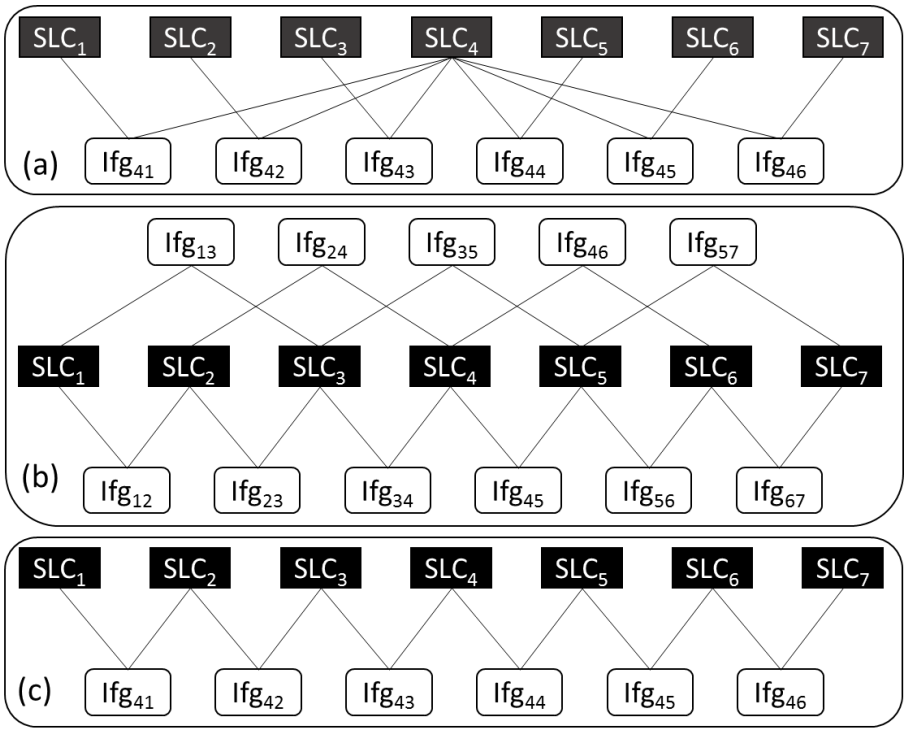

Figure 2.13. Schematic diagram of different types of interferogram networks based on seven single-look complex images (SLCs) in chronological order. Only the temporal baseline is considered in the network construction due to the spatial zero-baseline geometry of GBSAR data. Ifg_{MN} represents an interferogram that is generated by SLC_M (as the master) and SLC_N (as the slave). (a) A single-master network with SLC_4 is set as the unique master. (b) A redundant multiple-master network, in which a SLC image can link with the neighbouring two for the interferogram generation. (c) A non-redundant multiple-master network, comprising of only sequential interferograms.

2.3.2 Selection criteria for coherent pixels

InSAR time series analysis relies on the exploitation of coherent interferometric phase with high quality and low noise, which is held by only a particular class of pixels (Monserrat Hernández, 2012). The selection of coherent pixels plays an important role for a successful analysis as their quality and density are key factors to estimate the parameters of interest (e.g. Hooper et al., 2004; Perissin and Wang, 2012). Different selection criteria can be used to select coherent pixels. Among them, coherence and amplitude dispersion are the two most commonly adopted criteria.

Amplitude dispersion

Dispersion of amplitude (denoted as D_A), also termed as amplitude dispersion index (ADI), is an index that indicates the stability of amplitude time series for a pixel along a stack of SAR images, which is defined as (Ferretti et al., 2001):

$$D_A = \frac{\delta_A}{m_A}, \tag{2.25}$$

where m_A is the mean and δ_A the standard deviation of the amplitude time series, respectively. Reported by Ferretti et al. (2001), phase standard deviation δ_ϕ is highly correlated with the amplitude dispersion index D_A and the relationship $\delta_\phi \approx D_A$ is held by pixels with high signal-to-clutter ratio (SCR). A lower D_A implies a higher phase quality of a pixel. Typically, it requires a minimum of 20-30 SAR images to ensure the statistical reliability of D_A (Crosetto et al., 2008) and pixels with $D_A \leq 0.25$ are selected as persistent scatterer candidates (Osmanoğlu et al., 2016).

ADI-based PS selection is reported to be more suitable for urban areas with strong backscatterers, while the density of selected PS is generally too low to obtain a reliable measurement of surface deformation in rural areas with primarily natural terrains (Hooper et al., 2004). In order to improve such density, Hooper et al. (2004) proposed a method which identified initial pixels with a high threshold value $D_A \leq 0.4$ and further selected pixels with low phase residuals (i.e. good phase stability) after removing spatially correlated errors. An example of PS selection using FastGBSAR data is shown in Figure 2.14.

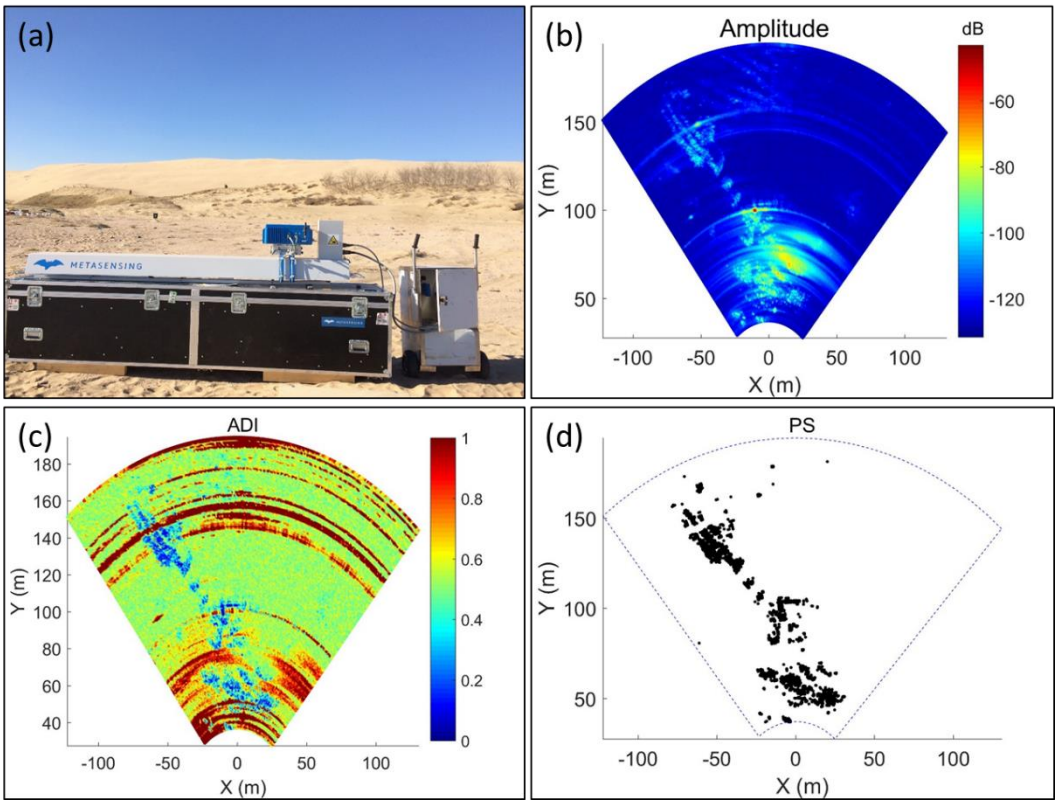

Figure 2.14. PS selection from a stack of 60 FastGBSAR images with a temporal resolution of one minute. Data collection was undertaken in a dune area located in Changli, Hebei, China. (a) Overview of the data collection. (b) Mean amplitude of the dataset. (c). ADI of the dataset. (d) The selection of PS pixels with ADI < 0.25.

Coherence

The coherence between two zero-mean complex signals, z_1 and z_2 (Touzi et al., 1999) is defined as:

$$\gamma = \frac{\mathbb{E}(z_1 z_2^*)}{\sqrt{\mathbb{E}(|z_1|^2)\mathbb{E}(|z_2|^2)}} = \rho \cdot e^{i\varphi} , \tag{2.26}$$

where the operation $\mathbb{E}[\cdot]$ represents the mathematical expectation and the superscript * denotes the complex conjugate operator. ρ is the coherence magnitude and φ is the interferometric phase. In practice, the ensemble average of signals cannot be achieved. The maximum likelihood coherence magnitude $\hat{\rho}$ for a pixel is the magnitude of the coherence estimation $\hat{\gamma}$ (i.e. $\hat{\rho} = |\hat{\gamma}|$), which is computed based on K samples related to the pixel (e.g. Jiang et al., 2014a; Touzi et al., 1999):

$$\hat{\gamma} = \frac{\sum_{l=1}^{K} z_{1,l} z_{2,l}^*}{\sqrt{\sum_{l=1}^{K} |z_{1,l}|^2} \sqrt{\sum_{l=1}^{K} |z_{2,l}|^2}}. \tag{2.27}$$

The coherence magnitude between two complex signals, ranging from 0 to 1, is strongly correlated with the standard deviation of the phase noise (e.g. Bamler and Hartl, 1998; Hanssen, 2001). Thus, coherence provides straightforward information on the SNR of interferometric phase and has been an efficient and commonly used indicator for masking out low-quality pixels in a SAR interferogram. Figure 2.15 shows two coherence maps estimated by a non-local estimator proposed in Chapter 3, one for a pair of images with a short time span of 10 seconds and the other for one hour.

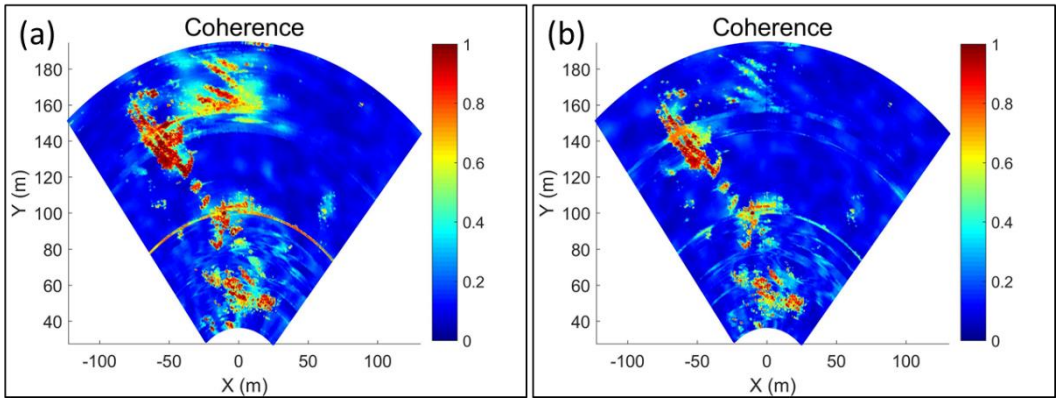

Figure 2.15. Coherence estimation examples using the data collected in Changli, Hebei, China. (a) Coherence map of a pair of SLCs with a 10-second time interval. (b) Coherence map of a pair of SLCs with a one-hour time interval.

Other selection criteria

Other measures such as thresholding on the amplitude or the SCR of a pixel are not widely used. For example, a pixel is selected as a PS point if its normalized radar cross section (i.e. the calibrated intensity) is above a specific threshold for a certain number of SLC images (Kamps and Adam, 2004). Additionally, a pixel is selected if the average SCR of the pixel is above a certain threshold (Adam et al., 2005). The relationship between the SCR and the standard deviation of phase noise δ_ϕ has been reported by Bert (2006) as:

$$\begin{cases} \delta_\phi = \frac{1}{\sqrt{2SCR}}, \\ SCR = \frac{s^2}{c^2}. \end{cases} \tag{2.28}$$

where s is the amplitude of the dominant scatterer that is surrounded by the clutter c (i.e. the unwanted echoes). A threshold SCR=2 can select pixels with phase standard deviation $\delta_\phi <$ 0.5 rad (~30◦). This method does not require calibrated amplitude to estimate the SCR or any assumptions on the temporal amplitude behaviour of the considered pixel. However, the

drawback is evident when it is applied to urban areas, where the clutter is likely to be overestimated using a spatial window because there are more point scatterers in close proximity to each other (Bert, 2006).

More recently, a new strategy based on the number of statistically homogeneous pixels (SHPs) has been increasingly adopted in spaceborne InSAR (e.g. Ferretti et al., 2011; Goel and Adam, 2012; Jiang et al., 2015). These algorithms aim to overcome the density limitation of PSI and improve the time series analysis over areas without enough persistent backscatterers by exploiting distributed scatterers (DSs) from areas with moderate coherence, where the neighbouring pixels share similar reflectivity values (e.g. Ferretti et al., 2011; Jiang et al., 2015). This type of area usually corresponds to non-cultivated lands with short vegetation, deserts, and debris areas (Ferretti et al., 2011). In these approaches (e.g. Ferretti et al., 2011; Goel and Adam, 2012; Jiang et al., 2015), statistically homogeneous pixels (SHPs) for each pixel are identified by means of statistical homogeneity testing techniques. Most PSs correspond to isolated pixels and DSs are associated with many SHPs, thus a DS can be identified by the number of its SHPs (Ferretti et al., 2011). Thereafter, the SNR of DSs can firstly be improved by means of spatial filtering (Goel and Adam, 2012) or so-called “phase triangulation” (Ferretti et al., 2011) and then integrated with PSs in time series analysis.

2.3.3 Phase filtering

Filtering of interferograms is not applied in conventional PSI, but typically used in SBAS approaches. Filtering can increase the SNR of interferograms (e.g. Bioucas-Dias et al., 2008; Deledalle et al., 2011; Goldstein and Werner, 1998). Increasing the SNR leads to better phase statistics and fewer problems at the phase unwrapping stage (Hanssen, 2001).

Phase information is contained in complex SAR images, and phase filtering is thus usually performed on the basis of complex numbers. A straightforward technique is “complex multilooking”, in which a number of looks in a rectangular window is simply averaged (Rodriguez and Martin, 1992). This technique is widely used because of its easy implementation and efficiency, but it results in resolution losses on the denoised images since the same smoothing effect is applied equally to homogeneous regions and to areas with edges or textures (Deledalle et al., 2011). InSAR phase filtering can be enhanced by dealing adaptively with the local phase noise and fringe rates in the frequency domain (Goldstein and Werner, 1998), which can be further improved by introducing coherence as a filtering parameter (Baran

et al., 2003). To mitigate the resolution loss issue while phase denoising, a number of techniques have been proposed. Lee et al. (1998) selected a directional window among eight edge-aligned windows according to the local phase noise level and fringe rates. Vasile et al. (2006) proposed an intensity-driven adaptive-neighbourhood approach, which selects adjacent pixels with similar intensity by means of a region-growing criterion. More recently, non-local filtering techniques have become a significant topic in the field of spaceborne InSAR as they can achieve favourable performance in preserving textures (e.g. Deledalle et al., 2011; Goel and Adam, 2012; Lin et al., 2015). The fundamental procedure of non-local methods comprises the identification of homogeneous or sibling pixels from a certain search window and the weighted means filtering of these resembling pixels. The majority of the non-local family can be primarily distinguished by the selection strategy of homogeneous or resembling pixels, e.g. by patch similarity (Deledalle et al., 2011) or by statistical homogeneity (Goel and Adam, 2012). In accordance with the coherence estimation in Figure 2.15, the non-local filter proposed in Chapter 3 is applied to the same data and the results are given in Figure 2.16. It is evident that interferograms after filtering are visibly smoother and less noisy.

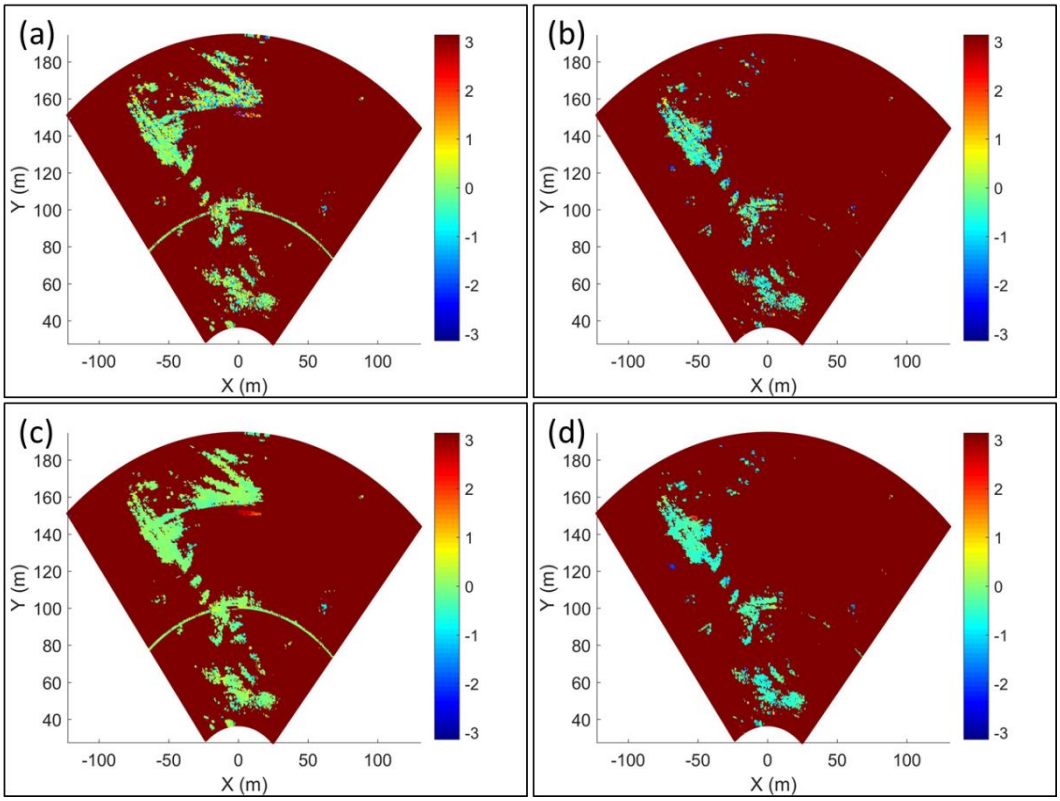

Figure 2.16. The interferometric phase at coherent pixels with γ>0.45. Pixels in decorrelated areas are marked in deep brown for the convenience of visualization. (a) The 10-second interferogram before filtering. (b) The 1-hour interferogram before filtering. (c) The 10-second interferogram after filtering. (d) The 1-hour interferogram after filtering.

2.3.4 Phase unwrapping

InSAR measurement of surface movements relies on the exploitation of interferometric phase between SAR acquisitions. Since the phase is observed on a circular and repeating space, the interferometric phase is actually a relative value that is wrapped into the range $[-\pi,\ \pi]$. The wrapped interferometric phase is always accompanied by the integer ambiguity or modulus n (Osmanoğlu et al., 2016). Phase unwrapping is therefore developed to recover the unambiguous interferometric phase from data with a modulo of 2π radian (e.g. Hooper and Zebker, 2007; Zebker and Lu, 1998). According to the dimension size of the processed data, unwrapping methods can be classified into three categories: 1D unwrapping (e.g. Huntley and Saldner, 1993; Itoh, 1982; Tribolet, 1977), 2D unwrapping (e.g. Chen and Zebker, 2001; Costantini, 1998; Flynn, 1997; Ghiglia and Romero, 1994; Goldstein et al., 1988) and three-dimensional (3D) unwrapping (e.g. Bert, 2006; Costantini et al., 2002; Hooper, 2010; Hooper and Zebker, 2007; Huntley, 2001).

An InSAR interferogram represents a 2D space with the range and cross-range dimensions, and 2D unwrapping techniques have been studied since the advent of InSAR (Goldstein et al., 1988). More recently, with the increasing number of SAR satellites and short revisiting periods, multi-temporal SAR acquisitions are often available during InSAR application, and 3D phase unwrapping techniques have become a research focus in advanced InSAR time series analysis. In essence, the 3D represents a spatio-temporal concept that is comprised of 2D space and 1D time. In this section, the 2D and 3D unwrapping are further reviewed, whereas the 1D unwrapping is not listed alone as it can be a part of 3D unwrapping in InSAR processing.

2D phase unwrapping

To find the unwrapped solution for interferograms, spatial unwrapping algorithms are commonly based on the Nyquist criteria, i.e. assuming that the phase difference between neighbouring pixels in an interferogram is limited to the interval [−π, π] (e.g. Bert, 2006; Carballo and Fieguth, 2000). An ideal situation is that the assumption is held for all phase gradients in the interferogram. In such a case, a deterministic and unique unwrapped solution can be obtained through a straightforward integral along an arbitrary path (e.g. Carballo and Fieguth, 2000; Gens, 2003) as pixels are in a continuity 2D surface, in which the integral depends only on the start and the end positions. This also implies the integral along any closed loops is always zero. However, the assumption often fails in areas that are locally undersampled

due to phase noise or large gradient movements (e.g. Bert, 2006; Carballo and Fieguth, 2000; Hooper and Zebker, 2007). The phase difference of two neighbouring pixels that exceeds a half cycle will result in a discontinuity (Huntley, 1989). The presence of phase discontinuities renders the surface disconnected and the integral result varies and depends on the selected path on this surface. The identification of phase discontinuities thus plays an important role in the process of spatial unwrapping. Since prior knowledge about the phase discontinuities is generally not available, the presence of non-zero (including positive and negative) residues along any closed loops can provide clues for their locations (Hooper and Zebker, 2007). The goal of the phase unwrapping procedure is to locate and accommodate such discontinuities and to eliminate potential integration paths enclosing unequal numbers of positive and negative residues (e.g. Chen and Zebker, 2001; Zebker and Lu, 1998).

To this end, the branch-cut (or residue-cut) algorithm firstly identifies the locations for all residues in an interferogram and then connects the residues with branch cuts to prevent the existence of integration paths that can encircle unbalanced number of positive and negative residues (Goldstein et al., 1988). This algorithm is computationally efficient and requires little computer memory, however, it typically generates regional errors in the noisy and layover portions of the interferogram. To enhance this algorithm, pre-processing strategies including spatial low-pass filtering and the formation of the so-called dipoles are suggested to mitigate the residues and make the selection of the appropriate path feasible (e.g. Goldstein and Werner, 1998; Huntley, 1989). In contrast to Goldstein's branch-cut algorithm, Flynn (1997) proposed a tree-growing approach which minimises the discontinuities by adding multiples of 2π to the phase values enclosed by the loops with residues. This algorithm can work with or without weighting factors.

Unlike branch-cut or tree-growing approaches, a popular approach to 2D unwrapping is the minimum cost flow (MCF) (Carballo and Fieguth, 2000), which uses the network flow theory to pose phase unwrapping as a constrained-optimisation problem, seeking the MCF on a network with the constraint that all loop integrals are zero. The main difference among MCF approaches lies in the objective functions and respective minimisation techniques (Chen and Zebker, 2001). A generic form for the cost functions under the phase unwrapping framework can be found in Ghiglia and Romero (1996):

$$\mathrm{g}(\Delta\varphi - \Delta\psi) = w|\Delta\varphi - \Delta\psi|^{p}, \tag{2.29}$$

where $g(\cdot)$ is the cost function; $\Delta\varphi$ and $\Delta\psi$ are the unwrapped and wrapped phase gradients, respectively; w is the weight that determines each cost function's scaling and it is often calculated based on the amplitude and/or the coherence of the interferometric phase (Carballo and Fieguth, 2000); p is the power of the difference between a pair of corresponding unwrapped and wrapped phase gradients. The difference between the unwrapped and wrapped phase gradients is denoted by L. Thus, the objective function results in a weighted minimum L^p-norm problem. According to previous studies, the values for p can be 0, 1, 2 and ∞.

The objective L^0-norm has been used in previous studies (e.g. Buckland et al., 1995; Chen and Zebker, 2000; Ghiglia and Romero, 1996). It is to minimise the number of discontinuities. The aforementioned residue-cut algorithm can be actually seen as a L^0 representative, which behaves well in areas of good coherence but poorly in other areas (Chen and Zebker, 2000). The L^0 minimum is not guaranteed to find a global optimisation as it generally contains extended discontinuities with many residues on them (Chen and Zebker, 2000). Moreover, the L^0 minimum has been demonstrated as a NP-hard (non-deterministic polynomial-time hardness) problem that is theoretically intractable (Chen and Zebker, 2000). Chen and Zebker (2000) proposed two algorithms to resolve the issue: (i) using the network ideas of shortest paths and spanning trees to improve the residue-cut algorithm and (ii) extending the ideas of linear network flow problems to the nonlinear L^0 case.

On the other hand, the objective L^1-norm has been employed by the MCF algorithms (e.g. Carballo and Fieguth, 2000; Costantini, 1998). L^1-norm seeks to minimise the cost with respect to the number of cycles added to the wrapped phase gradients but not the total cut length that is sought in the residue-cut algorithm. L^1 solutions can be usually calculated exactly and quite efficiently, however, the L^1 objective would assign high costs to multiple-cycle discontinuities, leading the MCF algorithms away from the correct unwrapped phase (e.g. Chen and Zebker, 2000; Costantini, 1998).

Some approaches on the basis of the L^2-norm have also been introduced, which actually treat phase unwrapping as a least-squares minimisation problem and the mean square of the discrete derivatives of the unwrapped phase is chosen as the error criterion (e.g. Fornaro et al., 1996; Fried, 1977; Ghiglia and Romero, 1994; Hunt, 1979; Pritt, 1996; Pritt and Shipman, 1994). The weight was not taken into consideration in initial least squares approaches (e.g. Fried, 1977; Hunt, 1979). In general, these approaches are computationally efficient by making use of fast

Fourier transform techniques. However, the unwrapping solution is not very accurate as errors are not well constrained within a limited set of points. The weighted least-squares algorithms were thus proposed to mitigate this problem, the procedure is iterative and not as efficient as the unweighted least-squares algorithms.

It is reported that choosing L^0-norm and L^1-norm instead of L^2-norm (the mean square) as the error criterion can reduce the spread of errors (e.g. Costantini, 1998; Ghiglia and Romero, 1996) and also L^0-norm and L^1-norm solutions are empirically more accurate than the L^2 solution (Chen and Zebker, 2000). Moreover, a quasi-L^∞ approach has been developed by Hooper and Zebker (2007). L^∞-norm is applicable to a surface with only single-cycle discontinuities and its solution is the same as L^0-norm in this case. The minimisation of the L^∞-norm objective function is equivalent to finding the minimal surface given that closed residue loop bounds an infinite number of surfaces. However, multiple-cycle discontinuities will lead to an incorrect L^∞-norm solution.

Moreover, Chen and Zebker (2001) developed a statistical framework for generalized cost functions, in which the objective function was defined as the conditional probability density function of the estimated unwrapped phase given the observed wrapped phase. An alternative to formulating phase unwrapping as a constrained-optimisation problem, this algorithm considers phase unwrapping as a maximum a posteriori probability estimation problem, the most likely unwrapped solution can always be obtained given the observable input data. Together with the network-flow algorithm (Chen and Zebker, 2000), the implementation of the statistical-cost 2D phase unwrapping leads to one of the most widely used open-source packages in spaceborne InSAR, namely SNAPHU (Chen and Zebker, 2001, 2002). It is noted that it is usually impossible to unwrap an interferogam correctly at every pixel using a conventional spatial unwrapping algorithm. Therefore, the 2D phase unwrapping technique has been extended with sparse grid data (e.g. Agram and Zebker, 2009; Costantini and Rosen, 1999).

3D phase unwrapping

InSAR time series analysis introduces 3D wrapped phase data in both 2D spatial and 1D temporal dimensions. Any 2D phase unwrapping algorithms can be simply and directly applied to such 3D data, processing interferograms independently. However, as pointed out by Costantini et al. (2002) and Hooper and Zebker (2007), unwrapping the data in a 3D concept leads to more reliable and accurate solutions than treating it as a series of 2D problems. In this

section, some representative works related to 3D unwrapping for both spaceborne and ground-based SAR data are briefly introduced.

Similar to Delaunay triangulation in a 2D space, Costantini et al. (2002) applied the Delaunay tetrahedrization to sparse points in the 3D space-time. The unwrapping solution was achieved by empirically formulating phase unwrapping as a linear integer minimisation problem and determining a "discrete" irrotational vector field in which no residues existed along any cycles.

Bert (2006) developed the spatial temporal unwrapping network algorithm for phase unwrapping on a spatially sparse grid, using the integer least-squares estimator and a linear temporal displacement model. In this approach, a portion of PS pixels were selected by spatial gridding whereby each candidate had the best coherence within a grid unit. A reference network was constructed based on such reference points. DEM errors and displacement parameters were first estimated at the arcs of the reference network using the interferometric phase time series. After this temporal estimation, the parameters at the reference points were obtained by a spatial least-squares adjustment of the estimated difference parameters. Once the reference network was estimated and unwrapped, other PS pixels were then connected to the network and estimated. The strategy of distinguishing the reference PS pixels from the ordinary PS library could reduce the requirement on computation memory and improve the computational efficiency.

Pepe and Lanari (2006) addressed the 3D phase unwrapping problem for sparse grid data in SBAS time series analysis through a procedure of 1D temporal unwrapping and a following 2D spatial unwrapping. The MCF algorithm was applied to the unwrapping in both time and space and formulated a constrained-optimisation problem (Costantini, 1998). Particularly, the temporal evolution of the ground deformation was considered for the 1D unwrapping and the 1D unwrapping solution was used to generate the weight in the following 2D unwrapping. An arc with a small temporal network cost would be assigned with a large weight in the 2D unwrapping.

Hooper and Zebker (2007) gave a deep insight of 3D unwrapping for multi-temporal spaceborne InSAR and developed a theoretical framework and two unwrapping algorithms for PS pixels. The first approach was the quasi-L^{∞}-norm 3D algorithm, which relied on the identification and processing residues along closed loops in the 3D space-time. The other approach is the stepwise 3D algorithm on the basis of a 1D plus 2D strategy: it combined a low-

pass filtering in the frequency domain of time and then unwrapped the double differenced phase in the spatial domain using an iterative weighted least-squares approach. This 3D unwrapping algorithm was further converted to a series of maximum a posteriori probability estimation problems (Hooper, 2010) and implemented in the Stanford method for persistent scatterers (StaMPS) software (Hooper et al., 2012) that has been widely used in spaceborne InSAR time series.

The aforementioned 3D unwrapping approaches are dedicated to spaceborne SAR data. The following paragraphs will introduce representative works about 3D unwrapping for GBSAR data.

Rödelsperger (2011) developed a real-time 3D unwrapping approach for continuous GBSAR data. The real-time technique detected PSs based on ADI of a stack of consecutive SLCs. Similar to Bert (2006), a subset of PS candidates (PSCs) were selected from the initial PS library by spatial gridding based on each having the minimum ADI within a grid unit. A triangulation network of PSCs was used for temporal and spatial phase unwrapping. In particular, a recursive temporal unwrapping was conducted by the use of multiple model adaptive estimation (MMAE) for GBSAR data. The MMAE used a number of parallel Kalman filters, one for an ambiguity set of an arc, each implementing different models. The spatial unwrapping was then performed using a MCF algorithm to ensure that the temporal solution was spatially consistent (i.e. the sum of the unwrapped double differenced phase within each triangle must be zero). Once a consistent ambiguity set was determined for each arc, all detected PSs were integrated into the triangulation network by spatial unwrapping. Thus, the unwrapping solutions for PSs are smoothed and dependent on the reliability of PSC results, which is a drawback of this approach. Additionally, sudden phase changes can occur on any single PSC pixel and may cause regional unwrapping errors and propagate to the final cumulative deformation.

Monserrat Hernández (2012) presented a two-stage procedure: a preliminary 2D phase unwrapping together with a subsequent 1D pixel-wise unwrapping. 2D phase unwrapping was first performed in this procedure and the 2D unwrapping errors for each pixel in the temporal dimension were then iteratively estimated and removed on the basis of the integer nature of the unwrapping errors (Biggs et al., 2007): the unwrapping errors in 2D space can be checked in any temporal close loops. In practice, unwrapping errors often occur in a region and an example can be found in Biggs et al. (2007). Thus, the pixel-wise operation could be inefficient and even destroy the spatial consistency obtained in the 2D unwrapping. A potential improvement on the

detection and correction of 2D unwrapping errors might be that extending the pixel-wise operation to a region-based operation.

Example of 3D unwrapping using synthetic data

To illustrate 3D phase unwrapping, a stack of data is simulated based on a gradual process of a spatially diffused model with the assumption of additive white Gaussian noise only on interferograms. The greatest deformation occurs in the central area and diffuses to the margins. A stack of 16 epochs $(t_0, t_1, \cdots, t_{15})$ are simulated. The first epoch is selected as the reference time. Thus, there are 15 temporal intervals. The lengths of temporal intervals are identical and each one is denoted as Δt. In the processing, the temporal baseline constraint is fixed as $1\Delta t$, i.e. the interval between the master and the slave cannot be longer than $1\Delta t$. Thus, 15 interferograms are formed. White Gaussian noise with the standard deviation of 1 rad is added to the interferograms. The interferograms are then filtered using a 5×5 "boxcar" filter and unwrapped using the StaMPS 3D unwrapping package (Hooper, 2010).

The wrapped interferograms with additive Gaussian noise (δ_{n_ph} = 1.0 rad) and their corresponding unwrapped interferograms are shown in Figure 2.17. The true and inverted incremental displacement maps, as well as their differences are given in Figure 2.18. Through visual inspection, it is evident that all the interferograms have been unwrapped correctly and the inverted displacement maps are consistent with the true counterparts. In the final cumulative displacement map (0-15) in Figure 2.18, the maximum displacement reaches up to 113.10 mm and the root mean square (RMS) of the difference is only 2.7 mm in the case of additive Gaussian noise (δ_{n_ph} = 1.0 rad).

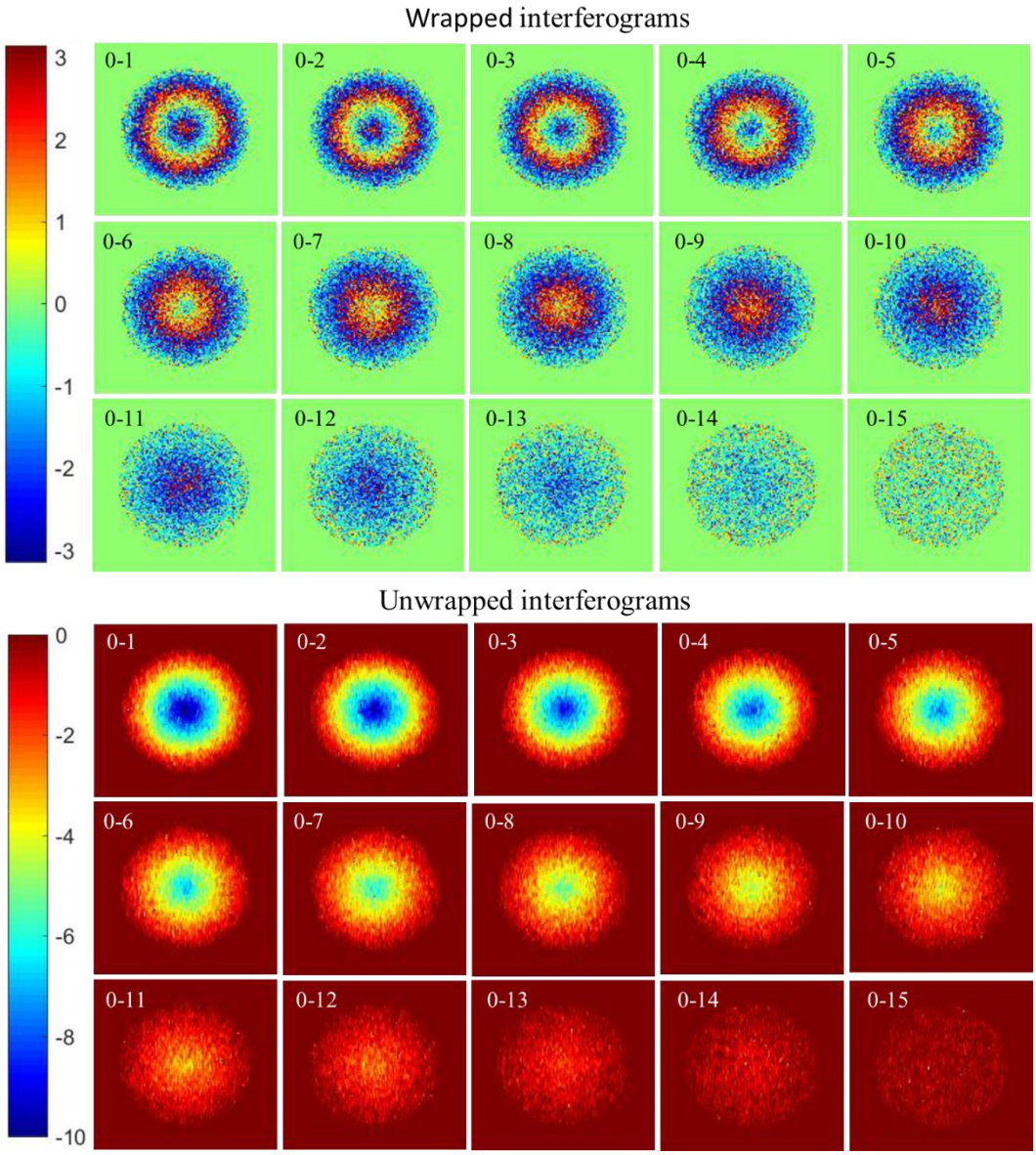

Figure 2.17. Wrapped and unwrapped interferograms with additive Gaussian noise (δn_ph=1.0 rad).

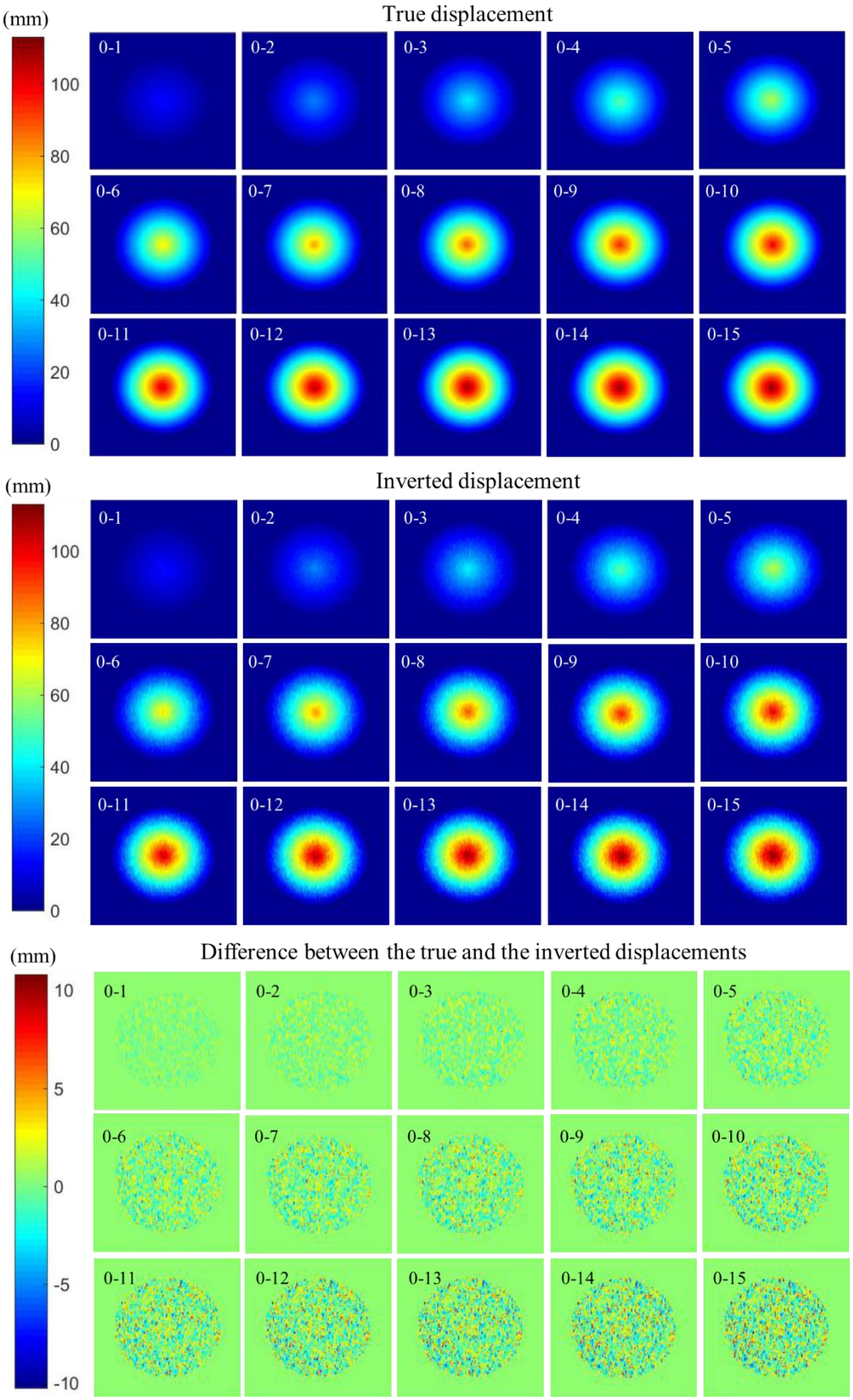

Figure 2.18. Deformation time series: true displacements without additional noise vs. inverted displacements from noisy interferograms (δn_ph=1.0 rad).

2.3.5 APS correction

Relevant work

Interferometric measurements can be strongly affected by variations in the troposphere, especially the atmospheric water vapour, even for those with a short time interval (e.g. Caduff et al., 2014; Caduff et al., 2015). Effort has been undertaken to correct atmospheric effects on GBSAR interferograms for deformation monitoring purposes. Representative works related to atmospheric correction in GBSAR deformation monitoring are reviewed in this section in chronological order.

In an early work (Luzi et al., 2004), atmospheric variation was compensated using an atmospheric millimetre-wave propagation model (Liebe, 1985) utilising input meteorological data (humidity, temperature, and pressure). This study pointed out that the supposed homogeneity of atmospheric parameters was weak for the entire monitoring site with a significant topography variation along the range. The input weather observations from a single position could not be applied to the correction of an image corresponding to different ranges.

Noferini et al. (2005) estimated the amount of interferometric phase variations by a term that was linear with the range and dependent on the measured humidity: $\varphi_{atm}(\vec{r},t) = Kh(\vec{r},t)r$, where $h(\vec{r},t)$ was the function that represented the atmospheric effect, depending on the position vector $\vec{r}$ (r $= |\vec{r}|$) and the time t; K was an unknown constant. The term $h(\vec{r},t)$ was assumed to be roughly constant and equal to the estimated $h(t)$ in a single point of a small scenario. It, thus, became a first-order approximation. In this case, one known stable point was required. For a large scenario, $h(\vec{r},t)$ could not be assumed constant over the entire observing area any longer. Instead it was modelled linearly with the range: $h(\vec{r},t) = A(t) + B(t)r$, thus, $\varphi_{atm}(\vec{r},t) = a(t)r + b(t)r^2$, where $A(t)$, $B(t)$, $a(t)$ and $b(t)$ are coefficients, varying with the time t. In this case, two stable points were required to solve the equation. The work was based on the empirical equations of atmospheric contribution without sufficient justification.

Pipia et al. (2006) presented several approaches to compensate for atmospheric artefacts in differential InSAR. The first two shared a similar procedure: a number of motionless and high-coherent pixels were selected and the unwrapped phase of these pixels was used to recover the linear regression model between the atmospheric phase ramp and the range. The two approaches were actually similar and their only difference was the unwrapped phase, one used 1D

unwrapping and the other 2D. In these two approaches, the linear phase ramp was modelled under an assumption of the spatial atmosphere homogeneity and the model consisted of an angular coefficient and an offset. The third proposed approach was based on spectral variations in an interferogram. A bi-dimensional Chirp-Z transform was used to remove low-frequency components caused by the atmospheric variations. The main drawback of this approach is that it requires a sufficiently-wide, highly-coherent and motionless area to apply the transform. The approach relies on the size of the observing site and the time delay between acquisitions. Finding such a kind of region might be troublesome.

Pipia et al. (2008) investigated the effects of atmospheric variations on displacement measurements using successive zero-baseline GBSAR polarimetric acquisitions. Four highly-coherent pixels at four different ranges were identified as reference points in the study. The temporal evolution of the unwrapped differential phase for these reference points was compared with the simulated differential phase under the basic assumption that the wave propagates through a homogeneous medium. A strong similarity was found between the simulated and actual observed profiles in terms of the shape of the curves, the proportionality of phase errors to the range between the radar position and observing targets, and the magnitude of the angular fluctuations. A linear relationship between the range and the unwrapped phase of these targets was found. Based on these findings, the study proposed a coherence-based procedure for the removal of time-series atmospheric phase artefacts, which utilised stable control points to recover the linear regression model under the medium homogeneity hypothesis.

Iannini and Guarnieri (2011) used meteorological measurements from a single weather station to model the slow-varying atmospheric variations under the hypothesis of a uniform atmosphere. One ground control point was required to calibrate the measured humidity. The procedure can be performed on the wrapped phase, thus not affected by phase unwrapping. As reported in the study, this approach is not as accurate as the compensation made by a set of ground control points distributed all across the scene.

Caduff et al. (2014) presented an approach to separate atmospheric contribution from deformation in multiple continuous campaigns for hillslope instability monitoring. The atmospheric phase was firstly modelled from actual weather observations. Areas that exhibited displacements were masked through visual inspection. The phase over the masked areas was interpolated and then computed using a spatial low-pass filter. In particular, the window size used for filtering was case-dependent. To avoid highly variable atmospheric phase at the time

of data acquisition, this study used a solar radiation model (Rich et al., 1994) to predict the spatial and temporal variability of the atmospheric phase, which was claimed to be able to facilitate post-processing in the study.

Iglesias et al. (2014b) highlighted the issue that in mountainous areas with steep topographic variations, the assumption of spatial homogeneity was no longer satisfied due to the fluctuations of atmospheric parameters such as temperature, pressure, and humidity in the spatial domain. The refractivity was considered vertically stratified. Therefore, for cases with a steep topography, atmospheric variation was modelled as a range- and height-dependent function ($\varphi^{atm} = \beta_0 + \beta_1 r + \beta_2 rh$, where h is the height) and corrected with the support of height information and a set of highly-coherent pixels selected from stable areas. This approach was used to compensate for the atmospheric artefacts in both short-term and long-term differential InSAR processing with zero-baseline GBSAR data.

Butt et al. (2016) treated the time-series APS as a so-called instationary, autocorrelated variate without second order stationarity. The atmospheric phase was interpreted by a blend of two components: (a) deterministic relations among atmospheric phase, refractive index and meteorological quantities and (b) stochastic relations of the unmodelled residuals to atmospheric phase deduced from the meteorological measurements. Towards modelling the deterministic component of atmospheric phase, PS points were identified out of the area potentially containing moving objects and then used as stable control points. The usual regularity assumption of the second order stationarity on PS measurements was replaced by a weaker assumption being an intrinsic random function of order k. The atmospheric effects were mitigated through the combination of this assumption with existing approaches that used the ordinary least-squares estimation of trend functions.

Based on the same theory as Iglesias et al. (2014b) (namely considering that the atmospheric conditions were constant in the horizontal direction and variable linearly with elevation), Dematteis et al. (2017) used a very similar approach with a slightly different range- and height-dependent model ($\varphi^{atm} = a_0 + a_1 r + a_2 z^2$, where z is the elevation) to compensate for the atmospheric contribution in a long-lasting campaign monitoring towards the Planpincieux glacier located on the Italian side of Mont Blanc.

Rigorous derivation of an APS correction model for GBSAR

As reported in previous studies (e.g. Dematteis et al., 2017; Iglesias et al., 2014b), atmospheric conditions including pressure (P), temperature (T) and relative humidity (RH) vary with elevation and result in the spatial inhomogeneity of atmospheric refractivity N. The rigorous derivation of the APS correction model for GBSAR starts by considering atmospheric refractivity N as a function of elevation z, i.e. $N(z)$. To clarify the derivation process, a schematic diagram of GBSAR observation geometry is depicted in Figure 2.19.

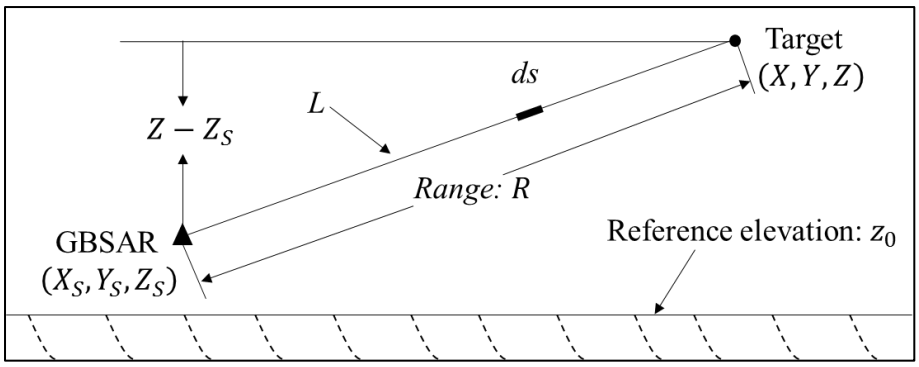

Figure 2.19. The schematic diagram of GBSAR observation geometry

As shown in Figure 2.19, for an arbitrary point at (X, Y, Z), the atmospheric phase variation $\varphi^{atm}(t_1, t_2)$ between two epochs t_1 and t_2 can be computed through a linear spatial integration (e.g. Dematteis et al., 2017; Iglesias et al., 2014b; Pipia et al., 2008):

$$\varphi^{atm}(t_1, t_2) = 10^{-6} \cdot \frac{4\pi}{\lambda} \int_L (N_{t_2}(z) - N_{t_1}(z)) ds, \tag{2.30}$$

where L is the integral path along the straight line from the GBSAR location (X_S, Y_S, Z_S) to the target (X, Y, Z); ds represents an elementary unit of definite integral. The length of L is equivalent to the range between the radar and the target: $R = \sqrt{(X - X_S)^2 + (Y - Y_S)^2 + (Z - Z_S)^2}$. The equation of the line L is:

$$\frac{x - X_S}{X - X_S} = \frac{y - Y_S}{Y - Y_S} = \frac{z - Z_S}{Z - Z_S} (X \neq X_S, Y \neq Y_S, Z \neq Z_S). \tag{2.31}$$

The integral path can be parameterized as follows:

$$\begin{cases} z = t, (Z_S \leq t \leq Z), \\ x = X_S + \frac{X - X_S}{Z - Z_S}(t - Z_S), \\ y = Y_S + \frac{Y - Y_S}{Z - Z_S}(t - Z_S). \end{cases} \tag{2.32}$$

In accordance with the parameterization, the elementary length can be written as:

$$ds = \sqrt{\left(\frac{dx}{dt}\right)^2 + \left(\frac{dy}{dt}\right)^2 + \left(\frac{dz}{dt}\right)^2}\sqrt{\left(\frac{X-X_S}{Z-Z_S}\right)^2 + \left(\frac{Y-Y_S}{Z-Z_S}\right)^2 + 1}\, dt\left[\frac{R}{Z-Z_S}\right]dt. \quad (2.33)$$

By substituting ds in Equation (2.30) with its expression in Equation (2.33), the atmospheric phase contribution can be further written as the following integral:

$$\varphi^{atm}(t_1, t_2) = 10^{-6} \cdot \frac{4\pi}{\lambda}\frac{R}{Z-Z_S}\int_{Z_S}^{Z}(N_{t_2}(t) - N_{t_2}(t))\, dt. \quad (2.34)$$

As far as the refractivity is concerned, its distribution through the whole troposphere can be modelled as a multilayer medium by an exponential function (Hall, 1980):

$$N(z) = N_0 exp(-\alpha(z - z_0)), \quad (2.35)$$

where α is the inverse of a height scale factor in km^{-1}; N_0 is the refractivity at the reference elevation z_0. For relatively small scenarios that GBSAR is suited, the refractivity can be approximated by the first two terms of the Taylor series expansion of Equation (2.35) around $z = z_0$ (Iglesias et al., 2014b), thus being a linear model that the refractivity varies linearly in the vertical at any epochs:

$$N(z) = N_0 - \alpha N_0(z - z_0). \quad (2.36)$$

The variation of refractivity at two epochs is:

$$\Delta N(z) = N_{t_2}(z) - N_{t_1}(z) = az + b, \quad (2.37)$$

where $a = -\alpha\left(N_{0_{t_2}} - N_{0_{t_1}}\right)$, and $\mathrm{b} = \left(N_{0_{t_2}} - N_{0_{t_1}} + \alpha N_{0_{t_2}} z_0 - \alpha N_{0_{t_1}} z_0\right)$. Combining Equations (2.34) and (2.37), the atmospheric phase variation for the arbitrary point at (X, Y, Z) at two epochs t_1 and t_2 is obtained as follows:

$$\begin{cases} \varphi^{atm}(t_1, t_2) = 10^{-6} \cdot \frac{4\pi}{\lambda}\left[\frac{R}{Z-Z_S}\right]\int_{Z_S}^{Z}(at + b)dt = c_0 + c_1 R + c_2 RZ, \\ c_0 = 0, c_1 = 10^{-6}\frac{4\pi}{\lambda}\left(\frac{a}{2}Z_S + b\right), c_2 = 10^{-6}\frac{4\pi}{\lambda}\frac{a}{2}. \end{cases} \quad (2.38)$$

Therefore, the APS model from the rigorous derivation is $\varphi^{atm} = c_0 + c_1 r + c_2 rz$, which is the same as Iglesias et al. (2014b) but different from Dematteis et al. (2017).

APS correction using synthetic data

Simulation of atmospheric stratification

The atmospheric phase contribution in InSAR can be attributed to the variation of the refractivity which depends on atmosphere parameters such as pressure, temperature and relative humidity (e.g. Iannini and Guarnieri, 2011; Iglesias et al., 2014b; Pipia et al., 2008). It is well known that the pressure through the Earth's atmosphere declines exponentially with altitude (McIlveen, 1991) and the temperature decreases with altitude by the environmental lapse rate, of which the average is defined as 6.49 K/km from sea level to 11 km (International Civil Aviation Organization, 2002). Unlike the atmospheric temperature and pressure, the relative humidity is diverse in different cases, but it typically decreases with altitude on a clear day (e.g. Folkins et al., 2006; Schmetz et al., 1995). The relative humidity is thus assumed to scale linearly with altitude in this simulation for simplicity. The aforementioned characteristics with respect to atmospheric parameters are summarised in Equation (2.39).

$$\begin{cases} P = P(z) = P_0 \exp\left(-\frac{z-z_0}{H}\right), \\ T = T(z) = T_0 - 6.49(z - z_0)/1000, \\ RH = RH(z) = RH_0 + k(z - z_0), \end{cases} \tag{2.39}$$

where P_0, T_0, RH_0 are the observations at the reference elevation z_0 for pressure P (in mbar or hPa), temperature T (in Kelvin) and relative humidity RH (in percentage), respectively; H is the so-called scale height; k is the changing rate of relative humidity with elevation. According to Equation (2.39), the variation of atmospheric pressure, temperature, relative humidity with elevation and the corresponding refractivity is drawn in line graphs, as shown in Figure 2.20.

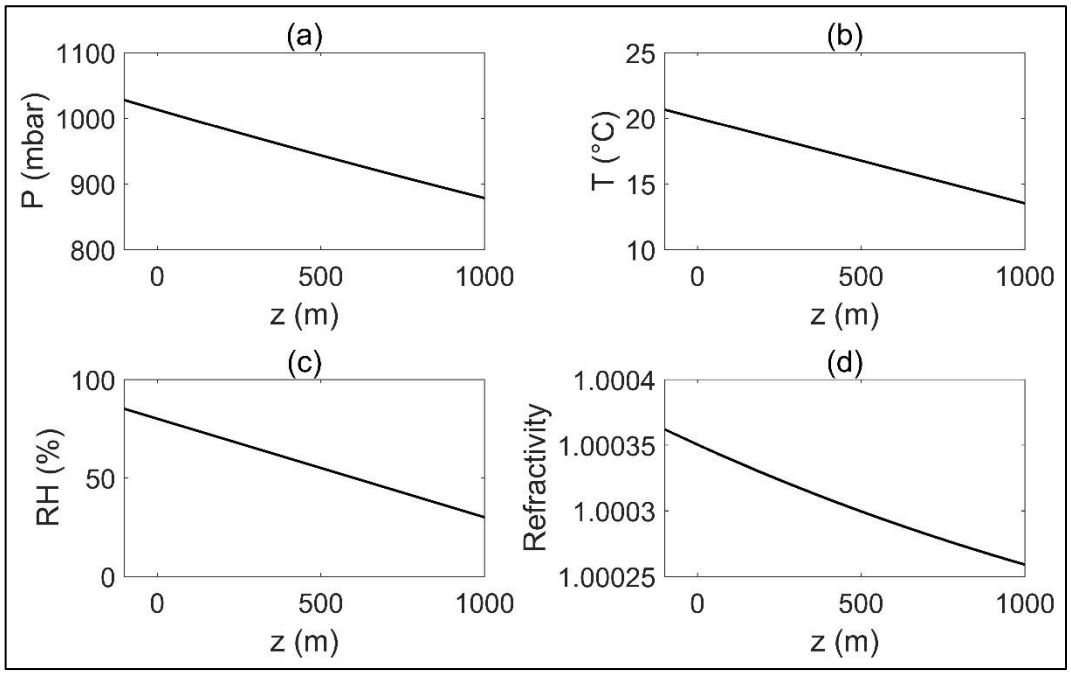

Figure 2.20. The variation of atmosphere parameters with altitude. Relevant simulation parameters: P_0=1,013 mbar, T_0=293.15 K (20 °C), RH_0=80%, k=5%, H=7,000 m, z_0=0 m.

Simulation of APS and deformation

On the basis of the synthetic DEM in Figure 2.10, atmospheric variations and surface displacements are simulated. In the simulation, the scale height H is set as 7,000 m and the reference elevation z_0 is at zero, GBSAR wavelength λ is 17.4 mm. The weather observations at the reference elevation for two epochs t_1 and t_2 are: $P_{0_{t_1}}$= 1013 mbar, $T_{0_{t_1}}$= 293.15 K (20 °C), $RH_{0_{t_1}}$=70%; $P_{0_{t_2}}$= 1,013 mbar, $T_{0_{t_2}}$= 288.15 K (15 °C, $RH_{0_{t_2}}$=75%). The changing rate of relative humidity with elevation is $k_{t_1} = k_{t_2}$=5%. The corresponding APS (in mm) is shown in Figure 2.21(a). Surface displacements along the LOS direction are simulated to follow a diffuse deformation model within the circular area: $\sqrt{X^2 + (Y - 500)^2} \leq 60$. The LOS displacement reaches a largest value of 1 mm at the centre and decreases gradually to zero at the margin of this area, as shown in Figure 2.21(b).

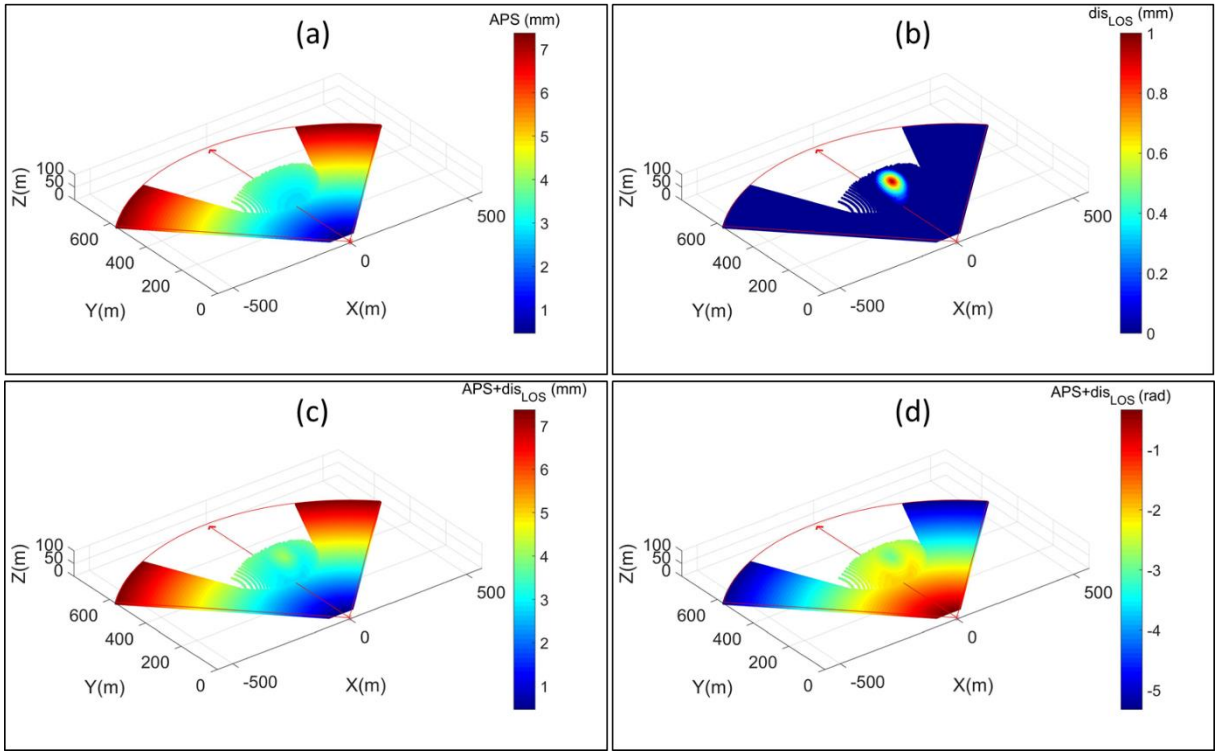

Figure 2.21. Simulation of atmospheric variations and displacements based on GBSAR observation. (a) Atmospheric variation map. (b) Displacement map. (c) The superposition map of atmospheric variations and displacements in mm. (d) The superposition map of atmospheric variations and displacements in radian.

Comparison of different APS correction models

The correction of APS is conducted using the synthetic data. Three APS correction models, employed in previous works, are compared. Specifically, a subset of points is selected from stable areas (stable areas are known in the synthetic data) and with each one from a 40 m × 40 m grid. These motionless points are used to recover APS models. The results are summarized in Table 2.3.

Table 2.3. Results for the separation of APS from displacements with the synthetic data.

APS model	R^2 of regression	RMS of displacement residuals (mm)	Max of displacement residuals (mm)
$\varphi^{atm} = c_0 + c_1 r$ (Pipia et al., 2008)	0.998929	2.66E-02	0.3050
$\varphi^{atm} = c_0 + c_1 r + c_2 z^2$ (Dematteis et al., 2017)	0.999964	4.03E-03	0.0785
$\varphi^{atm} = c_0 + c_1 r + c_2 rz$ (Iglesias et al., 2014b)	1.000000	8.05E-05	0.0028

Among the three models, the third one, of rigorous derivation, achieves the best accuracy.

Although the first model (without taking elevation into consideration) behaves the worst, it is still applicable to scenarios with smooth topography and its advantage is that an external DEM is not required for the correction of APS. In short, for scenarios with steep topography and available external DEM, the third model ($\varphi^{atm} = c_0 + c_1 r + c_2 rz$) is preferable. Otherwise, APS in cases with smooth topography or without external DEM, the first model ($\varphi^{atm} = c_0 + c_1 r$) can be used.

2.4 GBSAR deformation monitoring applications

To fulfil a GBSAR deformation monitoring task, the first step is to decide the repetition rate of data acquisitions, which depends on the kinematics of the deformation event at hand and practical requirements in the real-world situation and event. For a fast-changing site, an interferogram formed by a pair of GBSAR images with a long time interval often suffers serious decorrelations. It is known that decorrelation is a serious issue in InSAR, which can render the measurement impossible (e.g. Hanssen, 2001; Monserrat Hernández, 2012). In such a situation, continuous GBSAR data acquisition with a high temporal resolution (i.e. short repeat interval) is therefore required to minimise decorrelations caused by fast ground movements. On the other hand, repeat campaigns are suitable if the goal is to measure slow displacement processes in highly coherent areas, the GBSAR system can be installed and dismounted at each campaign, revisiting a given site periodically, e.g., weekly, monthly or yearly. Accordingly, GBSAR data acquisition can be performed using two modes: the continuous mode and the discontinuous mode.

Different data acquisition modes lead to different data processing techniques. Continuous GBSAR offers a zero-baseline geometry for all acquisitions, the topographic phase component for all interferograms is always zero and can be neglected. GBSAR data acquired under this operation mode can be processed by InSAR techniques including both D-InSAR and InSAR time series analysis, which allow users to have a (near-) real-time monitoring of the site of interest (e.g. Rödelsperger, 2011; Tarchi et al., 2005). In particular, Caduff et al. (2015) distinguished between short-term and long-term continuous interferometry. Continuous interferometry over a short time period can be applied to fast-changing sites where significant surface movements need to be detected during a short period, e.g. several hours up to a few days. By contrast, continuous interferometry over a long term, e.g. several days up to several months, may require substantial technical effort in terms of weather shelter, power-supply, and

data-transfer (Caduff et al., 2015).

To process discontinuous GBSAR data acquired in multiple campaigns, both differential InSAR and non-InSAR techniques can be exploited (Caduff et al., 2015). In differential InSAR processing, special attention should be paid to the repositioning errors between different campaigns. As reported by Crosetto et al. (2014a), repositioning errors at the millimetre level cannot be neglected. Monserrat et al. (2014) suggested that such a phase component due to repositioning errors can be treated and corrected together with the atmospheric phase because they have similar low spatial frequency characteristics. Alternatively to InSAR, a non-InSAR approach was developed by Crosetto et al. (2014b) for the processing of discontinuous GBSAR data, using an image matching technique performed on GBSAR amplitude images. This approach is not influenced by strong atmospheric perturbations or total decorrelations due to very high displacement rates, but it is less sensitive to surface movements and it may reveal only centimetre- or decimetre-scale displacement (e.g. Caduff et al., 2015; Crosetto et al., 2014a, b; Monserrat Hernández, 2012). Regarding discontinuous GBSAR deformation monitoring via repeat campaigns, Crosetto et al. (2014a) pointed out the main drawbacks of discontinuous GBSAR include reduced density, precision and reliability of deformation measurements. Moreover, hardware related technical issues, such as the precise installation of the instrument in a fixed position with the same looking attitudes between different campaigns and the difficulties in measuring the existing “orbit” and “attitude” parameters of a GBSAR system, render the data processing more complicated.

Based on the aforementioned data acquisition strategies and data processing techniques, a wide range of applications to which GBSAR is suited have been accomplished. Some representative works related to GBSAR deformation monitoring applications are summarized in Table 2.4 in chronological order.

Table 2.4. GBSAR deformation monitoring applications.

	Application	LOS displacement / velocity	Device, (Band)	Data acquisition information	Baseline	Data processing
Tarchi et al. (1999a)	Dam	20.6 mm	LISA (C) (Rudolf et al., 1999)	5 campaigns in 68 days	Non-zero	D-InSAR
Reeves et al. (2001)	Mine walls	2 mm	SSR (X)	Twelve days of continuous monitoring	Zero	D-InSAR
Leva et al. (2003)	Landslide	∽5 cm/week	LISA (Ku)	Measurements have been done almost continuously from the October 7–14, 1999.	Zero	D-InSAR
Antonello et al. (2004)	Landslides (a summary of several test sites)	0.2 - 36 mm/h	LISA (Ku)	Short-term and long-term monitoring for different test sites	NA	D-InSAR
Tarchi et al. (2005)	Rockslide	0.3 - 5 cm / day	LISA (Ku)	5-months radar permanent monitoring	Zero	D-InSAR
Harries et al. (2006)	Rockfall in open pit mines	Up to 250 mm	SSR (X)	Continuous monitoring was performed 6 hours prior to the rock fall event	Zero	D-InSAR
Luzi et al. (2009)	Snow-covered slope	Not mentioned	-- (C and S)	Continuous monitoring during the winter months of 2005–2006 and 2006–2007	Not mentioned	D-InSAR
Herrera et al. (2009)	Landslide	Max displacement during the observing period: 14.1 cm	-- (C)	Continuous working for 47 days, providing displacement map of the illuminated area at a rate of 1/h	Zero	InSAR[a]
Casagli et al. (2010)	Landslides & volcano	Not available	GB-InSAR LiSALab (Ku) (Del Ventisette et al., 2011)	Long-term monitoring with multiple campaigns	Zero	InSAR
Riesen et al. (2011)	Glacier ice motion	~25 cm / day	GPRI (Ku) (Werner et al., 2012)	55 hours of operation (six 5-hour interferograms)	Not mentioned	D-InSAR
Lowry et al. (2013)	Landslides	Max 18 mm / day	GPRI (Ku)	Two campaigns including 11.5 non-continuous hours and 36 continuous hours of monitoring	Zero	InSAR time series
Agliardi et al. (2013)	Rock slope instability of a quarry face	max 7.5 mm / day	GBSAR LiSALab (Ku)	4 days of short-term monitoring	Zero	InSAR
Tapete et al. (2013)	Surveillance of archaeological heritage	±0.5 mm / day	GBInSAR LiSALab (Ku)	Continuous monitoring in almost one year	Zero	InSAR time series
Crosetto et al. (2014b)	Landslide	max ~30 cm	IBIS-L (Ku)	Discontinuous monitoring mode	Non-zero	Non-InSAR
Caduff et al. (2014)	Landslide: hillslope instability	Up to 3 mm/day	GPRI-I & -II (Ku) (Werner et al., 2012)	Three short-term campaigns from two fixed positions	Zero	D-InSAR
Di Traglia et al. (2015)	Volcano deformation	1.2 – 2.1 mm/day	GBInSAR LiSALab	Multiple campaigns in in 2010–2014	Not mentioned	InSAR time series

Pratesi et al. (2015)	Urban structure (city walls)	0.1 - 1.77 mm/h	GBInSAR LISALab (Ku)	Continuous data collection in 12 days	Zero	InSAR
Mao and Chang (2015)	Dam test	Stable	IBIS-FL (Ku)	One continuous campaign in 15 hours with a temporal resolution of 6 minutes	Zero	InSAR time series
Frodella et al. (2016)	Rock fall, the San Leo cliff	Max 339 mm/year	GBInSAR LISALab (Ku)	One year monitoring campaign	Not mentioned	InSAR
	Urban buildings at a heritage site	Max ±10 mm	IBIS-L (Ku)	Two campaign in one month	Non-zero	D-InSAR
Serrano-Juan et al. (2016)	Structure stability for a railway station	> 3 mm	IBIS-L (Ku)	Continuous data collection in 10 days.	Zero	InSAR time series
Frukacz and Wieser (2017)	Rock fall in a quarry	Stable	IBIS-FM (Ku) (Farina et al., 2011)	Multiple campaigns in 2 days	Zero	InSAR time series
de Macedo et al. (2017)	Landslide	Max 4mm/h, average 20 mm/day	Sentir-Geo owned by Bradar, Brazil (X)	Two continuous monitoring campaigns in six days	Zero	InSAR time series
Schulz et al. (2017)	Landslide	max 154 mm	IBIS-L (Ku)	Continuous data collection for hourly intervals during 4.3 days	Zero	InSAR (particularly IBIS Guardian software)
(Di Traglia et al. (2018))	Volcano: slope instability	# 1: Cumulative displacement up to ∽2.85 m # 2: ±4.3 mm # 3: ±8.6 mm	GBInSAR LISALab (Ku)	Permanent-sited. # 1: > 4 years # 2: 8 hours # 3: ∽2 hours	Zero	InSAR
(Carlà et al. (2018))	Open pit mine	> 1 mm/day	GBInSAR LISALab (Ku)	Three weeks prior to the event, with a temporal resolution of 6 min	Not mentioned	InSAR

[a] InSAR: the data processing technique is not specifically specified as D-InSAR or InSAR time series analysis in some literature, for which the generic term InSAR is used.

As shown in Table 2.4, GBSAR has been used for a wide range of deformation monitoring applications over the last two decades. The applications include both slow-changing and fast-changing scenarios and cover landslide or rockslide related processes, volcanoes, slope stability of open pit mines, urban monitoring, man-made structures, and surface changes of glaciers and snow. The monitoring duration of these applications varies from a few hours to several years. Zero-baseline geometry is achieved by most applications and nearly all applications except Crosetto et al. (2014b) are accomplished using GBSAR interferometry (including D-InSAR and InSAR time series). These applications demonstrate the flexibility and adaptability of GBSAR interferometry to various scenarios.

However, there remain many deficiencies in these works. Firstly, these works are on the basis of conventional InSAR processing algorithms, e.g. the coherence estimation and phase filtering with local "boxcar" windows, the ADI-based PS selection, etc. The advanced and improved InSAR algorithms, such as robust coherence estimation (Jiang et al., 2014b), adaptive or non-local phase filtering (e.g. Deledalle et al., 2015; Lang et al., 2015), selection of partially coherent pixels (Perissin and Wang, 2012), exploitation of distributed scatterers (e.g. Ferretti et al., 2011; Jiang et al., 2015), and 3D phase unwrapping (Hooper, 2010), which have been demonstrated to be superior to conventional algorithms in spaceborne InSAR, but have not been applied in GBSAR interferometry. Secondly, the GBSAR systems adopted in the aforementioned studies usually take several minutes to half an hour for one acquisition, which is much longer than FastGBSAR that is able to repeat data acquisition every 10 seconds. Due to the high temporal-resolution and large data volumes (e.g. 360 images per hour) of FastGBSAR, there remains a significant challenge in processing such GBSAR data in real time. In addition, the accuracy of GBSAR interferometric measurement can be strongly affected by atmospheric and repositioning errors. Deep analysis should be conducted on the correction of these errors. All these mentioned research gaps will be discussed and addressed in the following chapters.

Chapter 3. A new non-local method for coherence estimation and phase filtering

The study in this Chapter has been published in the following research journal paper:

Wang, Z., Li, Z., Mills, J., 2018. A new non-local method for ground-based sar deformation monitoring. *IEEE Journal of Selected Topics in Applied Earth Observations and Remote Sensing* 11(10), 3769-3781.

3.1 Introduction

GBSAR (e.g. FastGBSAR) can acquire SAR imagery with a maximum temporal resolution of 10 seconds, and can be performed in continuous or campaign mode for different scenarios (e.g. Caduff et al., 2015; Crosetto et al., 2017; Monserrat et al., 2014). No matter which acquisition mode is adopted in a monitoring task, interferometry is the preferred fundamental data processing technique for deformation monitoring applications (Monserrat et al., 2014). It is known that the interferometric phase suffers from both temporal and spatial decorrelation noise (Zebker and Villasenor, 1992) which may lead to errors in phase measurements. Such noise can cause problems in phase unwrapping and hamper data interpretation (Hanssen, 2001). Therefore, the interferometric phase quality should be guaranteed for any applications of the technique. Effort to address this has been made via two different strategies: coherence estimation and phase filtering. Coherence is an efficient and commonly used indicator for detecting pixels with coherent phase in a SAR interferogram (Bamler and Hartl, 1998). Phase filtering can increase the SNR of interferograms and facilitate phase unwrapping (Hanssen, 2001).

The coherence of a pixel is often estimated based on a rectangular window around it and phase filtering is implemented using local spatial averaging (multilooking) (Goel and Adam, 2012). As reported in previous studies (e.g. Deledalle et al., 2011; Spaans and Hooper, 2016), the adoption of local windows could result in biased estimates and resolution losses due to local heterogeneity. To address these issues, a prevailing approach is to select homogeneous or resembling pixels from the wider surroundings of each resolution cell for the estimation (e.g. Deledalle et al., 2011; Deledalle et al., 2015; Ferretti et al., 2011; Goel and Adam, 2012; Jiang et al., 2015; Jiang et al., 2014a; Spaans and Hooper, 2016; Wang and Zhu, 2016). Although these methods are known by different names, here they are collectively termed “non-local”

methods. Non-local methods are primarily distinguished by the selection strategy of homogeneous or resembling pixels and the majority have been specially designed only for either coherence estimation or phase filtering. Some representative works are briefly introduced.

A patch-based method (termed "nl-InSAR") was proposed by Deledalle et al. (2011). The patch similarity was measured by the conditional probability of the intensity and the interferometric phase. Coherence, reflectivity and interferometric phase were jointly obtained by estimation of the covariance matrix. The process involved an iterative weighted maximum likelihood estimation with weights iteratively refined based on similarity. This technique used only an interferometric pair of co-registered SAR images. The iterative process, however, was not computationally efficient (e.g. Deledalle et al., 2011; Lang et al., 2015).

Ferretti et al. (2011), on the other hand, exploited the statistics of time-series amplitude of two pixels within a window and constructed a probability distribution on the basis of the statistics. SHPs were detected using a nonparametric hypothesis test, namely the Kolmogorov–Smirnov test (Kvam and Vidakovic, 2007). The method required at least twenty SAR acquisitions to effectively reject the null hypothesis and obtain reliable results (Jiang et al., 2015). This technique has been integrated into the "SqueeSAR*"* software**.** Jiang et al. (2015) improved the selection of SHPs by forming a different probability distribution (Chebyshev's inequality) which increased the interval estimate of the hypothesis test based on the central limit theorem (CLT). By taking this measure, the required number of acquisitions could be reduced. This method is termed fast SHP selection (i.e. "FaSHPS") due to its high computational efficiency. In addition, Goel and Adam (2012) utilised the Anderson-Darling test to identify SHPs which were then used for coherence estimation and adaptive multilooking. This non-local method was combined with the SBAS algorithm for high-resolution deformation monitoring in non-urban areas.

Spaans and Hooper (2016) named resembling pixels "siblings", with siblings extracted simply by utilising two statistics: mean amplitude over all interferometric combinations, and mean amplitude difference between master and slave images over all interferometric combinations. The simple computation ensured that the identification of siblings was a fast process and the method was thus termed "RapidSAR". Contrary to statistical hypothesis testing techniques, which tend to result in a binary outcome, this method could easily maintain a minimum number of pixels with similar statistics for robust calculation in cases of insufficient siblings.

The aforementioned non-local methods were originally developed for the purposes of processing spaceborne SAR imagery. This study is thus dedicated to developing a versatile non-local method which addresses the three critical issues in GBSAR interferometry for deformation monitoring and possesses advantages over conventional non-local methods originally developed for spaceborne SAR: (a) the efficient and reliable identification of sibling pixels; (b) the accurate estimation of accurate coherence estimation and phase filtering; and (c) the application of the developed non-local method in GBSAR time series analysis. To this end, several hypothesis tests and statistics, typically employed in representative works, are first investigated with actual FastGBSAR data. Based on investigation and analysis, a new similarity measure is developed to overcome current limitations in terms of accuracy and computational efficiency. The similarity is based on the mean of time series amplitude. Pixels with high similarity are selected from a non-local window for each point. Coherence is calculated based on the selected sibling pixels and then enhanced by a second statistical estimator (e.g. Abdelfattah and Nicolas, 2006; Jiang et al., 2014c). Non-local means filtering is also performed using the extracted siblings to reduce interferometric phase noise.

3.2 Methodology

3.2.1 Identification of siblings

The identification of sibling pixels is the basis of any non-local method. To investigate the feasibility of several non-local methods to GBSAR imagery, twelve pixels were manually selected from four different types of ground target using a stack of 60 FastGBSAR SLC images of the dataset depicted in Section 3.3.1 for the identification analysis. The time series of amplitude values for the selected pixels are shown in Figure 3.1.

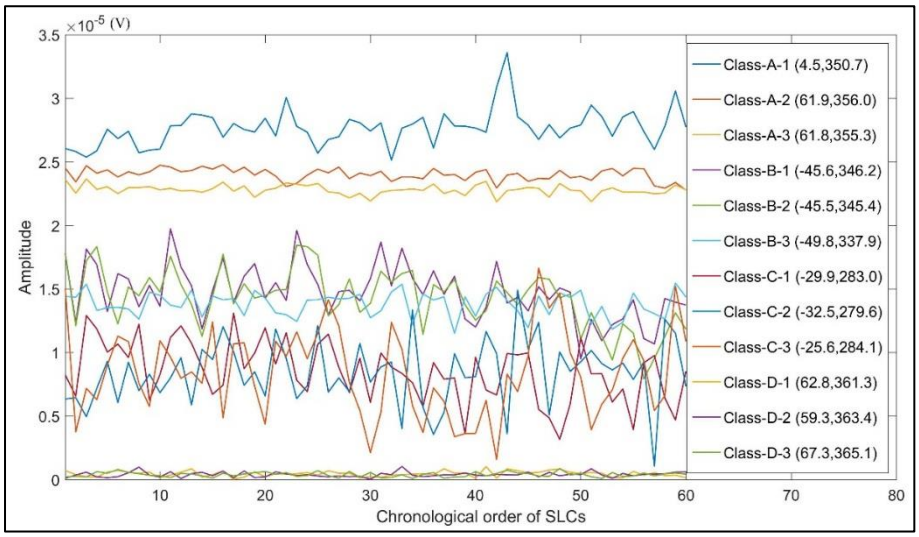

Figure 3.1. Time series of unnormalized amplitude values for the twelve selected pixels. Pixels with the prefix "A-" were selected from castle roofs which is made of stone. The properties of "B-" and "C-" pixels are not clear, but based on knowledge of the illuminated region most likely correspond to weathered rocks and earth / vegetation. Pixels of prefix "D-" were selected from the background area without backscatterers. The coordinates of each pixel in the GBSAR local coordinate system are given inside the parenthesis after the pixel identifier.

Statistics (i.e. mean amplitude and mean amplitude difference over all interferometric combinations) used in Spaans and Hooper (2016) were firstly computed by considering the first SLC as the single master in the interferogram network and all the successive images as slaves. The percentage values of the two statistics for all pixel pairs are summarized in Tables 3.1 and 3.2, respectively.

Table 3.1. Percentage of the mean amplitude for all pixel pairs.

	A-1	A-2	A-3	B-1	B-2	B-3	C-1	C-2	C-3	D-1	D-2	D-3
A-1	0.00	0.19	0.25	0.64	0.65	0.72	0.90	0.93	0.83	1.00	1.00	1.00
A-2	0.23	0.00	0.08	0.56	0.57	0.66	0.88	0.91	0.79	1.00	1.00	1.00
A-3	0.34	0.09	0.00	0.51	0.53	0.63	0.87	0.90	0.77	1.00	1.00	1.00
B-1	1.76	1.25	1.06	0.00	0.04	0.24	0.73	0.79	0.52	1.00	1.00	1.00
B-2	1.86	1.33	1.13	0.04	0.00	0.21	0.72	0.79	0.50	1.00	1.00	1.00
B-3	2.63	1.96	1.71	0.32	0.27	0.00	0.65	0.73	0.37	1.00	1.00	1.00
C-1	9.28	7.37	6.67	2.72	2.59	1.83	0.00	0.24	0.79	1.00	1.00	1.00
C-2	12.47	9.97	9.04	3.88	3.70	2.71	0.31	0.00	1.34	0.99	1.00	1.00
C-3	4.74	3.68	3.28	1.08	1.01	0.58	0.44	0.57	0.00	1.00	1.00	1.00
D-1	2285.8	1861.7	1704.3	827.3	797.9	628.53	221.4	168.82	397.14	0.00	0.88	0.73
D-2	18553.0	15112.3	13835.4	6719.9	6481.3	5106.8	1803.7	1376.9	3229.4	7.11	0.00	1.19
D-3	8487.7	6913.5	6329.3	3073.9	2964.7	2335.9	824.7	629.4	1476.9	2.71	0.54	0.00

Current pixels are arranged in row order while sibling candidates are in column order. A value < 0.15 is marked in blue, which indicates the resemblance of the corresponding pixel pair.

Table 3.2. Percentage of the mean amplitude difference for all pixel pairs.

	A-1	A-2	A-3	B-1	B-2	B-3	C-1	C-2	C-3	D-1	D-2	D-3
A-1	0.00	1.31	1.51	2.86	3.09	1.37	0.82	0.27	5.02	1.15	0.82	0.89
A-2	4.21	0.00	0.62	4.96	5.70	0.18	1.57	5.09	11.89	0.51	1.58	1.34
A-3	2.97	0.38	0.00	2.66	3.12	0.27	1.35	3.51	6.93	0.70	1.36	1.21
B-1	1.54	0.83	0.73	0.00	0.12	0.80	1.10	1.69	1.16	0.92	1.10	1.06
B-2	1.48	0.85	0.76	0.11	0.00	0.82	1.09	1.61	0.93	0.93	1.09	1.05
B-3	3.71	0.16	0.37	4.03	4.66	0.00	1.48	4.45	9.89	0.59	1.49	1.29
C-1	4.59	2.74	3.83	11.38	12.67	3.06	0.00	6.12	23.47	1.85	0.01	0.40
C-2	0.21	1.24	1.40	2.46	2.64	1.29	0.86	0.00	4.15	1.12	0.86	0.92
C-3	1.25	0.92	0.87	0.54	0.48	0.91	1.04	1.32	0.00	0.96	1.04	1.03
D-1	7.55	1.04	2.32	11.16	12.67	1.42	2.17	9.34	25.32	0.00	2.18	1.70
D-2	4.56	2.73	3.81	11.31	12.59	3.05	0.01	6.08	23.32	1.85	0.00	0.41
D-3	8.36	3.92	5.74	18.38	20.54	4.46	0.67	10.93	38.62	2.43	0.69	0.00

(Values < 0.30 (suggested threshold in Spaans and Hooper (2016)) are marked in blue, indicating the resemblance of the corresponding pixel pair.)

Unfortunately, the two measures were not able to identify resembling pixels, no matter what threshold values were chosen. Firstly, both of the two percentage measures depend on the statistics owned by the current pixel as denominators. Therefore, they cannot provide symmetric results and the results may fluctuate dramatically when denominators are close to zero, which can be witnessed by pixels of class "D". Secondly, the amplitude time series of some samples, such as pixels "A-2", "A-3" and all "D-", remain relatively stable over all acquisitions. For these pixels, the mean amplitude difference between the master and slaves can be close to zero. Thus, the percentage of the mean amplitude difference for these pixels also varies dramatically and cannot be used as a valid estimator.

To overcome these limitations, a new similarity measure is proposed to identify siblings. Unlike Spaans and Hooper (2016), the developed similarity measure is not based on the interferogram network, but on the mean amplitude over all SLC images. Based on a stack of N SLC images, the similarity measure (denoted as S) between two pixels at (x_1, r_1) and (x_2, r_2) is defined as:

$$S = 1 - |\bar{A}(x_1, r_1) - \bar{A}(x_2, r_2)|/(\bar{A}(x_1, r_1) + \bar{A}(x_2, r_2)), \quad (3.1)$$

where $\bar{A}(x_i, r_i)(i = 1,2)$ is the mean amplitude of a pixel at (x_i, r_i) over the N SLC images. The proposed similarity measure ranges from zero to one. Larger values imply more

resemblance between the pixel pairs. A candidate is considered as a sibling of the current pixel when the similarity between them exceeds a specified threshold. Typical values for the similarity threshold range from 0.85 to 0.95 according to the relevant analysis in Section 3.4. The proposed similarity measure was tested with the selected samples, with siblings for all pixels detected correctly (Table 3.3). According to the achieved results, it is clear that the proposed similarity provides symmetry and is robust for pixels with sharply different amplitude levels. Moreover, the proposed similarity inherits advantages introduced by Spaans and Hooper (2016), including fast computation and low RAM requirements.

Table 3.3. Similarity among selected pixels

	A-1	A-2	A-3	B-1	B-2	B-3	C-1	C-2	C-3	D-1	D-2	D-3
A-1	1.00	0.93	0.90	0.70	0.68	0.67	0.47	0.47	0.47	0.03	0.03	0.03
A-2	0.93	1.00	0.97	0.76	0.75	0.73	0.52	0.52	0.52	0.04	0.03	0.03
A-3	0.90	0.97	1.00	0.79	0.77	0.75	0.54	0.54	0.54	0.04	0.03	0.03
B-1	0.70	0.76	0.79	1.00	0.98	0.97	0.73	0.73	0.73	0.06	0.05	0.05
B-2	0.68	0.75	0.77	0.98	1.00	0.98	0.75	0.74	0.74	0.06	0.05	0.05
B-3	0.67	0.73	0.75	0.97	0.98	1.00	0.76	0.76	0.76	0.06	0.06	0.06
C-1	0.47	0.52	0.54	0.73	0.75	0.76	1.00	0.99	1.00	0.10	0.09	0.09
C-2	0.47	0.52	0.54	0.73	0.74	0.76	0.99	1.00	1.00	0.10	0.09	0.09
C-3	0.47	0.52	0.54	0.73	0.74	0.76	1.00	1.00	1.00	0.10	0.09	0.09
D-1	0.03	0.04	0.04	0.06	0.06	0.06	0.10	0.10	0.10	1.00	0.93	0.93
D-2	0.03	0.03	0.03	0.05	0.05	0.06	0.09	0.09	0.09	0.93	1.00	1.00
D-3	0.03	0.03	0.03	0.05	0.05	0.06	0.09	0.09	0.09	0.93	1.00	1.00

(Values > 0.85 are marked in blue, indicating the resemblance status of a pair of pixels. Several common hypothesis tests, including the Kolmogorov-Smirnov test (Ferretti et al., 2011), the CLT-based test (Jiang et al., 2015), the Anderson-Darling test (Goel and Adam, 2012), the paired *t*-test, and the Wilcoxon signed-rank test (a non-parametric statistical hypothesis test used when comparing two matched samples) (Wilcoxon, 1945) were also applied to the selected samples in this study. The significance level for all hypothesis tests was set as 0.05 and the results of the identification of SHPs are illustrated in Figure 3.2.)

Contrary to the result of the developed similarity measure shown in Figure 3.2(a), hypothesis tests tend to reject three samples of class "A" as heterogeneous. Obviously, the mean amplitude values of three "A-" pixels are different, but relatively close. They are considered as heterogeneous by the applied hypothesis testing methods, but as resembling by the developed similarity measure. This is not a paradox, but symptomatic of a difference between the two

types of methods. It reflects that the hypothesis testing techniques are prone to distinguish heterogeneity between pixels with similar mean amplitude. On the other hand, "B-1", "B-2" and "C-1" are incorrectly recognized as homogeneous pixels by the Anderson-Darling test. For deformation monitoring purposes, performance should be evaluated via coherence estimation and phase filtering.

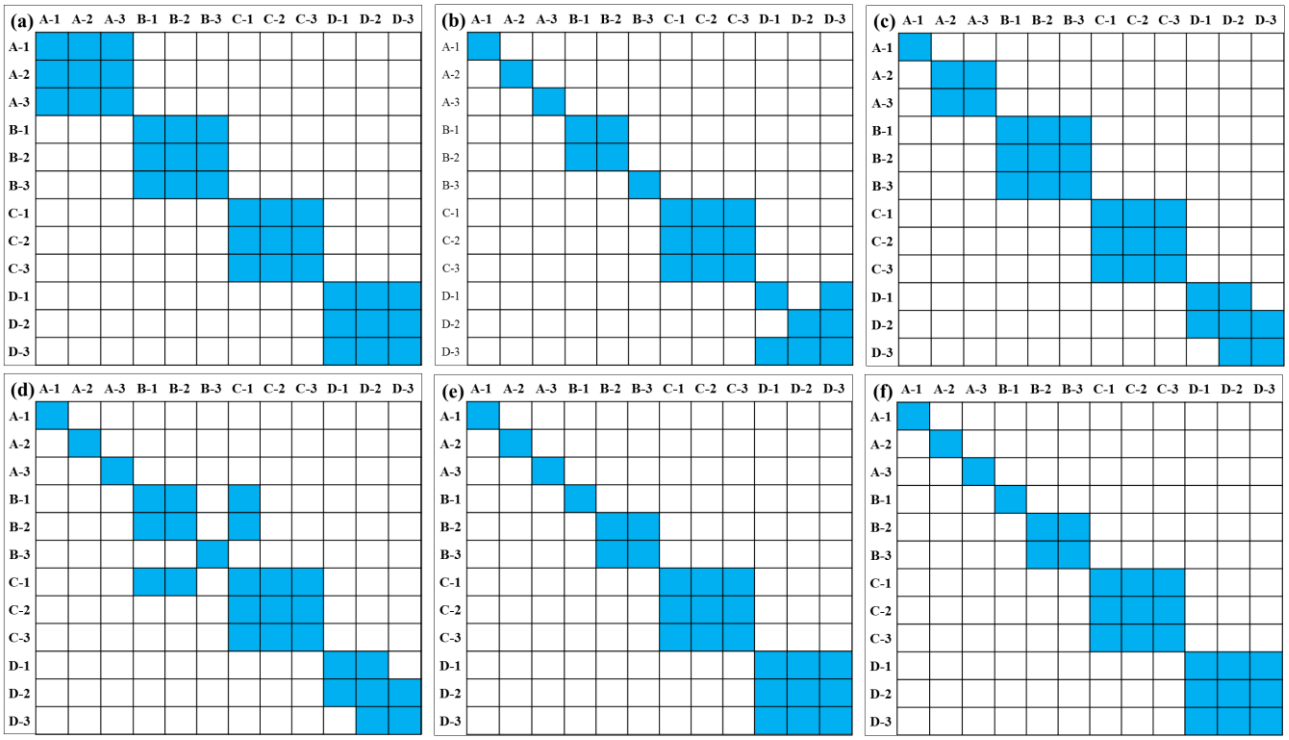

Figure 3.2. Identification of resembling or homogeneous pixels. Blue grids indicate the homogeneity of the corresponding pixel pair. (a) The proposed similarity. (b) Kolmogorov-Smirnov test. (c) Hypothesis test using CLT. (d) Anderson-Darling test. (e) Paired t-test. (f) Wilcoxon signed-rank test.

3.2.2 Estimation of coherence and interferometric phase

The maximum likelihood estimation of the coherence for a pixel is based on K samples related to the pixel, as shown in Equation (3.3). In this study, the siblings identified by the developed similarity measure are used as K samples for the estimation of coherence. The siblings-based coherence magnitude $\hat{\rho}$ is further estimated based on the second kind statistics (e.g. Abdelfattah and Nicolas, 2006; Jiang et al., 2014c):

$$\bar{\hat{\rho}} = \exp\left(\frac{1}{K}\sum_{l=1}^{K}\ln(\hat{\rho}_l)\right). \tag{3.2}$$

The coherence magnitude obtained by the second kind statistics is less biased and the variance

of the log-estimate is globally lower than that of the regular estimate (e.g. Abdelfattah and Nicolas, 2006; Jiang et al., 2014c).

In addition, the filtered interferometric phase $\hat{\varphi}$ for each pixel is achieved by the non-local averaging of the complex values of its siblings:

$$\begin{cases} e^{i\hat{\varphi}} = \sum_{l=1}^{K} e^{i\, w_l \varphi_l} \\ w_l = \bar{\hat{\rho}}_l / \sum_{l=1}^{K} \bar{\hat{\rho}}_l \end{cases}. \tag{3.3}$$

3.3 Experimental results

3.3.1 Data used in experiments

The data used in the experiments was collected by mounting the FastGBSAR system on a stationary concrete base, continuously observing the cliff on the north side of Tynemouth Priory and Castle, near to Newcastle upon Tyne, UK. The scene mainly comprises the cliff façade, the castle buildings, some areas of beach and the sea close to the south side of King Edward's Bay. An overview of the observed site and the geometric configuration for the data collection is shown in Figure 3.3(a). A close-up of the surface of the cliff façade can be seen in Figure 3.3(b), which mainly consists of outcrops, bare earth and vegetation, and a section of an artificial concrete wall. The mean amplitude, corresponding to 60 sequential SLC images, was manually aligned and projected onto the top view of the observed site for a better visual interpretation (see Figures 3.3(c) and 3.3(d)). The dimension of each SLC image was 294 by 254 pixels. A mask, displayed in Figure 3.3(e), was generated by thresholding the mean amplitude image, in which the area of interest in white indicates the illuminated region and the background in black corresponds to the shadow zones and sea areas. The background area without useful information should not be considered for precise interferometry analysis. The grey area in the mask was added to mark the ambiguous border between the area of interest and the background. The mask was then used for quantitative analysis in Sections 3.3.3 and 3.3.4.

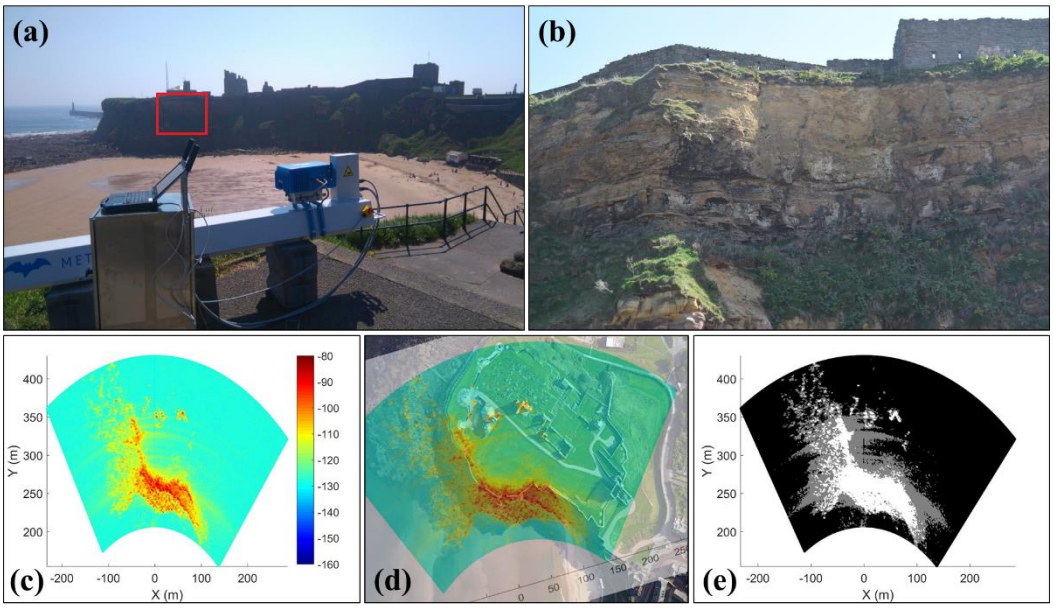

Figure 3.3. An overview of data collection and the observed Tynemouth Cliff. (a) The deployment of the FastGBSAR system for the data collection. (b) A close-up of the cliff façade with respect to the area marked in red box in (a). (c) The mean amplitude image of 60 GBSAR SLCs (shown in decibels). (d) Co-registration of the mean amplitude image with the top view of the site in Google Earth. (e) An image mask, containing the area of interest (in white), the background (in black) and the ambiguous area (in grey) between them.

Based on the same data acquisition configuration, two datasets with different acquisitions and different sampling temporal resolutions were used in the experiments. Dataset I-1 consisted of 60 SLC images and the data acquisition frequency was every 10 seconds. Dataset I-2 consisted of 30 SLC images with a temporal resolution of four minutes.

3.3.2 Identification of Siblings

The identification of siblings was performed using the two datasets and results compared to the "FaSHPS" algorithm, namely the identification of SHPs using the CLT-based hypothesis test, which is representative of the SHP methods and possesses high computational efficiency (Jiang et al., 2015). The dimension of the non-local search window was fixed to 15 x 15. The similarity threshold for the proposed method was set as 0.85 and the significance level for the "FaSHPS" hypothesis test as 0.05. It is known that insufficient siblings can lead to inaccuracies in coherence estimation (Spaans and Hooper, 2016) and phase de-noising (Deledalle et al., 2011). If a pixel does not have sufficient siblings within the threshold, a minimum number of siblings are required for the sake of reliable coherence estimation and phase de-noising for this pixel. In such a case the most similar pixels (quantified by the developed similarity measure) beyond the threshold can be added as siblings. On the basis of previous relevant studies (e.g. Deledalle et

al., 2011; Spaans and Hooper, 2016) and analysis conducted and reported in Section 3.4, the minimum number of siblings was set as 10. The number of siblings and SHPs for the two datasets are shown in Figure 3.4. It can be observed that the identified siblings and SHPs in the background area are more than the area of interest . This is because the background contains no useful information and suffers from noise. Pixels in the background have similar amplitude statistics contributed by such noise, thus are likely to be siblings or SHPs to each other. The histograms with respect to the number of siblings and SHPs for the area of interest are given in Figure 3.5. Based on the histograms, it is seen that the overall number of siblings identified by the developed method is greater than the number of SHPs detected by "FaSHPS", and a large number of isolated pixels without SHPs can also be seen from the histograms of SHPs.

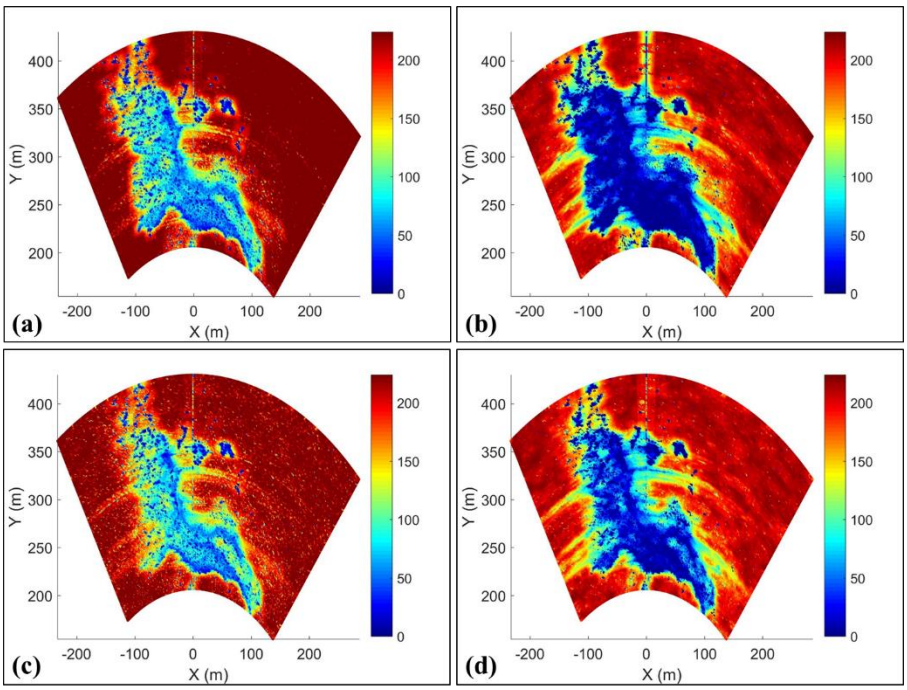

Figure 3.4. Number of identified resembling pixels. (a) Number of siblings for Dataset I-1. (b) Number of SHPs for Dataset I-1. (c) Number of siblings for Dataset I-2. (d) Number of SHPs for Dataset I-2.

"FaSHPS" is reported to be computationally efficient when compared with other multitemporal algorithms (Jiang et al., 2015). The computational efficiency of the developed method, termed Multi-temporal Interferometry based on Amplitude Similarity ("MIAS"), was compared with "FaSHPS" using the same computer with MATLAB R2016b software and an Intel i7 2.40 GHz CPU. For Dataset I-1 with 60 SLCs, "MIAS" cost 0.9 s completing the identification process, while "FaSHPS" cost 9.1 s. The time costs of Dataset I-2 with 30 SLCs was 0.8 s for "MIAS" and 7.6 s for "FaSHPS".

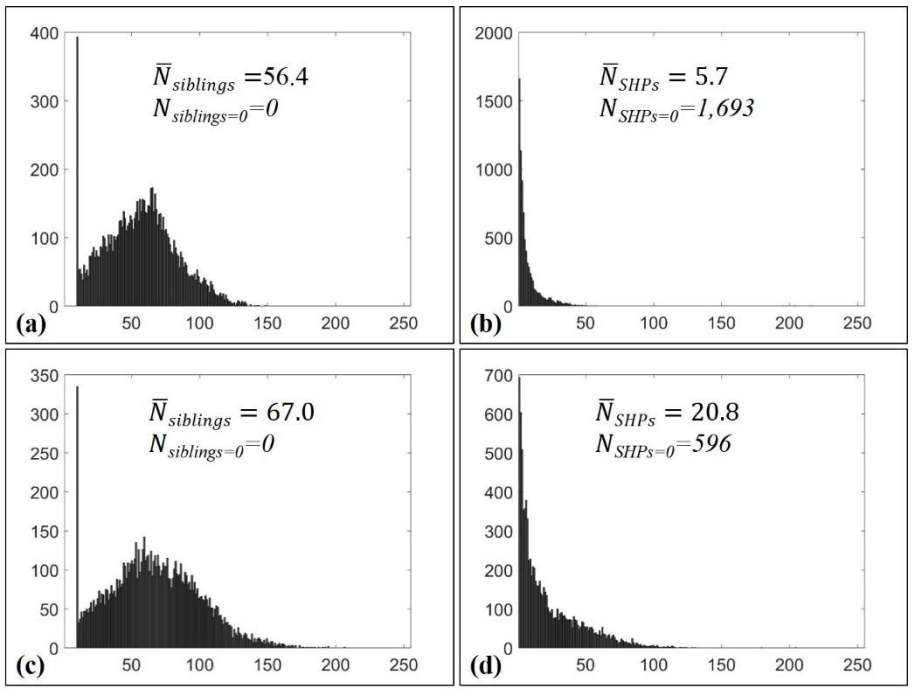

Figure 3.5. Histograms of siblings and SHPs in the area of interest for two datasets. $\overline{N}_{\text{siblings}}$ and $\overline{N}_{\text{SHPs}}$ are the average number of siblings and SHPs respectively. $\overline{N}_{\text{siblings}}$=0 and $\overline{N}_{\text{SHPs}}$=0 represent the number of isolated pixels without siblings or SHPs respectively. (a) Histogram of siblings for Dataset I-1. (b) Histogram of SHPs for Dataset I-1. (c) Histogram of Sibling for Dataset I-2; (d) Histogram of SHPs for Dataset I-2.

3.3.3 Coherence Estimation

Two GBSAR interferometric pairs were utilised in the experiments for coherence estimation. One interferogram was constructed by two temporally consecutive SLC images in Dataset I-1, with a time difference between the two acquisitions of 10 s. The second interferogram was constructed from two SLC images with a 2-hour interval from Dataset I-2. The coherence for the two interferometric pairs was obtained by the following methods: the "boxcar" estimator, the "nl-InSAR" technique, the direct SHPs-based estimator (denoted as "SHPs-based"), the direct siblings-based (denoted as "Siblings-based"), the SHPs-based estimation with the second kind statistics (denoted as "SHPs+Sec") and the improved siblings-based coherence estimation with the second kind statistics (denoted as "Siblings+Sec"). Note that "SHPs+Sec" is the coherence estimation algorithm proposed in "FaSHPS" and "Siblings+Sec" is the developed coherence estimation method in this study. The coherence maps for the interferogram with short time difference are shown in Figure 3.6.

In comparison to all non-local methods, it is visible that the "boxcar" estimator tends to overestimate the coherence in the background and suffer resolution losses in the area of interest.

The findings are consistent with previous spaceborne SAR studies (e.g. Goel and Adam, 2012; Spaans and Hooper, 2016). The coherence maps in Figures 3.6(d) and (f) achieved based on the second kind statistics are visibly smoother than the direct non-local estimation in Figures 3.6(c) and (e).

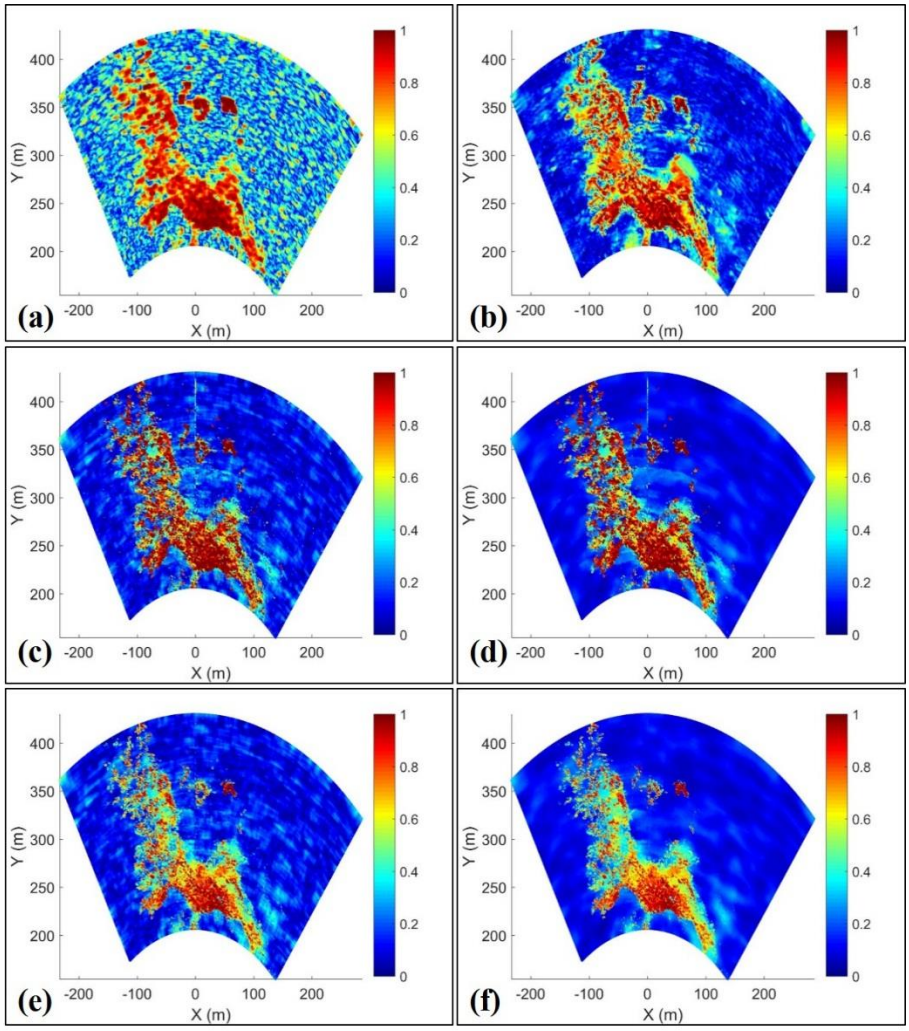

Figure 3.6. The coherence maps of the interferogram with a 10 s time interval from Dataset I-1. (a) "Boxcar" (5×5 window). (b) "nl-InSAR" (search window: 21×21, patch window: 7×7, minimum equivalent number of looks: 10, number of iterations: 10). (c) "SHPs-based". (d) "SHPs+Sec". (e) "Siblings-based". (f) "Siblings+Sec".

To quantitatively compare the performance of these methods, the mean and standard deviation of the coherence for the area of interest and the background were calculated. Moreover, the number of pixels in the area of interest and the background with coherence greater than a specified threshold value was recorded. The background, consisting of shadow zones and sea areas, was dominated by high noise and was expected to show low coherence. Thus, a greater number of coherent pixels in the background means a lower performance of the method in coping with GBSAR signal noise. These statistics are summarised in Table 3.4.

Table 3.4. The statistics of the coherence for the interferogram with 10 s elapse.

	Area of interest			Background		
	mean	std[a]	pixels	mean	std	pixels
Boxcar	0.82	0.17	8,480 (γ>0.6)	0.33	0.17	3,559 (γ>0.6)
nl-InSAR	0.80	0.18	8,189 (γ >0.6)	0.17	0.13	950 (γ>0.6)
SHPs-based	0.83	0.22	7,905 (γ >0.6)	0.14	0.09	216 (γ>0.6)
SHPs+Sec	0.82	0.22	7,808 (γ >0.6)	0.12	0.07	105 (γ>0.6)
Siblings-based	0.70	0.22	8,064 (γ >0.45)	0.13	0.08	131 (γ >0.45)
Siblings+Sec	0.67	0.14	8,031 (γ >0.45)	0.12	0.05	4 (γ >0.45)

[a] std is the standard deviation of the estimated coherence.

The overestimation of the "boxcar" coherence for the de-correlated area was again confirmed by the high mean and standard deviation values and the large amount of false coherence in the background. The "nl-InSAR" approach obtains high coherence in the area of interest but with too many false coherent pixels in the background. Overall, SHPs or sibling-related coherence estimation methods were more robust to the noisy background than "boxcar" and "nl-InSAR". In particular, the methods based on the second kind statistics can significantly mitigate the false coherence estimation in the background. The overall sibling-related coherence in the area of interest was lower than other methods. Thus, a different threshold value was used for the statistics of "Siblings-based" and "Siblings+Sec". From Table 3.4, it can be observed that the number of false coherent pixels detected by the developed method ("Siblings+Sec") was much less than that of the other methods, indicating the best performance in this experiment. Furthermore, the coherence estimation was also conducted for the second interferogram with a 2-hour interval. Figure 3.7 displays coherence maps and Table 3.5 compares the statistics in the area of interest and the background.

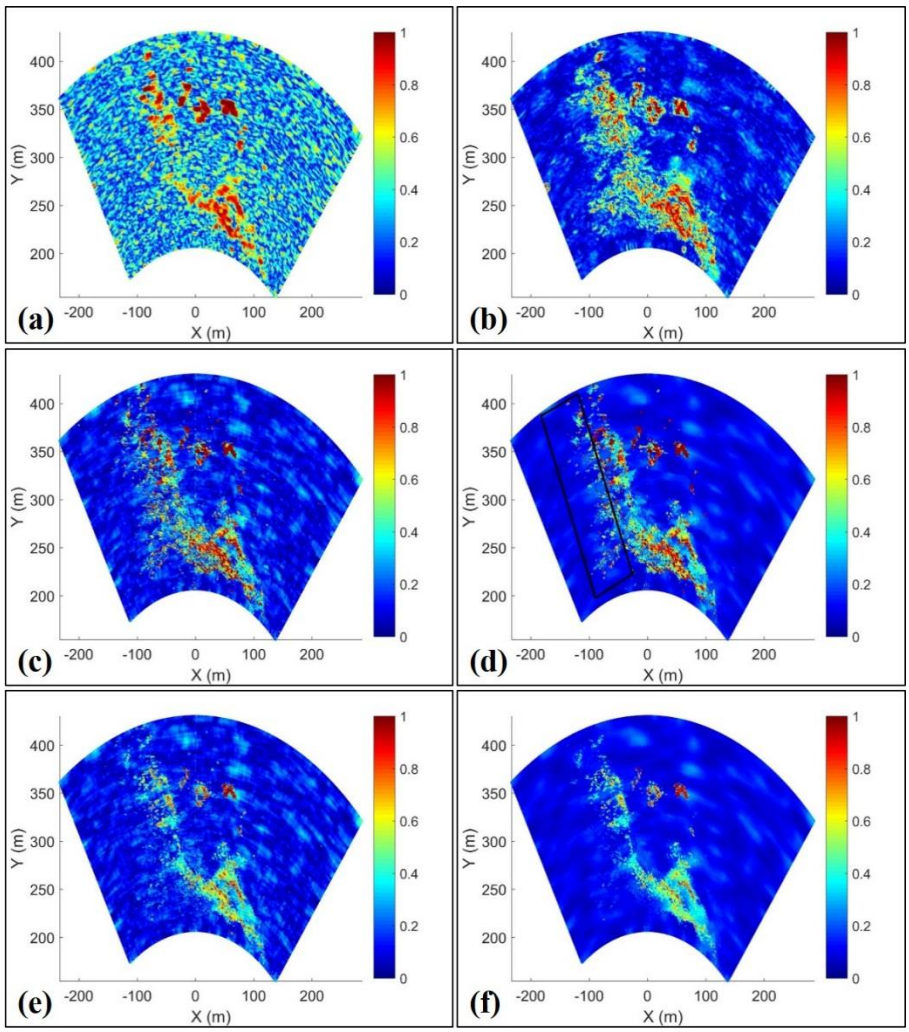

Figure 3.7. Coherence of the interferogram with a 2-hour interval from Dataset I-2. (a) "Boxcar". (b) "nl-InSAR". (c) "SHPs-based". (d) "SHPs+Sec" (the decorrelated area caused by the sea level rise is roughly marked in the black box). (e) "Siblings-based". (f) "Siblings+Sec".

Table 3.5. Coherence statistics for the interferogram with a 2-hour time span.

	Area of interest			Background		
	mean	std	pixels	mean	std	pixels
Boxcar	0.51	0.24	3,444 (γ>0.6)	0.31	0.15	1,875 (γ>0.6)
nl-InSAR	0.52	0.25	3,516 (γ>0.6)	0.14	0.10	365 (γ>0.6)
SHPs-based	0.51	0.30	3,567 (γ>0.6)	0.12	0.07	44 (γ>0.6)
SHPs+Sec	0.48	0.29	3,083 (γ>0.6)	0.11	0.04	19 (γ>0.6)
Siblings-based	0.34	0.22	2,575 (γ>0.45)	0.12	0.06	12 (γ>0.45)
Siblings+Sec	0.31	0.19	1,973 (γ>0.45)	0.10	0.04	3 (γ>0.45)

From comparison of the coherence maps shown in Figures 3.6 and 3.7, it is evident that the 2-hour interferogram suffers temporal decorrelation. As mentioned previously, FastGBSAR works at Ku band and the short wavelength is sensitive to surface changes and atmospheric variations. The vegetation coverage on the illuminated cliff façade increases the decorrelation. Moreover, decorrelation on the left part of the area of interest that is roughly marked by the black box in Figure 3.7(d) was likely caused by the tide that submerged the beach and rocks close to the sea over the course of the 2-hour interval. The temporal decorrelation also demonstrates the requirement for GBSAR time series analysis.

According to the experimental results, the coherence statistics (including the mean, standard deviation and coherence amounts) in the area of interest achieved by "Siblings-based" and "Siblings+Sec" are lower than the counterparts of "SHPs-based" and "SHPs+Sec", which is related to the fact that the number of siblings identified by the proposed "MIAS" was greater than the number of SHPs detected by "FaSHPS". There are a number of isolated pixels without SHPs detected by "FaSHPS" and the coherence for an isolated pixel is always one (Ferretti et al., 2011) as coherence in this case is estimated merely using two complex pixel values (one on the master and the other on the slave). Reported by Jiang et al. (2014a) and Spaans and Hooper (2016), the estimation with insufficient samples would produce a biased result.

Table 3.5 shows that "SHPs-based" and "SHPs+Sec" selected more coherent pixels in the area of interest than "Siblings-based" and "Siblings+Sec". However, some coherent pixels selected by "SHPs-based" and "SHPs+Sec" can actually be decorrelated in the left part of the area of interest . To explain this, assume a pixel in the left part of the area of interest, which corresponds to a ground rock close to the sea, was visible in the master image but was submerged by water two hours later and became invisible in the slave image. The pixel should be decorrelated with a low coherence value in the 2-hour interferogram. However, this target is prone to be an isolated pixel with high coherence in "FaSHPS", as hypothesis tests tend to reject samples with a strong reflection as heterogeneous. A number of this kind of submerged isolated targets were de-correlated but still showed high coherence in the 2-hour interferogram. This can be confirmed by the discontinuous interferometric phase of coherent pixels selected by "SHPs+Sec", shown in Figure 3.9. On the other hand, the proposed method obtained the least number of false coherent pixels. In the proposed method, a minimum number of ten siblings were kept. Admittedly, the coherence of an isolated scatterer surrounded by distributed scatterers would be degraded in this case. Experimental results demonstrate that maintaining a

minimum number of siblings is able to reduce the bias in coherence estimation, which was also reported in previous studies (e.g. Jiang et al., 2014a; Spaans and Hooper, 2016).

3.3.4 Phase filtering

Coherence is an indicator of the interferometric phase quality. Usually, the deformation measurement only focuses on coherent pixels. Thus, filtering is further carried out to increase the SNR of the interferometric phase for coherent pixels. To validate the feasibility of the developed non-local method on phase filtering, experiments were conducted using the two interferograms introduced previously. The results achieved by the developed method were compared with results from the "boxcar" multilooking, the "nl-InSAR" and the SHPs-based filtering method. Pixels for each filtering process were separately detected by their own coherence. Only pixels with coherence above the specified threshold values were processed. The performance of filtering methods can be indicated by a Quality Factor (denoted as Q) (Serkan et al., 2008). Q for the original image before filtering is always equal to one. Any shift in the mean value of the interferometric phase before and after filtering will decrease Q and be evaluated as a degradation in filter capability. A reduction of the standard deviation of the interferometric phase will increase Q. A higher Q value implies a better performance of the filtering technique. Thus, the quality factor Q is used to quantitatively compare the performance of these filtering methods.

For the interferogram formed by two sequential acquisitions with only ten seconds time difference, an assumption is that no significant surface movements took place and the atmospheric conditions remained relatively stable over such a short period. Accordingly, the phase change of coherent pixels should be close to zero. The wrapped interferometric phase of coherent pixels and phase histograms before and after filtering for this interferogram are given in Figure 3.8. Q values achieved by different methods are annotated to the phase histograms in Figure 3.8.

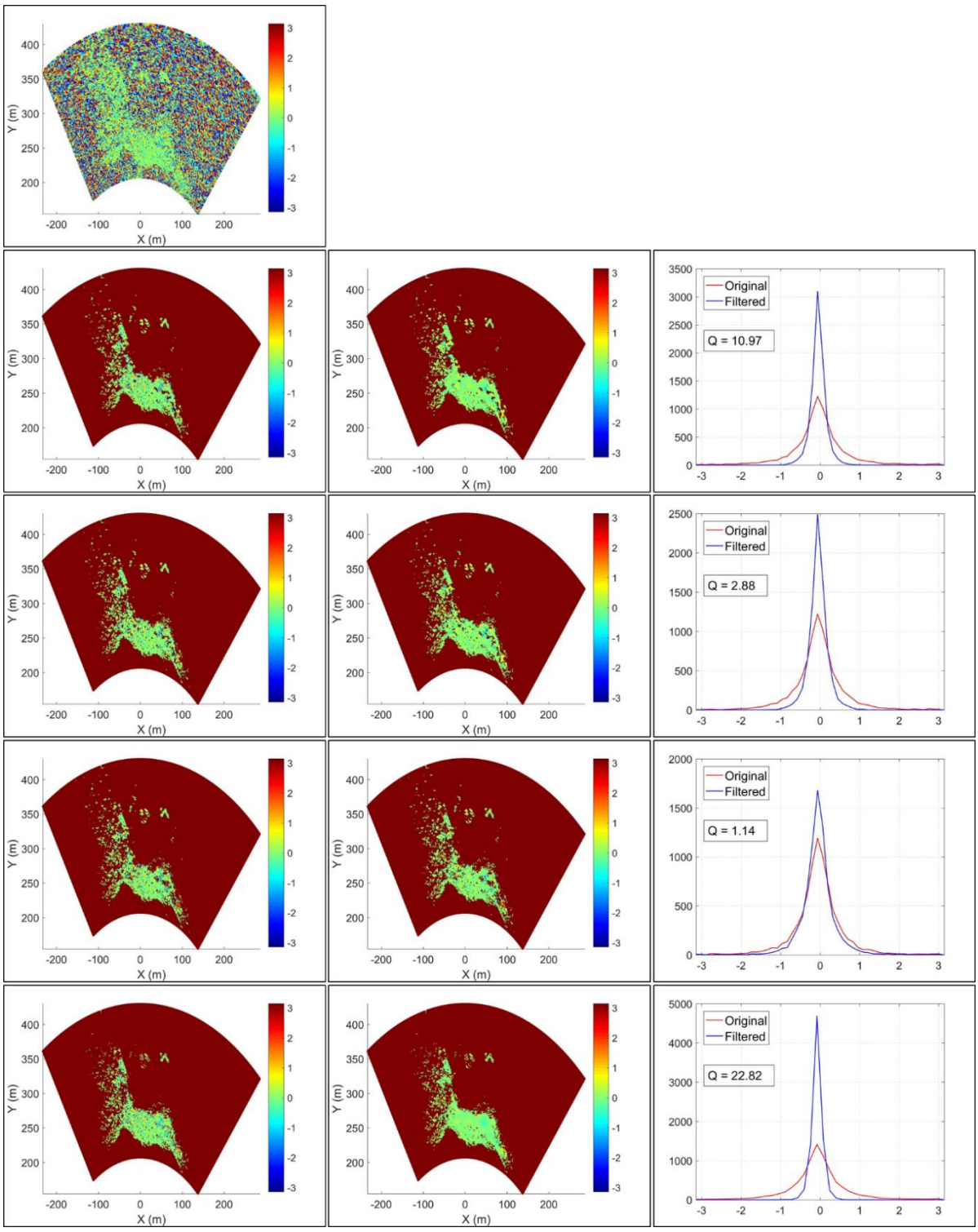

Figure 3.8. Filtering results for the interferogram with 10 s elapse. (First line) The original wrapped interferogram. (Following lines) (a) the interferometric phase of coherent pixels before filtering; (b) the filtered interferometric phase, and (c) phase histograms and the filtering quality factor, obtained by (top to bottom) the "boxcar" multilooking (5×5 window), the "nl-InSAR", the SHPs-based filtering and the developed siblings-based filtering. Correspondingly, coherent pixels are respectively determined by the "boxcar" estimation (γ>0.6), "nl-InSAR" (γ>0.6), "SHPs+Sec" (γ>0.6) and "Siblings+Sec" (γ>0.45). Pixels in decorrelated areas are marked in brown for the convenience of visualization.

From the phase histograms in Figure 3.8(c), it can be seen that the mean values of the interferometric phase in the coherent areas before and after filtering are close to zero. This supports the assumption that no significant surface movements and environmental variations occurred during the short time elapse in the observed area. Among the four filtering methods, the developed siblings-based filtering achieved the best Q values (22.82), followed by "boxcar" multilooking (10.97), nl-InSAR (2.88) and SHPs-based filtering (1.14).

The number of pixels with an absolute phase change greater than $\pi/3$ were also recorded. A larger number implies a poorer filtering performance under the assumption of no significant surface movements and environmental variations. The values for "boxcar", "nl-InSAR", the SHPs-based filtering and the developed siblings-based filtering were 6, 16, 145 and 1 respectively. Similarly, the developed siblings-based filtering outperformed other methods based on this experiment and the SHPs-based filtering obtained a large number of pixels with an absolute phase change greater than $\pi/3$. To discern the reason, the average number of detected SHPs and siblings for all 145 pixels was calculated. A striking contrast between the two values was witnessed: the average SHPs was 0.9 while the average siblings was 37.4. This finding agrees with previous studies (e.g. Ferretti et al., 2011; Spaans and Hooper, 2016) that maintaining a minimum number of resembling samples can facilitate spatial filtering and coherence estimation. The SHPs-based method was able to distinguish heterogeneity and lead to a large number of isolated pixels, this, however, may bring problems in phase filtering. It is worth noting that the "FaSHPS" algorithm was originally proposed only for coherence estimation. These findings were also verified by the experimental results for the 2-hour interferogram, as shown in Figure 3.9. The overall performance of different methods for this interferometric pair with a longer time elapse was similar to that with a shorter time elapse. The developed siblings-based filtering showed good filtering performance with a Q factor reaching 9.41, which was much higher than the other techniques.

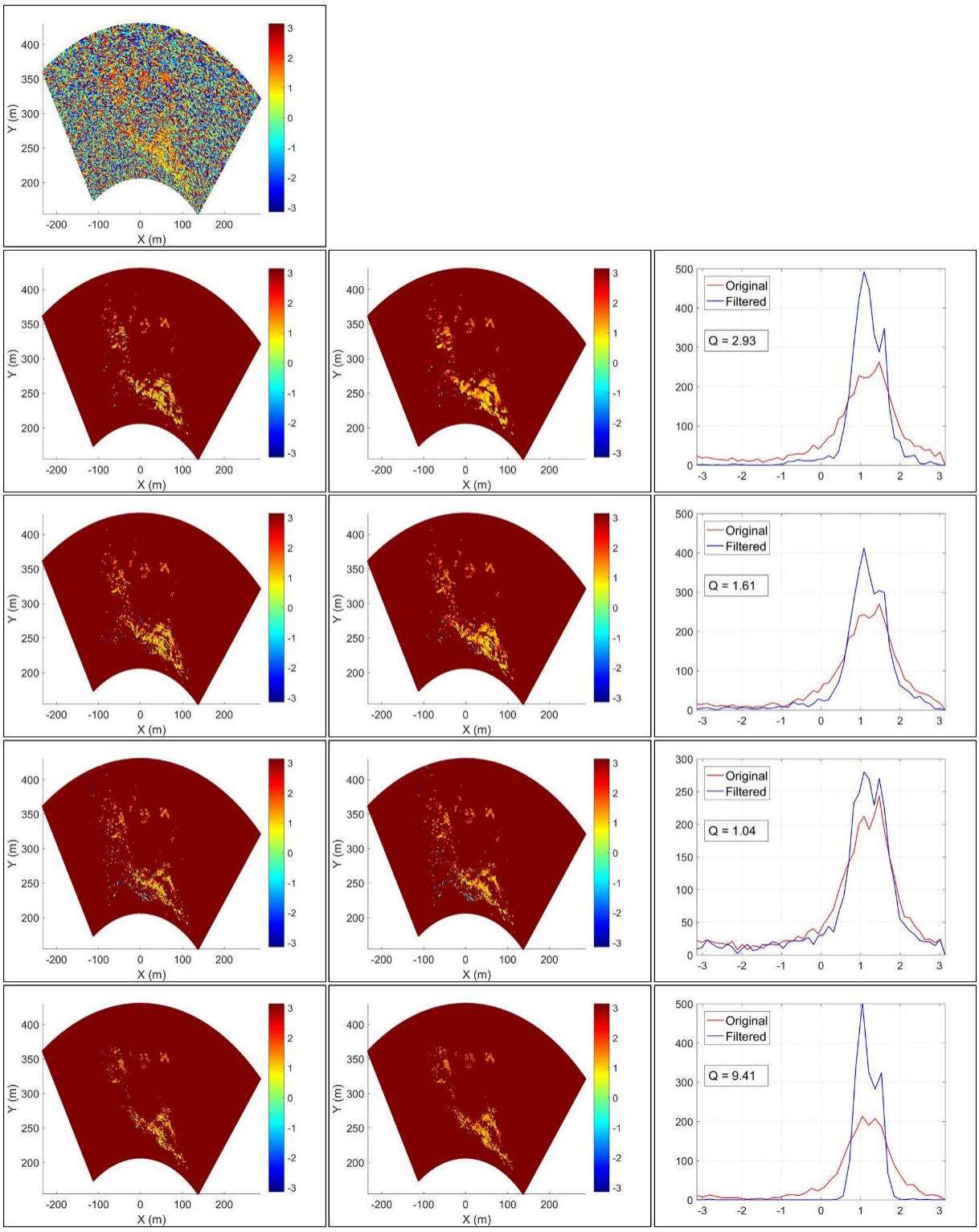

(a) (b) (c)

Figure 3.9. Filtering results for the 2-hour interferogram. The implication of subfigures is as for Figure 3.8. Pixels in de-correlated areas are marked in brown for the convenience of visualization.

3.3.5 Demonstration

Interferograms suffering from temporal decorrelation will have limited use for deformation monitoring. The interferogram with a 2-hour interval in this study displayed temporal decorrelation. Time series analysis is thus proposed to overcome this limitation. The proposed non-local method was integrated into a real time ground-based SAR (RT-GBSAR) time series chain (see Chapter 4 for details) based on the SBAS algorithm. The coherence of each interferogram in the network was calculated by the developed method, namely the siblings-based coherence with the estimation of the second kind statistics. Coherent pixels were detected via a full-rank criterion (see Chapter 4 for details), which enables the selection of not only qualified PCPs, but also PSs. The interferometric phase of detected pixels was firstly de-noised using the non-local filter. The unwrapped phase of detected pixels was then obtained using the Minimum Cost Flow approach (Costantini and Rosen, 1999). Finally, atmospheric artefacts must be properly compensated in order to obtain precise displacement time series. Considering the moderate size of the test site, the atmospheric variation was modelled as a range-dependent model through highly-coherent pixels selected from stable areas and under the medium homogeneity hypothesis, referring to the approach presented in Pipia et al. (2008).

In the experiments, the temporal baseline constraints were set as one minute for Dataset I-1 and 20 minutes for Dataset I-2, with consideration for the computational efficiency and temporal decorrelation. Thus, there were 339 interferograms for Dataset I-1 and 135 for Dataset I-2. A full combination of interferograms can provide the most redundant observations, but it also increases the computation load and degrades the real-time performance in urgent situations. Parameter configurations were kept the same for both datasets: the similarity threshold was set to 0.85; the minimum number of siblings was set to 10; the non-local window size was 15 x 15 pixels and the coherence threshold value was 0.45. A subset of highly-coherent pixels with mean coherence over all interferograms of > 0.85 was selected from stable areas to perform the linear regression of atmospheric variations (i.e. $y = a_0 + a_1 x$, where y denotes the atmospheric variation and x the range between the radar sensor and the coherent target; a_0 and a_1 are coefficients). The stable areas can be identified through a priori knowledge and visual inspection of the superposition map of atmospheric variations and displacements. Based on the linear range-dependent model, the atmospheric variations of all coherent pixels were compensated and thus separated from the cumulative displacements.

Regarding Dataset I-1, the correction of atmospheric variations and the obtainment of cumulative displacements are given in Figure 3.10. The superposition map of atmospheric variations and displacements in Figure 3.10(a) can be used as an auxiliary visual material to identify stable areas. According to Figures 3.10(b) and 3.10(c), it appeared that the atmospheric conditions remained relatively stable during the 10-minute observation period. However, obvious deformation signals can be observed in three areas (Figure 3.10(d)). These areas are near the sea and the ground targets are primarily rocks and sands. To investigate these signals, three pixels (P1, P2 and P3) were selected to look into their temporal evolution. The physical feature of pixels P1, P2 and P3 are rocks. A stable pixel (P4) was also selected as a comparison. The line graphs in Figure 3.10(c) show the time series of the SLC raw phase (ψ), the 1D unwrapped phase ($\varphi_{1\mathrm{D}}$) and cumulative displacements (d) for these pixels. Particularly, $\varphi_{1\mathrm{D}}$ is a vector of temporally unwrapped phase on interferograms formed with the first (earliest) SLC as the master and others as slaves. It is worth noting that $\varphi_{1\mathrm{D}}$ is not the phase used in time series analysis and it is only used here as an auxiliary evidence of the high phase quality and the rough change trend of these pixels. In general, pixels P1, P2, and P3 experienced a gradual process of change. All the three pixels exhibited negative displacements which suggested the targets were moving towards the radar direction during the observation period. The overall trend of cumulative displacements agreed with the trend of $\varphi_{1\mathrm{D}}$. On the other hand, there is inconsistency in scale as $\varphi_{1\mathrm{D}}$ is likely to have unwrapping errors and it is not the unwrapped phase used in time series analysis. Moreover, non-local filtering and atmospheric estimation also altered the principal value of the interferometric phase used for deformation derivation.

The results of Dataset I-2 are shown in Figure 3.11. It can be observed that pixels P1 and P3 in Figure 3.10(d) disappeared from the results of Dataset I-2. This is because the first image of Dataset I-2 was acquired at around midday and the last one was captured two hours later. During that time, the areas where P1 and P3 were located became submerged due to the sea tide. Besides, the linear trend between the atmospheric variation and the range is visible in Figure 3.11(b). The superposition (Figure 3.11(a)) is dominated by the atmospheric variation (Figure 3.11(c)). From the deformation map in Figure 3.11(d), no significant signals can be found in the cliff façade or the castle buildings as the cumulative displacements at these areas vary within 2 mm. Similar to Dataset I-1, deformation signals appeared in the areas near the sea. Pixels P2 and P5 experienced approximate displacements of -3.5 mm, suggesting the targets moved towards the radar direction, while P4 remained stable over the 2-hour observation period (Figure 3.11(e)).

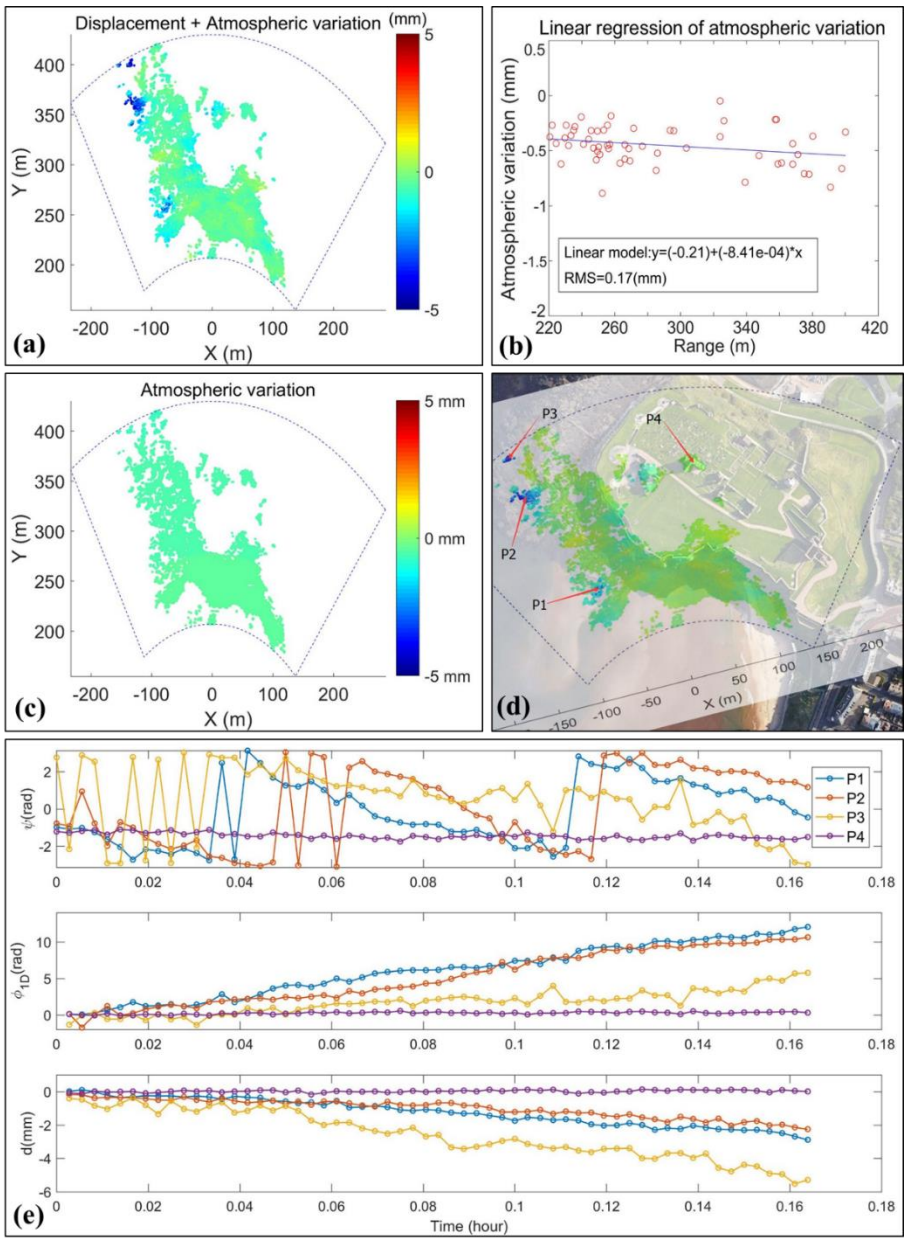

Figure 3.10. GBSAR time series analysis results of Dataset I-1. (a) The superposition map of displacements and atmospheric variations. (b) Linear regression of atmospheric variation. (c) Atmospheric variation map over 10 minutes of the acquisition time. (d) Co-registration of the displacement map with the top view of the site in Google Earth. (e) The time series raw phase, 1D unwrapped phase and cumulative displacements of the four pixels.

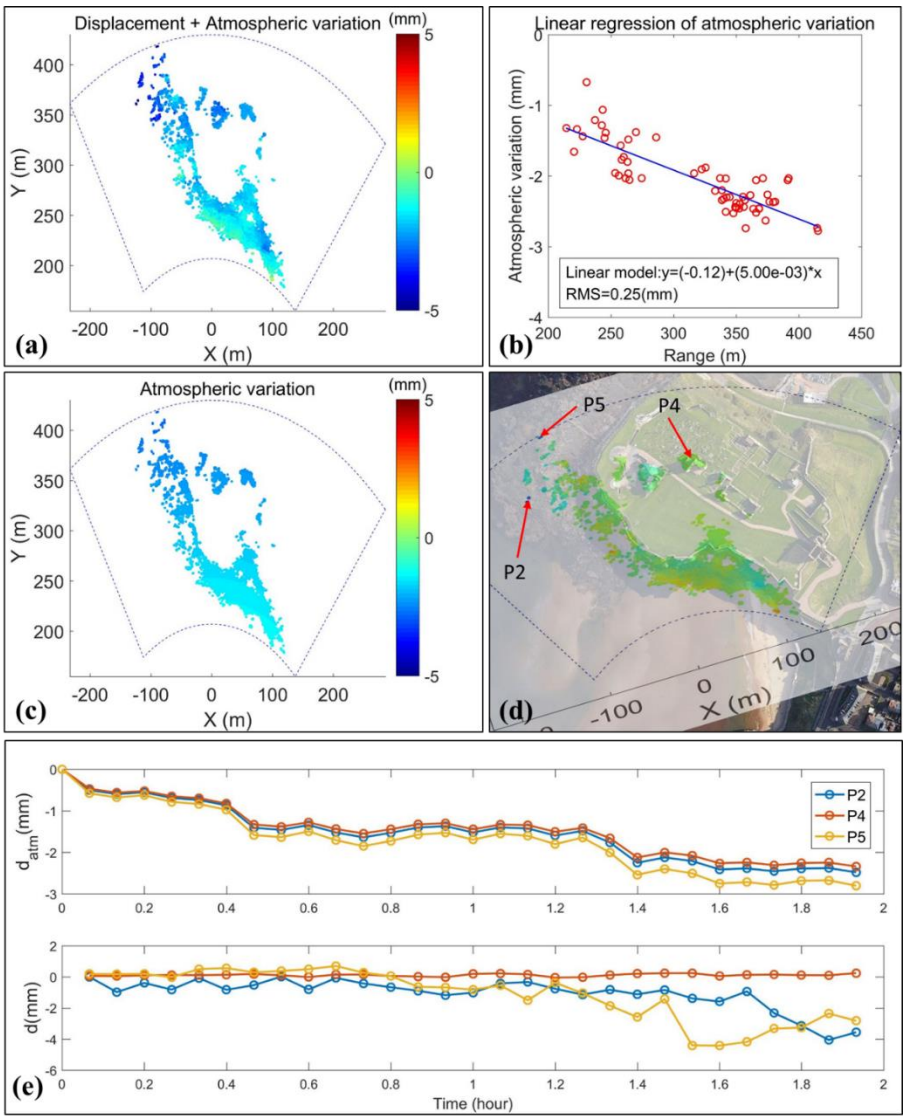

Figure 3.11. GBSAR time series analysis results of Dataset I-2. (a) The superposition map of displacements and atmospheric variations over two hours of the acquisition time. (b) Linear regression of atmospheric variation. (c) The atmospheric variation map over 2-hour acquisition time. (d) The displacement map co-registered with the top view of the site in Google Earth. Note that the coverage of this displacement map is smaller than that of Dataset I-1 due to sea tides. (e) The time series atmospheric variations (datm) and cumulative displacements of pixels P2, P4 and P5.

3.4 Analysis and discussions

The performance of the developed non-local method on coherence estimation and phase filtering has been demonstrated and evaluated. Here the focus is on justification of parameters involved in the developed non-local method: the similarity threshold, the coherence threshold, the non-local window size and the minimum siblings. Based on Dataset I-2, different combinations of these parameters were used in time series analysis. The number of detected coherent pixels, the RMS of inversion precision (defined in Appendix A) for all coherent pixels

and the time cost is recorded in Table 3.6.

Table 3.6. Results of different parameter configurations in GBSAR time series analysis.

	S_{thr} [a]	M_{sib} [b]	γ_{thr} [c]	W [d]	n_{CPS} [e]	RMS [f]	t [g]
1	0.8	10	0.85	15×15	417	0.06 mm	310 s
2	0.85	10	0.85	15×15	469	0.06 mm	283 s
3	0.9	10	0.85	15×15	540	0.07 mm	267 s
4	0.95	10	0.85	15×15	595	0.08 mm	211 s
5	0.8	10	0.45	15×15	5,312	0.12 mm	304 s
6	0.85	10	0.45	15×15	5,283	0.14 mm	300 s
7	0.9	10	0.45	15×15	5,441	0.16 mm	277 s
8	0.95	10	0.45	15×15	5,867	0.21 mm	211 s
9	0.85	10	0.35	15×15	7,520	0.18 mm	297 s
10	0.85	10	0.55	15×15	3,429	0.10 mm	296 s
11	0.85	10	0.45	11×11	5,630	0.18 mm	206 s
12	0.85	10	0.45	19×19	5,120	0.12 mm	378 s
13	0.85	5	0.45	15×15	5,312	0.15 mm	277 s
14	0.85	5	0.85	15×15	511	0.06 mm	275 s
15	0.85	25	0.45	15×15	5,226	0.13 mm	276 s
16	0.85	25	0.85	15×15	363	0.05 mm	272 s

[a] S_{thr} is the similarity threshold; [b] M_{sib} is the number of minimum siblings; [c] γ_{thr} is the coherence threshold; [d] W is the window size; [e] n_{CPS} is the number of coherent pixels; [f] RMS is the root mean square of inversion precision; [g] t is the time cost.

By comparing Configurations 1 - 8, it is found that the similarity threshold affects the number of coherent pixels. Particularly, Configurations 5 - 8 show that a higher similarity increases the number of highly-coherent pixels ($\gamma > 0.85$) and degrades the precision. This is because a higher similarity threshold means fewer siblings, which leads to increased computational efficiency and less smoothness in the coherence estimation and interferometric phase. Meanwhile, a too low similarity threshold should also be avoided as it would detect too many inaccurate siblings. Figure 3.12 compares the effect of the similarity threshold on coherence estimation. A low similarity threshold leads to serious resolution loss.

Configurations 2, 6, 9 and 10 demonstrate that a lower coherence threshold value can enlarge the number of coherent pixels at the expense of precision. Based on Configurations 2, 11 and 12, it is clear that the non-local window size has a considerable effect on computation efficiency. A small window size is efficient but may have limited ability in phase de-noising. In addition, maintaining more siblings will also degrade coherence estimation, especially for highly-

coherent pixels in the areas with rich texture according to Configurations 2, 6 and 13 - 16. On the other hand, too few siblings would cause issues in phase filtering, which has been reported in the experiments. The parameter configuration is therefore a trade-off between characteristics.

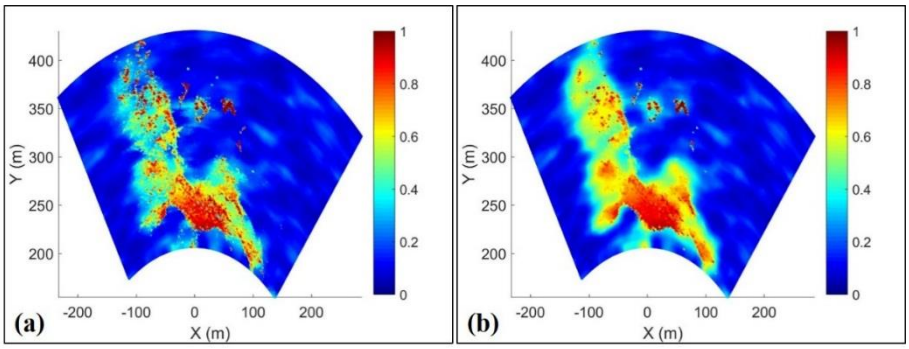

Figure 3.12. Coherence estimation by the developed method with different similarity threshold values. (a) Thresholding by 0.85. (b) Thresholding by 0.6.

3.5 Summary

In this chapter, a simple but efficient similarity measure has been presented to identify resembling pixels for distributed targets, together with a comprehensive non-local method ("MIAS") based upon this concept. The accurate estimation of coherence and interferometric phase can be achieved by the developed method and has been integrated into a complete GBSAR time series analysis. The following conclusions are reached on the basis of the experimental results and related analysis:

(1) The feasibility of the developed similarity on the identification of resembling samples from a non-local window has been verified by using a number of selected pixels. The proposed similarity measure overcomes the limitations of existing methods on processing FastGBSAR datasets and extracts all test samples correctly.

(2) Experiments have been performed with two FastGBSAR datasets. It has been successfully demonstrated that the identification process of the proposed "MIAS" method is more efficient and faster than the "FaSHPS" algorithm.

(3) Qualitative and quantitative analysis has been conducted to assess the performance of "MIAS" on coherence estimation and phase filtering. "MIAS" can largely mitigate the coherence estimation bias and avoid overestimating the de-correlated area without the cost of resolution. The non-local means filtering based on the identified siblings achieves a high quality factor in de-noising the interferometric phase.

(4) The integration of the proposed “MIAS” into a complete GBSAR time series analysis demonstrates the potential of “MIAS” in continuous deformation monitoring, thereby facilitating a range of applications for which GBSAR interferometry is suited.

Although the experimental datasets were acquired with only short-term observation periods, the combination of the proposed non-local method and the SBAS algorithm is potentially suitable for GBSAR acquisitions for long-term observation periods as long as coherence exists between acquisitions with small temporal baselines. It is also worth noting that the developed non-local method can produce accurate results for coherence estimation and phase filtering but it may have limited use in low coherent areas, such as natural slopes with thick vegetation coverage. Decorrelation becomes a serious issue in this case due to the short-wavelength character of a typical GBSAR system, thus hampering the reliable use of microwave interferometry. Deformation monitoring in low coherent areas can, however, be achieved using artificial corner reflectors (Crosetto et al., 2014a). The application of the developed approach to discontinuous GBSAR acquisitions will be addressed in Chapter 6 in this thesis.

Chapter 4. A new approach to selecting coherent pixels

The study in this Chapter has been published in the following research journal paper:

Wang, Z., Li, Z., Mills, J., 2018. A new approach to selecting coherent pixels for ground-based SAR deformation monitoring. *ISPRS Journal of Photogrammetry and Remote Sensing* 144, 412-422.

4.1 Introduction

A critical step in InSAR time series analysis is the selection of coherent pixels with high SNR in interferometric phase (Blanco-Sanchez et al., 2008). Following selection, further analysis and interpretation is then conducted only on the selected pixels. ADI and coherence are two commonly used criteria (Iglesias et al., 2014c) for the selection of coherent pixels as they are strongly correlated with the standard deviation of the interferometric phase noise (e.g. Bamler and Hartl, 1998; Ferretti et al., 2001). According to the selection strategy and the processing of selected pixels, a number of InSAR time series analysis algorithms have been developed over the last two decades (Osmanoğlu et al., 2016). As introduced in Section 2.2.2, these algorithms fall into two broad categories: PSI (e.g. Ferretti et al., 2001; Hooper, 2008) and SBAS (e.g. Berardino et al., 2002; Lanari et al., 2004).

PSI techniques are commonly based on a single-master configuration, with the main drawback of PSI techniques being the low spatial density of targets that behave coherently over the whole observation span (Perissin and Wang, 2012). By contrast, SBAS approaches construct a network of interferograms with multiple master images and small baselines (Shanker et al., 2011). However, as pointed out by Spaans and Hooper (2016), coherent points are variable from one interferogram to another, rendering time series analysis complicated. In other words, there are some partially coherent pixels (PCPs) that are coherent in some interferograms but not in others. Regarding the selection of coherent pixels in a redundant network, Crosetto et al. (2008) selected only pixels for which coherence was greater than a given threshold for all interferograms. PCPs were discarded in this approach, meaning the loss of some useful observations. Perissin and Wang (2012) formed a pixel-dependent network for each pixel by imposing a threshold on the coherence and only pixels with a connected network were analysed. The subset of interferograms with respect to the minimum spanning tree graph in the network were used for the estimation of height and deformation trends. Such an approach fails to make

the most effective use of redundancies and thus degrades the accuracy since a higher redundancy implies a more reliable displacement rate estimation. Therefore, a new selection criterion of PCPs is proposed in this chapter that aims to maximise the density of selected pixels and optimise the reliability of GBSAR time series analysis by making the most of coherent phase redundancies.

Specifically, the approach proposed in this chapter forms a redundant interferogram network with a specified baseline threshold. A pixel-dependent matrix is then constructed for each pixel based on its coherence occurrences over all interferograms in the network. Pixels with a full-rank matrix are selected for further time series analysis. The proposed criterion enables the selection of not only qualified PCPs, but also PSs that behave coherently over the whole time span. Interferometric phase observations of selected pixels are spatially filtered and unwrapped. The inversion of the deformation trend is achieved only based on the coherent interferometric phase after filtering and unwrapping, which guarantees a reliable solution. In principle, the proposed approach supports any co-registered SAR data, but this chapter only focuses on GBSAR deformation monitoring.

4.2 Methodology

4.2.1 Selection criterion of coherent pixels

Analysis starts with a stack of SLC images $(E_0,\ E_1, \dots, E_N)$ relative to the same illuminated region, acquired at times $\mathbf{t}$ $(t_0,\ t_1, \dots, t_N)$ in chronological order. A redundant network of L interferograms formed by SLC images is assumed. According to the description in Section 2.2.1, the differential interferometric phase for a target between the SAR acquisitions at times t_M (for the master image) and t_S (for the slave image) always comprises at least three terms (Crosetto et al., 2015):

$$\varphi_{t_M t_S} = \varphi_{t_M t_S}^{disp} + \varphi_{t_M t_S}^{atm} + \varphi_{t_M t_S}^{noise}. \tag{4.1}$$

The goal of InSAR time series analysis for deformation monitoring is to obtain the deformation time series, denoted as $d_{t_i}^{disp}(i = 1, \cdots, N)$ with respect to a reference acquisition t_0. As recognised in previous studies (e.g. Berardino et al., 2002; Li et al., 2009), the mean velocity between time-adjacent acquisitions is a preferable choice in InSAR time series analysis in order to avoid large discontinuities in cumulative deformations and to obtain a physically reliable

solution. In this case, no prior knowledge about the deformation is required in the network inversion. The displacement term in the interferometric phase can be expressed as:

$$\varphi_{t_M t_S}^{disp} = \frac{4\pi}{\lambda}\left[d_{t_M}^{disp} - d_{t_S}^{disp}\right] = \frac{4\pi}{\lambda}\sum_{k=M}^{S-1} v_k^{disp}\,\Delta t_k = \sum_{k=M}^{S-1}\varphi_{t_k t_{k+1}}^{disp}, \tag{4.2}$$

where v_k^{disp} is the displacement velocity and $\varphi_{t_k t_{k+1}}^{disp}$ is the associated phase change between the k^{th} and the $(k+1)^{th}$ acquisitions and t_k is the time interval between them. Similarly, the time-series atmospheric variation is denoted as $d_{t_i}^{atm}(i = 1, \cdots, N)$ and the atmospheric phase contribution in the interferometric phase can be written as:

$$\varphi_{t_M t_S}^{atm} = \frac{4\pi}{\lambda}\left[d_{t_M}^{atm} - d_{t_S}^{atm}\right] = \sum_{k=M}^{S-1}\varphi_{t_k t_{k+1}}^{atm}, \tag{4.3}$$

where $\varphi_{t_k t_{k+1}}^{atm}$ represents the atmospheric phase variation between the k^{th} and the $(k+1)^{th}$ acquisitions. Together with Equations (4.2) and (4.3), the matrix form with respect to Equation (4.1) can be generalized for the entire interferogram network:

$$\begin{cases} \mathbf{B}_{L\times N}\,\mathbf{\Phi}_{N\times 1} = \boldsymbol{\delta\Phi}_{L\times 1} + \boldsymbol{\varepsilon}_{L\times 1}, \\ \mathbf{\Phi} = \left[(\varphi_{t_0 t_1}^{disp} + \varphi_{t_0 t_1}^{atm}) \;\; (\varphi_{t_1 t_2}^{disp} + \varphi_{t_1 t_2}^{atm}) \;\; \cdots \;\; (\varphi_{t_{N-1} t_N}^{disp} + \varphi_{t_{N-1} t_N}^{atm})\right]^{\mathrm{T}}, \\ \boldsymbol{\delta\Phi} = \left[\varphi_{t_1 t_2} \;\; \cdots \;\; \varphi_{t_M t_S} \;\; \cdots \;\; \varphi_{t_{N-1} t_N}\right]^{\mathrm{T}}, \end{cases} \tag{4.4}$$

where **B** is the coefficient matrix; **Φ** is the matrix containing the incremental time series of phase change with respect to the superposition of both displacement and atmospheric variation; **δΦ** is the matrix of redundant unwrapped interferometric phase $\varphi_{t_M t_S}$; **ε** is the noise matrix. Based on Equation (4.4), the inversion can be performed via least squares using reliable interferometric phase with high SNR and low noise for a reliable solution. Thereafter, to obtain the displacement trend, the atmospheric variations should be compensated by any suitable methods (e.g. Iannini and Guarnieri, 2011; Li et al., 2009).

Within this context, a new approach for the robust selection of coherent pixels is proposed. Specifically, a threshold is imposed on coherence to determine whether a pixel is coherent for one interferogram or not. The coherence of the pixel above the threshold means an acceptable phase quality of the corresponding interferometric phase in the inversion. Considering a number of pixels are partially coherent in the network, the coherence occurrences with respect to a pixel must ensure Equation (4.4) is a well-determined system, namely the rank of matrix **B** is equal to the number of unknowns. Accordingly, all elements in the k^{th} row of **B** will be set as zero if

the coherence on the k^{th} interferogram is lower than the specified threshold. The selection criterion is that provided the matrix **B** related to a particular pixel is full-rank, then this pixel is selected for the time series analysis. Consequently, the constructed matrix **B** is based on the coherence occurrences over the entire interferogram network. For instance, it is assumed that there is a vector of interferograms $(I_{0,1}, I_{0,2}, I_{1,2}, I_{1,3}, I_{2,3})$ formed by a vector of images (E_0, E_1, E_2, E_3) acquired at times (t_0, t_1, t_2, t_3) with t_0 as the reference. For a pixel that is only coherent on $I_{0,1}, I_{1,3}$ and $I_{2,3}$, the corresponding matrix **B** is:

$$\mathbf{B} = \begin{bmatrix} 1 & 0 & 0 \\ 0 & 0 & 0 \\ 0 & 0 & 0 \\ 0 & 1 & 1 \\ 0 & 0 & 1 \end{bmatrix}. \tag{4.5}$$

As **B** is a full-rank matrix in this case, this pixel is selected. A completely coherent pixel always has a full-rank matrix **B**, thus can be selected by the proposed criterion. A pixel, associated with a full-rank **B,** is selected for time series analysis. A full-rank **B** means that the interferogram network is connected and the inversion in the time series estimation via least squares is enabled using only the coherent phase of this pixel. The proposed approach makes the most of redundant observations and allows an adjustment to be made in order to obtain a final reliable value for the unknown.

Particularly, coherence is estimated by the non-local method "MIAS" introduced in the previous chapter. Also, non-local filtering of "MIAS" is applied to improve the SNR of the interferometric phase of the selected pixels.

4.2.2 Time series analysis procedure

The aforementioned coherent pixel selection approach has been incorporated into an RT-GBSAR time series analysis chain (see Chapter 5 for details) based on the SBAS algorithm. As datasets can be acquired continuously with a zero-baseline, only the temporal baseline is considered in this analysis. Specifically, a temporal baseline constraint is set to construct the redundant interferogram network. The coherence of each interferogram in the network is calculated by the non-local method "MIAS", namely the siblings-based coherence with the estimation of the second kind statistics. Coherent pixels are detected via the criterion presented in this chapter. Further analysis and interpretation are then conducted only on the detected coherent pixels. The interferometric phase of detected pixels is de-noised using the non-local

filter of “MIAS”. The unwrapped phase of detected pixels is then obtained using the StaMPS 3D unwrapping approach (Hooper, 2010). Thereafter, the least-squares solution for each pixel can be achieved in the time series estimation using only the coherent phase of this pixel.

The inverted result at this stage is the sum of the surface displacements and the atmospheric variations. To obtain precise displacement time series, any atmospheric artefacts should be properly compensated, which can be approached by means of different techniques (Iannini and Guarnieri, 2011). The proposed approach adopts two previous representative works (e.g. Iglesias et al., 2014b; Pipia et al., 2008) to achieve this. For scenarios with flat topography, the atmospheric variations are modelled as a linear function of range under the medium homogeneity hypothesis (Pipia et al., 2008) and separated from the displacements. In scenes with significant topographic variations, the assumption of spatial homogeneity no longer applies due to the fluctuations of atmospheric parameters such as temperature, pressure, and humidity on the spatial domain (Iglesias et al., 2014b). Therefore, for cases with significant topography, atmospheric variation can be considered as a range- and height-dependent model and compensated with the support of the height information (Iglesias et al., 2014b).

4.3 Experimental results

4.3.1 Data used in experiments

Two datasets were used to validate the proposed approach. The first dataset was Dataset I-2 of the Tynemouth Cliff (30 SLC images with a temporal resolution of four minutes), which was introduced in Section 3.3.1. The second dataset (Dataset II) was collected by monitoring the Queen Elizabeth II Metro Bridge, spanning the River Tyne in Newcastle upon Tyne, UK. The FastGBSAR unit was tilted up to an angle of 30 degrees to scan the bridge superstructure which has a steel truss with fabricated box chords construction. The four concrete piers of the bridge and their expansion joints were also imaged. An overview of the site is given in Figure 4.1. Dataset II consisted of 16 acquisitions collected within two and a half minutes with an equal repeat interval of 10 seconds. The dimension of each image was 256 by 88 pixels. The polarization and spatial resolution of this dataset were identical to the first dataset. A train crossed the bridge during the period of data acquisition, taking around 16 seconds from entering the bridge to completely exiting. Consecutive acquisitions over this short period of time were used to detect the movements of the bridge as the train travelled across it.

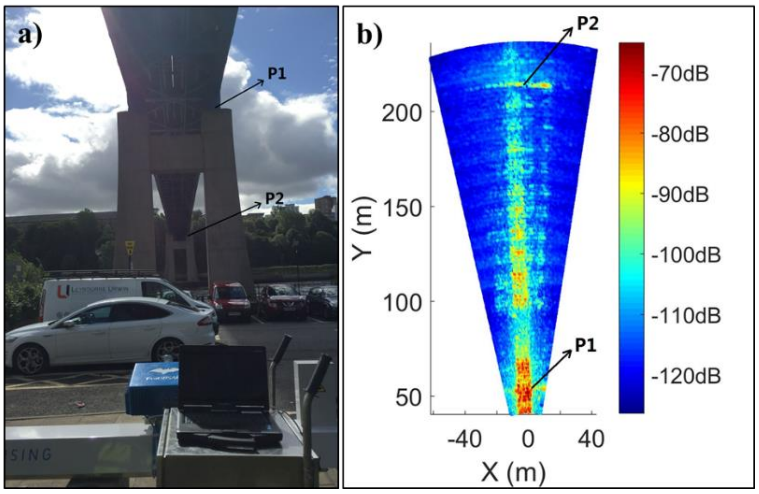

Figure 4.1. An overview of Dataset II. (a) The deployment of the FastGBSAR system for data collection. (b) The mean amplitude image of this dataset, shown in decibel. Two reference points are identified, based on the relative geometry parameters between the bridge and the radar system, added to assist interpretation of the GBSAR image geometry.

4.3.2 Demonstration

The temporal baseline constraint was set as 24 minutes for Dataset I-2, considering the computational efficiency and the temporal decorrelation, the justification for which is given in Section 4.4.2. Thus, one image was used to generate interferograms with its six previous and six subsequent images and there were 159 interferograms in the network. A full combination of interferograms can provide the most redundant observations, but it also increases the computation load and degrades the real-time performance in time-critical applications. The coherence threshold value was set as 0.45 and other parameters related to non-local coherence estimation and phase filtering were set as follows: the similarity threshold was empirically set as 0.85; the non-local window size was 15 by 15; a minimum of 10 siblings were kept for each pixel for a reliable estimation.

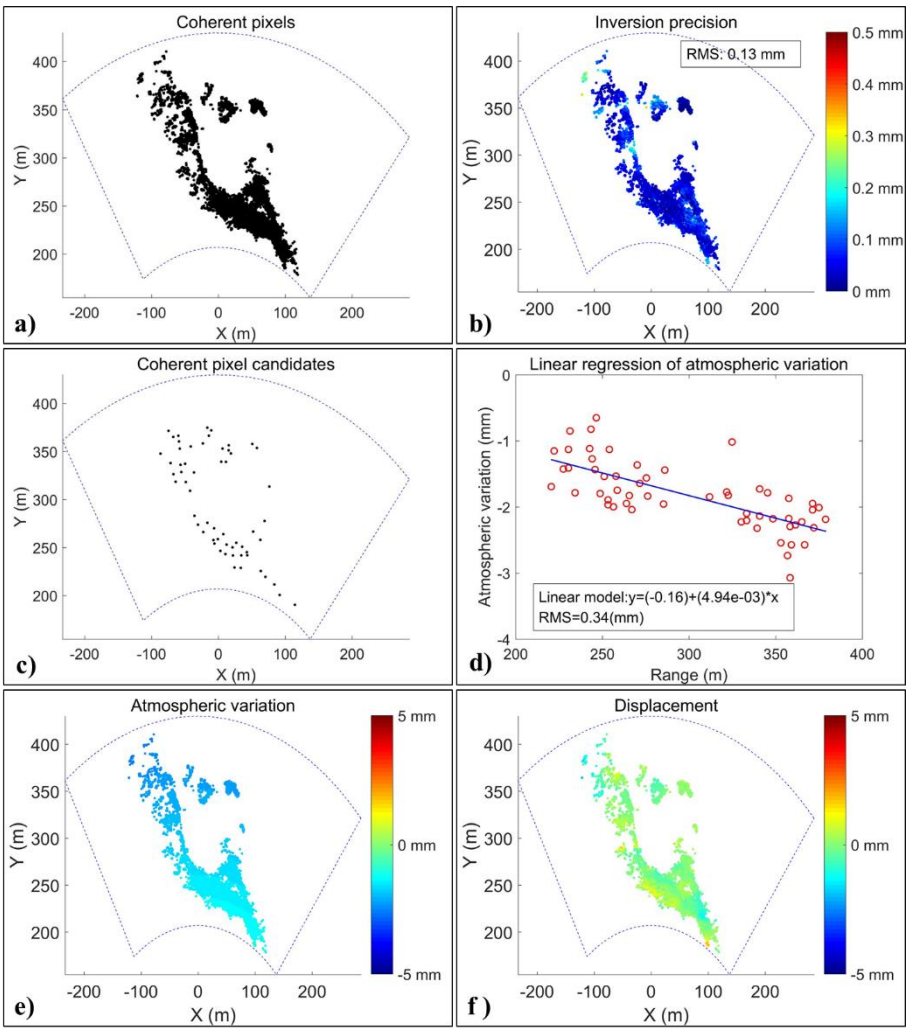

Figure 4.2. Results of the GBSAR time series analysis. (a) Coherent pixels. (b) Inversion precision (Appendix A). (c) Coherent pixel candidates. (d) Linear regression of atmospheric variations. (e) The atmospheric variation map over the entire period of acquisition (two hours). (f) The cumulative displacement map over the whole period of acquisition time (two hours).

The results of Dataset I-2 are summarized in Figure 4.2. The number of detected coherent pixels was 5,068 (Figure 4.2(a)), consisting of 2,042 fully- and 3,026 partially-coherent pixels. Further analysis was carried out only on detected coherent pixels. Least squares inversion with redundant observations allows a precision assessment of the solution. The inversion precision for each pixel was achieved on the basis of phase residuals, with the definition of inversion precision for each pixel given in Appendix A. The overall precision is appraised by the RMS of the inversion precision values. Small precision values were achieved in this experiment, as summarized in Figure 4.2(b), implying a high consistency of the filtered and unwrapped interferometric phase in the least squares inversion. Drawing on previous studies (e.g. Pipia et al., 2008; Rödelsperger, 2011), a subset of highly coherent pixels, termed coherent pixel candidates (Figure 4.2(c)), were selected by spatial gridding whereby each candidate had the

best coherence within a grid unit. Coherent pixel candidates were used to perform the linear regression of atmospheric variations with the assumption that their displacement components were randomly distributed along the range. The regression result is summarized in Figure 4.2(d), which shows a reasonable trend that atmospheric variation increases with the range. Residuals of the linear regression can be mainly attributed to atmospheric turbulence and stratification (e.g. Hanssen, 2001; Iglesias et al., 2014b). Based on the linear model in Figure 4.2(d), the atmospheric variations of all coherent pixels were compensated, and thus separated from any cumulative displacements. The modelled atmospheric variation map over the whole acquisition period (two hours) is shown in Figure 4.2(e) and the final cumulative displacement map is shown Figure 4.2(f). It is clear that the atmospheric variation dominates the change and no significant local signals can be found in the final cumulative displacement map. Moreover, the cumulative displacements of all coherent pixels are within 2 mm, which can be contributed by observation noise and the residuals of atmospheric compensation. Thus, it is a fair conclusion to state the cliff and castle buildings were stable over the observation time.

Regarding Dataset II and the bridge monitoring, deformation took place in a short period when a train travelled across the bridge. To produce a quick response for the fast-changing process, the temporal baseline constraint was set as half a minute for Dataset II. In this case, each image was involved in the interferogram generation with its three previous and three subsequent images. Thus, 42 interferograms were formed in the redundant network. Based on a priori geometry information about the bridge and the radar system, a shadow zone, caused by the near expansion joint and ranging from 70 m to 90 m, was masked out before the selection of coherent pixels. The coherence threshold was set as 0.6 to select qualified coherent pixels. The parameters related to the non-local estimation were the same as the first dataset. In this experiment, a total of 5,720 pixels were selected, comparing 4,446 fully- and 1,274 partially-coherent pixels (Figure 4.3(a)). The RMS of the inversion precision was 0.08 mm (Figure 4.3(b)).

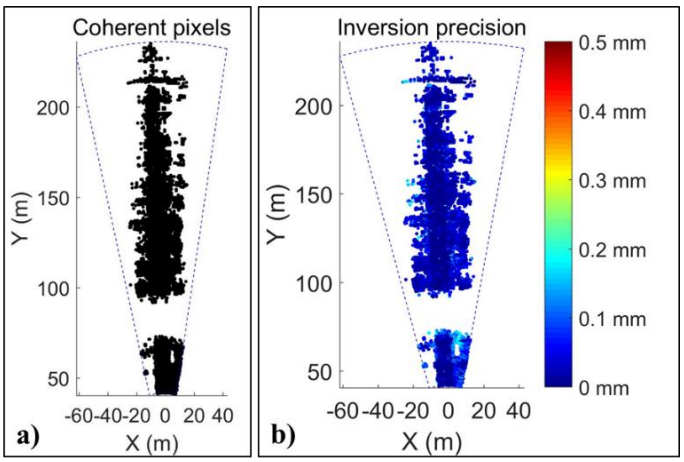

Figure 4. 3. Results of Dataset II. (a) Detection of coherent pixels. (b) Inversion precision of coherent pixels.

As the acquisition time for this dataset was only two and a half minutes, an assumption made was that the environmental conditions were stable over this extremely short observation period. In other words, the atmospheric phase change was deemed to be zero and not considered in time series analysis. Based on this assumption, the time series of displacement was achieved without compensation for the atmospheric artefacts. To highlight the bridge deformation as the train travelled across it, the incremental displacement maps with regard to coherent pixels are shown in Figure 4.4.

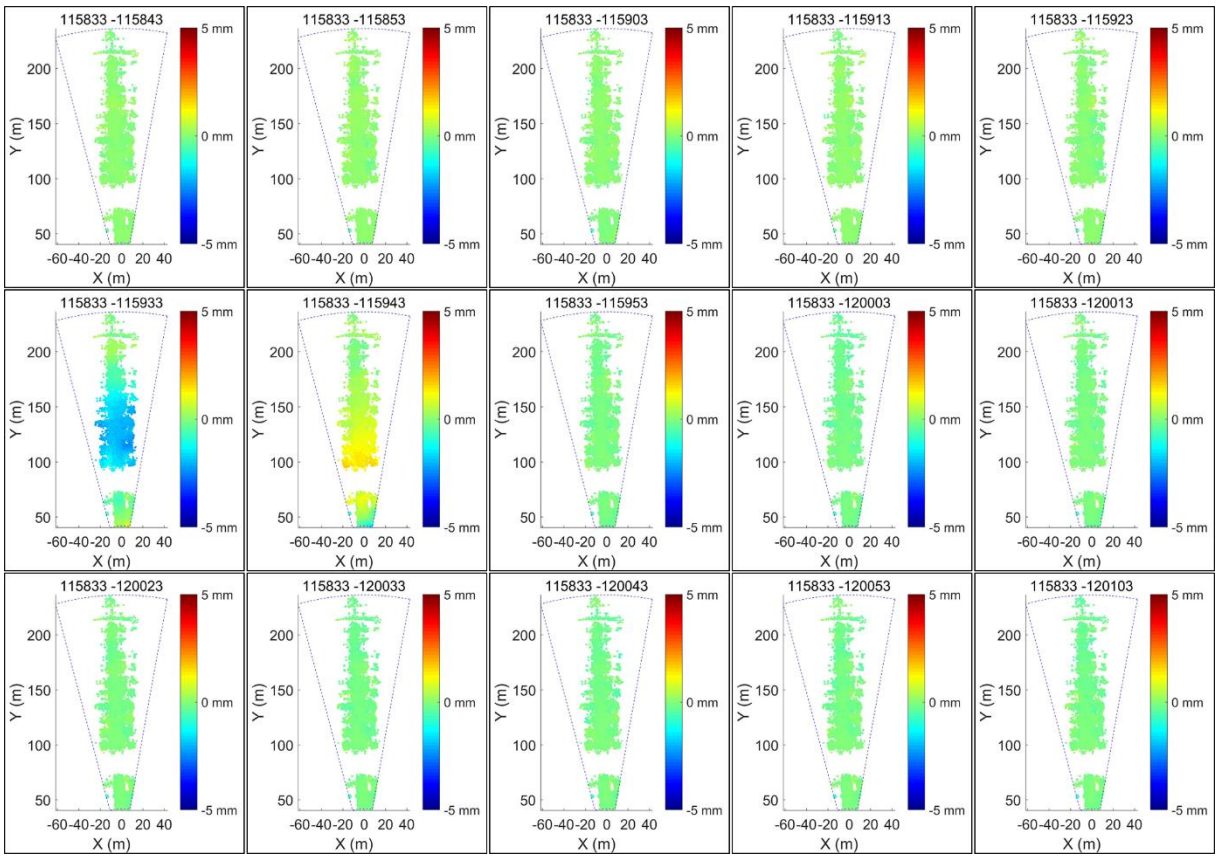

Figure 4.4. Dataset II: time series of cumulative displacements at selected coherent pixels. The time interval was 10 s. The first image acquired at 11:58:33 was selected as the reference. A train crossed the bridge, resulting in significant deformation signals in the 6th and 7th displacement maps (first two of the second row).

A synchronous video shows that a train crossed the bridge from the far side of the bridge (relative to the location of the FastGBSAR) at around 11:59:28 and completely exited the nearest end at around 11:59:44, taking approximately 16 seconds and spanning two FastGBSAR acquisitions created at UTC times 11:59:33 and 11:59:43, respectively. Constrained by the field of view of the video camera, the complete crossing of the bridge could not be recorded. Three video frames are given in Figure 4.5 to illustrate the situation.

Figure 4.5. Three video frames showing the train crossing the bridge.

Negative displacement values mean targets move closer to the radar system along the LOS direction relative to their reference positions. In this case, negative deformation implies a lowering of the bridge superstructure and positive deformation means uplift, as the radar was tilted up to observe the bridge. The first obvious deformation signal appears in “115833-115933” and shows that the middle bridge superstructure lowers by approximately 2 mm and the near portion of the bridge superstructure uplifting by several sub-millimetres, suggesting the train was primarily located at the far side of the bridge during the period of the acquisition “115933”. The next deformation map “115833-115943”, shows an uplift of approximately 1.4 to 0.5 mm for the superstructure from ranges between 95 to 150 m, respectively, and subsidence occurring at the very nearside, which implies the train was primarily located at the near side of the bridge during the period of the acquisition “115943”. The deformation signals are therefore consistent with the synchronous video recording.

Note that the aliasing of the near two piers with the nearside bridge superstructure exists due to the inherent azimuth ambiguities caused by the oblique view geometry of the radar system. It is possible that results are degraded with respect to the corresponding area as a consequence. Moreover, the bridge might have vibrated with a certain magnitude whilst the train crossed. In SAR mode, it is not possible to measure higher-frequency vibrations of the bridge, however, the experiment demonstrates the potential of GBSAR time series analysis for monitoring sites with a fast-changing rate.

4.4 Analysis and discussions

4.4.1 Coherent pixels selection

The proposed approach was compared with: (a) the selection of coherent pixels using a single pair of GBSAR images; and (b) the PS selection based on ADI using a stack of GBSAR SLC images. Based on the same coherence estimation algorithm and threshold value used in the time series analysis, the coherence between the first and the last SLCs in Dataset I-2 was calculated. Coherent pixels were then selected on the basis of the single pair of GBSAR images, as shown in Figure 4.6. By comparing the coherence of the single pair of GBSAR images (Figure 4.6(a)) with the mean coherence image of the entire network of interferograms formed in the time series analysis (Figure 4.6(b)), it is clear that the interferogram suffers temporal decorrelations. The number of coherent pixels selected in this single interferogram was 2,340 (Figure 4.6(c)), which is much fewer than that (5,068, Figure 4.2(a)) achieved by the proposed selection approach. The displacement map produced by single-pair interferometry is shown in Figure 4.6(d). With the exception of several pixels near the top-left position (-110, 385) that show approximately 2.5 mm of displacement and is probably due to residual atmospheric artefacts, no other significant signals can be observed. However, the limited density of coherent pixels can result in difficulties in phase unwrapping due to local under-sampling and phase discontinuities (e.g. Hooper and Zebker, 2007; Perski et al., 2009), and thus impede the interpretation of the GBSAR data.

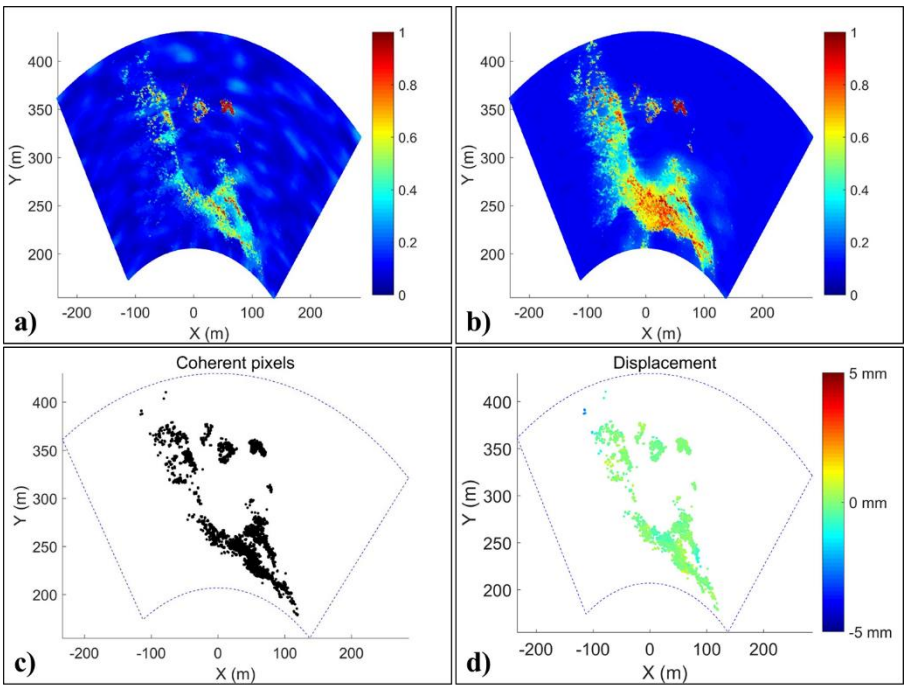

Figure 4.6. (a) Coherence between the first and the last SLCs in Dataset I-2. (b) The mean coherence of the entire interferogram network, shown for comparison. (c) Coherent pixels selected based on the single-pair of GBSAR images. (d) Displacement over the 2-hour observation period, achieved by single-pair interferometry.

For Dataset II, the analysis focused on the two key images ("115933" and "115943") acquired when the train was on the bridge. The selection of coherent pixels and the inversion of deformation were achieved by using this single pair of acquisitions and the same parameters used in the time series analysis. Figure 4.7 shows the coherence and displacement maps between the two acquisitions. It is visible that the decorrelation for this 10-second data is not significant and the results achieved by the single-pair interferometry and the time series analysis are consistent.

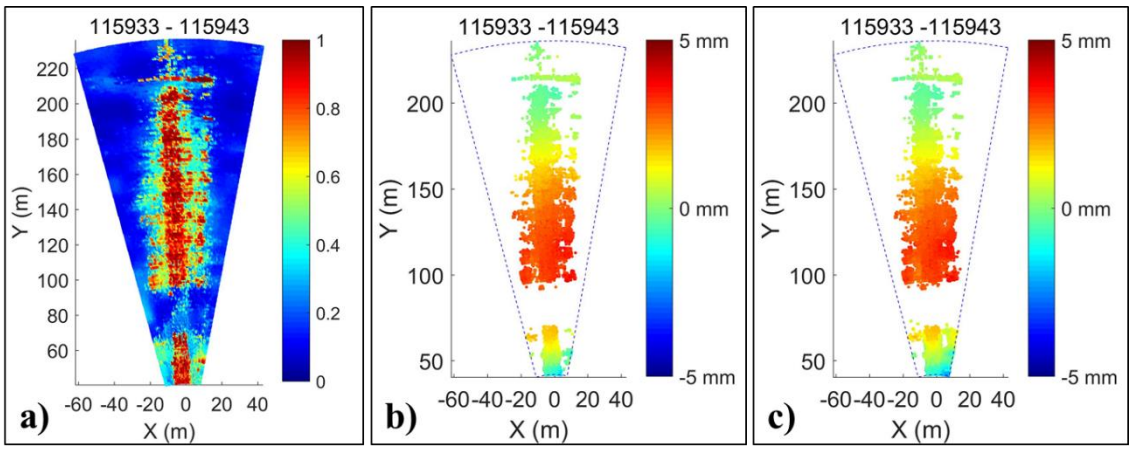

Figure 4.7. Results of the pair of acquisitions: "115933" and "115943". (a) The coherence map. (b) The displacement map achieved by the single-pair interferometry (coherent pixel count: 4,742). (c) The displacement map by the proposed times series analysis (coherent pixel count: 5,720), namely the difference between the 6th and 7th maps in Figure 4.4.

PS detection was also conducted using Dataset I-2, as depicted in Figure 4.8. A pixel with an ADI lower than 0.25 (a commonly used threshold) is considered as a PS target. 1,312 PSs were detected from Dataset I-2. By comparing the detected PSs in Figure 4.8(b) and coherent pixels in Figure 4.2(a), the former is found to be only a subset of the latter, which demonstrates the feasibility of the proposed approach in selecting persistent scatterers. In addition, the ADI threshold values were also increased to investigate the performance of PS detection. Figure 4.8(c) shows that several PSs were detected from shadow zones and sea areas where the ADI threshold was set as 0.30. The situation worsened (Figure 4.8(d)) when the ADI threshold was set as 0.35. This result demonstrates an advantage of the proposed approach on selecting dense and reliable coherent pixels over the ADI-based PS selection technique. The conclusions are confirmed by the PS analysis on Dataset II, as depicted in Figure 4.9.

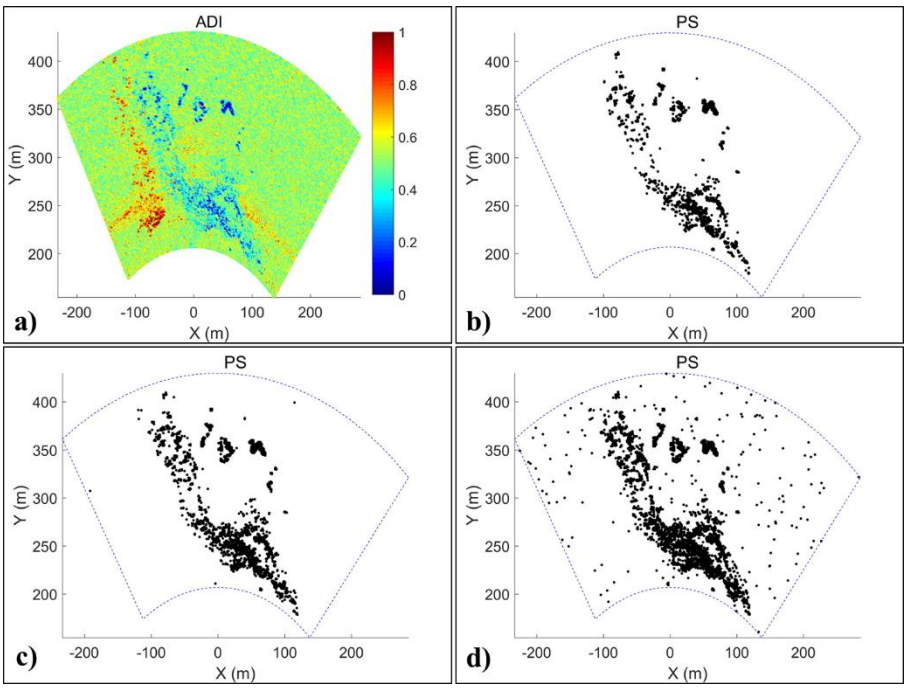

Figure 4.8. Dataset I-2: PS detection via ADI. (a) ADI for Dataset I-2. (b) PSs with ADI<0.25 (PS count: 1,312). (c) PSs with ADI<0.30 (PS count: 2,052). (d) PSs with ADI<0.35 (PS count: 3,273).

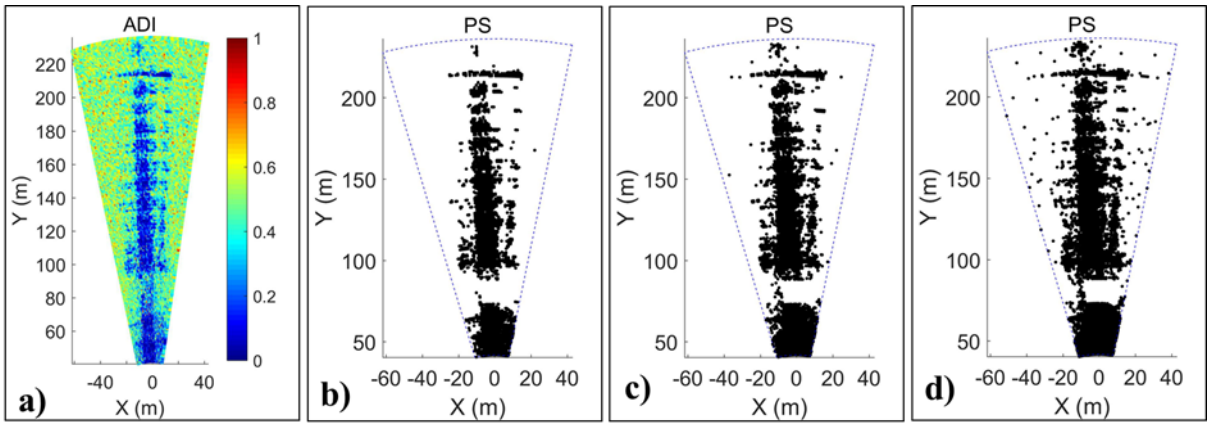

Figure 4.9. Dataset II: PS detection via ADI. (a) ADI for Dataset II. (b) PSs with ADI<0.20 (PS count: 3,924). (c) PSs with ADI<0.25 (PS count: 5,016). (d) PSs with ADI<0.30 (PS count: 6,135).

4.4.2 Justification of relevant parameters

There are two main parameters in the proposed approach for the selection of coherent pixels: (a) the coherence threshold; (b) the temporal baseline constraint. A higher coherence means better statistics for the interferometric phase. Accordingly, a higher coherence threshold will lead to fewer coherent pixels but with better interferometric phase quality. As mentioned previously, the density of coherent pixels plays an important role in the time series analysis, and a trade-off between the quantity and quality of coherent pixels should be exercised in

practice.

In addition, the temporal baseline directly determines the network of interferograms, thus it is a key factor in GBSAR time series analysis for deformation monitoring. Therefore, the entire GBSAR time series analysis based on Datasets I-2 and II with different temporal baseline constraints was performed to investigate the effects of this parameter on the number of selected coherent pixels, the RMS of inversion precision and the computational efficiency. The results are illustrated in Figure 4.10.

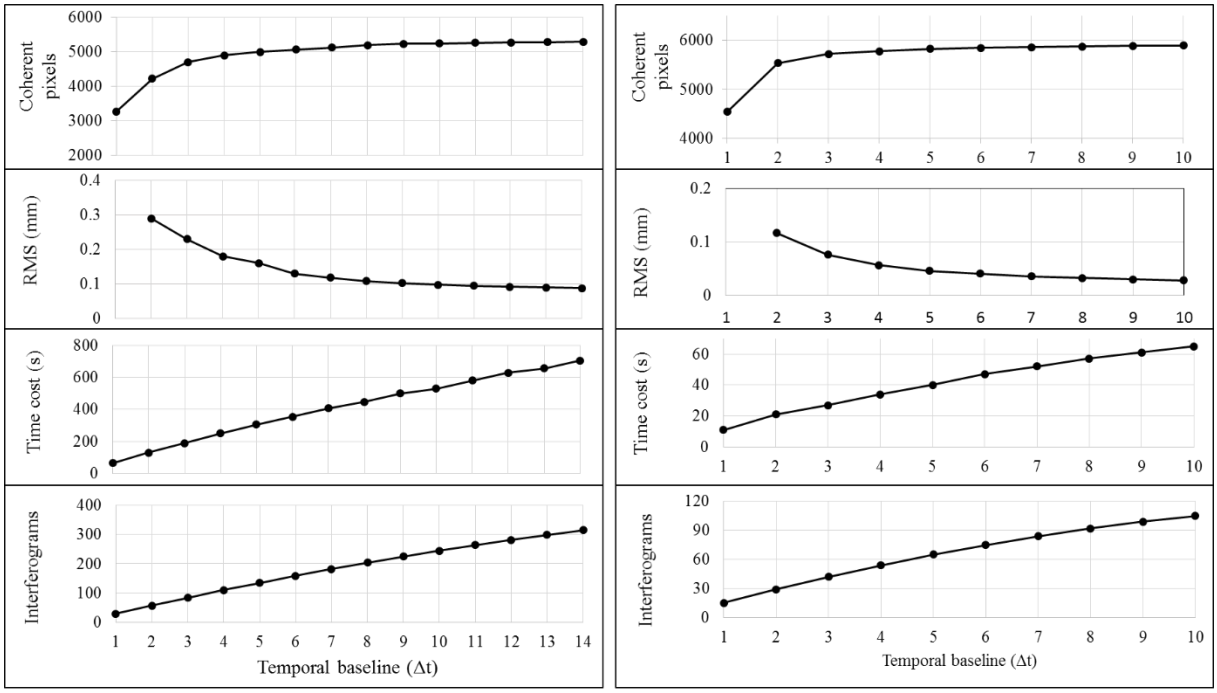

Figure 4.10. Influence of the temporal baseline on the selection of coherent pixels, inversion precision and computational efficiency. Δt is the repeat interval (4 minutes for Dataset I-2 and 10 seconds for Dataset II). The RMS of inversion precision is not applicable when the temporal baseline is set as 1Δt as a zero-redundancy network is formed in this case. (a) Dataset I. (b) Dataset II.

Unsurprisingly, the number of coherent pixels increases with the temporal baseline. This is because a longer temporal baseline leads to more redundancy in the network and thus offers more coherent opportunities for a pixel to construct a connected network and achieve a full-rank matrix **B**. It is worth noting, however, that the improvement achieved by increasing the temporal baseline is not significant after a certain value is reached since the majority of coherent pixels have been excavated and temporal decorrelation also becomes significant.

Moreover, a longer temporal baseline will lead to more redundancy in the network and obtain

more reliable results, but at the expense of computational efficiency. Similarly, the improvement in the achieved precision is limited when the temporal baseline reaches a certain value (around 7 for Dataset I-2 and 5 for Dataset II). However, processing time keeps increasing with the temporal baseline, and is approximately proportional to the number of interferograms being processed. Moreover, there is little purpose to enlarging the temporal baseline once the density of coherent pixels reaches a density sufficient for the interpretation requirements. Therefore, in practice, the selection of the temporal baseline is made on the basis of computational efficiency and the required accuracy.

4.5 Summary

In this chapter, a criterion for the selection of coherent pixels from a redundant network of interferograms has been demonstrated. The proposed approach has been incorporated into the RT-GBSAR time series analysis for deformation monitoring. The following conclusions are reached from the experiments reported in this paper:

(1) Experiments were performed on two continuous observational datasets, one for a coastal cliff and the other for a rail bridge. The cliff was stable during the monitoring period while deformation signals of several mm were detected when a train crossed the bridge. The time series estimation for both datasets reached up to a few sub-millimetres, which supports the feasibility of the proposed approach for GBSAR deformation monitoring purpose.

(2) Temporal decorrelation is a serious issue in SAR interferometric measurement (Caduff et al., 2015), especially for short-wavelength GBSAR systems. In comparison with the single-master InSAR technique, the proposed approach is able to largely overcome the temporal decorrelation problem and ensure a successful interpretation.

(3) The proposed approach enables the selection of not only qualified PCPs, but also all PSs. The proposed approach makes the most of redundant observations and allows an adjustment to obtain a final reliable value for the unknown. Finally, a reliable solution was achieved in least squares inversion.

On the basis of these findings, the proposed approach appears to facilitate a range of deformation monitoring applications to which GBSAR is suited. Although the experimental datasets were acquired continuously under zero-base line mode, the proposed selection criterion

is potentially suitable for any well co-registered discontinuous SAR datasets.

Chapter 5. A novel processing chain for real-time GBSAR deformation monitoring

The study in this Chapter has been submitted as a research journal paper for publication:

Wang, Z., Li, Z., Liu Y., Peng J., Long S., and Mills, J., A novel processing chain for real-time ground-based SAR (RT-GBSAR) deformation monitoring, *Manuscript submitted to IEEE Transactions on Geoscience and Remote Sensing on 31st January, 2019 for publication*.

5.1 Introduction

In comparison to spaceborne SAR, GBSAR has an inherent flexibility of allowing adjustable temporal resolution in data acquisitions. Depending on the rate of change in any particular case study, or the practical environment for instrument deployment, GBSAR data acquisition can be performed in either continuous or discontinuous mode (e.g. Caduff et al., 2015; Crosetto et al., 2017; Monserrat et al., 2014). According to its temporal resolution and spatial geometry, GBSAR data can be further divided into two types: (I) zero-baseline single-campaign data, which is acquired continuously with zero-baseline geometry and equal temporal resolution; (II) multi-campaign data with/without rail repositioning errors, which contains certain (short or long) discontinuities between different campaigns. The schematic graphs with respect to the two data types are illustrated in Figure 5.1. Data type (I) can actually be an individual campaign in type (II). Moreover, the entire type (I) and the zero-baseline type (II) (i.e. without repositioning errors) correspond to the continuous data acquisition mode defined in Monserrat et al. (2014). According to Crosetto et al. (2017), the continuous mode of operation is the more commonly deployed technique. The continuous mode employs a zero-baseline geometry for all acquisitions, thus avoiding influences of hardware related technical issues and leading to better performance in terms of the density, precision, and reliability of deformation measurements (e.g. Crosetto et al., 2014a; Tarchi et al., 2005). This chapter therefore focuses only on continuous GBSAR deformation monitoring.

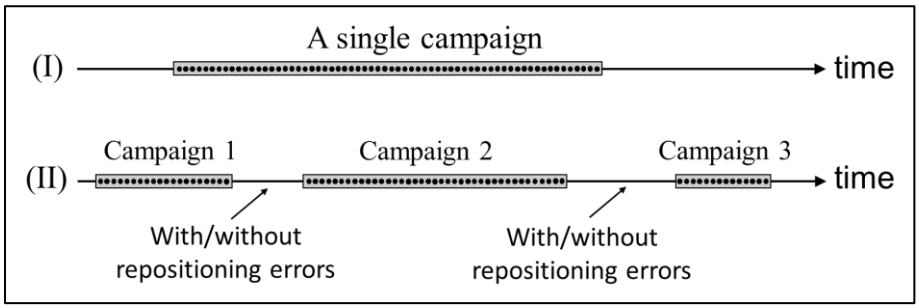

Figure 5.1. Schematic diagram of GBSAR data types (I) and (II). A black dot represents one acquisition and a rectangle represents a single campaign of GBSAR data.

In the continuous mode, consecutive acquisitions with a high temporal resolution (up to several seconds) enable time series analysis of fast-changing scenarios that can provide insight into mechanisms and triggering factors of hazardous events, or even act as the basis for early warning systems. However, in practice, the processing of continuous GBSAR data has the following characteristics:

(1) A large number of image acquisitions are usually performed in a continuous campaign due to the requirement or desire for high temporal resolution GBSAR data. For instance, the current FastGBSAR system can repeat an acquisition at the best resolution every ten seconds, implying up to 360 images can be acquired every hour. There are significant challenges in processing such a large volume of consecutive GBSAR imagery: (a) the management of computational random-access memory (RAM) for such a large number of images, and (b) the inevitable presence of targets which are temporally coherent for a certain length of time, but not for the entire observation period.

(2) Real-time processing of GBSAR imagery may be required in urgent situations, e.g. landslide early-warning systems, where the creation of displacement maps is required in as short a time frame as possible.

(3) Continuous data collection is performed by fixing the radar instrument in a stationary position. In this case, the spatial baseline is always zero and the topographic effect is absent in the interferometric phase (e.g. Caduff et al., 2015; Monserrat et al., 2014). Therefore, the operations related to a spatial baseline, such as the co-registration of master and slave images, the removal of topographic phase contribution, and the estimation of orbital errors in spaceborne InSAR processing, can be omitted in GBSAR interferometric processing.

(4) APS is usually considered spatially correlated and temporally uncorrelated for spaceborne

SAR (e.g. Ferretti et al., 2000; Li et al., 2009). The estimation of APS in spaceborne SAR data is often performed through temporal high pass and spatial low pass filtering, which is not applicable in the GBSAR case due to the extremely short time intervals between SAR acquisitions (Rödelsperger, 2011).

With consideration of these characteristics, a novel processing chain has been developed for real-time continuous GBSAR deformation monitoring, termed Real-Time GBSAR (RT-GBSAR). This chapter describes the main endeavours addressing RAM management, real-time capability and the reliability of processing continuous GBSAR data with high temporal resolution and large data volumes.

5.2 Methodology

In a continuous GBSAR monitoring campaign, attempted simultaneous processing of all data together in a time series procedure leads to three issues: (i) delay in production of displacement maps, (ii) extreme cost of computational memory; (iii) the loss of temporal evolution. To address these issues, the proposed RT-GBSAR chain exploits the SBAS concept and processes consecutive GBSAR SLC images on a unit by unit basis. SLC images within a temporal window form a basic unit in the chain. The flow is controlled by two parameters: the window size and the temporal baseline constraint. The window size represents the number of SLC images in a unit, and the temporal baseline constraint specifies the number of preceding images which are allowed to form interferograms with the current image. The overlap of two neighbouring units is fixed as a twofold temporal baseline constraint. A schematic of the proposed strategy is illustrated in Figure 5.2. A complete time series analysis is performed within each unit and adjacent units are connected via the overlapping SLC images.

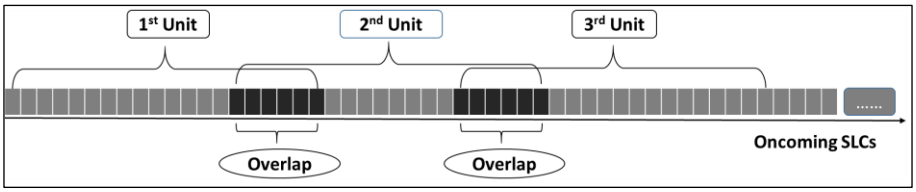

Figure 5.2. Schematic of the RT-GBSAR processing flow.

By adopting this strategy, the RT-GBSAR chain has several merits. Firstly, the RAM requirement is limited to only one unit of SLC images, and the chain can theoretically process an infinite number of oncoming images. Secondly, it affords the opportunity to investigate the evolution of surface movements since it preserves temporally-coherent pixels which are present

in one or more units, but not in the entire observation period. Thirdly, this chain supports real-time processing of oncoming data and any latency of the creation of displacement maps can be minimised since there is no requirement to wait for the entire dataset before processing commences.

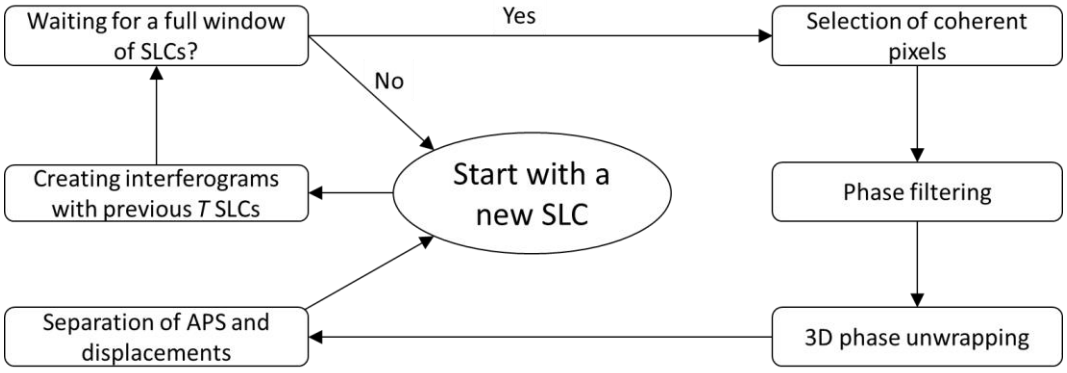

Figure 5.3. Flowchart of the SBAS time series analysis in the RT-GBSAR chain.

The SBAS concept in the proposed RT-GBSAR chain is illustrated in Figure 5.3. The procedure in each unit starts with a new SLC. Once a new SLC is received, interferograms can be created using the new SLC and its previous T SLC images (where T denotes the temporal baseline constraint). As reported in Chapter 4, in practice the selection of the temporal baseline is made on the basis of both computational efficiency and the required accuracy. A longer temporal baseline constraint results in a more redundant network of interferograms at the expense of computational efficiency. Additionally, the temporal baseline should be relatively short for rapidly changing scenarios as temporal decorrelations can become significant. In the procedure, the SBAS analysis will not begin until the number of available SLC images is sufficient (i.e. equivalent to a full time window). Details about the SBAS time series analysis procedure have been given in Section 4.2.2.

The SBAS time series estimation produces a least-squares solution, which is the optimal solution within the individual unit. However, the solution for an individual unit is not necessarily globally optimal when deformation spanning multiple consecutive units is required. To address this issue, adjacent units can be linked by their common coherent pixels in the proposed RT-GBSAR chain. The adjacent units are then merged into a longer unit and the optimal solution for the resultant merged unit can be achieved. For example, assume two units defined with a window size of 30 and a temporal baseline constraint of 3 (i.e. overlap size of 6). The first unit runs from the 1st to the 30th image and the second unit from the 25th to the 54th

image. These two units can be merged into a new contiguous unit running from the 1st to the 54th image. As time series analysis is performed within each unit independently, the selected coherent pixels in these two units (denoted as CPs_{unit1} and CPs_{unit2}, respectively) may be different. To pursue an optimal solution for the newly merged contiguous unit, the time series analysis may be performed again on the basis of the intersection of the two coherent pixel sets, i.e. $CPs_{unit1} \bigcap CPs_{unit2}$.

5.3 Applications

To demonstrate the feasibility of the proposed RT-GBSAR chain for continuous deformation monitoring, two applications involving short-term but large-volume continuous FastGBSAR data were conducted. The case studies include a coastal cliff and a sand dune.

5.3.1 Coastal cliff case study

The first application was conducted on 16 November 2016 by continuously observing the Tynemouth Cliff. The FastGBSAR observation lasted two hours from 12:31:24 to 14:29:24 with a temporal resolution of 10 seconds and a spatial resolution of 0.75 m in range and 5 mrad in azimuth. Somehow, a small percentage (3.3%) of images was occasionally not recorded by the system, probably due to the hardware insufficiency in data acquisition at such a high temporal and spatial resolution. The continuous dataset in this application (Dataset I) consisted of 696 continuous SLC images. The dimension of each SLC image was 294 by 254 pixels. An overview of the data collection was introduced in Figure 3.3 in Section 3.3.1. Dataset I was processed using the proposed RT-GBSAR chain with a temporal baseline constraint of five images, implying that any one image can be allowed to generate interferograms with its five previous and five subsequent images. Overlap size was fixed as a twofold temporal baseline constraint, namely 10 images, in this experiment. The entire dataset of 696 images was processed in 14 units with a unit size of 60 images. The information about each unit is given in Table 5.1.

To display the temporal evolution, displacement maps for all 14 units of Dataset I are shown in Figure 5.4. In addition, the final cumulative displacement map for pixels that are coherent over the entire observation period is also given in Figure 5.4.

Table 5.1. Information about processing units of Dataset I.

Unit	Start	End	Coherent pixels
1	1	60	11,859
2	51	110	10,975
3	101	160	10,671
4	151	210	10,046
5	201	260	10,303
6	251	310	9,273
7	301	360	9,508
8	351	410	8,887
9	401	460	8,391
10	451	510	7,503
11	501	560	6,661
12	551	610	5,691
13	601	660	4,531
14	651	696	4,331

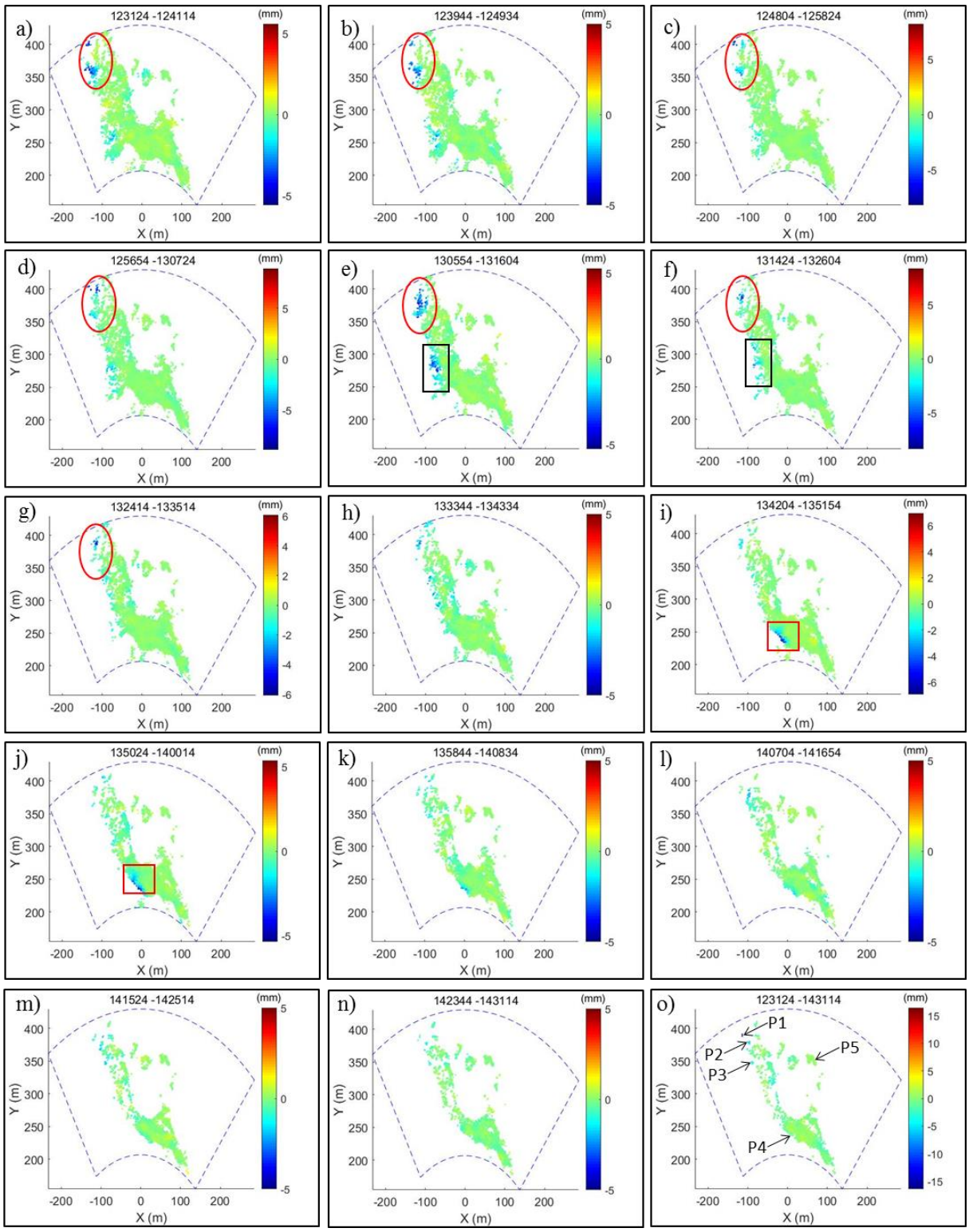

Figure 5.4. RT-GBSAR results of Dataset I. The displacement maps of all units from the first to the last are respectively shown in subfigures (a) to (n). The cumulative displacement map with respect to pixels that are coherent over the entire observation period is given in (o).

As shown in Figure 5.4, three areas of interest with deformation signals are visible in some units but not in the final cumulative displacement map. Specifically, the deformation signals indicated by the red ellipse were obvious from the 1st to the 7th unit and faded from the 8th unit

onwards. The deformation signals in the black rectangles were weak at the beginning and became active in the 5th unit, and the deformation signal indicated by the red square temporally existed from the 9th to the 10th unit. The practical locations of these areas of interest are all near the sea. Among them, the area of interest indicated by the red ellipse is at the lowest altitude and nearest to the sea and the red square is at the highest altitude and furthest from the sea. During the observation period, the water level rose with the sea tides and gradually submerged these areas. The tidal elevation for the observation area on the day of data collection is given in Figure 5.5.

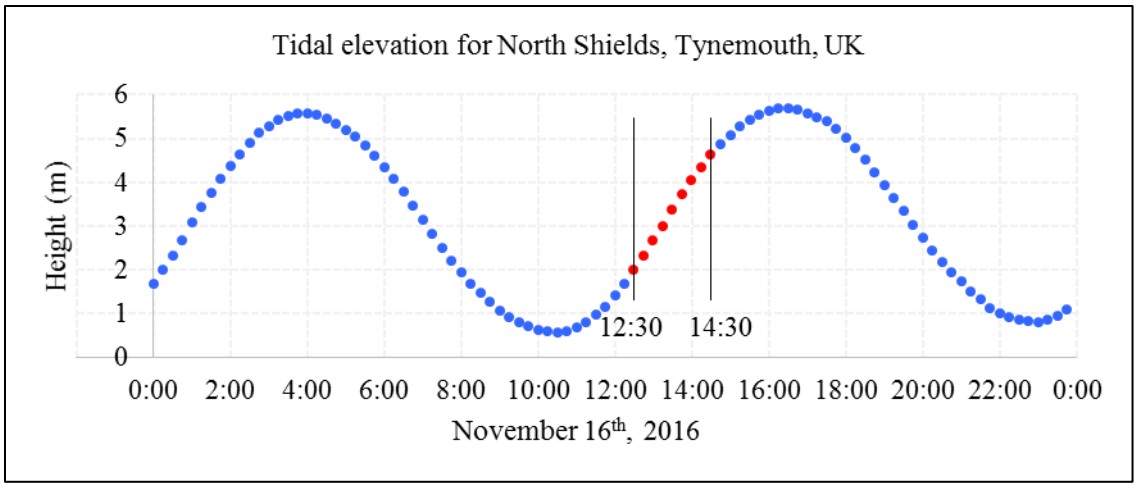

Figure 5.5. Tidal elevation for North Shields, Tynemouth, UK on 16 November 2016, obtained from the National Tidal and Sea Level Facility (NTSLF, 2018). The variation of tidal elevation over the period of GBSAR observation is marked as red.

With the increasing water level, the number of coherent pixels in each unit generally decreased. The number of coherent pixels shared by all units totals only 3,428. However, only a very few pixels with significant deformation can be found in the total cumulative displacement map in Figure 5.4(o), and the temporal evolution of the marked areas of interest near the sea are nearly lost. This demonstrates the importance of exploiting temporally-coherent pixels and processing continuous GBSAR data on a unit by unit basis. Otherwise, the temporal evolution of ground deformation cannot be detected.

In order to investigate the time series process, a set of pixels (P1, P2, P3, P4, and P5) were selected from the results of units 1-14 in Figure 5.4(o). Pixels P1-P4 correspond to beach rocks near the sea while P5 is located on a building. The time series of displacements and APS for these pixels are shown in Figure 5.6. According to the displacement time series, pixels P1-P4 were stable for the first 0.6 hour. After that these pixels gradually moved as the sea tide approached these targets. In contrast, pixel P5 remained stable for the entire observation period.

Besides, the APS time series show that the smallest APS was experienced by P4 as it is the nearest target to the radar system, while the greatest by P1 as it is the furthest among the selected targets. This is consistent with the APS correction model (APS $= a_0 + a_1 r$, where a_0, a_1 are coefficients and r the slant range between the radar and the target) used in this experiment. The deformation maps, time-series displacements and relevant analysis therefore suggest that the ground deformation is related to the sea tides. Without proper validation data, it is difficult to interpret the deformation signals. The findings which may be useful for the interpretation are summarised as follows: (i) the physical feature of the moving targets was rock; (ii) targets moved always from the sea and towards the coast during the observation period with incoming tide; (iii) the occurrence of movement was consistent with the sequence of the sea tide approaching these targets; and (iv) deformations behaved as local signals.

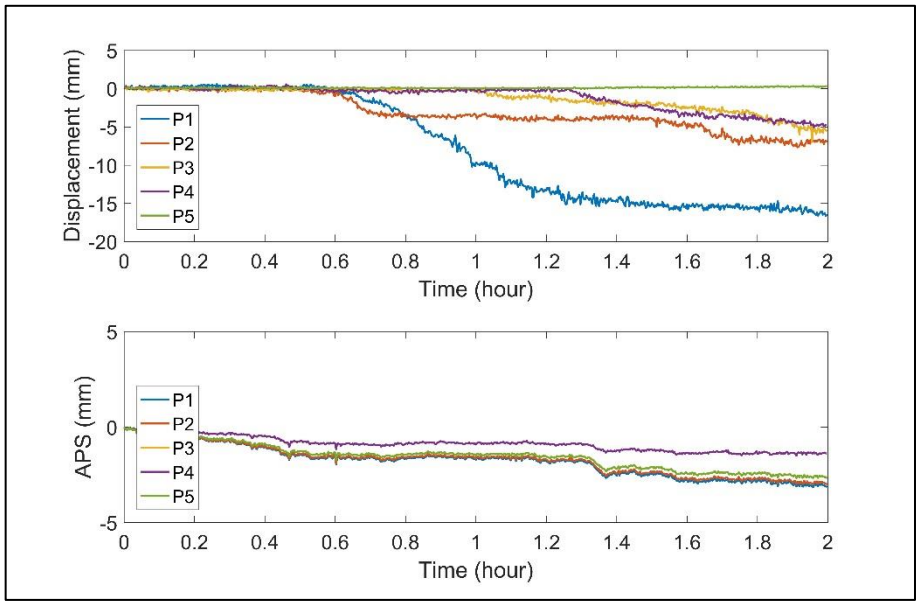

Figure 5.6. The time series of displacements and APS for the five selected pixels (P1, P2, P3, P4, and P5).

5.3.2 Sand dune case study

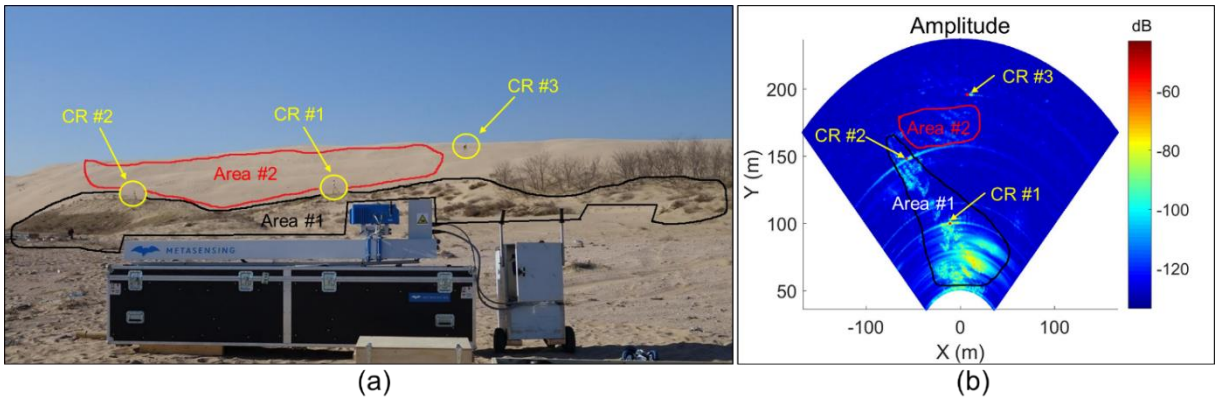

(a) (b)

Figure 5.7. Overview of the sand dune at Feicuidao on the Changli Gold Coast, Hebei Province, China. (a) Optical view of the site. Three corner reflectors (CRs) were marked in yellow circles. Two areas of interest were roughly outlined: Area #1 is covered with sparse vegetation and Area #2 is devoid of vegetation. (b) A corresponding amplitude image of this site.

An experiment was also conducted on another dataset (Dataset III) collected on 5 January 2015 and consisted of a sand dune area at Feicuidao on the Changli Gold Coast, Hebei, China. It was reported that this area experienced a fast-changing process during the period of 2006-2008 with a significant movement of up to 10.68 m at the leeward slope bottom and up to 7.12 m at the crest of the dune (Dong et al., 2013). An overview of this site can be seen in Figure 5.7.

The image size of Dataset III was 371 × 306 pixels and the spatial resolution 0.5 m × 5 mrad. Dataset III consisted of 478 continuous SLC images with a temporal resolution of 10 seconds over an observation period of 1 hour 20 minutes. Two acquisitions were not recorded by the system due to hardware related issues. Dataset III was processed using the proposed RT-GBSAR chain with the same parameters as Dataset I. The entire dataset of 478 images was processed in 10 units. Information about these units is summarised in Table 5.2.

Table 5.2. Information about processing units of Dataset III.

Unit	Start	End	Coherent pixels
1	1	60	5,085
2	51	110	3,643
3	101	160	5,222
4	151	210	5,664
5	201	260	6,128
6	251	310	6,102
7	301	360	3,298
8	351	410	4,569
9	401	460	6,887
10	451	478	6,831

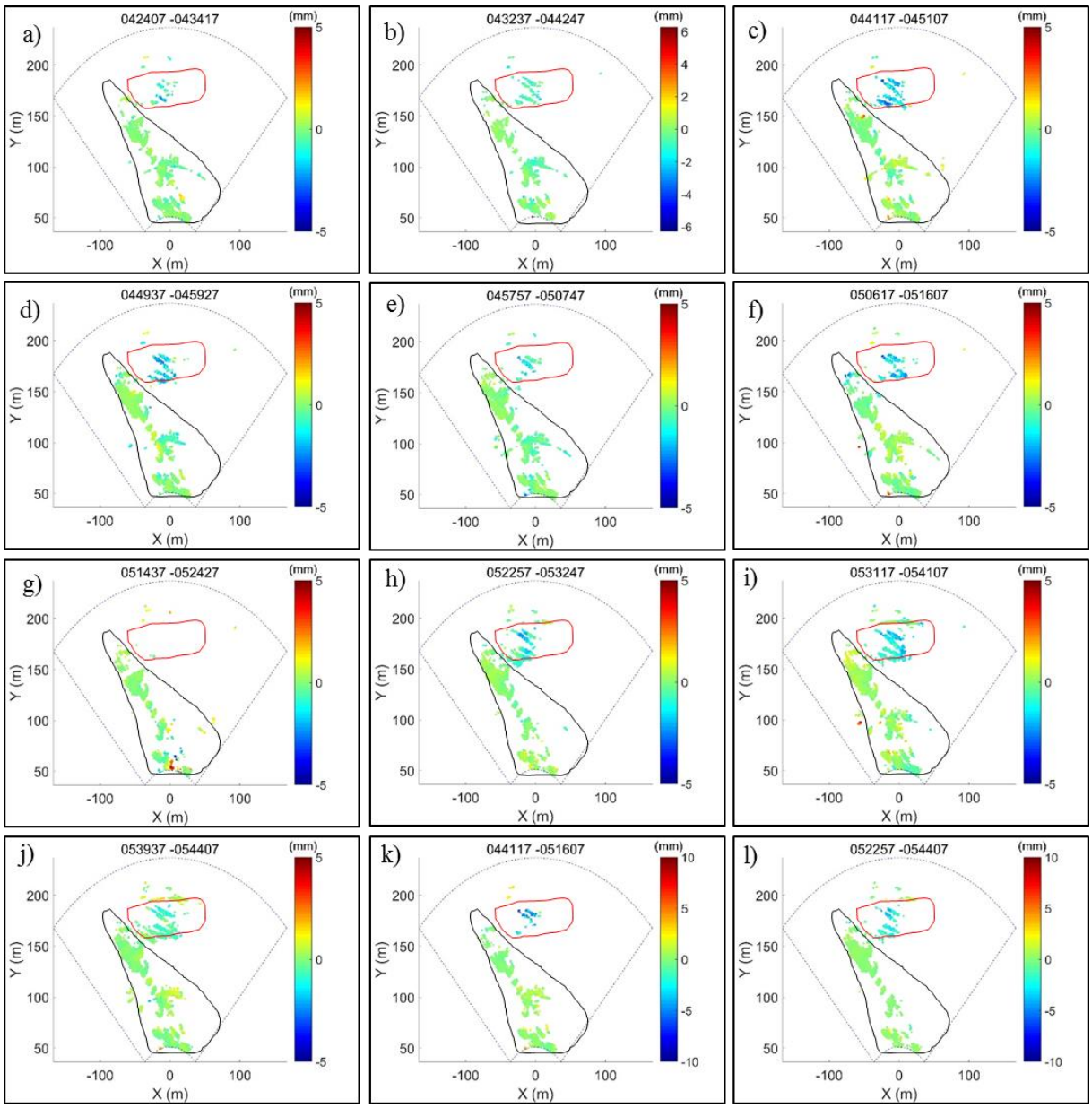

Figure 5.8. RT-GBSAR results of Dataset III. The displacement maps of all units from the first to the last are shown in subfigures (a) to (j), respectively. The cumulative displacement map with respect to units 3-6 is given in (k) and that of units 8-10 in (l). Note that Area #1 is indicated in a black loopand Area #2 in a red one.

Deformation maps for all 10 units of Dataset III are shown in Figure 5.8. It should be noted that coherent pixels in Area #2 disappear in unit 7. This is because the corner reflector CR #2 was moved to the location of CR #3 during the period of data collection in unit 7. The process is illustrated by the sequential amplitude images shown in Figure 5.9. The moving corner reflector produced side-lobe patterns and contaminated Area #2. Therefore, very few coherent pixels are present in Area #2 of unit 7. Thus, two cumulative displacement maps (before and after unit 7) are also plotted in Figure 5.8. The displacement map of units 3-6 is shown in Figure 5.8(k) and that for units 8-10 in Figure 5.8(l). It is apparent that Area #1 was generally stable over the

entire observation period, with deformation primarily exhibited in Area #2. Here a maximum cumulative displacement of up to 8 mm within a period of 35 minutes spanning units 3-6 can be seen in Figure 5.8(k) and 5 mm over another 22 minutes spanning units 8-10 in Figure 5.8(l). Negative displacement values imply that targets moved closer to the radar system along the line-of-sight direction. Thus, the observed deformation most likely arises due to the process of sand sliding down the slope, which is consistent with the prevalent wind observed during fieldwork.

Area #1 is covered with sparse and shallow vegetation while Area #2 comprises only loose sand devoid of any vegetation. During the short period of data collection, the Beaufort wind force scale was recorded at the level of light air, approximately 1~2 miles per hour. In addition, both areas were occasionally intruded by humans over the observation period. Therefore, the sand motion can be attributed to three factors, namely natural slope instability of the dune, wind force and human intrusion/activity. No matter what triggered the sand motion, the FastGBSAR results provide evidence that the presence of vegetation in coastal dunes plays an important role in helping stabilise the surface against sand motion.

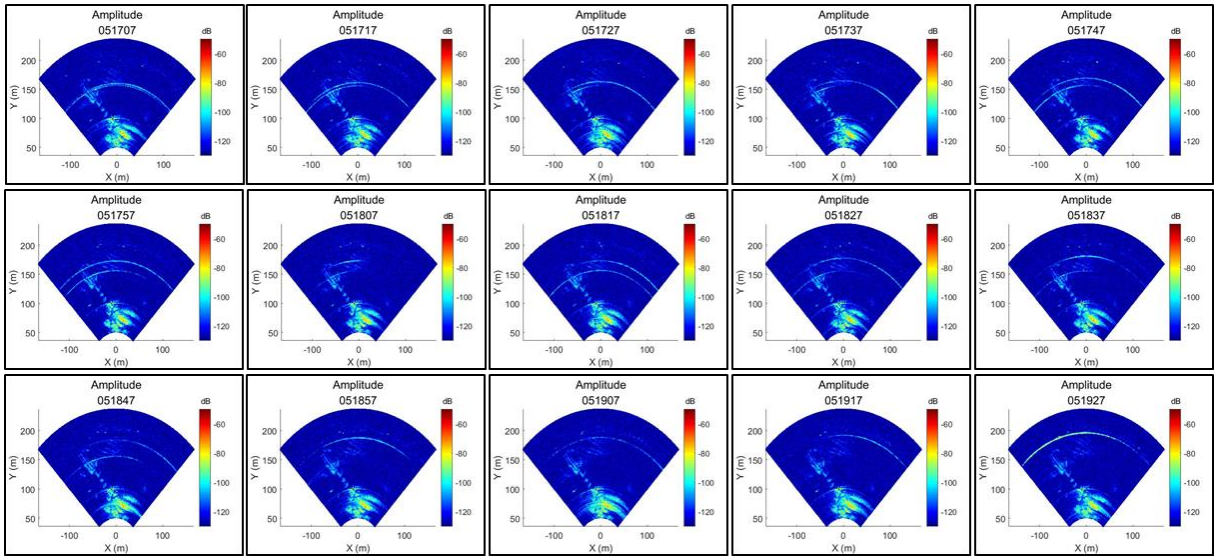

Figure 5.9. Sequential amplitude image during the period from 05:17:07 to 05:19:27.

5.4 Analysis and discussions

5.4.1 Identification of unwrapping errors

Computation of a successful InSAR time series analysis heavily relies on the performance of phase unwrapping. In this study, the detection and identification of unwrapping errors was

accomplished. Assuming that there is a set of three interferograms (I_{lm}, I_{mn}, I_{ln}) formed by three complex SAR images (E_l, E_m, E_n), the raw phase for a pixel on the three complex images is denoted as (ψ_l, ψ_m, ψ_n) and the interferometric phase on the three interferograms is ($\varphi_{lm}, \varphi_{mn}, \varphi_{ln}$). If phase unwrapping is correct for all three interferograms, the relationship $\varphi_{lm} + \varphi_{mn} - \varphi_{ln} = 0$ should be held by any coherent pixel on these interferograms (e.g. Biggs et al., 2007; Usai, 2003). The three interferograms form a closed temporal loop. Unwrapping errors always result in multiples of 2π phase misclosures and can be identified by summing round a closed temporal loop or checking a misclosure map (Biggs et al., 2007). Note that the spatial filtering is often applied before phase unwrapping, which breaks the phase triangularity in a closed loop (e.g. Ferretti et al., 2011; Samiei-Esfahany et al., 2016). Therefore, the phase misclosure threshold for the identification of unwrapping errors was empirically and conservatively set as π, namely an unwrapping error was defined by $|\varphi_{lm} + \varphi_{mn} - \varphi_{ln}| > \pi$ in this study.

For a unit of 60 images with a temporal baseline constraint of five images, there are 560 closed temporal loops. The proposed chain summed the unwrapping errors along all the temporal loops, which can be used to identify unwrapping errors that are present. Note that the displacement maps shown in Figures 5.4 and 5.8 are only for coherent pixels without unwrapping errors. The number of coherent pixels, both with and without unwrapping errors, for units in the two case studies are shown in Tables 5.3 and 5.4. As can be seen from the results in Tables 5.3 and 5.4, phase unwrapping is correct for the vast majority of selected coherent pixels in the applications. The average percentage of correct unwrapping is 99.95% for Dataset I and 99.47% for Dataset III. The results achieved by the RT-GBSAR chain for the two datasets can thus be considered reliable. Between the two results, a few more unwrapping errors can be identified in Dataset III, an issue related to data quality. The scene of Dataset I primarily consisted of rocks, concrete structures, and buildings, which can provide backscattering signals with better SNR than the sand dune with its smooth sand or sparse vegetation. Moreover, human intrusion onto the sand dune also added noise to Dataset III.

Table 5.3. Statistics w.r.t unwrapping errors for Dataset I.

Unit	Coherent pixels	Pixels without unwrapping errors (percentage)	Pixels with unwrapping errors (percentage)
1	11,859	11,857 (99.98%)	2 (0.02%)
2	10,975	10,973 (99.98%)	2 (0.02%)
3	10,671	10,668 (99.97%)	3 (0.03%)
4	10,046	10,032 (99.86%)	14 (0.14%)
5	10,303	10,297 (99.94%)	6 (0.06%)
6	9,273	9,272 (99.99%)	1 (0.01%)
7	9,508	9,506 (99.98%)	2 (0.02%)
8	8,887	8,868 (99.79%)	19 (0.21%)
9	8,391	8,388 (99.96%)	3 (0.04%)
10	7,503	7,502 (99.99%)	1 (0.01%)
11	6,661	6,659 (99.97%)	2 (0.03%)
12	5,691	5,691 (100.00%)	0 (0.00%)
13	4,531	4,531 (100.00%)	0 (0.00%)
14	4,331	4,331 (100.00%)	0 (0.00%)
1-14	3,428	3,421 (99.80%)	7 (0.20%)

Table 5.4. Statistics w.r.t unwrapping errors for Dataset III.

Unit	Coherent pixels	Pixels without unwrapping errors (percentage)	Pixels with unwrapping errors (percentage)
1	5,085	5,070 (99.71%)	15 (0.29%)
2	3,643	3,613 (99.18%)	30 (0.82%)
3	5,222	5,219 (99.94%)	3 (0.06%)
4	5,664	5,660 (99.93%)	4 (0.07%)
5	6,128	6,119 (99.85%)	9 (0.15%)
6	6,102	6,043 (99.03%)	59 (0.97%)
7	3,298	3,255 (98.70%)	43 (1.30%)
8	4,569	4,528 (99.10%)	41 (0.90%)
9	6,887	6,868 (99.72%)	19 (0.28%)
10	6,831	6,781 (99.27%)	50 (0.73%)
3-6	4,030	4,021 (99.78%)	9 (0.22%)
8-10	3,712	3,690 (99.41%)	22 (0.59%)

5.4.2 Precision of time series analysis

The inversion precision of SBAS time series analysis for a pixel is defined in Appendix A. The precision maps for both applications are shown in Figures 5.10 and 5.11, respectively. The overall precision indicator for all the coherent pixels is the RMS of the inversion precision values, which is deduced on the basis of misclosure of the redundant interferometric phase in the time series estimation. A small precision value represents good consistency in the redundant observations. According to the precision maps shown in Figures 5.10 and 5.11, the overall precision reaches a few submillimetres, which supports the feasibility of the proposed chain for high-precision GBSAR deformation monitoring.

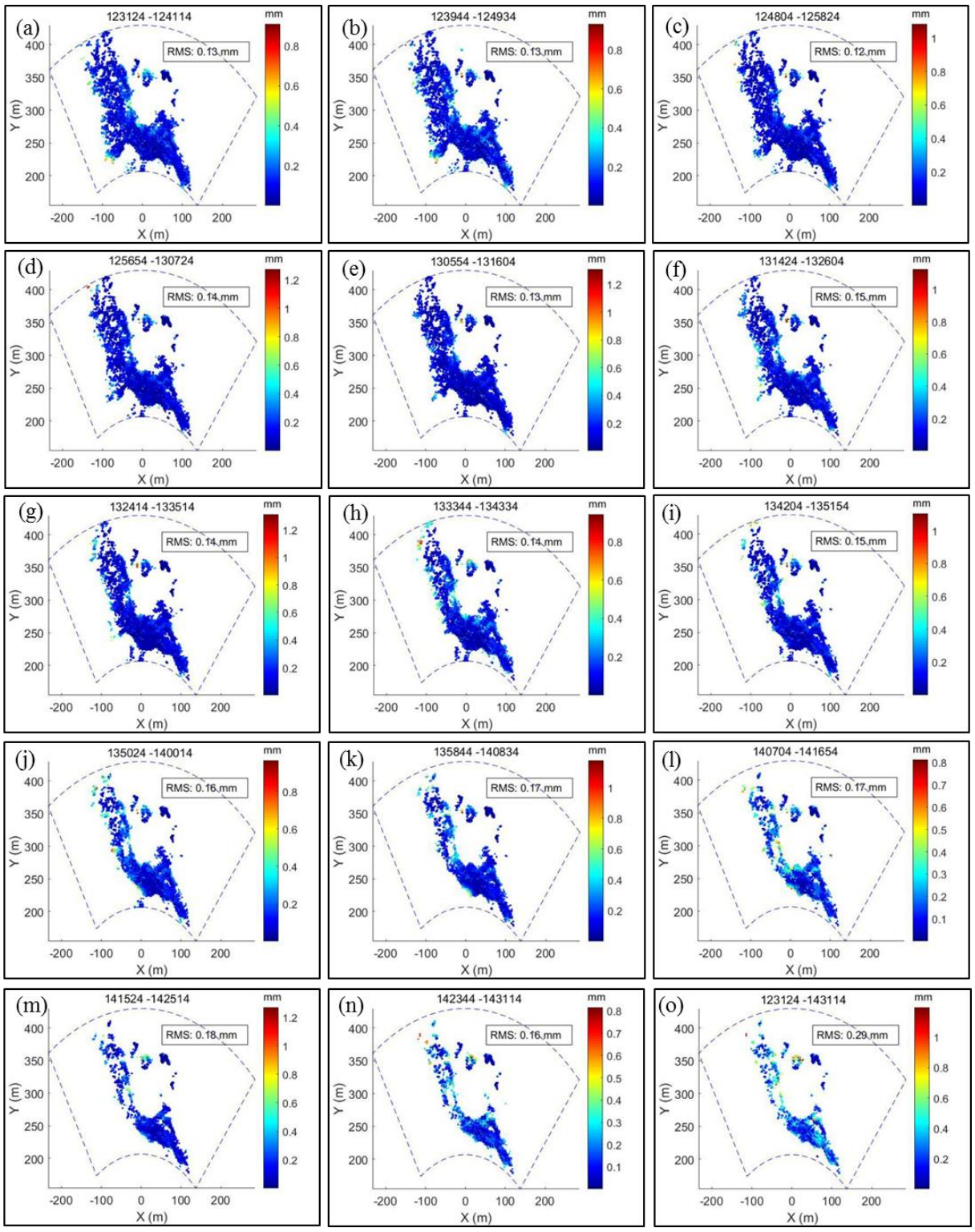

Figure 5.10. Dataset I: precision maps for coherent pixels without unwrapping errors. The precision maps for unit 1 to unit 14 are shown in subfigures (a) to (n), respectively. The precision map with respect to the total units 1-14 is given in subfigure (o).

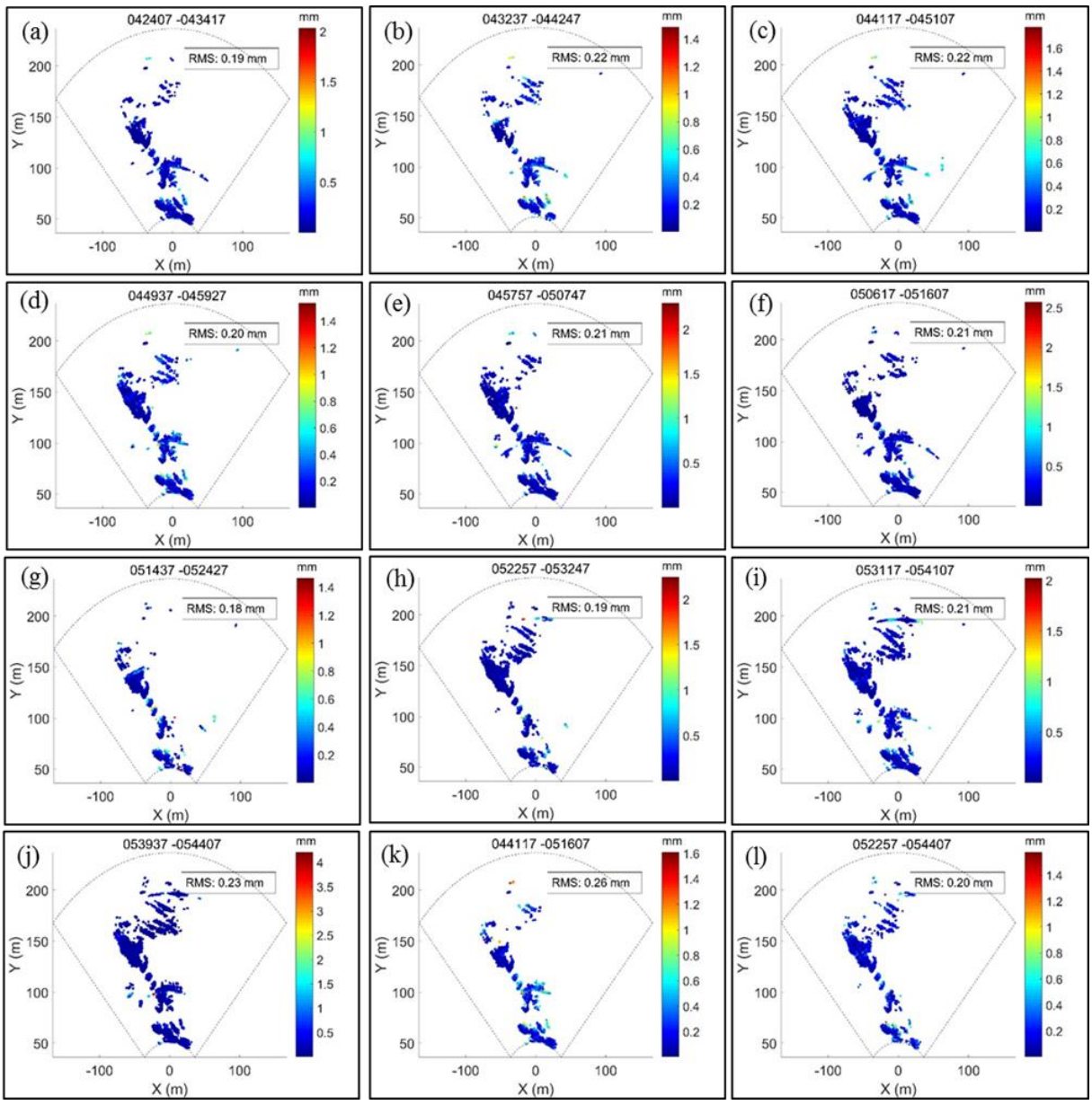

Figure 5.11. Dataset III: precision maps for coherent pixels without unwrapping errors f. The precision maps for unit1 to unit 10 are shown in subfigures (a) to (j), respectively. The precision map with respect to units 3-6 is given in (k) and that of units 8-10 in (l).

5.4.3 Real-time capability of RT-GBSAR

The proposed RT-GBSAR chain supports the real-time processing of a continuous stream of GBSAR images. Real-time capability depends on the theory of the time series strategy and its implementation. The latency (time cost) is thus twofold: (i) the acquistion time for a full window of images (denoted as T_{W}); and (ii) the processing time for time series analysis (denoted as T_{P}). Accordingly, the real-time capability is actually controlled by two parameters in the proposed RT-GBSAR chain, namely the window size of a unit (denoted as W) and the temporal baseline constraint (denoted as T). Note that the overlap size is fixed as the twofold

temporal baseline constraint (i.e. $2T$). The acquisition time for a full window of images in a unit is thus $T_{\mathrm{W}} = (W - 2T)\Delta t$, where Δt denotes the temporal resolution. The effects of the two parameters on the real-time capability, the density of coherent pixels, and the overall precision for the coherent pixels in the time series estimation have been analysed using 100 images of the sand dune dataset (i.e. Dataset III). The temporal resolution is 10 s, i.e. $\Delta t = 10\ s$. The results of multiple sets of the two parameters based on this test dataset are summarized in Table 5.5.

Table 5.5. Real-time capability and time-series results of different sets of parameters.

W	T (Δt)	Overlap: 2T (Δt)	Ifgs[a] in a full unit	Units	CPs[b] over all units	L^c	CPs with uw[d] errors	RMS[e] (mm)	Total ifgs	T_{W} (Δt)	T_{P} (s)
5	1	2	4	33	1,826	0	NA	NA	131	3	467
10	1	2	9	9	2,122	0	NA	NA	111	8	320
15	1	2	14	8	2,264	0	NA	NA	106	13	319
20	1	2	19	6	2,319	0	NA	NA	104	18	293
5	2	4	7	94	2,194	98	0	0.33	662	1	1,881
10	2	4	17	16	2,997	98	0	0.38	272	6	713
15	2	4	27	9	3,229	98	0	0.4	237	11	645
20	2	4	37	6	3,410	98	0	0.44	222	16	620
5	3	NA	NA	NA	NA	NA	NA	NA	NA	NA	NA
10	3	6	24	23	3,166	292	0	0.27	558	4	1,443
15	3	6	39	11	3,673	292	1	0.3	414	9	1,102
20	3	6	54	7	3,691	292	0	0.31	366	14	927
5	4	NA	NA	NA	NA	NA	NA	NA	NA	NA	NA
10	4	8	30	44	3,175	580	0	0.19	1336	2	3,231
15	4	8	50	13	3,670	580	7	0.23	654	7	1,632
20	4	8	70	8	3,972	580	6	0.26	544	12	1,386

[a] "Ifgs": interferograms; [b] "CPs": coherent pixels; [c] *L:* the number of temporal closed loops; [d] uw: unwrapping; [e] RMS: the precision indicator for time series estimation.

The following conclusions can be reached according to the results presented in Table 5.5:

(1) The total time cost comprises the data acquisition time (T_{W}) and the data processing time (T_{P}). It is intuitive that a higher temporal resolution leads to a shorter latency since data is provided more quickly to begin processing. The latency is also dependent on the difference between the unit size and the overlap size ($W - 2T$). The processing time increases with the number of interferograms ("Total ifgs"), which mainly depends on the temporal baseline constraint. Therefore, the real-time capability can be jointly enhanced by improving the temporal resolution and reducing the temporal baseline constraint.

(2) The density of coherent pixels (i.e. "CPs over all units") increases with the temporal baseline constraint when using the full-rank approach presented in Chapter 4. A longer temporal baseline constraint will lead to increased redundancy in the interferogram

network and to more reliable results (indicated by a lower RMS value), but at the expense of the computational efficiency (indicated by a longer processing time T_P). An insufficiently small unit size (e.g. W=5) may reduce the density of coherent pixels over all units. Thus, a small unit size is only recommended if the monitoring campaign is involves an extremely fast-changing site with a high real-time demand, e.g. for early warning purposes. Otherwise, the unit size can be increased.

It is worth noting that processing time T_P depends on the adopted programming language, the algorithm implementation and the computer configuration. Here, processing time cost was based on MATLAB R2016b software and a laptop with an Intel i7 2.40 GHz CPU. Processing time could therefore be significantly improved with effort made on high-performance computation.

5.4.4 RT-GBSAR versus SePSI

FastGBSAR is accompanied by an InSAR time series analysis software package, i.e. "SePSI" (Metasensing, 2015a). The algorithms adopted in this package were developed by Rödelsperger (2011). SePSI starts with the detection of PS pixels on the basis of ADI. A subset of PSCs are then selected for temporal and spatial phase unwrapping. Note that FastGBSAR "Ranger" (Metasening, 2016) is a more recently developed software package with an improved user interface, using the same algorithms as SePSI. Therefore, RT-GBSAR was compared only with "SePSI".

30 images in Dataset II (i.e. the Queen Elizabeth II Metro Bridge) were used for analysis. In SePSI, PSs were detected by ADI<0.35 and PSCs by ADI<0.2 with at most one PSC in each 10 m × 10 m grid. The number of time steps was set as three, which meant the a-posteriori solution was achieved with a delay of three acquisitions ($3\Delta t$). The processing time (excluding focusing) in SePSI was 168 seconds. In RT-GBSAR, the data was processed in eight units with a window size of seven images and a temporal baseline constraint of two images. Thus, the acquisition time for a full window of images in RT-GBSAR was equivalent to the delay of the a-posteriori solution in SePSI (i.e. $3\Delta t$). The processing time in RT-GBSAR (excluding focusing) was 121 seconds. Considering the observation period was short, no APS correction was applied in both SePSI and RT-GBSAR. Several key displacement maps from the results achieved by SePSI and RT-GBSAR are shown in Figure 5.12.

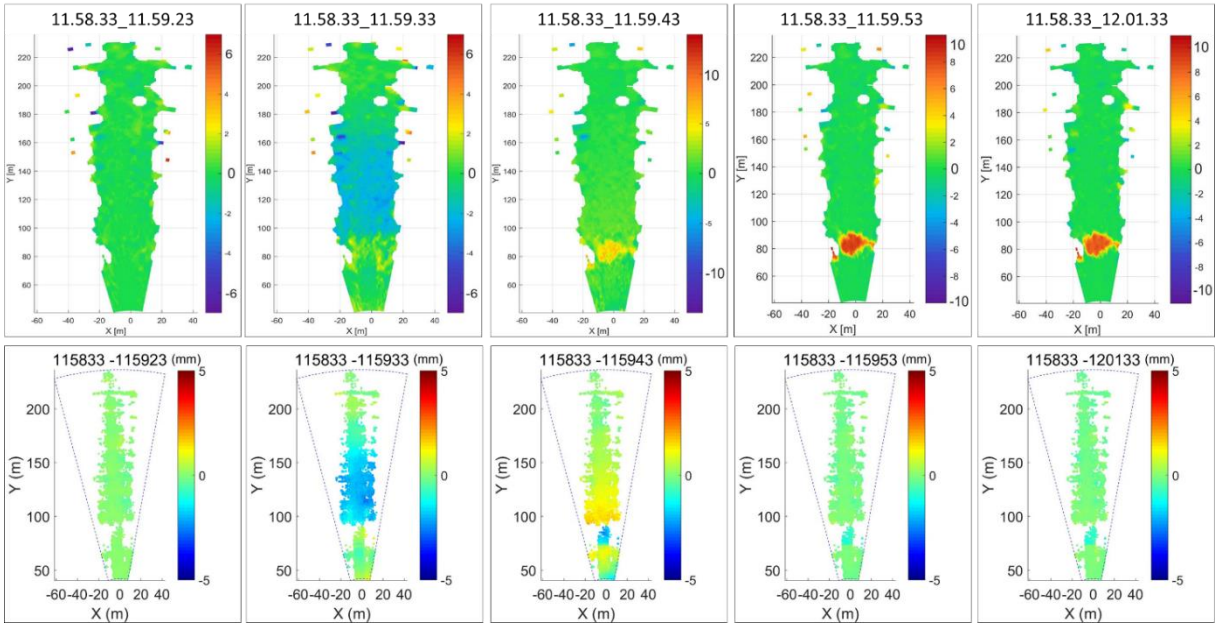

Figure 5.12. The displacement maps achieved by SePSI are shown in the first row and the counterparts by RT-GBSAR in the second row.

To further analyse the results, interferograms with respect to the displacement maps shown in Figure 5.12 are generated and shown in Figure 5.13.

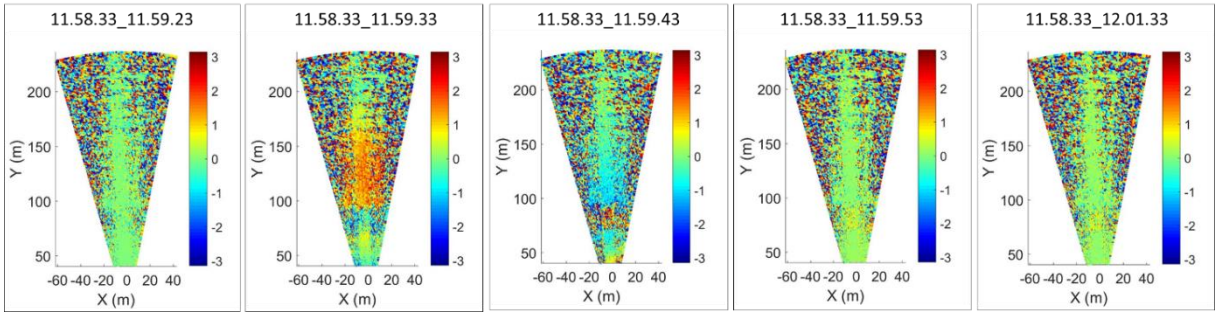

Figure 5.13. Interferograms corresponding to the displacement maps in Figure 5.12.

Interferograms ("11.58.33_11.59.33" and "11.58.33_11.59.43" in Figure 5.13) suggest that the bridge vibrated during the train crossing and then the bridge recovered (see "11.58.33_11.59.53" and "11.58.33_12.01.33" in Figure 5.13). It is intuitive that the RT-GBSAR results are reasonable and consistent with the practical process. However, SePSI produced a false deformation signal around the position (x=0, y=80), which is visible in the displacement maps after 11.59.43.

SePSI utilises a two-step unwrapping strategy, which firstly unwraps the PSC network and then extends the unwrapping to all PS pixels. As pointed out by Rödelsperger (2011), sudden phase changes at any arc would probably lead to unwrapping errors. Accordingly, all PS pixels

connected to the incorrectly unwrapped arcs are affected. Figure 5.14 displays the PSC network, the phase time series, and the displacement time series for PSCs and arcs that are related to the false deformation signal. Sudden phase changes of two PSCs near the position (x=0, y=80) at the moments “11.59.33” and “11.59.43” (in Figure 5.14(c)) lead to unwrapping errors on these PSCs related arcs (in Figure 5.14(d)). These errors propagated to the subsequent displacement maps and led to the false deformation signal.

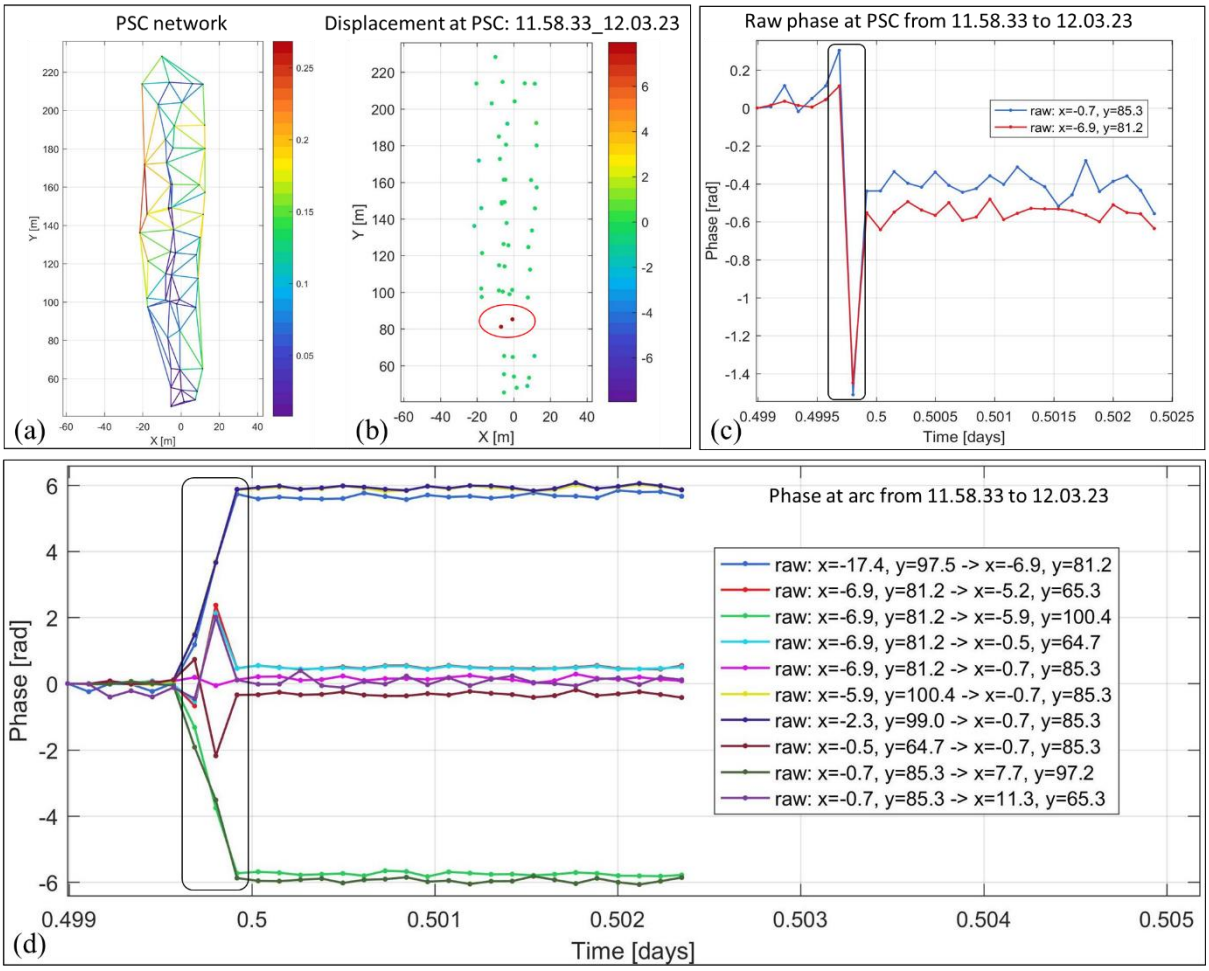

Figure 5.14. The occurrence of unwrapping errors and the production of false deformation in SePSI.

5.5 Summary

The significant challenges in processing continuous GBSAR data have been resolved through the implementation of the proposed RT-GBSAR chain. The chain has three notable features: (i) low computational requirement; (ii) insights into the evolution of surface movements through temporally-coherent pixels; and (iii) real-time capability to process a theoretically infinite number of images.

The applications of monitoring a fast-changing sand dune and a coastal cliff have demonstrated that the proposed chain can achieve a inversion precision of a few submillimetres in time series estimation. In the sand dune application, the movement took place only at areas without any vegetation while areas with sparse vegetation coverage remained stable over the short observation period of 1 hour and 20 minutes, which suggests that the preservation of vegetation in the dune area plays an important role in stabilising the surface against sand motion. In the coastal cliff application, the RT-GBSAR results reveal displacements only in the area near the sea and suggest that the triggering of ground deformation is related to the sea tides.

Chapter 6. A new interferometric processing chain for discontinuous GBSAR deformation monitoring

The study in this Chapter has been submitted as a research journal paper for publication:

Wang, Z., Li, Z., Mills, J., Modelling of instrument repositioning errors in discontinuous Multi-Campaign Ground-Based SAR (MC-GBSAR) deformation monitoring, *Manuscript submitted to ISPRS Journal of Photogrammetry and Remote Sensing on 5th May 2019 for publication*.

6.1 Introduction

In practice, GBSAR data acquisition can be performed either in a continuous or discontinuous (campaign) mode, depending on the rate of surface motion, and/or the environment for instrument deployment (e.g. Caduff et al., 2015; Crosetto et al., 2014a; Crosetto et al., 2017; Monserrat et al., 2014). Continuous mode is more commonly deployed and has been demonstrated in Chapter 5. The discontinuous mode with repeated campaigns is especially useful for monitoring an event whereby the deformation becomes significant over a relatively long period and the deployment of continuous GBSAR cannot be easily achieved (e.g. Caduff et al., 2015; Crosetto et al., 2017; Monserrat et al., 2014). Therefore, this chapter focuses on discontinuous GBSAR deformation monitoring, namely the monitoring of surface deformation between two or more campaigns.

In discontinuous mode, the radar instrument is required to be installed over the same monitoring station in each campaign, but repositioning errors may occur due to the lack of forced centring and/or the instability of the monitoring station, which can lead to inaccuracies in GBSAR interferometric observations (e.g. Barla et al., 2017; Caduff et al., 2015; Crosetto et al., 2014a; Monserrat et al., 2014). However, the effects of repositioning errors on GBSAR interferometry has not been investigated before. It was only simply considered as a low-frequency signal and removed by low-pass filtering (Crosetto et al., 2014a). This study thus aims to accurately model and correct the effects of repositioning errors between different campaigns of GBSAR data for interferometric measurement.

To illustrate the effects of such repositioning errors, this study starts with the geometry of GBSAR. In 3D object space, a GBSAR system (including radar sensor and rail), can be considered as a rigid body. Repositioning errors of the radar instrument can be expressed as a

set of rigid transformation parameters (Challis, 1995). As illustrated in Figure 6.1, a GBSAR system is moved from the position s to another position s' with a 3D rotation, including a roll angle (denoted as ϕ, around the y axis), a yaw angle (denoted as ω, around the x axis), and a pitch angle (denoted as κ, around the z axis). The position and orientation of the radar before repositioning can be expressed by the sensor-centred coordinate system $s - xyz$, where x is parallel to the GBSAR rail, y is the look direction, and z is perpendicular to the $x - y$ plane. After repositioning, the transition coordinate system becomes $s' - x'y'z'$. The geometric transformation between the two coordinate systems before and after repositioning can be expressed as:

$$\begin{bmatrix} x' \\ y' \\ z' \end{bmatrix} = \mathbf{R} \begin{bmatrix} x \\ y \\ z \end{bmatrix} + \begin{bmatrix} t_x \\ t_y \\ t_z \end{bmatrix}, \tag{6.1}$$

where $[t_x\ t_y\ t_z]$ is the translation vector from s to s'; $\mathbf{R}$ is the rotation matrix of (ϕ, ω, κ).

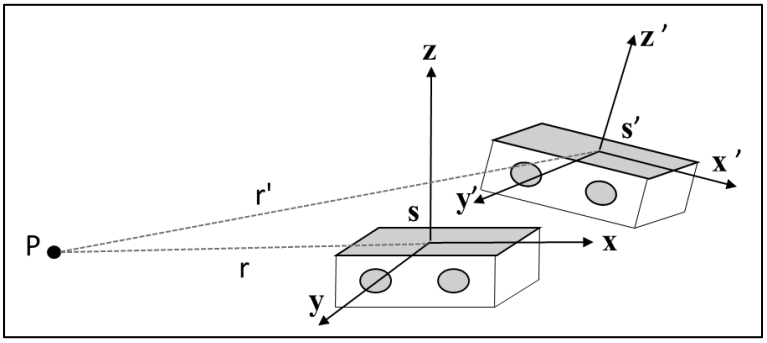

Figure 6.1. The geometries of GBSAR before and after repositioning.

Due to repositioning errors, GBSAR images before and after repositioning can be shifted. Besides, an additional phase component is introduced as the range between the radar and the target changes with the radar position and orientation, which is illustrated in Figure 6.1. Hence, the additional phase component due to repositioning errors can be termed as repositioning phase errors, and denoted as φ_{repos} in this study.

To quantify these effects, FastGBSAR observations were simulated over a dome-shaped topography with additional considerable repositioning errors $\left(\phi = \omega = \kappa = 1^{\circ}, t_x = t_y = t_z = 0.1\ m\right)$ (Figure 6.2(a)). The shadow area was masked out in the simulation. It appeared that the additional phase component caused by the repositioning errors (Figure 6.2(b)) resembled the orbital ramps in spaceborne InSAR (Shirzaei and Walter, 2011). In addition, the

azimuth offsets were bigger than the range ones (Figures 6.2(c) and 6.2(d)).

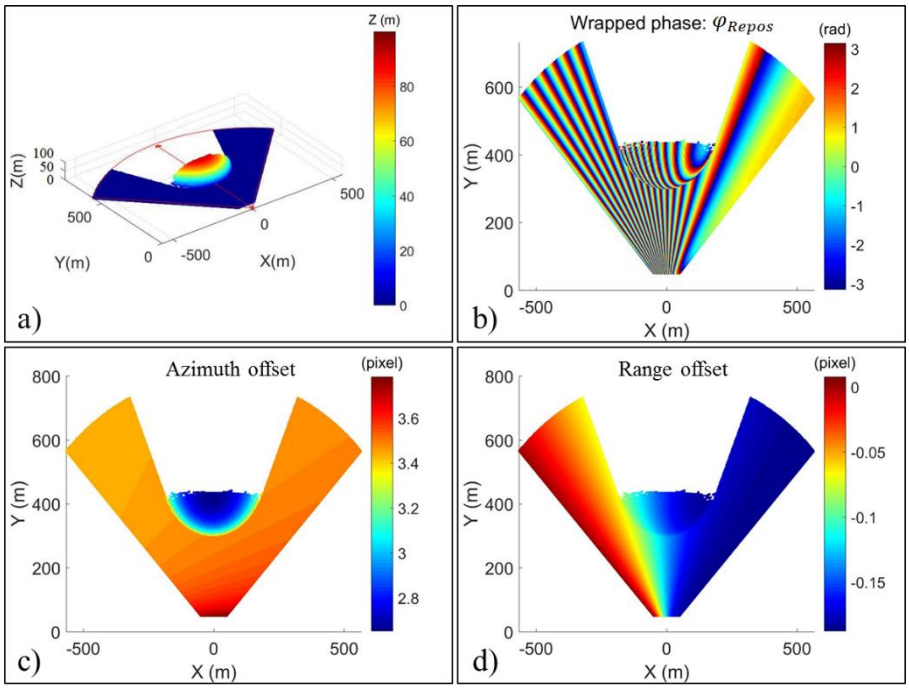

Figure 6.2. Simulation of repositioning errors $(\phi = \omega = \kappa = 1^{\circ}, t_x = t_y = t_z = 0.1\ m)$. (a) Topography. (b) Repositioning phase errors. (c) Azimuth offsets. (d) Range offsets.

In GBSAR deformation monitoring, it is optimal to install the radar equipment on a stable and reproducible monitoring station for data collection (e.g. Bardi et al., 2016; Barla et al., 2017; Del Ventisette et al., 2011; Iglesias et al., 2015a; Montuori et al., 2016). The majority of previous GBSAR studies (e.g. Barla et al., 2017; Casagli et al., 2010; de Macedo et al., 2017; Frukacz and Wieser, 2017; Lowry et al., 2013; Tarchi et al., 2005) managed to obtain a zero-baseline geometry in repeated campaigns by means of precise mechanical positioning systems, such as a forced centring device. However, repositioning errors are present in many practical cases, where the monitoring station is not stable or a precise mechanical positioning device cannot be deployed (Crosetto et al., 2014a). In this study, a steady concrete base was placed at a stable area. Simple marks were engraved onto the top surface of the concrete base to aid in positioning and orientating the instrument rail. According to practical experience, the repositioning errors can be easily controlled within a moderate tolerance (i.e. $|t_x| < 5mm, |t_y| < 5mm, |t_z| < 5mm, |\varphi| < 0.3^{\circ}, |\omega| < 0.3^{\circ}, |\kappa| < 0.3^{\circ}$). Thus, another simulation was made with a set of moderate repositioning errors $(\phi = \omega = \kappa = 0.3^{\circ}, t_x = t_y = t_z = 5mm)$.

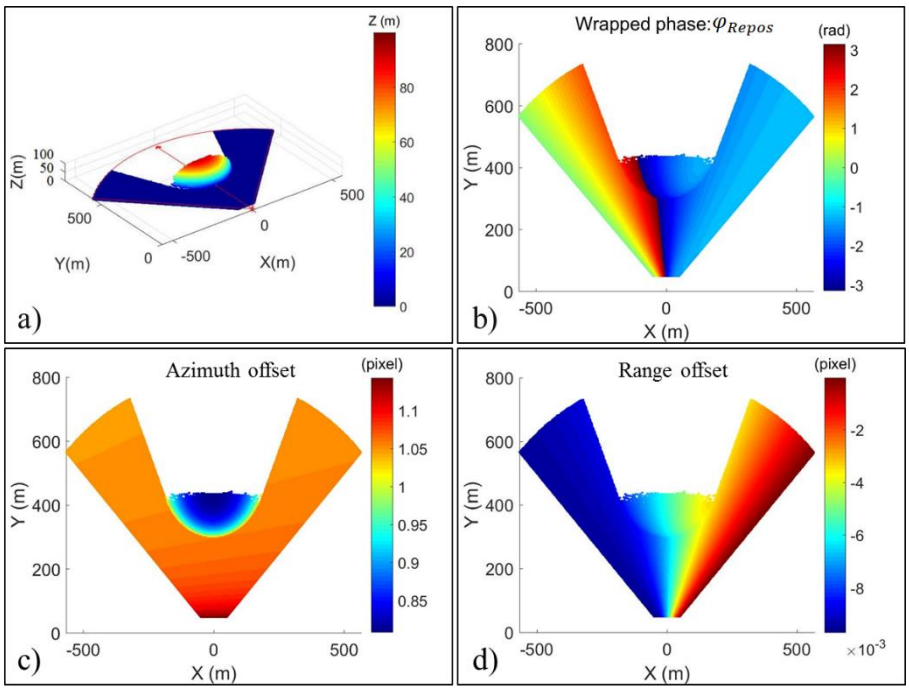

Figure 6.3. Simulation of repositioning errors $(\phi = \omega = \kappa = 0.3^{\circ}, t_x = t_y = t_z = 5\ mm)$. (a) Topography. (b) Repositioning phase errors. (c) Azimuth offsets. (d) Range offsets.

It is clear from Figure 6.3 that, although the repositioning errors are only at the level of several millimetres, the resultant phase ramps and azimuth offsets are significant and cannot be neglected. Effort must be made to mitigate the impacts of the repositioning errors between different campaigns. It has been reported that such repositioning errors in discontinuous GBSAR can be addressed by a non-interferometric approach (Crosetto et al., 2014b). However, non-interferometric measurement is not sensitive to surface movement and the measurement inaccuracies can be a few decimetres (e.g. Caduff et al., 2015; Crosetto et al., 2017). Therefore, a new interferometric processing chain has been developed for discontinuous GBSAR deformation monitoring. The proposed discontinuous GBSAR chain aims to measure deformation between two or more campaigns, and is thus termed "MC-GBSAR" (Multi-Campaign GBSAR). Details about the methodology are introduced in Section 6.2. Experiments with both synthetic and real-world data are given in Section 6.3 and a discussion presented in Section 6.4.

6.2 Methodology

6.2.1 Overview of methodology

In MC-GBSAR, temporal averaging is first carried out on a stack of SLC images in a single campaign in order to improve the SNR and minimise the loss of coherence (e.g. Caduff et al.,

2015; Iglesias et al., 2015b; Iglesias et al., 2014a). Without loss of generality, this chain supports the processing of multi-campaign GBSAR data both with and without repositioning errors. As illustrated in Figure 6.4, the main difference between the two scenarios is that the presence of repositioning errors requires (i) co-registration of GBSAR images and (ii) correction of repositioning errors. Adaptive estimation of coherence with respect to interferograms is achieved using the non-local "MIAS" method presented in Chapter 3. Coherent pixels are selected for further analysis via the full-rank criterion presented in Chapter 4. The interferometric phase of the detected coherent pixels is then de-noised using the non-local "MIAS" filter. Thereafter, unwrapped phase of the detected coherent pixels can be achieved using 2D/3D phase unwrapping algorithms provided in StaMPS (Hooper, 2010).

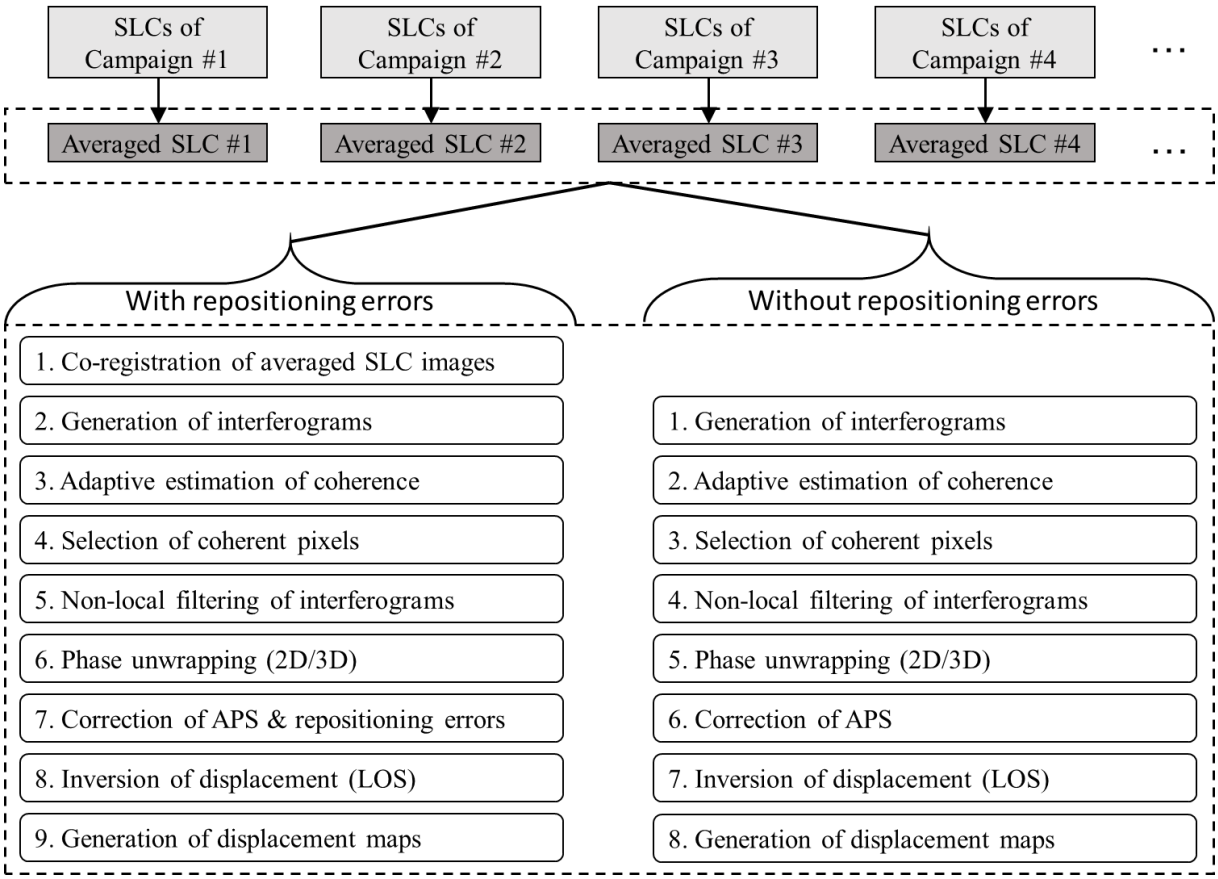

Figure 6.4. The procedure of MC-GBSAR.

6.2.2 Automatic co-registration of GBSAR images

Co-registration in spaceborne and ground-based InSAR is often based on cross correlation (e.g. Crosetto et al., 2014b; Hanssen, 2001; Hooper et al., 2007; Li and Bethel, 2008) or feature matching (e.g. Suri et al., 2010; Wang and Zhu, 2015) of the amplitude images. Given that the GBSAR instrument may be rotated after repositioning, an amplitude-based feature matching

approach is developed for the automatic co-registration of GBSAR images in this study as feature matching tends to be invariant to image rotation (Bay et al., 2008). The commonly used features such as Harris corner points (Harris and Stephens, 1988) and speeded-up robust features (SURF) (Bay et al., 2008) are supported in MC-GBSAR. Before feature extraction, oversampling is applied to the GBSAR images as it is able to avoid aliasing and improve the co-registration accuracy (e.g. Li and Bethel, 2008; Sousa et al., 2011). To co-register the master and slave images, the slave image is resampled to the master image coordinate system via a polynomial function, the affine transformation is typically used for GBSAR co-registration (Crosetto et al., 2014b). An example of GBSAR co-registration is given in Figure 6.5.

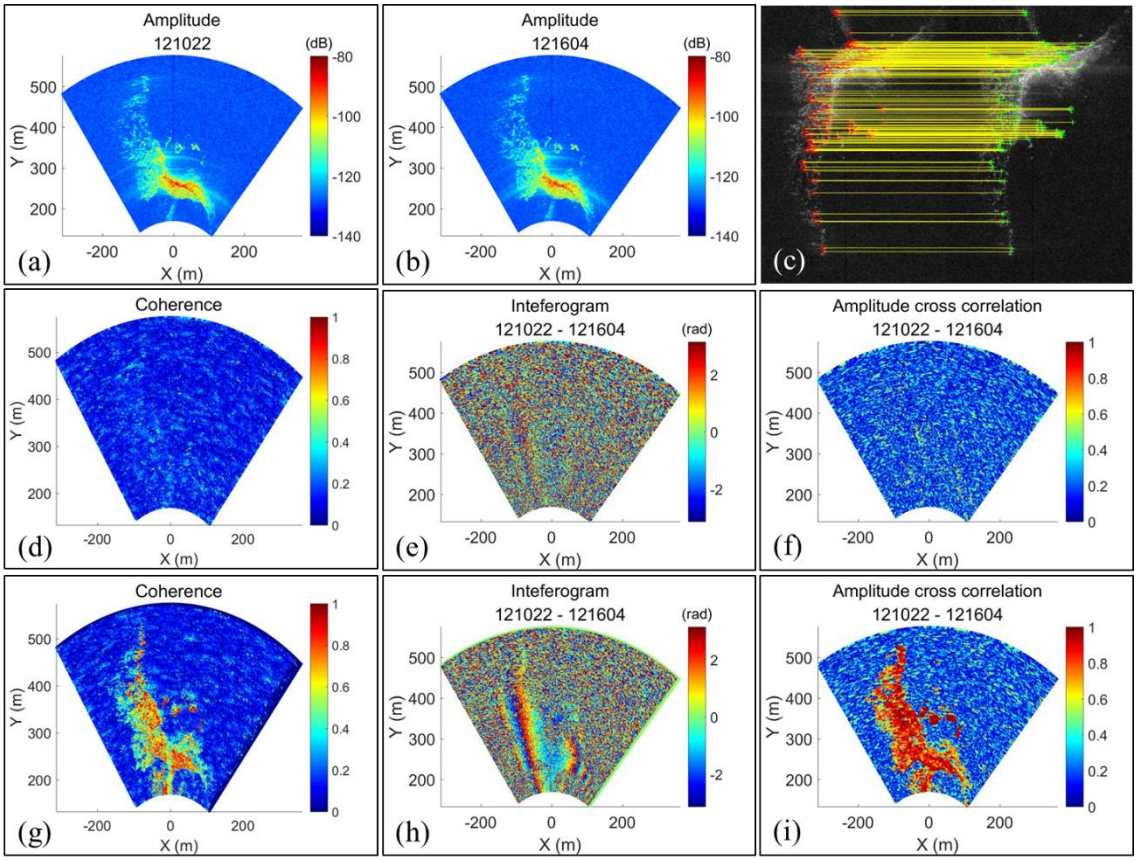

Figure 6.5. An example of co-registration between two campaigns of FastGBSAR data. Between the two campaigns, the radar rail was deliberately moved approximately 15 cm backwards and slightly rotated with a small unknown angle. The time difference between the two campaigns is 342 s and each campaign consists of 15 continuous images. (a) The averaged amplitude image of the first campaign. (b) The averaged amplitude of the second campaign. (c) Feature matching based Harris corner points with an accuracy of 0.19 pixels (i.e. RMS of the image coordinate residuals for corresponding points between the master and slave images). (d) Coherence without co-registration with an assumption of no repositioning error. (e) Interferogram without co-registration. (f) Amplitude cross correlation without co-registration. (g) Coherence after co-registration. (h) Interferogram after co-registration. (i) Amplitude cross correlation after co-registration.

As shown in Figure 6.5, the coherence (6.5(d)) between the averaged images of the two campaigns suggests that they are completely decorrelated without co-registration, and their interferogram (6.5(e)) is dominated by noise. After co-registration, the coherence (6.5(g)) is significantly improved and the resultant phase ramps are visible (6.5(h)), suggesting the necessity of co-registration in the scenario with considerable repositioning errors. The robustness of the co-registration is evidenced by comparing the amplitude cross correlations in Figures 6.5(f) and 6.5(i).

6.2.3 Correction of geometric phase ramps

In spaceborne InSAR, the most widely used approach to correct for orbital ramps is to estimate a best-fit plane using a 1st-order polynomial function (e.g. Biggs et al., 2007; Shirzaei and Walter, 2011):

$$\varphi^{geom}(\eta, \xi) = \alpha_0 + \alpha_1 \eta + \alpha_2 \, \xi, \tag{6.2}$$

where $\alpha_i (i = 0,1,2)$ are coefficients; η and ξ are the range and azimuth in the radar image coordinate system, respectively; φ_{geom} is the geometric phase error at (η, ξ). Given that the geometric phase ramps in GBSAR resemble the orbital ramps in spaceborne InSAR, the best-fit plane model was firstly investigated in this study. Specifically, three types of topography were simulated (in Figure 6.6): flat, slope, and dome. Together with the simulated topography, two sets of additional repositioning error parameters were investigated: $\left(\text{Errors} - \text{I}: \phi = \omega = \kappa = 0.3^{\circ}, t_x = t_y = t_z = 5\ mm\right)$ and $\left(\text{Errors} - \text{II}: \phi = \omega = \kappa = 1^{\circ}, t_x = t_y = t_z = 0.1\ m\right)$. As mentioned earlier, Errors-I represents the margin of repositioning errors in practice (with moderate effort given to instrument installation), while Errors-II is a set of considerable errors for comparison.

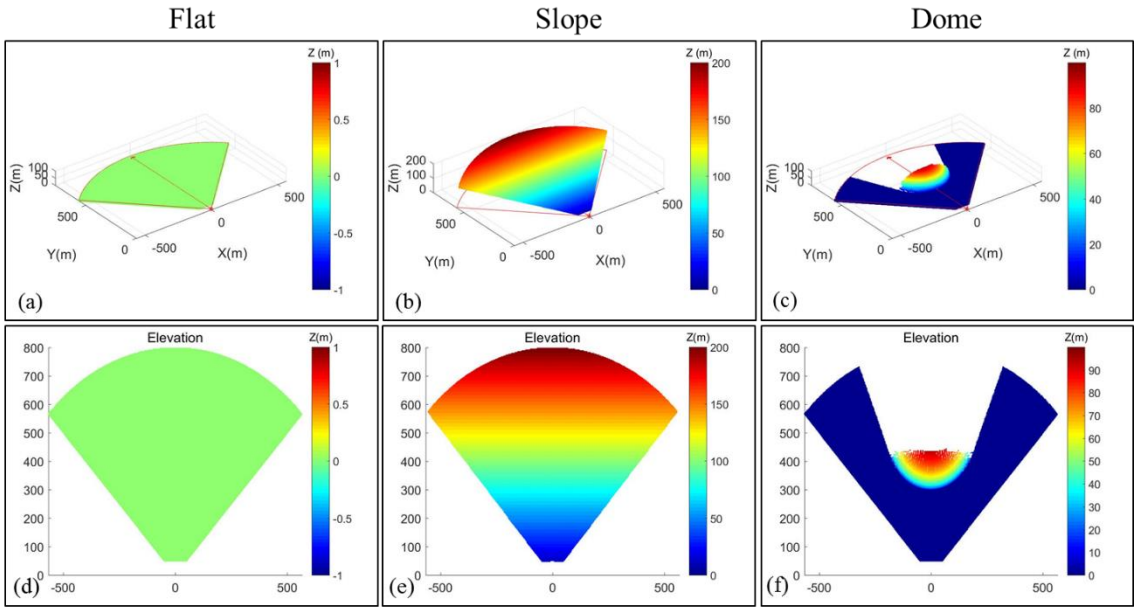

Figure 6.6. Three types of topography and their corresponding elevation maps in the GBSAR coordinate system.

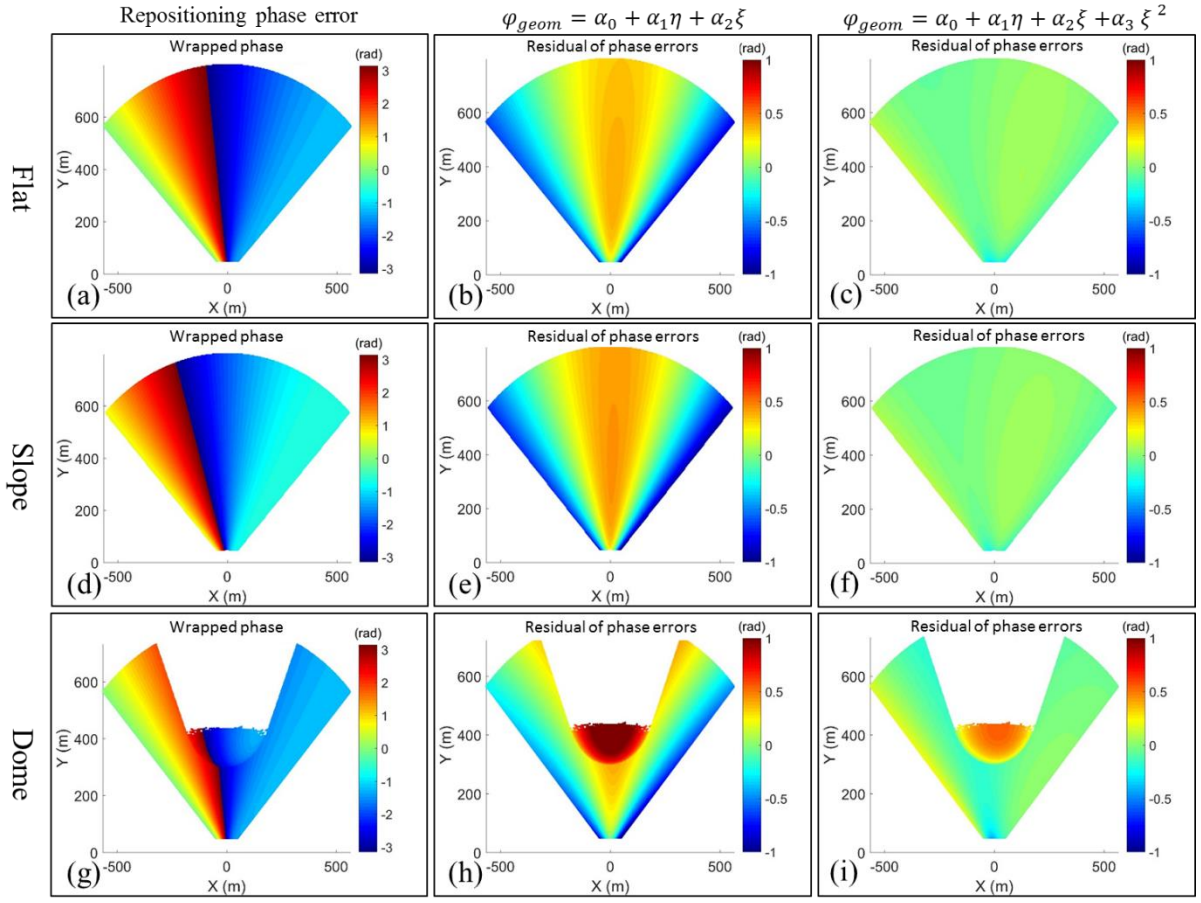

Figure 6.7. Simulation and correction of geometric phase errors with respect to Errors-I for all three types of topography: flat, slope and dome.

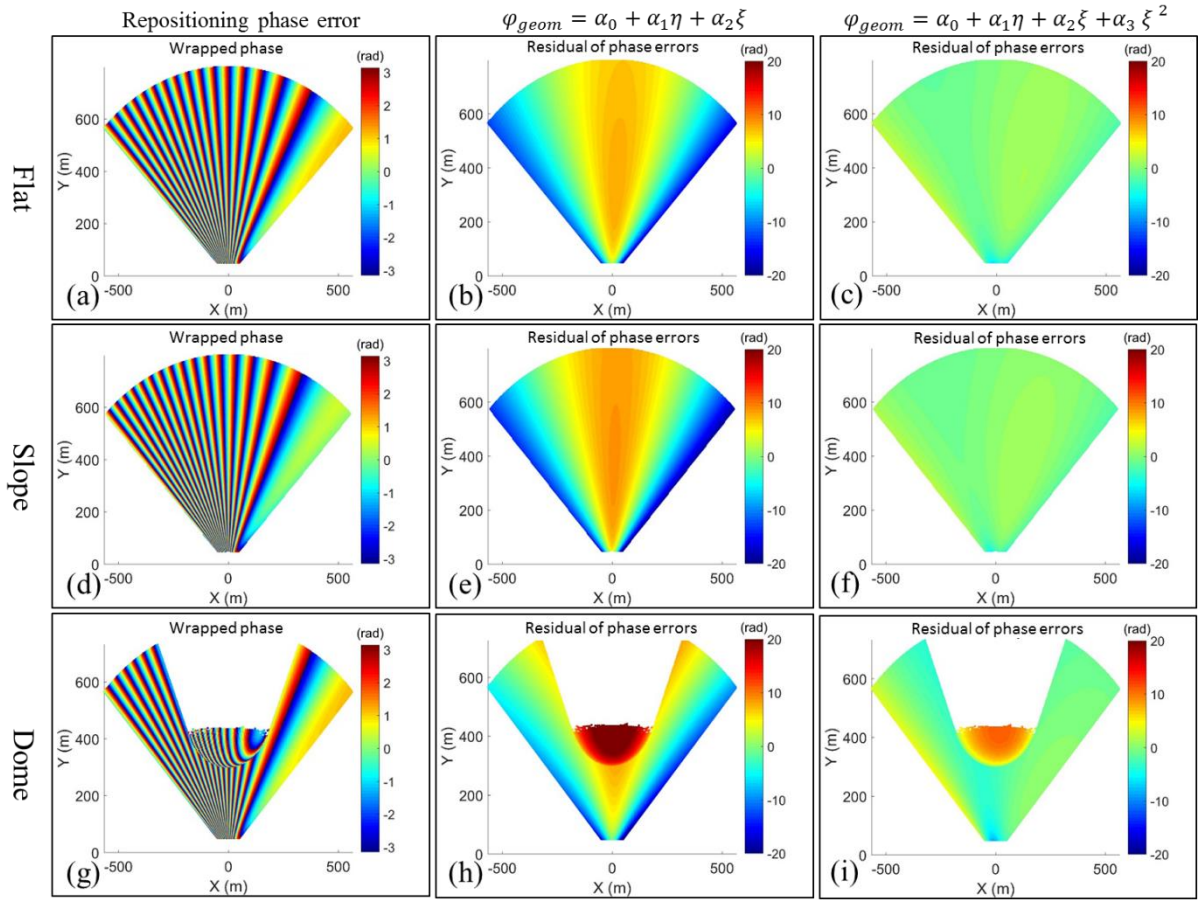

Figure 6.8. Simulation and correction of geometric phase errors with respect to Errors-II for all three types of topography: flat, slope and dome.

It is clear in the first column of Figures 6.7 and 6.8 that both repositioning error sets lead to significant phase ramps in all topography scenarios. To correct such errors, the conventional 1st-order correction model (in Equation (6.2)) was firstly applied. The residual maps for the two error sets are given in the second column of Figures 6.7 and 6.8, respectively. The geometric phase errors are largely mitigated by the 1st-order model, but there are obvious residuals remaining that are clearly correlated with the azimuth coordinate ξ. Therefore, the correction model was raised to the 2nd-order of ξ as follows.

$$\varphi_{geom} = \alpha_0 + \alpha_1\eta + \alpha_2\xi + \alpha_3\xi^2. \tag{6.3}$$

The residual maps with respect to the 2nd-order model for the two error sets are shown in the third column of Figures 6.7 and 6.8, respectively. The RMS and maximum of residuals are summarised in Table 6.1. In all the scenarios, the RMS and maximum of residuals from the 2nd-order correction model are much less than those from the 1st-order correction model, suggesting the geometric phase correction with the 2nd-order model outperforms the 1st-order model.

Therefore, the 2nd-order model was chosen to correct the geometric phase error ramps in this study.

Table 6.1. Statistics of geometric error correction.

Type	Error	$\varphi_{geom} = c_0 + c_1\eta + c_2\xi$		$\varphi_{geom} = c_0 + c_1\eta + c_2\xi + c_3\xi^2$	
		RMS of residuals: rad (mm)	Max of residuals: rad (mm)	RMS of residuals: rad (mm)	Max of residuals: rad (mm)
Flat	I	0.32 (0.45)	0.91 (1.26)	0.05 (0.07)	0.30 (0.42)
Slope	I	0.37 (0.52)	1.00 (1.39)	0.04 (0.05)	0.24 (0.34)
Dome	I	0.36 (0.50)	1.18 (1.63)	0.14 (0.20)	0.55 (0.77)
Flat	II	6.46 (8.94)	18.27 (25.27)	0.95 (1.32)	6.28 (8.70)
Slope	II	7.52 (10.41)	20.12 (27.87)	0.79 (1.10)	5.02 (6.95)
Dome	II	7.23 (10.02)	23.54 (30.60)	2.87 (3.97)	11.10 (15.38)

In the simulation, the 2nd-order model was able to reduce the errors from ~-6.8 mm (the value was converted from the unwrapped φ_{repos}) to ~-0.7 mm (the value was converted from the max of residuals after geometric correction) for Errors-I and from ~-137 mm to ~-15 mm for Errors-II in the dome area with a 100 m height variation. However, the residuals after correction are dependent on local topography variations to some extent and even the 2nd-order model cannot completely remove the phase errors for areas with local topography variations (Figures 7(i) and 8(i)). Additional effort should be made to further correct the systematic residuals due to topographic variation for accurate InSAR measurement.

6.2.4 Correction of topographic phase errors

The topographic phase (denoted as φ_{topo}) in InSAR is a function of the perpendicular spatial baseline $B_\perp$ and the elevation z along the axes defined by the antenna vertical motion, which can be approximated by the linear term in GBSAR configuration (e.g. Noferini et al., 2007; Rödelsperger et al., 2010) as follows:

$$\varphi_{topo} = \frac{4\pi}{\lambda}\frac{B_\perp z}{r}. \tag{6.4}$$

where r is the range to the target when the antenna is positioned at z = 0. According to Equation (6.4), the removal of the topographic effect requires both an appropriate DEM and known perpendicular spatial baseline. However, in practice, the precise measurement of the position and orientation of a GBSAR system (e.g. a FastGBSAR) is usually not achievable without significant technical effort. This implies that the perpendicular spatial baseline is unknown.

Therefore, this subsection focuses on the correction of the topographic effect without knowing the spatial baseline. Due to the linear relationship between the elevation and the topographic phase in Equation (6.4), the topographic correction model in the case of an unknown spatial baseline can be written as:

$$\varphi_{topo} = \alpha_0 + \alpha_1 \frac{z}{r}. \tag{6.5}$$

where α_0 and α_1 are coefficients of the linear topographic correction mode.

On the basis of such geometric correction, the topographic correction is further applied. The results before and after topographic correction for the simulated three types of topography with respect to both Errors-I and Errors-II are shown in Figures 6.9 and 6.10, respectively.

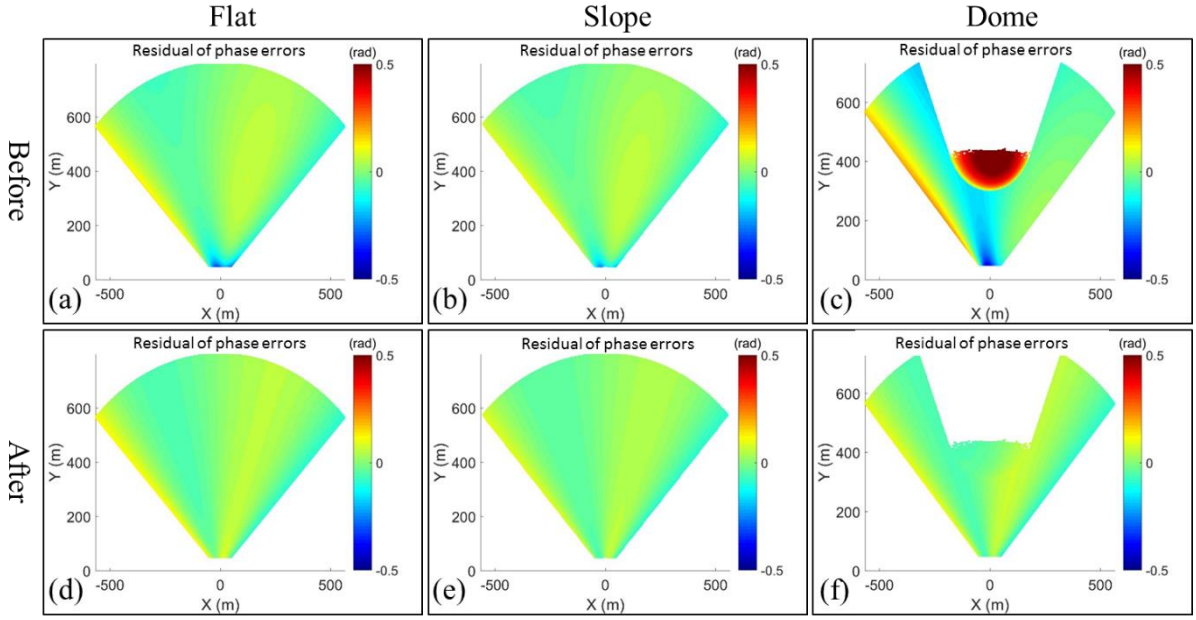

Figure 6.9. Topographic correction with respect to Errors-I.

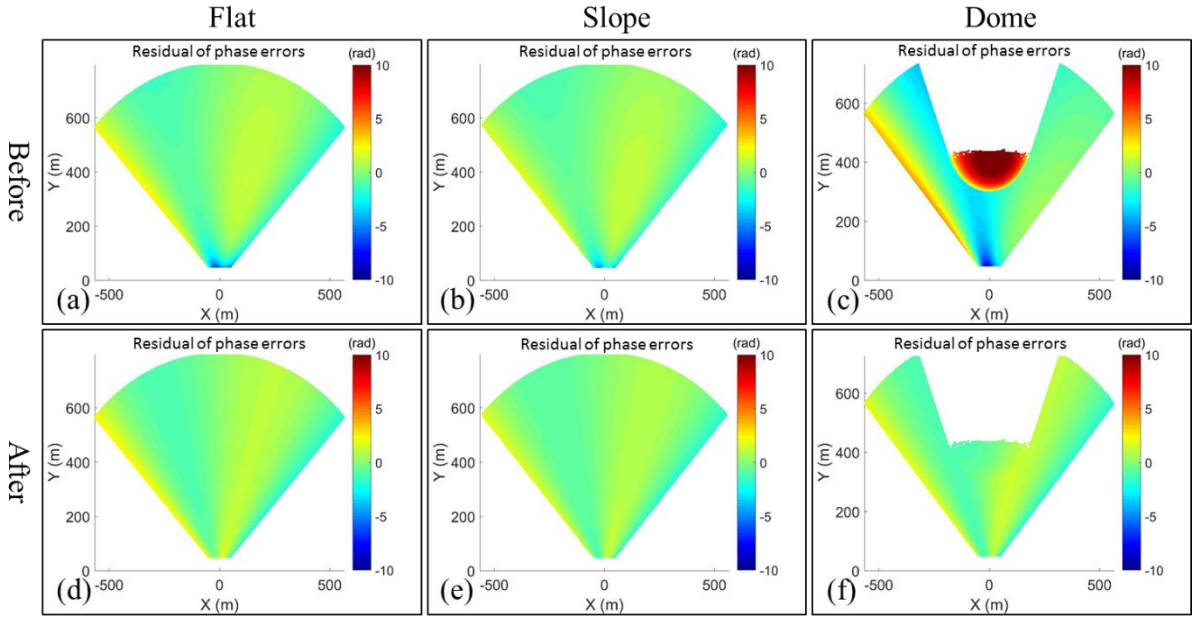

Figure 6.10. Topographic correction with respect to Errors-II.

It is evident from Figures 6.9 and 6.10 that the topographic phase errors have been effectively removed for both repositioning error sets in all topography scenarios. The statistics of topographic correction are summarized in Table 6.2. The feasibility of the proposed topographic correction approach can be straightforwardly demonstrated by the efficient mitigation of both the RMS and maximum of residuals for all the simulation cases. It is worth noting that greater repositioning errors lead to greater residuals by comparing the residuals of Errors-I and Errors-II in Table 6.2. Therefore, the repositioning of GBSAR instrument between different campaigns should be as precise as possible.

Table 6.2. Statistics of topographic correction.

Error	Topographic correction	RMS of residuals: rad (mm)			Max of residuals: rad (mm)		
		Flat	Slope	Dome	Flat	Slope	Dome
I	Before	0.05 (0.07)	0.04 (0.06)	0.14 (0.20)	0.30 (0.42)	0.24 (0.34)	0.55 (0.77)
I	After	0.04 (0.06)	0.03 (0.05)	0.04 (0.06)	0.15 (0.21)	0.09 (0.13)	0.10 (0.14)
II	Before	0.95 (1.32)	0.79 (1.10)	2.87 (3.97)	6.28 (8.70)	5.02 (6.95)	11.1 (15.38)
II	After	0.86 (1.20)	0.72 (1.00)	0.89 (1.23)	3.08 (4.26)	1.91 (2.65)	2.10 (2.91)

6.2.5 Combined correction of atmospheric, geometric, and topographic errors

Modelling approach

As demonstrated in Section 2.3.5, the rigorous model for atmospheric correction is a range- and

height-dependent function:

$$\varphi_{atm} = \beta_0 + \beta_1 r + \beta_2 rz. \tag{6.6}$$

The range r is linear with η: $r = \eta\Delta r$. Thus, Equations (6.3), (6.5) and (6.6) can be combined to give Equation (6.7) and used to correct for atmospheric, geometric and topographic errors.

$$\varphi_{atm+geom+topo} = c_0 + c_1 r + c_2\xi + c_3\xi^2 + c_4 rz + c_5 z/r. \tag{6.7}$$

where $c_i (i = 0, \cdots, 5)$ represents the model parameters that can be estimated using the unwrapped phase of a set of highly-coherent pixels from stable areas . The stable areas can be identified through *a-priori* knowledge of the study site and visual inspection of interferograms (Caduff et al., 2014). However, in some situations without sufficient knowledge, or if the interferogram is dominated by atmospheric, geometric, and/or topographic phase errors, pixels carrying deformation information may be selected for modelling. To mitigate the potential inaccuracies caused by these pixels, this study employs an IRLS (iteratively reweighted least squares) algorithm to estimate the model parameters (Green, 1984). The weight for any pixel in the first iteration is set as one and is subsequently updated by its deviation to the model estimated in the previous iteration. A pixel with a large deviation will be assigned a small weight in the next iteration and its contribution to the solution can be minimised.

Filtering approach

Apart from the modelling approach, the APS and geometric errors can be mitigated by filtering as they share low spatial frequency characteristics (Crosetto et al., 2014a, b). In this study, the filtering of low-frequency atmospheric and geometric phase errors refers to the approach proposed by Hooper et al. (2007), namely a band-pass filter combined with a low-pass filter is applied in the frequency domain.

Simulation results

Synthetic data was used to validate the modelling and filtering approaches for the combined correction of atmospheric, geometric, and topographic errors. The simulation was based on the three types of topography with the additional repositioning Errors-I. Surface displacements along the LOS direction were simulated as a diffuse deformation model within a circular area. The displacement reached the largest magnitude of -5 mm at the centre and decreased gradually

to zero at the margin of this area. Details of the APS was given in Section 2.3.5. The dimensions of the simulated images were 999×313 pixels (i.e. 999 pixels in range and 313 in azimuth). Figure 6.11 displays the common displacement map and different APS maps for the three types of topography.

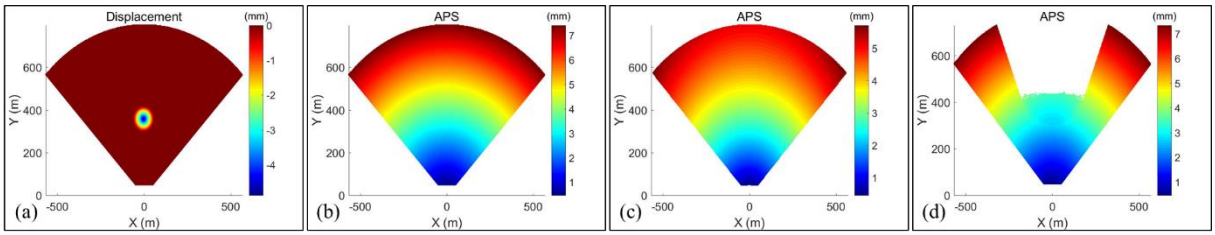

Figure 6.11. Simulation of deformation and APS. (a) The common displacement map for all the three types of topography. (b) APS map for flat topography. (c) APS map for slope topography. (d) APS map for dome topography.

Both the modelling and filtering approaches were used to remove APS and repositioning errors and then extract the deformation signal. In the modelling approach, only one percent of points that were evenly distributed in space and outside the deformation area were used to recover the model in Equation (6.5). In the band-pass filtering approach, the interferometric phase (complex number) was firstly transformed from the spatial domain to the frequency domain using a two-dimensional fast Fourier transform (2D FFT) with a typical grid size of 64×64 cells. The intensity of the 2D FFT was then smoothed with a 7×7 Gaussian convolution filter. Low-frequency errors were finally removed by a 5^{th}-order Butterworth filter with a cut-off wavelength of 100 cells. The results are shown in Figure 6.12 and the statistics of the displacement residuals are summarised in Table 6.3.

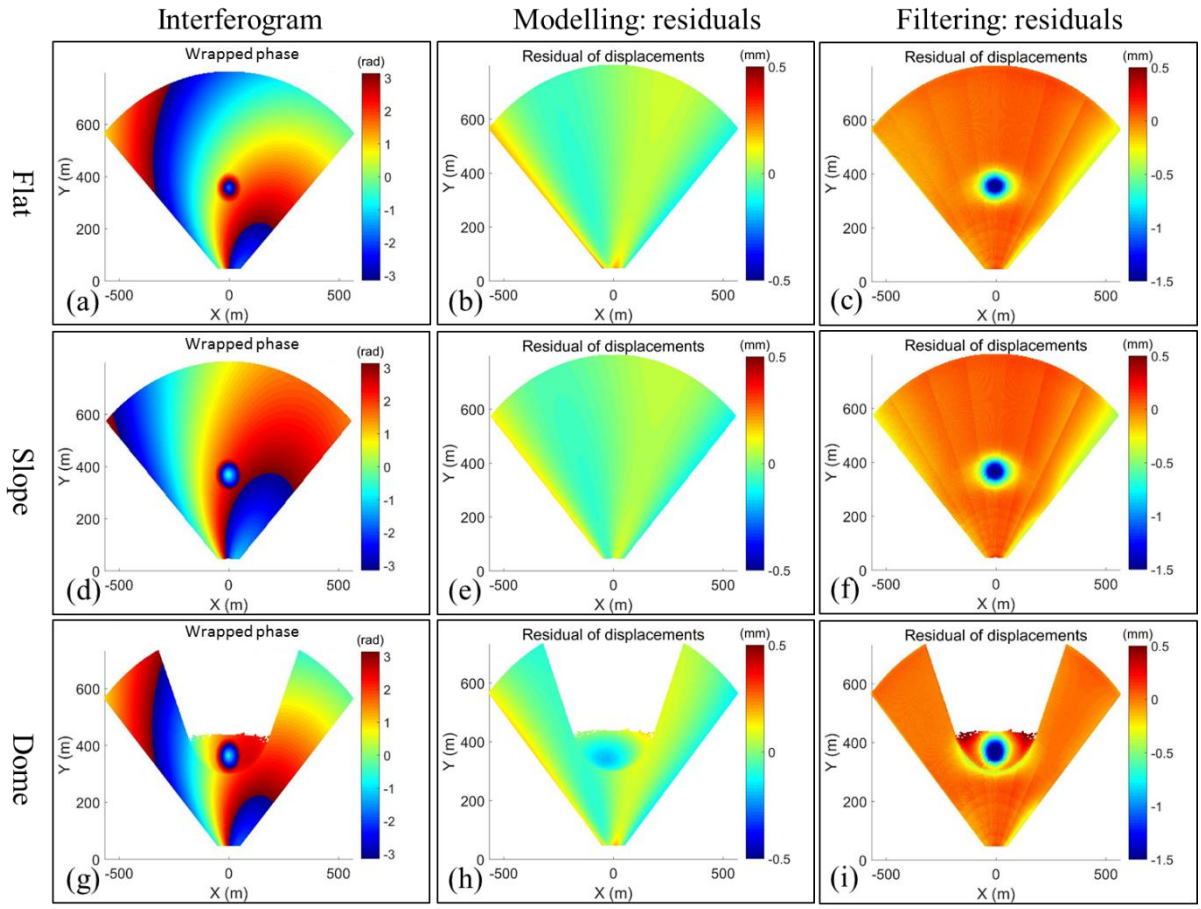

Figure 6.12. Simulation and separation of deformation from APS, geometric and topographic errors (Errors-I).

Table 6.3 . Statistics of separation of deformation from APS and repositioning errors.

Topography	Error	Modelling		Filtering	
		RMS of displacement residuals	Max of displacement residuals	RMS of displacement residuals	Max of displacement residuals
Flat	I	0.07 mm	0.27 mm	0.17 mm	1.78 mm
Slope	I	0.05 mm	0.14 mm	0.19 mm	1.83 mm
Dome	I	0.06 mm	0.19 mm	0.20 mm	1.97 mm

As shown in Figure 6.12, displacement residuals in the filtering approach for all three topography types are much greater than those in the modelling approach, which is also evidenced in Table 6.3. Smaller residuals imply better accuracy for surface displacements. Therefore, the modelling approach outperformed the filtering approach in the simulation. The maximum displacement residual in the filtering approach was 6.6 – 10.1 times greater than that

of the modelling approach.

6.3 Experimental results with real-world GBSAR data

To validate the proposed discontinuous GBSAR processing approach, experiments were conducted using a real-world FastGBSAR dataset acquired in discontinuous mode. The dataset was collected by observing the southern hillside of Tynemouth Priory and Castle, Tynemouth, UK. Two campaigns were performed at the same site. Each campaign consisted of 30 SLC images with a temporal resolution of 10 seconds and a spatial resolution of 0.75 m × 5 mrad. Concrete blocks were used as the FastGBSAR monitoring station. The radar system was taken away from the concrete base after the first campaign and then repositioned in the subsequent campaign. Simple marks were made onto the top of the concrete blocks in order to install the radar precisely and minimise repositioning errors. The radar system and the observing hillside were scanned by using a Leica P40 laser scanner (https://leica-geosystems.com/en-gb/products/laser-scanners/scanners/leica-scanstation-p40--p30). In this case, the topography was linked to GBSAR by transferring the point cloud of the hillside to the GBSAR image coordinate system. An overview of the data collection and the topography in this case study is illustrated in Figure 6.13.

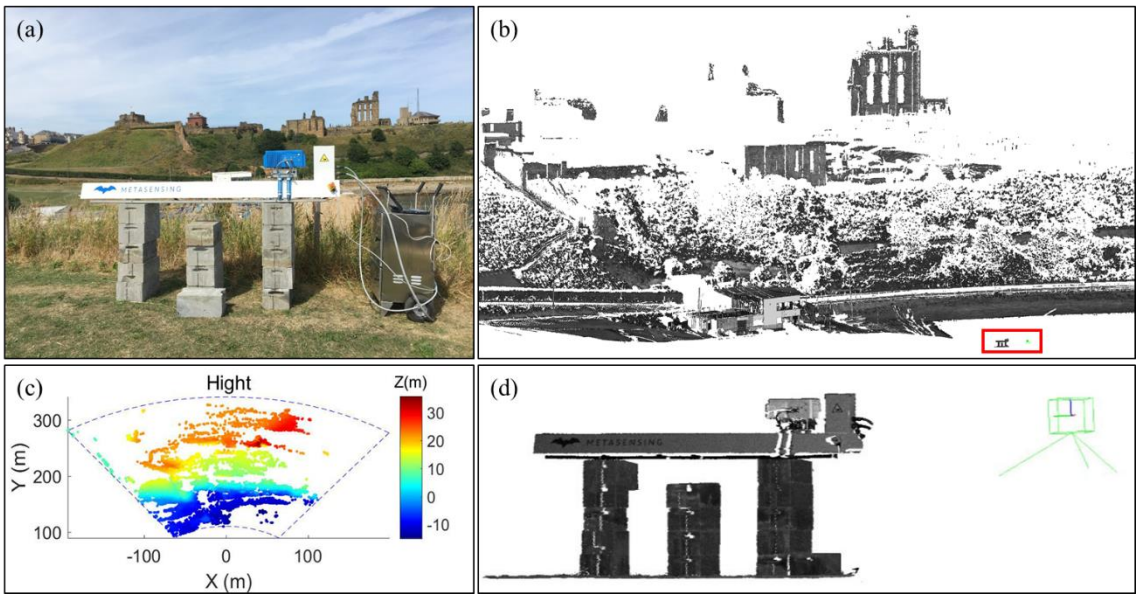

Figure 6.13. Overview of the case study. (a) Deployment of the FastGBSAR system. (b) Point cloud of the radar system and the observing hillside. (c) Height in the GBSAR coordinate system. (d) A close-up of the FastGBSAR and the laser scanner geometry, corresponding to the area in the red box of subfigure (b).

This FastGBSAR dataset was processed with the MC-GBSAR chain using the modelling

approach for the correction of APS and geometric errors. The temporally averaged image of the first campaign was named as “145219” and that of the second was “165024”. The time difference between the two averaged images was approximately two hours. Figure 6.12 shows the interferogram and coherence between the two averaged images, as well as the estimated low-frequency errors (APS and repositioning errors) and displacements. The results achieved by the procedure, both with and without co-registration processing, are given for comparison purposes.

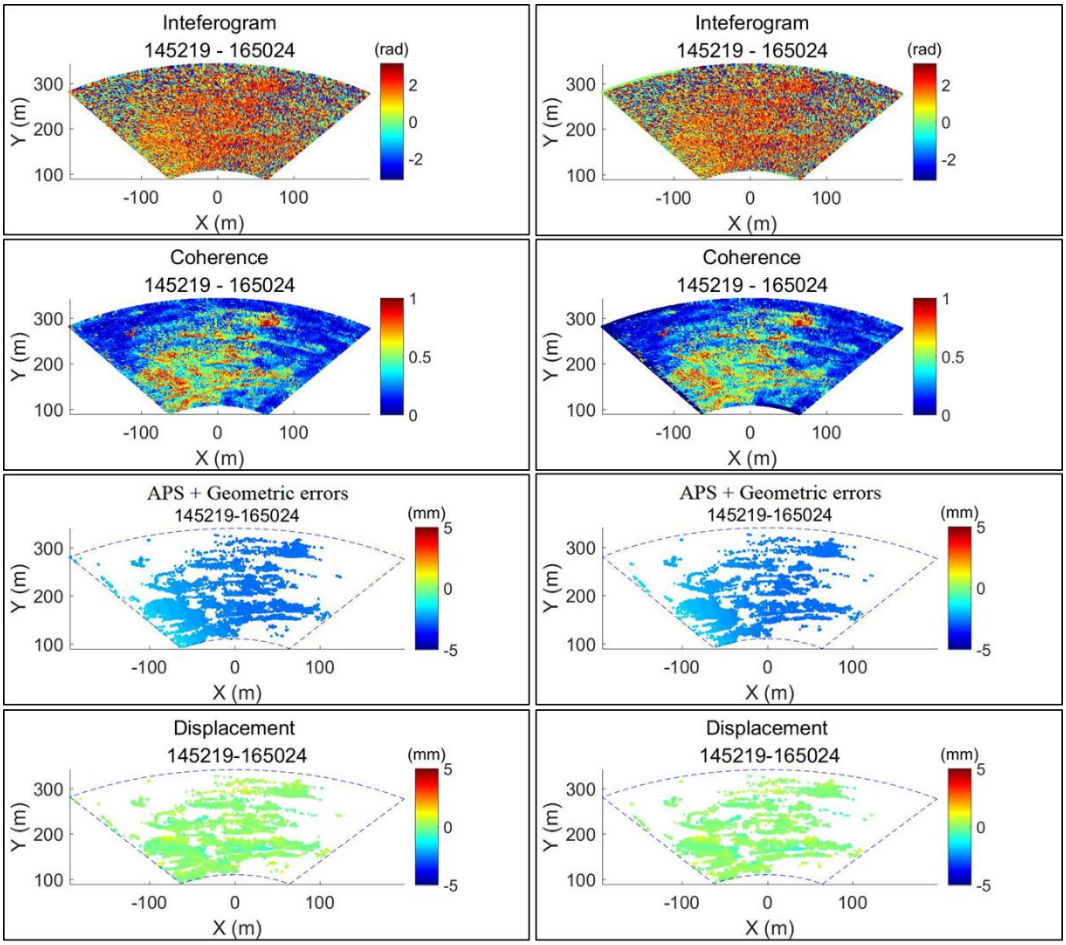

Figure 6.14. The results achieved by the MC-GBSAR using the modelling approach for the correction of APS and geometric errors.

As can be seen in Figure 6.14, the results with respect to the two situations are consistent with each other, coherence is retained and no phase ramps can be seen from the interferograms, which means that the image shift due to repositioning errors was not significant in this case. Finally, no significant deformation is detected in the hillside over the 2-hour observation period.

6.4 Discussion

Experiments have been conducted using both synthetic and real-world GBSAR datasets in this study. Both moderate and considerable repositioning errors have been investigated in experiments. Based on these experiments, it is observed that greater repositioning errors lead to greater residuals and less reliable displacements. Therefore, in any multi-epoch campaign, the installation of the GBSAR instrument should be replicated as precisely as possible for accurate interferometric measurement. In other words, repositioning errors should be kept as small as possible. The proposed MC-GBSAR chain offers two approaches for the correction of APS and repositioning errors, either through modelling or filtering. The modelling approach produced better results than filtering, based on the synthetic data results in this study.

In addition, highly-coherent pixels from unstable areas carrying unknown displacements may be selected for modelling, which can lead to a biased estimation of APS and repositioning errors. To mitigate the inaccuracies contributed by these pixels, an IRLS algorithm has been implemented. The IRLS estimation is an iterative process: the more that a pixel deviates from the estimated model, the smaller its weight will be in the following iteration. Thus, the weight for a pixel that is carrying deformation but accidently selected for modelling will decrease gradually in the ILRS estimation. An analysis was conducted based on the synthetic data together with repositioning Errors-I (introduced in Section 6.2.5). One percent of pixels were used to estimate the model for the correction of APS and geometric errors, these pixels were evenly distributed in space (including the deformation area). Some pixels were thus selected from the deformation area. Figure 6.15 shows the RMS and maximum of displacement residuals decreasing with the number of iterations, which converges after a very limited number of iterations. This suggests the feasibility of the IRLS estimation for modelling in the presence of some pixels that are selected from unstable areas.

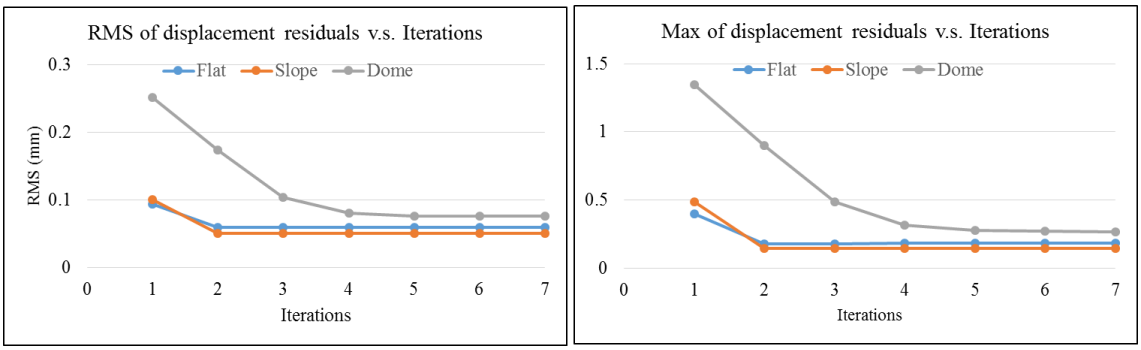

Figure 6.15. The RMS and maximum of displacement residuals for the synthetic data together with additional repositioning Errors-I.

6.5 Summary

This chapter has reported a new interferometric processing chain, MC-GBSAR, that has been developed for discontinuous GBSAR deformation monitoring. Automatic co-registration of GBSAR images has been implemented through the feature matching of amplitude images and integrated into this processing procedure. A sub-pixel co-registration precision can be achieved. The additional phase component due to repositioning errors was further identified as geometric and topographic phase errors. The geometric phase error ramps have been removed by recovering a polynomial function of the range and azimuth image coordinates. Topographic phase errors can be corrected in the case of an unknown spatial baseline. The approach therefore overcomes the practical difficulty of measuring the precise position and orientation of a linear GBSAR system.

A new model has been proposed for the combined correction of atmospheric, geometric and topographic phase errors in a single step. Simulations have shown that the proposed model outperformed the traditional filtering approach. The maximum displacement residual of the filtering was 6.6 – 10.1 times greater than that of the proposed model over different types of topography.

Experiments using both synthetic and real-world GBSAR data have demonstrated the feasibility of the proposed MC-GBSAR chain for measuring deformation between discontinuous campaigns. In addition, advanced InSAR algorithms presented in previous chapters, including adaptive coherence estimation, non-local filtering, and selection of (partially) coherent pixels, have been integrated into the MC-GBSAR chain, creating a unique and complementary tool to the RT-GBSAR chain for a comprehensive GBSAR interferometry processing framework. MC-GBSAR, together with RT-GBSAR, facilitates a range of engineering and environmental deformation monitoring applications to which GBSAR is potentially suited.

It is worth highlighting that zero-baseline geometry is strongly recommended during data collection as it ensures the optimal performance of GBSAR interferometry. In cases where the zero-baseline cannot be achieved, moderate technical effort is still encouraged to minimise the repositioning errors as much as possible for deformation monitoring purposes.

Chapter 7. Conclusions

7.1 Contributions of this research

The goal of this research was to design and develop a framework to effectively utilise GBSAR interferometry for deformation monitoring applications. A range of aspects of GBSAR interferometry has been involved. This section summarises the main research outcomes from this project, as follows:

1. Non-local "MIAS" method.

A simple but efficient similarity measure has been presented to identify resembling pixels for distributed scatterers, together with a comprehensive non-local "MIAS" method based upon this concept, which is able to accurately estimate coherence and interferometric phase. "MIAS" can largely mitigate the coherence estimation bias and avoid overestimating the decorrelated area without the cost of the spatial resolution.

2. Selection of (partially) coherent pixels.

A full-rank criterion for the selection of coherent pixels from a redundant network of interferograms has been developed, which enables the selection of not only qualified partially coherent pixels, but also all persistent scatterers. The proposed method makes the most of redundant observations and allows an adjustment to obtain a reliable value for the unknown. Finally, a reliable solution can be achieved in the InSAR time series analysis.

3. RT-GBSAR.

A novel processing chain (i.e. RT-GBSAR) for continuous GBSAR deformation monitoring has been demonstrated on the basis of the SBAS time series concept. The SBAS procedure in RT-GBSAR integrates the non-local "MIAS" method and the presented coherent pixel selection approach. RT-GBSAR processes continuous GBSAR images on a unit by unit basis. Significant issues in processing continuous GBSAR data (including the delay of displacement maps, the extreme cost of computational memory, and the loss of temporal evolution in the simultaneous processing of all data together) have been addressed by the proposed RT-GBSAR chain with three notable features: (i) low requirement of computational memory; (ii) insights into the temporal evolution of surface movements through temporally-coherent pixels; and (iii) real-

time capability for processing an infinite number of images.

4. MC-GBSAR.

A new interferometric processing chain (i.e. MC-GBSAR) has been proposed for discontinuous GBSAR deformation monitoring, in which repositioning errors often occur in repeated campaigns and cause inaccuracies in interferometric observations. In this processing chain, GBSAR imagery can be automatically co-registered through amplitude-based feature matching with sub-pixel precision. By analysing the characteristics and effects of the typical errors (including atmospheric and repositioning errors) in GBSAR interferometry from its fundamental geometry, a new model has been developed and integrated into this chain for the combined correction of these errors. Based on experiments using both synthetic and real-world GBSAR data, it was found that greater repositioning errors always lead to less reliable displacement determination. With moderate effort in hardware deployment, the MC-GBSAR chain will potentially facilitate a range of deformation monitoring applications, especially in slow-changing scenarios. The MC-GBSAR chain can be a complementary tool to the RT-GBSAR chain for processing GBSAR data collected from all operation modes.

5. Deformation monitoring applications.

The presented algorithms and processing chains have been fully implemented and integrated into an in-house GBSAR data processing package (see Appendix B), making it a versatile tool for GBSAR deformation monitoring. Using this package, four deformation monitoring applications have been undertaken, including three continuous (a dune, a bridge, and a coastal cliff) and one discontinuous (a hillside) scenarios. The results were verified quantitatively via a defined precision indicator for the time series estimation and validated qualitatively via a priori knowledge of these observing sites. These successful applications have demonstrated the feasibility and effectiveness of the presented algorithms and chains for reliable, high-precision GBSAR deformation monitoring.

In the application of monitoring a fast-changing sand dune, observed movement took place only in areas devoid of vegetation while the area with sparse vegetation coverage remained stable over a short observing period of 1 hour 20 minutes, which suggests that the preservation of vegetation in the dune area plays an important role in stabilising the surface against sand motion.

The application of monitoring the Queen Elizabeth II Metro Bridge showed that the bridge

superstructure vibrated with a few millimetres of deflection when a train crossed it. It presents the feasibility of GBSAR interferometry for measuring rapid structural deformation.

In the application of monitoring the cliff on the north side of Tynemouth Priory and Castle, displacement maps reveal deformation signals only at locations near the sea. Time-series displacements, cumulative displacement maps, and relevant analysis suggest that the triggering of ground deformation is related to sea tides.

In the discontinuous monitoring of the southern hillside of Tynemouth Priory and Castle, two GBSAR campaigns were processed by the MC-GBSAR chain with and without co-registration processing, using both modelling and filtering approaches for the correction of atmospheric and geometric errors. The achieved results with respect to the two situations were consistent with each other. Finally, no significant movement was detected on the hillside over the observing period of two hours, presenting an anticipated result.

On the basis of these successful applications, it is fair to conclude that the research outcomes from this project will facilitate a range of deformation monitoring applications to which GBSAR is potentially suited.

7.2 Revisiting research objectives

This research aimed *to design and develop a framework to effectively utilise GBSAR interferometry for deformation monitoring applications*. The research emphasizes the performance of InSAR techniques in terms of accuracy, robustness, and real-time capability. The aim has been achieved through the accomplishment of the original four objectives as follows:

1. To evaluate the suitability and, where necessary, make necessary improvement to current fundamental InSAR techniques and advanced time series analysis algorithms for processing GBSAR imagery.

This has been addressed in Chapters 3 and 4, corresponding to research outcomes 1, 2 and 4 (in part). The non-local “MIAS” method overcomes the limitations in the conventional algorithms and achieves accurate coherence estimation and phase filtering. The new approach to selecting coherent pixels based on the full-rank criterion is able to maximise the density of selected pixels and optimise the reliability of GBSAR time series analysis by making the most of coherent

phase redundancies. The atmospheric and repositioning errors in GBSAR interferometry have been investigated and a new model has been proposed for the correction of these errors.

2. To develop a (near-) real-time processing procedure with high degree of automation for a current FastGBSAR instrument to minimise delay after each data acquisition and to maximise the precision and reliability of the output deformation maps.

This has been addressed in Chapter 5, corresponding to research outcome 3: the novel RT-GBSAR processing chain for continuous GBSAR deformation monitoring. The real-time capability of RT-GBSAR was evaluated in Chapter 5 and successful applications have demonstrated that sub-millimetre measurement precision can be achieved in the time series estimation aspects of the RT-GBSAR chain.

3. To develop a discontinuous GBSAR procedure as a complementary module to the continuous pipeline for a complete GBSAR interferometry framework.

This has been addressed in Chapter 6, corresponding to research outcome 4: a new interferometric processing chain, MC-GBSAR, for discontinuous GBSAR deformation monitoring. MC-GBSAR has integrated the automatic co-registration of GBSAR images and the correction of atmospheric and repositioning errors between repeated campaigns. With moderate effort on hardware deployment in practice, MC-GBSAR can be a complementary tool to RT-GBSAR for a complete GBSAR interferometry framework.

4. To establish case studies to demonstrate the feasibility of the developed GBSAR data processing software system for a range of deformation monitoring applications to which GBSAR is suited.

Multiple applications have been completed in Chapters 4, 5, and 6. A summary of these applications is given in research outcome 5.

7.3 Recommendations for future research and applications

This research has involved a range of aspects of GBSAR interferometry and produced a complete in-house software package (see Appendix B) for deformation monitoring. Additional research effort is now needed to further improve the performance of the developed package and exploit its value in geohazard monitoring and structural deformation surveying. The following work could be considered to add value in the future.

1. Automatic correction of phase unwrapping errors

The detection of phase unwrapping errors has been integrated into the developed package. However, the automatic correction of unwrapping errors has not been achieved, and would represent a valuable topic for future work. Although several previous studies in both spaceborne and ground-based SAR (e.g. Biggs et al., 2007; Crosetto et al., 2011; López-Quiroz et al., 2009; Monserrat et al., 2009; Zhao et al., 2016) attempted to address this issue, these approaches perform pixel-wise correction of unwrapping errors in post-processing, and generally require visual inspection (Biggs et al., 2007). Unwrapping errors usually present regional patterns (Biggs et al., 2007), and the accurate identification of regional unwrapping errors is required. In the case that unwrapping errors are detected, RT-GBSAR requires the fully automatic correction of unwrapping errors to be achieved in real time.

2. Graphical processing unit (GPU) acceleration

The whole data processing package has been developed using MATLAB release 2016b (The MathWorks, Inc.), with some code converted into C++. The entire program is currently based on central processing unit computation. To meet the increasing requirements associated with the advancement of GBSAR hardware, especially the ground-based MIMO radar (or MIMO-SAR) which is potentially capable of generating a number of images per second, the real-time capability of this package should be enhanced, possibly via high-performance computational techniques such as GPU acceleration (e.g. Reza et al., 2018; Zhang et al., 2014).

3. 1D (LOS) measurements to 3D measurements

Like other InSAR techniques, GBSAR interferometry provides 1D surface displacements along the LOS direction. In comparison to 3D measurements, 1D LOS displacements may be insufficient to interpret some of the processes behind observations (e.g. Caduff et al., 2015; Kristensen et al., 2013). To achieve 3D measurements, GBSAR observation can be performed from multiple stations, which is similar to the concept of multiple geometries in spaceborne InSAR (e.g. Hu et al., 2012; Wright et al., 2004). Alternative strategies could include prior knowledge (or assumption) about the displacement direction (Caduff et al., 2015) and integration with other measurements, such as GNSS, TLS, and spaceborne InSAR (e.g. Bardi et al., 2016; Kristensen et al., 2013; Rödelsperger et al., 2010).

4. Long-term deformation monitoring

Although all of the applications presented in this research are short-term cases, the developed software package is actually ready for both short- and long-term deformation monitoring applications. Long-term monitoring cases may require extra effort in hardware deployment and management. In terms of data acquisition, it can be carried out through long-term continuous operation or multi-campaign discontinuous operation. Data acquisition in any operation mode can be processed by the developed package together with RT-GBSAR and MC-GBSAR chains. It should be noted that in the long-term monitoring of a natural slope with thick vegetation coverage, temporal decorrelations can be serious, thus constraining the feasibility of GBSAR interferometric measurement. The use of corner reflectors may be beneficial in such cases (Crosetto et al., 2014a).

5. Early warning systems for landslides and infrastructure failures

Early warning systems work as risk mitigation tools by calling for actions in specific circumstances and in areas where hazard risk goes beyond a tolerable level (Calvello, 2017). Apart from monitoring, an efficient landslide early warning system also comprises analysis and forecasting, warning, and response elements (Intrieri et al., 2012). GBSAR interferometry has been increasingly adopted to implement landslide early warning systems (e.g. Atzeni et al., 2015; Casagli et al., 2010; Intrieri et al., 2012). Future effort should be made on combining the proposed GBSAR interferometric framework with appropriate forecasting, warning, and response to implement a more effective landslide early warning system. In addition, future work also includes exploiting the GBSAR monitoring of structural deformation for dams, levees, embankments, and other infrastructure, in order to effectively analyse abnormal behaviour that may threaten the safety of the structures, implement maintenance and remedial measures, and predict potential failures.

Appendix A: Inversion precision

The goal of InSAR time series analysis for deformation monitoring is to obtain the deformation time series. The mean velocity between time-adjacent acquisitions is a preferred choice in InSAR time series analysis to avoid large discontinuities in cumulative deformations and to obtain a physically sound solution (e.g. Berardino et al., 2002; Li et al., 2009). Accordingly, the prerequisite is to obtain the incremental time series of phase change between time-adjacent acquisitions. We assume a redundant network of L interferograms formed by *N* SLC images. Each pixel is associated with a system in the following matrix representation:

$$\mathbf{B}_{L\times N}\,\mathbf{\Phi}_{N\times 1} = \boldsymbol{\delta\Phi}_{L\times 1} + \boldsymbol{\varepsilon}_{L\times 1}, \tag{A.1}$$

where $\mathbf{B}$ is the coefficient matrix; $\mathbf{\Phi}$ is the matrix containing the incremental time series of phase change with respect to the superposition of both displacement and atmospheric variation; $\boldsymbol{\delta\Phi}$ is the matrix of redundant unwrapped interferometric phase; $\boldsymbol{\varepsilon}$ is the noise matrix. With redundant interferometric phase, the optimal estimation of the incremental time series of phase change $\widehat{\mathbf{\Phi}}$ for each pixel can be performed based on equation (A.1) via any appropriate solvers (e.g. singular value decomposition, normal least squares). The phase residuals in the inversion are:

$$\mathbf{V}_{L\times 1} = \mathbf{B}_{L\times N}\,\widehat{\mathbf{\Phi}}_{N\times 1} - \boldsymbol{\delta\Phi}_{L\times 1}. \tag{A.2}$$

The root mean square of phase residuals for a pixel is:

$$\sigma_0 = \sqrt{\frac{\mathbf{V}^{\mathrm{T}}\mathbf{V}}{r}} = \sqrt{\frac{\mathbf{V}^{\mathrm{T}}\mathbf{V}}{n-N+1}}, \tag{A.3}$$

where r is the number of redundancies and n is the number of coherence occurrences in the redundant network. Accordingly, the covariance matrix of the estimated $\widehat{\mathbf{\Phi}}_{N\times 1}$ can be calculated by:

$$\mathrm{D}_{\widehat{\mathbf{\Phi}}\widehat{\mathbf{\Phi}}} = \sigma_0\sqrt{(\mathbf{B}^{\mathrm{T}}\mathbf{B})^{-1}}. \tag{A.4}$$

As the final cumulative displacement is obtained by removing atmospheric variation from the sum of them, we introduce an estimator $\hat{d}$ which is the sum of the cumulative displacement and atmospheric variation between the first image and the last image:

$$\hat{d} = -\frac{\lambda}{4\pi}\sum_{k=0}^{N-1}\left(\hat{\varphi}_{t_k t_{k+1}}^{dis} + \hat{\varphi}_{t_k t_{k+1}}^{atm}\right) = \mathbf{F}_{1\times N}\hat{\mathbf{\Phi}}_{N\times 1}, \tag{A.5}$$

where $\mathbf{F} = [-\lambda/4\pi \quad \cdots \quad -\lambda/4\pi]$. The theoretical precision of $\hat{\mathrm{d}}$ is used as the precision indicator in the estimation for each pixel, which is calculated by:

$$\sigma_{\hat{d}\hat{d}} = \sqrt{\mathrm{D}_{\hat{d}\hat{d}}} = \sqrt{\mathbf{F}\mathrm{D}_{\hat{\mathbf{\Phi}}\hat{\mathbf{\Phi}}}\mathbf{F}^{\mathrm{T}}}. \tag{A.6}$$

Appendix B: Ground-based Synthetic Aperture Radar Interferometry Software (GBSAR-InS)

Ground-based Synthetic Aperture Radar Interferometry Software (GBSAR-InS) is a GBSAR data processing software package for deformation monitoring developed by the author. The relevant InSAR algorithms, processing strategies described in this thesis have been implemented and integrated into GBSAR-InS. The software package is able to process GBSAR data acquired in any operation modes and therefore supports both continuous and discontinuous GBSAR monitoring, and it was used to generate the results shown in this thesis. The notable features of GBSAR-InS are highlighted as follows:

(1) A fully automatic chain, RT-GBSAR presented in Chapter 5, has been developed and integrated into GBSAR-InS for the (near-) real-time processing of continuous GBSAR data. RT-GBSAR possesses three features: (i) low requirement of computational memory; (ii) insights into the temporal evolution of surface movements through temporally-coherent pixels; and (iii) (near-) real-time capability of processing an infinite number of images.

(2) Another fully automatic chain, MC-GBSAR presented in Chapter 6, has been developed and integrated into GBSAR-InS for processing discontinuous multi-campaign GBSAR data. In MC-GBSAR, (i) images from different campaigns with repositioning errors can be automatically co-registered; and (ii) atmospheric, geometric, and topographic errors can be corrected in a single step without any additional materials or *a-priori* knowledge.

(3) GBSAR-InS uses advanced InSAR techniques in every processing step, including (i) the non-local "MIAS" method, presented in Chapter 3, for accurate coherence estimation and phase filtering; and (ii) the approach to selecting fully and partially coherent pixels, which is presented in Chapter 4.

(4) GBSAR-InS provides user interfaces for data management and data visualisation. The package is able to output cumulative displacement maps, deformation velocity maps, atmospheric and/or repositioning error maps between any two epochs, as well as the line graph of time-series displacement for every coherent pixel. It is also able to output precision maps and unwrapping error maps to assess the reliability of InSAR

time series analysis.

GBSAR-InS was developed based on Matlab release 2016b software. The data processing of GBSAR-InS starts with focused single-look complex images, and it uses SNAPHU (https://web.stanford.edu/group/radar/softwareandlinks/sw/snaphu/, accessed: 08 December, 2018) for 2D phase unwrapping and partial StaMPS unwrapping source codes (https://homepages.see.leeds.ac.uk/~earahoo/stamps/, accessed on 08 December, 2018) for 3D phase unwrapping. Using the continuous GBSAR dataset (i.e. Dataset I), Figures B.1 to B.6 show the key user interfaces and outputs of GBSAR-InS.

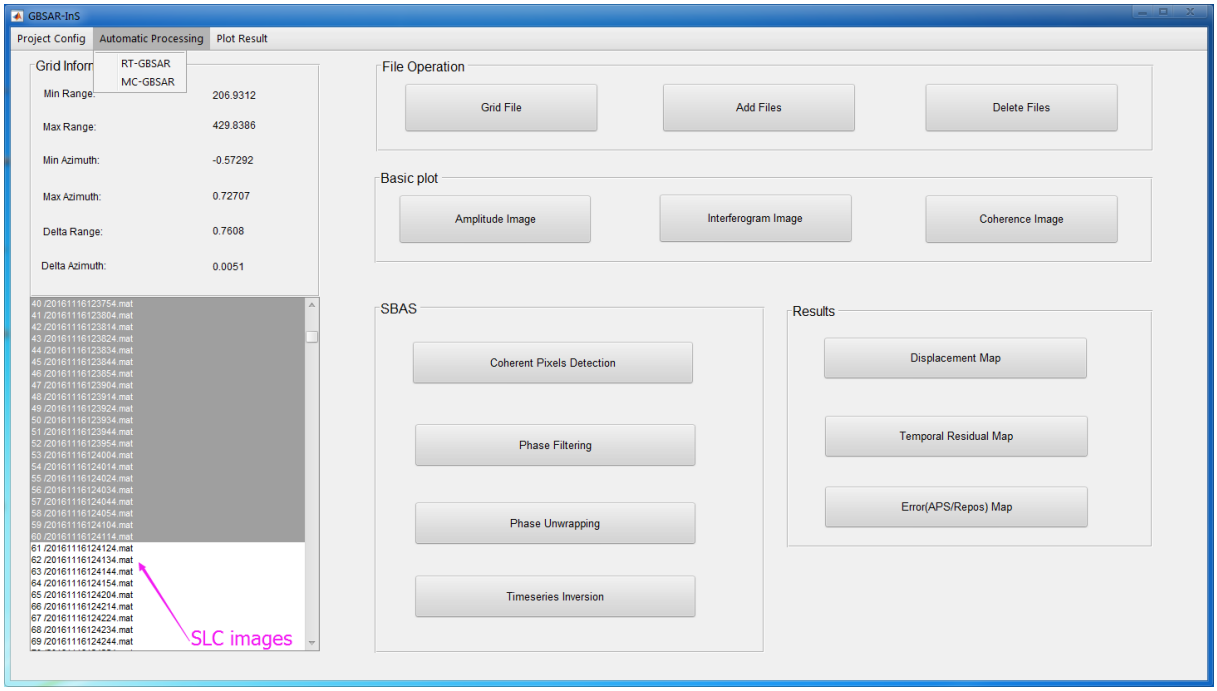

Figure B.1. The main user interface of GBSAR-InS.

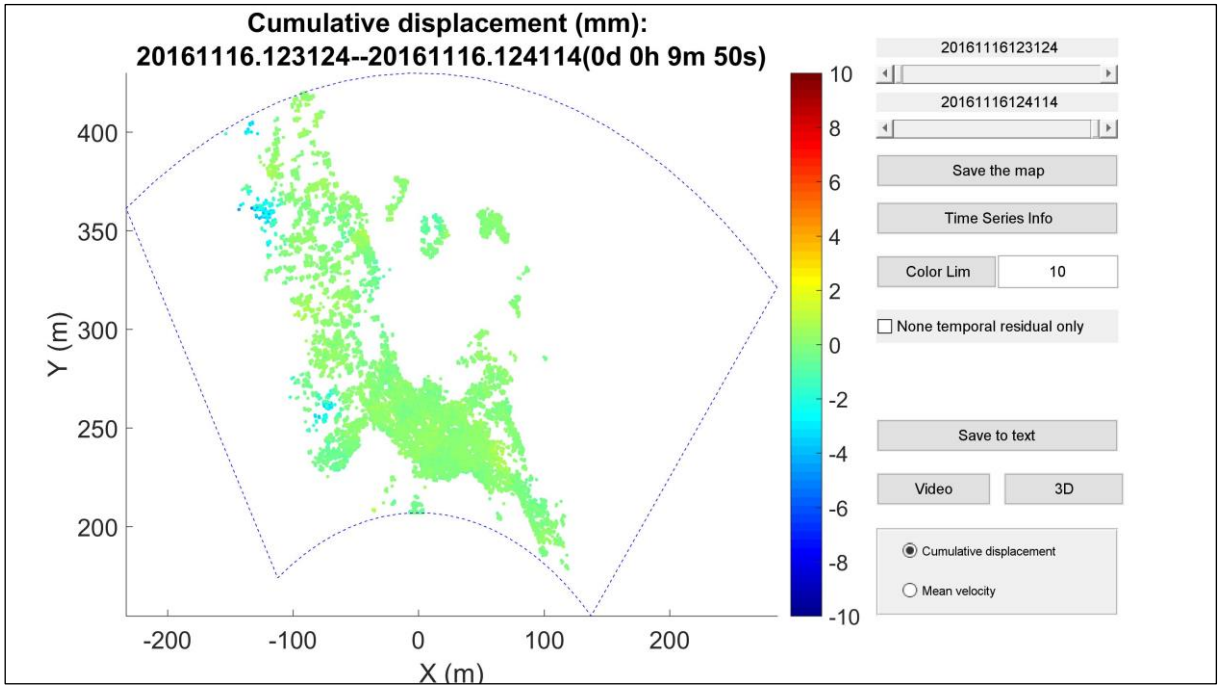

Figure B.2. The user interface for cumulative displacement map plotting.

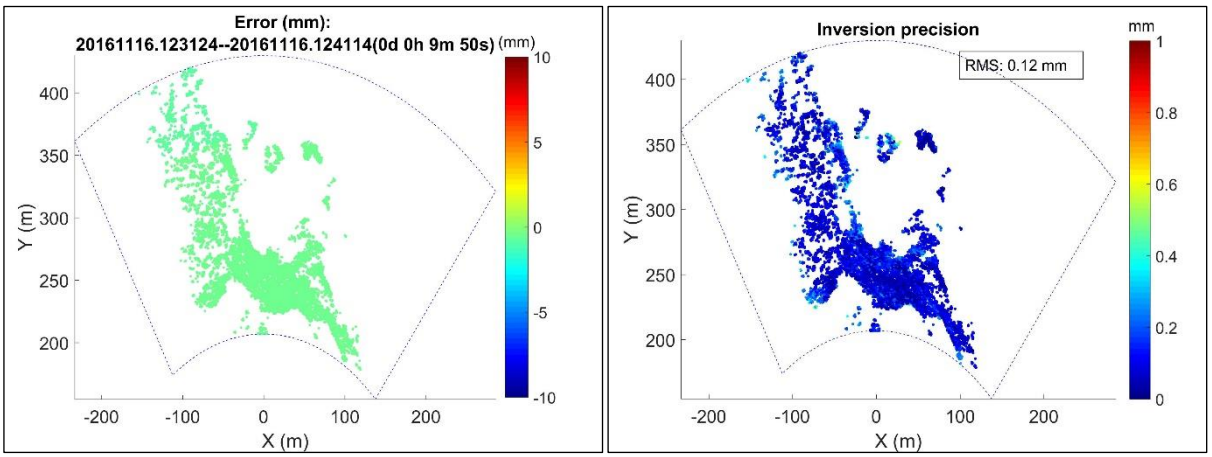

Figure B.3. Error map (APS map in this case) and inversion precision map.

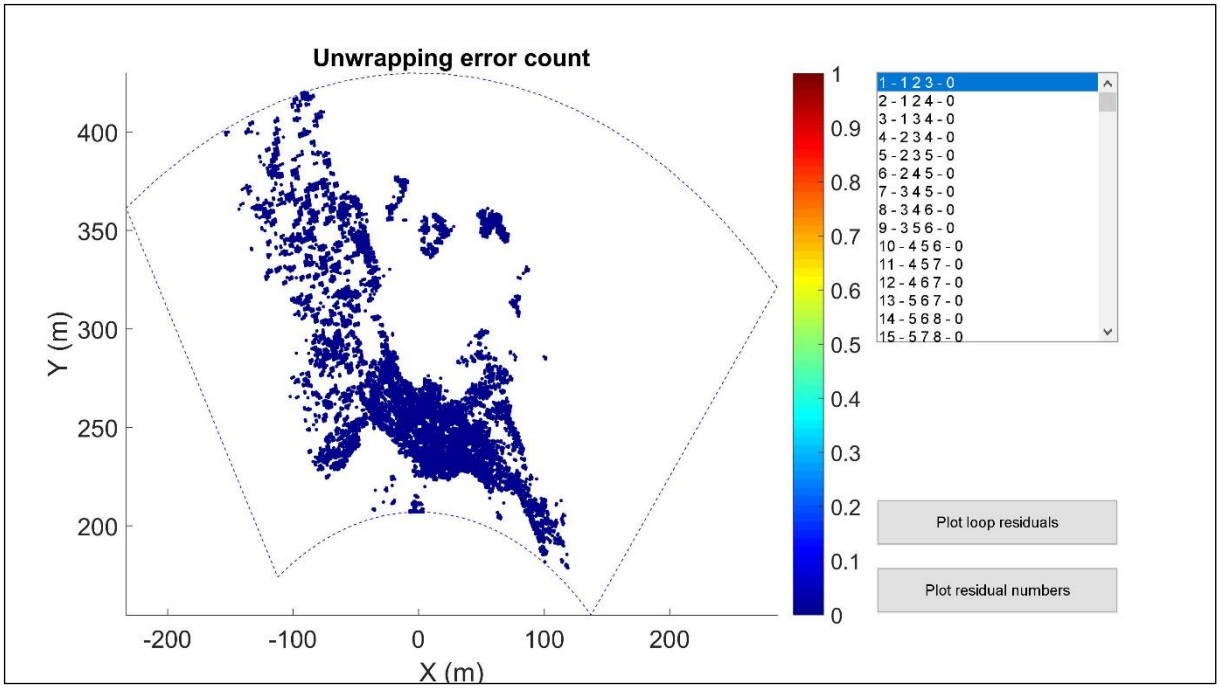

Figure B.4. The user interface for examining phase unwrapping errors.

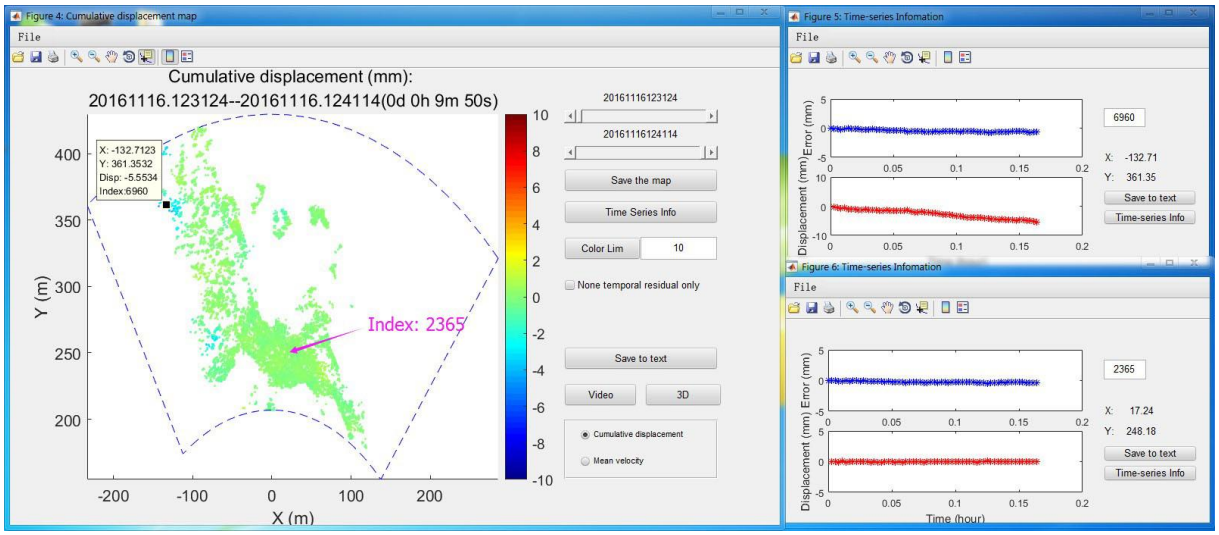

Figure B.5. Cumulative displacement map (the left one) and line graphs of displacement and error time series (the right two).

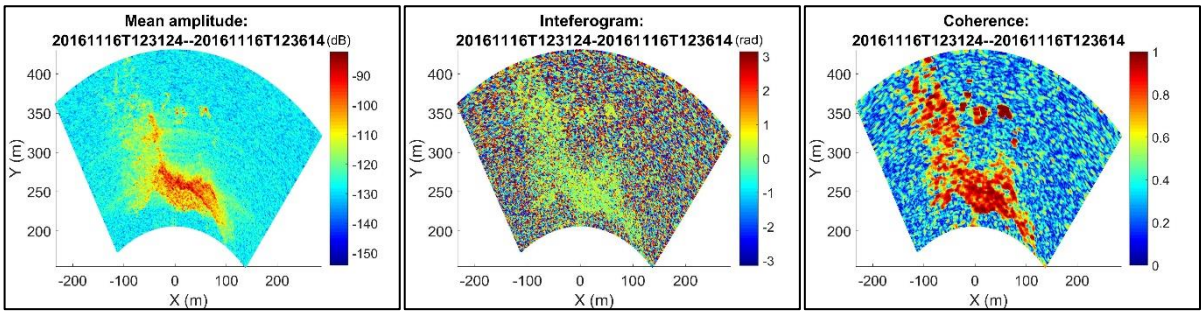

Figure B.6. Basic plots: (mean) amplitude, interferogram, and coherence maps.

References

Abdelfattah, R., Nicolas, J.-M., 2006. Interferometric SAR coherence magnitude estimation using second kind statistics. IEEE Transactions on Geoscience and Remote Sensing 44, 1942-1953.

Abellán, A., Oppikofer, T., Jaboyedoff, M., Rosser, N.J., Lim, M., Lato, M.J., 2014. Terrestrial laser scanning of rock slope instabilities. Earth Surface Processes And Landforms 39, 80-97.

Adam, N., Kampes, B., Eineder, M., 2005. Development of a scientific permanent scatterer system: Modifications for mixed ERS/ENVISAT time series, Envisat & ERS Symposium, 572, id.73.1.

Agliardi, F., Crosta, G., Meloni, F., Valle, C., Rivolta, C., 2013. Structurally-controlled instability, damage and slope failure in a porphyry rock mass. Tectonophysics 605, 34-47.

Agram, P.S., Zebker, H.A., 2009. Sparse two-dimensional phase unwrapping using regular-grid methods. IEEE Geoscience and Remote Sensing Letters 6, 327-331.

Antonello, G., Casagli, N., Farina, P., Leva, D., Nico, G., Sieber, A., Tarchi, D., 2004. Ground-based SAR interferometry for monitoring mass movements. Landslides 1, 21-28.

Aria, D.D., Falcone, P., Maggi, L., Amoroso, G., 2018. Advanced calibration techniques for MIMO radar, EUSAR 2018; 12th European Conference on Synthetic Aperture Radar, 1-5.

Atzeni, C., Barla, M., Pieraccini, M., Antolini, F., 2015. Early warning monitoring of natural and engineered slopes with ground-based synthetic-aperture radar. Rock Mechanics and Rock Engineering 48, 235-246.

Bamler, R., Hartl, P., 1998. Synthetic aperture radar interferometry. Inverse problems 14, R1.

Baran, I., Stewart, M.P., Kampes, B.M., Perski, Z., Lilly, P., 2003. A modification to the Goldstein radar interferogram filter. IEEE Transactions on Geoscience and Remote Sensing 41, 2114-2118.

Barbarella, M., Fiani, M., Lugli, A., 2015. Multi-temporal terrestrial laser scanning survey of a landslide, Modern Technologies for Landslide Monitoring and Prediction. Springer, 89-121.

Bardi, F., Raspini, F., Ciampalini, A., Kristensen, L., Rouyet, L., Lauknes, T.R., Frauenfelder, R., Casagli, N., 2016. Space-borne and ground-Based InSAR data integration: the Åknes test site. Remote Sensing 8, 237.

Barla, M., Antolini, F., Bertolo, D., Thuegaz, P., D'Aria, D., Amoroso, G., 2017. Remote monitoring of the Comba Citrin landslide using discontinuous GBInSAR campaigns. Engineering Geology 222, 111-123.

Barzaghi, R., Cazzaniga, N.E., De Gaetani, C.I., Pinto, L., Tornatore, V., 2018. Estimating and comparing dam deformation using classical and GNSS techniques. Sensors 18, 756.

Bay, H., Ess, A., Tuytelaars, T., Van Gool, L., 2008. Speeded-up robust features (SURF). Computer Vision And Image Understanding 110, 346-359.

Benoit, L., Briole, P., Martin, O., Thom, C., Malet, J.-P., Ulrich, P., 2015. Monitoring landslide displacements with the Geocube wireless network of low-cost GPS. Engineering Geology 195, 111-121.

Berardino, P., Fornaro, G., Lanari, R., Sansosti, E., 2002. A new algorithm for surface deformation monitoring based on small baseline differential SAR interferograms. IEEE Transactions on Geoscience and Remote Sensing 40, 2375-2383.

Berber, M., Ustun, A., Yetkin, M., 2012. Comparison of accuracy of GPS techniques. Measurement 45, 1742-1746.

Berry, R.M., 1976. History of geodetic leveling in the United States. American Congress on Surveying and Mapping.

Bert, M.K., 2006. Radar interferometry: persistent scatterers technique. The Netherlands: Springer.

BGS Landslides Team, 2018. Rainfall and landslide data for the UK, England, Scotland and Wales: updated monthly. Available at: https://www.bgs.ac.uk/landslides/landslidesAndRainfall.html (Accessed: 10 October, 2018)

Biggs, J., Wright, T., Lu, Z., Parsons, B., 2007. Multi-interferogram method for measuring interseismic deformation: Denali Fault, Alaska. Geophysical Journal International 170, 1165-1179.

Bioucas-Dias, J., Katkovnik, V., Astola, J., Egiazarian, K., 2008. Absolute phase estimation: adaptive local denoising and global unwrapping. Applied Optics 47, 5358-5369.

Bitelli, G., Bonsignore, F., Unguendoli, M., 2000. Levelling and GPS networks to monitor ground subsidence in the Southern Po Valley. Journal of Geodynamics 30, 355-369.

Blanco-Sanchez, P., Mallorquí, J.J., Duque, S., Monells, D., 2008. The coherent pixels technique (CPT): An advanced DInSAR technique for nonlinear deformation monitoring. Pure and Applied Geophysics 165, 1167-1193.

Borghi, A., Aoudia, A., Riva, R.E., Barzaghi, R., 2009. GPS monitoring and earthquake prediction: a success story towards a useful integration. Tectonophysics 465, 177-189.

Brimacombe, J., Macfie, A., McCrirrick, A., 1991. The extensometer: Potential applications in anaesthesia and intensive care. Anaesthesia 46, 756-761.

Buckland, J., Huntley, J., Turner, S., 1995. Unwrapping noisy phase maps by use of a minimum-cost-matching algorithm. Applied Optics 34, 5100-5108.

Butt, J., Wieser, A., Conzett, S., 2016. Intrinsic random functions for mitigation of atmospheric effects in ground based radar interferometry, Proc. of JISDM.

Caduff, R., Kos, A., Schlunegger, F., McArdell, B.W., Wiesmann, A., 2014. Terrestrial radar interferometric measurement of hillslope deformation and atmospheric disturbances in the Illgraben debris-flow catchment, Switzerland. IEEE Geoscience and Remote Sensing Letters 11, 434-438.

Caduff, R., Schlunegger, F., Kos, A., Wiesmann, A., 2015. A review of terrestrial radar interferometry for measuring surface change in the geosciences. Earth Surface Processes and Landforms 40, 208-228.

Cai, C., Gao, Y., Pan, L., Zhu, J., 2015. Precise point positioning with quad-constellations: GPS, BeiDou, GLONASS and Galileo. Advances in Space Research 56, 133-143.

Calvello, M., 2017. Early warning strategies to cope with landslide risk. Rivista Italiana di Geotecnica 2, 63-91.

Carballo, G.F., Fieguth, P.W., 2000. Probabilistic cost functions for network flow phase unwrapping. IEEE Transactions on Geoscience and Remote Sensing 38, 2192-2201.

Carlà, T., Farina, P., Intrieri, E., Ketizmen, H., Casagli, N., 2018. Integration of ground-based radar and satellite InSAR data for the analysis of an unexpected slope failure in an open-pit mine. Engineering Geology 235, 39-52.

Casagli, N., Catani, F., Del Ventisette, C., Luzi, G., 2010. Monitoring, prediction, and early warning using ground-based radar interferometry. Landslides 7, 291-301.

Casciati, F., Fuggini, C., 2011. Monitoring a steel building using GPS sensors. Smart Structures and Systems 7, 349-363.

Challis, J.H., 1995. A procedure for determining rigid body transformation parameters. Journal of Biomechanics 28, 733-737.

Chen, C.W., Zebker, H.A., 2000. Network approaches to two-dimensional phase unwrapping: intractability and two new algorithms. JOSA A 17, 401-414.

Chen, C.W., Zebker, H.A., 2001. Two-dimensional phase unwrapping with use of statistical models for cost functions in nonlinear optimization. JOSA A 18, 338-351.

Chen, C.W., Zebker, H.A., 2002. Phase unwrapping for large SAR interferograms: Statistical segmentation and generalized network models. IEEE Transactions on Geoscience and Remote Sensing 40, 1709-1719.

Chen, J., Dowman, I., Li, S., Li, Z., Madden, M., Mills, J., Paparoditis, N., Rottensteiner,

F., Sester, M., Toth, C., 2016. Information from imagery: ISPRS scientific vision and research agenda. ISPRS Journal of Photogrammetry and Remote Sensing 115, 3-21.

Ching, K.E., Hsieh, M.L., Johnson, K.M., Chen, K.H., Rau, R.J., Yang, M., 2011. Modern vertical deformation rates and mountain building in Taiwan from precise leveling and continuous GPS observations, 2000–2008. Journal of Geophysical Research: Solid Earth 116.

Clague, J.J., Stead, D., 2012. Landslides: types, mechanisms and modeling. Cambridge University Press.

Clancy, J., 2013. Site surveying and levelling. Routledge.

Coalition, N., 2007. Talking about disaster: Guide for standard messages, National Disaster Education: Washington, DC.

Corominas, J., Moya, J., Lloret, A., Gili, J., Angeli, M., Pasuto, A., Silvano, S., 2000. Measurement of landslide displacements using a wire extensometer. Engineering Geology 55, 149-166.

Costantini, M., 1998. A novel phase unwrapping method based on network programming. IEEE Transactions on Geoscience and Remote Sensing 36(3), 813-821.

Costantini, M., Malvarosa, F., Minati, F., Pietranera, L., Milillo, G., 2002. A three-dimensional phase unwrapping algorithm for processing of multitemporal SAR interferometric measurements, IEEE International Geoscience and Remote Sensing Symposium, 3, 1741-1743.

Costantini, M., Rosen, P.A., 1999. A generalized phase unwrapping approach for sparse data, Geoscience and Remote Sensing Symposium, IEEE 1999 International Geoscience and Remote Sensing Symposium. IGARSS'99 Proceedings. 1, 267-269.

Crosetto, M., Biescas, E., Duro, J., Closa, J., Arnaud, A., 2008. Generation of advanced ERS and Envisat interferometric SAR products using the stable point network technique. Photogrammetric Engineering & Remote Sensing 74, 443-450.

Crosetto, M., Monserrat, O., Cuevas-González, M., Devanthéry, N., Crippa, B., 2016. Persistent scatterer interferometry: a review. ISPRS Journal of Photogrammetry and Remote Sensing 115, 78-89.

Crosetto, M., Monserrat, O., Cuevas, M., Crippa, B., 2011. Spaceborne differential SAR interferometry: Data analysis tools for deformation measurement. Remote Sensing 3, 305-318.

Crosetto, M., Monserrat, O., Luzi, G., Cuevas-González, M., Devanthéry, N., 2014a. Discontinuous GBSAR deformation monitoring. ISPRS Journal of Photogrammetry and Remote Sensing 93, 136-141.

Crosetto, M., Monserrat, O., Luzi, G., Cuevas-González, M., Devanthéry, N., 2014b. A noninterferometric procedure for deformation measurement using GB-SAR imagery. IEEE Geoscience and Remote Sensing Letters 11, 34-38.

Crosetto, M., Monserrat, O., Luzi, G., Cuevas, M., Devanthéry, N., 2015. Deformation monitoring using ground-based SAR data. Engineering Geology for Society and Territory-Volume 5. Springer, pp. 137-140.

Crosetto, M., Monserrat, O., Luzi, G., Devanthéry, N., Cuevas-González, M., Barra, A., 2017. Data processing and analysis tools based on ground-based synthetic aperture radar imagery. ISPRS-International Archives of the Photogrammetry, Remote Sensing and Spatial Information Sciences, 593-596.

Cruden, D.M., 1991. A simple definition of a landslide. Bulletin of Engineering Geology and the Environment 43, 27-29.

Dai, K., Li, Z., Tomás, R., Liu, G., Yu, B., Wang, X., Cheng, H., Chen, J., Stockamp, J., 2016. Monitoring activity at the Daguangbao mega-landslide (China) using Sentinel-1 TOPS time series interferometry. Remote Sensing of Environment 186, 501-513.

de Macedo, K.A.C., Ramos, F.L.G., Gaboardi, C., Moreira, J.R., Vissirini, F., da Costa, M.S., 2017. A compact ground-based interferometric radar for landslide monitoring: the Xerém experiment. IEEE Journal of Selected Topics in Applied Earth Observations and Remote Sensing 10, 975-986.

Del Ventisette, C., Intrieri, E., Luzi, G., Casagli, N., Fanti, R., Leva, D., 2011. Using ground based radar interferometry during emergency: the case of the A3 motorway (Calabria Region, Italy) threatened by a landslide. Natural Hazards and Earth System Sciences 11, 2483.

Delacourt, C., Allemand, P., Berthier, E., Raucoules, D., Casson, B., Grandjean, P., Pambrun, C., Varel, E., 2007. Remote-sensing techniques for analysing landslide kinematics: a review. Bulletin de la Société Géologique de France 178, 89-100.

Deledalle, C.-A., Denis, L., Tupin, F., 2011. Nl-insar: Nonlocal interferogram estimation. IEEE Transactions on Geoscience and Remote Sensing 49, 1441-1452.

Deledalle, C.-A., Denis, L., Tupin, F., Reigber, A., Jäger, M., 2015. NL-SAR: A unified nonlocal framework for resolution-preserving (Pol)(In) SAR Denoising. IEEE Transactions on Geoscience and Remote Sensing 53, 2021-2038.

Dematteis, N., Luzi, G., Giordan, D., Zucca, F., Allasia, P., 2017. Monitoring Alpine glacier surface deformations with GB-SAR. Remote Sensing Letters 8, 947-956.

Di Traglia, F., Battaglia, M., Nolesini, T., Lagomarsino, D., Casagli, N., 2015. Shifts in the eruptive styles at Stromboli in 2010–2014 revealed by ground-based InSAR data. Scientific Reports 5, 13569.

Di Traglia, F., Nolesini, T., Ciampalini, A., Solari, L., Frodella, W., Bellotti, F., Fumagalli, A., De Rosa, G., Casagli, N., 2018. Tracking morphological changes and slope instability using spaceborne and ground-based SAR data. Geomorphology 300, 95-112.

Ding, X., Liu, G., Li, Z., Li, Z., Chen, Y., 2004. Ground subsidence monitoring in Hong

Kong with satellite SAR interferometry. Photogrammetric Engineering & Remote Sensing 70, 1151-1156.

Djuknic, G.M., Richton, R.E., 2001. Geolocation and assisted GPS. Computer 34, 123-125.

Dong, Y., Huang, D., Du, J., 2013. Observations of coastal aeolian dune movements at Feicuidao, on the Changli Gold Coast in Hebei Province. Sciences in Cold and Arid Regions 5, 0324-0330.

Dunnicliff, J., Green, G.E., 1993. Geotechnical instrumentation for monitoring field performance. John Wiley & Sons.

Edde, B., 1993. Radar-Principles, technology, applications. NASA STI/Recon Technical Report A 93.

Farina, P., Leoni, L., Babboni, F., Coppi, F., Mayer, L., Ricci, P., 2011. IBIS-M, an innovative radar for monitoring slopes in open-pit mines, Proc. Int. Symp. Rock Slope Stabil. Open Pit Mining Civil Eng.

Ferretti, A., Fumagalli, A., Novali, F., Prati, C., Rocca, F., Rucci, A., 2011. A new algorithm for processing interferometric data-stacks: SqueeSAR. IEEE Transactions on Geoscience and Remote Sensing 49, 3460-3470.

Ferretti, A., Prati, C., Rocca, F., 2000. Nonlinear subsidence rate estimation using permanent scatterers in differential SAR interferometry. IEEE transactions on Geoscience and Remote Sensing 38, 2202-2212.

Ferretti, A., Prati, C., Rocca, F., 2001. Permanent scatterers in SAR interferometry. IEEE Transactions on Geoscience and Remote Sensing 39, 8-20.

Fielding, E.J., Milillo, P., Bürgmann, R., Yun, S.-H., Samsonov, S., 2009. Coseismic and Postseismic Deformation from the August 2014 Mw 6.0 South Napa Earthquake Measured with InSAR Time Series. Nature 458, 64-68.

Flynn, T.J., 1997. Two-dimensional phase unwrapping with minimum weighted discontinuity. JOSA A 14, 2692-2701.

Folkins, I., Bernath, P., Boone, C., Donner, L., Eldering, A., Lesins, G., Martin, R., Sinnhuber, B.M., Walker, K., 2006. Testing convective parameterizations with tropical measurements of HNO3, CO, H2O, and O3: Implications for the water vapor budget. Journal of Geophysical Research: Atmospheres 111.

Fornaro, G., Franceschetti, G., Lanari, R., Sansosti, E., 1996. Robust phase-unwrapping techniques: a comparison. JOSA A 13, 2355-2366.

Fried, D.L., 1977. Least-square fitting a wave-front distortion estimate to an array of phase-difference measurements. JOSA 67, 370-375.

Frodella, W., Ciampalini, A., Gigli, G., Lombardi, L., Raspini, F., Nocentini, M., Scardigli, C., Casagli, N., 2016. Synergic use of satellite and ground based remote sensing

methods for monitoring the San Leo rock cliff (Northern Italy). Geomorphology 264, 80-94.

Frukacz, M., Wieser, A., 2017. On the impact of rockfall catch fences on ground-based radar interferometry. Landslides 14, 1431-1440.

Fujisawa, K., Higuchi, K., Koda, A., Harada, T., 2007. Landslide detection, monitoring, prediction, emergency measures and technical instruction in a busy city, Atami, Japan, Proceedings, First North American Landslide Conference, Vail, Colorado, pp. 65-73.

Gens, R., 2003. Two-dimensional phase unwrapping for radar interferometry: developments and new challenges. International Journal of Remote Sensing 24, 703-710.

Ghiglia, D.C., Romero, L.A., 1994. Robust two-dimensional weighted and unweighted phase unwrapping that uses fast transforms and iterative methods. JOSA A 11, 107-117.

Ghiglia, D.C., Romero, L.A., 1996. Minimum Lp-norm two-dimensional phase unwrapping. JOSA A 13, 1999-2013.

Gibson, A., Culshaw, M., Dashwood, C., Pennington, C., 2013. Landslide management in the UK—the problem of managing hazards in a 'low-risk'environment. Landslides 10, 599-610.

Goel, K., Adam, N., 2012. An advanced algorithm for deformation estimation in non-urban areas. ISPRS journal of photogrammetry and remote sensing 73, 100-110.

Goldstein, R.M., Werner, C.L., 1998. Radar interferogram filtering for geophysical applications. Geophysical Research Letters 25, 4035-4038.

Goldstein, R.M., Zebker, H.A., Werner, C.L., 1988. Satellite radar interferometry: Two‐dimensional phase unwrapping. Radio Science 23, 713-720.

Green, P.J., 1984. Iteratively reweighted least squares for maximum likelihood estimation, and some robust and resistant alternatives. Journal of the Royal Statistical Society. Series B (Methodological), 149-192.

Hall, M.P., 1980. Effects of the troposphere on radio communication. Stevenage Herts England Peter Peregrinus Ltd IEE Electromagnetic Waves Series 8.

Hanssen, R.F., 2001. Radar interferometry: data interpretation and error analysis. Springer Science & Business Media.

Haque, U., Blum, P., da Silva, P., Andersen, P., Pilz, J., Chalov, S., Malet, J., Auflič, M., Andres, N., Poyiadji, E., 2016. Fatal landslides in Europe. Landslides 13(6), 1545-1554.

Harries, N., Noon, D., Rowley, K., 2006. Case studies of slope stability radar used in open cut mines. Stability of Rock Slopes in Open Pit Mining and Civil Engineering Situations, 335-342.

Harris, C., Stephens, M., 1988. A combined corner and edge detector, Alvey Vision Conference 15(50), 147-151.

Harris, R. and Baumann, I., 2015. Open data policies and satellite Earth observation. Space Policy 32, 44-53.

Herrera, G., Fernández-Merodo, J., Mulas, J., Pastor, M., Luzi, G., Monserrat, O., 2009. A landslide forecasting model using ground based SAR data: The Portalet case study. Engineering Geology 105, 220-230.

Hooper, A., 2008. A multi‐temporal InSAR method incorporating both persistent scatterer and small baseline approaches. Geophysical Research Letters 35.

Hooper, A., 2010. A statistical-cost approach to unwrapping the phase of InSAR time series, proceeding of international workshop on ERS SAR interferometry, Frascati, Italy.

Hooper, A., Bekaert, D., Spaans, K., Arıkan, M., 2012. Recent advances in SAR interferometry time series analysis for measuring crustal deformation. Tectonophysics 514, 1-13.

Hooper, A., Segall, P., Zebker, H., 2007. Persistent scatterer interferometric synthetic aperture radar for crustal deformation analysis, with application to Volcán Alcedo, Galápagos. Journal of Geophysical Research: Solid Earth (1978–2012) 112.

Hooper, A., Zebker, H., Segall, P., Kampes, B., 2004. A new method for measuring deformation on volcanoes and other natural terrains using InSAR persistent scatterers. Geophysical research letters 31.

Hooper, A., Zebker, H.A., 2007. Phase unwrapping in three dimensions with application to InSAR time series. JOSA A 24, 2737-2747.

Hu, J., Li, Z., Ding, X., Zhu, J., Zhang, L., Sun, Q., 2012. 3D coseismic displacement of 2010 Darfield, New Zealand earthquake estimated from multi-aperture InSAR and D-InSAR measurements. Journal of Geodesy 86, 1029-1041.

Hu, J., Li, Z., Ding, X., Zhu, J., Zhang, L., Sun, Q., 2014. Resolving three-dimensional surface displacements from InSAR measurements: A review. Earth-Science Reviews 133, 1-17.

Hunt, B., 1979. Matrix formulation of the reconstruction of phase values from phase differences. JOSA 69, 393-399.

Huntley, J., 1989. Noise-immune phase unwrapping algorithm. Applied Optics 28, 3268-3270.

Huntley, J.M., 2001. Three-dimensional noise-immune phase unwrapping algorithm. Applied Optics 40, 3901-3908.

Huntley, J.M., Saldner, H., 1993. Temporal phase-unwrapping algorithm for automated interferogram analysis. Applied Optics 32, 3047-3052.

Iannini, L., Guarnieri, A.M., 2011. Atmospheric phase screen in ground-based radar: Statistics and compensation. IEEE Geoscience and Remote Sensing Letters 8, 537-541.

IEEE, 2003. IEEE standard letter designations for radar-frequency bands. IEEE Std 521-2002 (Revision of IEEE Std 521-1984), 0_1-3.

Iglesias, R., Aguasca, A., Fabregas, X., Mallorqui, J.J., Monells, D., López-Martínez, C., Pipia, L., 2015a. Ground-based polarimetric SAR interferometry for the monitoring of terrain displacement phenomena–part I: theoretical description. IEEE Journal of Selected Topics in Applied Earth Observations and Remote Sensing 8, 980-993.

Iglesias, R., Aguasca, A., Fabregas, X., Mallorqui, J.J., Monells, D., López-Martínez, C., Pipia, L., 2015b. Ground-based polarimetric SAR interferometry for the monitoring of terrain displacement phenomena–part II: applications. IEEE Journal of Selected Topics in Applied Earth Observations and Remote Sensing 8, 994-1007.

Iglesias, R., Fabregas, X., Aguasca, A., Mallorqui, J.J., Lopez-Martinez, C., Gili, J., Corominas, J., 2014a. Atmospheric phase screen compensation in ground-based SAR with a multiple-regression model over mountainous regions. IEEE Transactions on Geoscience and Remote Sensing 52, 2436-2449.

Iglesias, R., Fabregas, X., Aguasca, A., Mallorqui, J.J., Lopez-Martinez, C., Gili, J., Corominas, J., 2014b. Atmospheric phase screen compensation in ground-based SAR with a multiple-regression model over mountainous regions. IEEE Transactions on Geoscience and Remote Sensing 52, 2436-2449.

Iglesias, R., Mallorqui, J.J., López-Dekker, P., 2014c. DInSAR pixel selection based on sublook spectral correlation along time. IEEE Transactions on Geoscience and Remote Sensing 52, 3788-3799.

Iglesias, R., Monells, D., Fabregas, X., Mallorqui, J.J., Aguasca, A., Lopez-Martinez, C., 2014d. Phase quality optimization in polarimetric differential SAR interferometry. IEEE Transactions on Geoscience and Remote Sensing 52, 2875-2888.

Iglesias, R., Monells, D., Lopez-Martinez, C., Mallorqui, J.J., Fabregas, X., Aguasca, A., 2015c. Polarimetric optimization of temporal sublook coherence for dinsar applications. IEEE Geoscience and Remote Sensing Letters 12, 87-91.

International Civil Aviation Organization, 2002. Manual of the ICAO Standard Atmosphere: Extended to 80 Kilometres (262 500 Feet). ICAO.

Intrieri, E., Gigli, G., Mugnai, F., Fanti, R., Casagli, N., 2012. Design and implementation of a landslide early warning system. Engineering Geology 147, 124-136.

Itoh, K., 1982. Analysis of the phase unwrapping algorithm. Applied Optics 21(14), 2470-2470.

James, M.R., Robson, S., d'Oleire-Oltmanns, S., Niethammer, U., 2017. Optimising UAV topographic surveys processed with structure-from-motion: Ground control quality,

quantity and bundle adjustment. Geomorphology 280, 51-66.

Jiang, M., Ding, X., Hanssen, R.F., Malhotra, R., Chang, L., 2015. Fast statistically homogeneous pixel selection for covariance matrix estimation for multitemporal InSAR. IEEE Transactions on Geoscience and Remote Sensing 53, 1213-1224.

Jiang, M., Ding, X., Li, Z., 2014a. Hybrid approach for unbiased coherence estimation for multitemporal InSAR. IEEE Transactions on Geoscience and Remote Sensing 52, 2459-2473.

Jiang, M., Ding, X., Li, Z., Tian, X., Wang, C., Zhu, W., 2014b. InSAR coherence estimation for small data sets and its impact on temporal decorrelation extraction. IEEE Transactions on Geoscience and Remote Sensing 52, 6584-6596.

Jiang, M., Ding, X., Li, Z., Tian, X., Zhu, W., Wang, C., Xu, B., 2014c. The improvement for Baran phase filter derived from unbiased InSAR coherence. IEEE Journal of Selected Topics in Applied Earth Observations and Remote Sensing 7, 3002-3010.

Jin, S., Luo, O., 2009. Variability and climatology of PWV from global 13-year GPS observations. IEEE Transactions on Geoscience and Remote Sensing 47, 1918-1924.

Jones, D.H., Rose, M., 2015. Measurement of Relative Position of Halley VI modules (MORPH): GPS monitoring of building deformation in dynamic regions. Cold regions Science and Technology 120, 56-62.

Kalkan, Y., 2014. Geodetic deformation monitoring of Ataturk Dam in Turkey. Arabian Journal of Geosciences 7, 397-405.

Kamps, B., Adam, N., 2004. Deformation parameter inversion using Permanent Scatterers in Interferogram time series, EUSAR, 4, 341-344.

Kang, M.-K., Kim, K.-E., Lee, H.-Y., Cho, S.-J., Lee, J.-H., 2009. Preliminary results of polarimetric characteristics for C-band quad-polarization GB-SAR images using H/A/α polarimetric decomposition theorem. Korean Journal of Remote Sensing 25, 531-546.

Kavanagh, Barry F.; Bird, S. J. Glenn (1996). Surveying: Principles and applications (4th ed.). Prentice Hall. 257–264.

Kristensen, L., Rivolta, C., Dehls, J., Blikra, L., 2013. GB-InSAR measurement at the Åknes rockslide, Norway, Proceedings of the International Conference Vajont. 339-348

Kvam, P.H., Vidakovic, B., 2007. Nonparametric statistics with applications to science and engineering. John Wiley & Sons.

López-Quiroz, P., Doin, M.-P., Tupin, F., Briole, P., Nicolas, J.-M., 2009. Time series analysis of Mexico City subsidence constrained by radar interferometry. Journal of Applied Geophysics 69, 1-15.

Lagios, E., Sakkas, V., Novali, F., Bellotti, F., Ferretti, A., Vlachou, K., Dietrich, V., 2013. SqueeSAR™ and GPS ground deformation monitoring of Santorini Volcano (1992–2012): tectonic implications. Tectonophysics 594, 38-59.

Lanari, R., Casu, F., Manzo, M., Zeni, G., Berardino, P., Manunta, M., Pepe, A., 2007. An overview of the small baseline subset algorithm: A DInSAR technique for surface deformation analysis. Pure and Applied Geophysics 164, 637-661.

Lanari, R., Mora, O., Manunta, M., Mallorquí, J.J., Berardino, P., Sansosti, E., 2004. A small-baseline approach for investigating deformations on full-resolution differential SAR interferograms. IEEE Transactions on Geoscience and Remote Sensing 42, 1377-1386.

Lang, F., Yang, J., Li, D., 2015. Adaptive-window polarimetric SAR image speckle filtering based on a homogeneity measurement. IEEE Transactions on Geoscience and Remote Sensing 53, 5435-5446.

Larson, K.M., Poland, M., Miklius, A., 2010. Volcano monitoring using GPS: Developing data analysis strategies based on the June 2007 Kīlauea Volcano intrusion and eruption. Journal of Geophysical Research: Solid Earth 115.

Lee, J.-S., Papathanassiou, K.P., Ainsworth, T.L., Grunes, M.R., Reigber, A., 1998. A new technique for noise filtering of SAR interferometric phase images. IEEE Transactions on Geoscience and Remote Sensing 36, 1456-1465.

Leva, D., Nico, G., Tarchi, D., Fortuny-Guasch, J., Sieber, A.J., 2003. Temporal analysis of a landslide by means of a ground-based SAR interferometer. IEEE Transactions on Geoscience and Remote Sensing 41, 745-752.

Li, X., Dick, G., Ge, M., Heise, S., Wickert, J., Bender, M., 2014. Real‐time GPS sensing of atmospheric water vapor: Precise point positioning with orbit, clock, and phase delay corrections. Geophysical Research Letters 41, 3615-3621.

Li, X., Ge, M., Dai, X., Ren, X., Fritsche, M., Wickert, J., Schuh, H., 2015. Accuracy and reliability of multi-GNSS real-time precise positioning: GPS, GLONASS, BeiDou, and Galileo. Journal of Geodesy 89, 607-635.

Li, Z., Bethel, J., 2008. Image coregistration in SAR interferometry. The International Archives of the Photogrammetry, Remote Sensing and Spatial Information Sciences 37, 433-438.

Li, Z., Fielding, E.J., Cross, P., 2009. Integration of InSAR time-series analysis and water-vapor correction for mapping postseismic motion after the 2003 Bam (Iran) earthquake. IEEE Transactions on Geoscience and Remote Sensing 47, 3220-3230.

Liebe, H.J., 1985. An updated model for millimeter wave propagation in moist air. Radio Science 20, 1069-1089.

Lin, Q., Wang, Y., 2018. Spatial and temporal analysis of a fatal landslide inventory in China from 1950 to 2016. Landslides, 1-16.

Lin, X., Li, F., Meng, D., Hu, D., Ding, C., 2015. Nonlocal SAR interferometric phase filtering through higher order singular value decomposition. IEEE Geoscience and Remote Sensing Letters 12, 806-810.

Liu, Y., Lee, C., Yong, H., Jia, L., Youshi, W., Placidi, S., Roedelsperger, S., 2015. FastGBSAR case studies in China: Monitoring of a dam and instable slope, Synthetic Aperture Radar (APSAR), 2015 IEEE 5th Asia-Pacific Conference on. IEEE, pp. 849-852.

Liu, Y., Xu, X., Xu, G., 2018. MIMO radar calibration and imagery for near-field scattering diagnosis. IEEE Transactions on Aerospace and Electronic Systems 54, 442-452.

Lowry, B., Gomez, F., Zhou, W., Mooney, M., Held, B., Grasmick, J., 2013. High resolution displacement monitoring of a slow velocity landslide using ground based radar interferometry. Engineering Geology 166, 160-169.

Lucieer, A., Jong, S.M.d., Turner, D., 2014. Mapping landslide displacements using Structure from Motion (SfM) and image correlation of multi-temporal UAV photography. Progress in Physical Geography 38, 97-116.

Luzi, G., Noferini, L., Mecatti, D., Macaluso, G., Pieraccini, M., Atzeni, C., Schaffhauser, A., Fromm, R., Nagler, T., 2009. Using a ground-based SAR interferometer and a terrestrial laser scanner to monitor a snow-covered slope: Results from an experimental data collection in Tyrol (Austria). IEEE Transactions on Geoscience and Remote Sensing 47, 382-393.

Luzi, G., Pieraccini, M., Mecatti, D., Noferini, L., Guidi, G., Moia, F., Atzeni, C., 2004. Ground-based radar interferometry for landslides monitoring: atmospheric and instrumental decorrelation sources on experimental data. IEEE transactions on geoscience and remote sensing 42, 2454-2466.

Mao, W.-J., Chang, W.-l., 2015. Deformation monitoring by ground-based SAR interferometry (GB-InSAR): a field test in dam. Advances in Information Sciences & Service Sciences 7(2), 133-140.

Marshall, G.F., Stutz, G.E., 2004. Handbook of optical and laser scanning. CRC Press.

McGlone, J.C., 2013. Manual of photogrammetry. American Society of photogrammetry.

McIlveen, R., 1991. Fundamentals of weather and climate. Psychology Press.

Melvin, W.L., Scheer, J., 2014. Principles of modern radar: radar applications. Scitech Publishing.

Meta, A., Hoogeboom, P., Ligthart, L.P., 2007. Signal processing for FMCW SAR. IEEE Transactions on Geoscience and Remote Sensing 45, 3519-3532.

Metasensing, 2016. FastGBSAR_Ranger_UserManual_v1.2_20161214.

Metasensing, 2015a. FastGBSAR SePSI Software Manual (v3.2.0.1).

Metasensing, 2015b. FastGBSAR User Manual.

Mikhail, E.M., Bethel, J.S., McGlone, J.C., 2001. Introduction to Modern

Photogrammetry.

Monserrat Hernández, O., 2012. Deformation measurement and monitoring with Ground-Based SAR.

Monserrat, O., Crosetto, M., Iglesias, R., Rossi, G., Calcagni, L., Crippa, B., 2009. A tool for 2+ 1D phase unwrapping: application examples, Proc. Fringe 2009 Workshop.

Monserrat, O., Crosetto, M., Luzi, G., 2014. A review of ground-based SAR interferometry for deformation measurement. ISPRS Journal of Photogrammetry and Remote Sensing 93, 40-48.

Montuori, A., Luzi, G., Bignami, C., Gaudiosi, I., Stramondo, S., Crosetto, M., Buongiorno, M.F., 2016. The interferometric use of radar sensors for the urban monitoring of structural vibrations and surface displacements. IEEE Journal of Selected Topics in Applied Earth Observations and Remote Sensing 9, 3761-3776.

Mukupa, W., Roberts, G.W., Hancock, C.M., Al-Manasir, K., 2017. A review of the use of terrestrial laser scanning application for change detection and deformation monitoring of structures. Survey Review 49, 99-116.

Nadim, F., Lacasse, S., 2008. Strategies for mitigation of risk associated with landslides. Landslides-Disaster Risk Reduction.

Nickitopoulou, A., Protopsalti, K., Stiros, S., 2006. Monitoring dynamic and quasi-static deformations of large flexible engineering structures with GPS: Accuracy, limitations and promises. Engineering Structures 28, 1471-1482.

Noferini, L., Pieraccini, M., Mecatti, D., Luzi, G., Atzeni, C., Tamburini, A., Broccolato, M., 2005. Permanent scatterers analysis for atmospheric correction in ground-based SAR interferometry. IEEE Transactions on Geoscience and Remote Sensing 43, 1459-1471.

Noferini, L., Pieraccini, M., Mecatti, D., Macaluso, G., Luzi, G., Atzeni, C., 2007. DEM by ground-based SAR interferometry. IEEE Geoscience and Remote Sensing Letters 4, 659-663.

NTSLF, 2018. The UK National Tidal Gauge Network [online]. Available at: https://www.ntslf.org/data (Accessed: 20 November, 2018).

Osmanoğlu, B., Sunar, F., Wdowinski, S., Cabral-Cano, E., 2016. Time series analysis of InSAR data: Methods and trends. ISPRS Journal of Photogrammetry and Remote Sensing 115, 90-102.

Park, C., 2013. NATURAL HAZARDS [online]. Available at: http://www.lancaster.ac.uk/staff/gyaccp/hazards/default.htm (Accessed: 10 August, 2018).

Paton, D., 2008. Risk communication and natural hazard mitigation: how trust influences its effectiveness. International Journal of Global Environmental Issues 8, 2-16.

Paul, F., 1997. Theory of Synthetic Aperture Radar. Atlantis Scientific.

Pennington, C., Freeborough, K., Dashwood, C., Dijkstra, T., Lawrie, K., 2015. The National Landslide Database of Great Britain: Acquisition, communication and the role of social media. Geomorphology 249, 44-51.

Pepe, A., Lanari, R., 2006. On the extension of the minimum cost flow algorithm for phase unwrapping of multitemporal differential SAR interferograms. IEEE Transactions on Geoscience and remote sensing 44, 2374-2383.

Peppa, M., Mills, J., Moore, P., Miller, P., Chambers, J., 2019. Automated SfM co-registration for landslide change detection. Earth Surface Processes and Landforms 44(1), 287-303.

Perissin, D., Wang, T., 2012. Repeat-pass SAR interferometry with partially coherent targets. IEEE Transactions on Geoscience and Remote Sensing 50, 271-280.

Perski, Z., Hanssen, R., Wojcik, A., Wojciechowski, T., 2009. InSAR analyses of terrain deformation near the Wieliczka Salt Mine, Poland. Engineering Geology 106, 58-67.

Pipia, L., Fabregas Canovas, F.J., Aguasca Solé, A., Mallorquí Franquet, J.J., 2006. A comparison of different techniques for atmospheric artefact compensation in GBSAR differential acquisitions, IGARSS 2006: IEEE International Geoscience and Remote Sensing Symposium: 31 July-4 August 2006: Denver, Colorado. IEEE, pp. 3722-3725.

Pipia, L., Fabregas, X., Aguasca, A., López-Martínez, C., 2013. Polarimetric temporal analysis of urban environments with a ground-based SAR. IEEE Transactions on Geoscience and Remote Sensing 51, 2343-2360.

Pipia, L., Fabregas, X., Aguasca, A., Lopez-Martinez, C., 2008. Atmospheric artifact compensation in ground-based DInSAR applications. IEEE Geoscience and Remote Sensing Letters 5, 88-92.

Placidi, S., Meta, A., Testa, L., Rödelsperger, S., 2015. Monitoring structures with FastGBSAR, 2015 IEEE Radar Conference. IEEE, pp. 435-439.

Pratesi, F., Nolesini, T., Bianchini, S., Leva, D., Lombardi, L., Fanti, R., Casagli, N., 2015. Early warning GBInSAR-based method for monitoring Volterra (Tuscany, Italy) city walls. IEEE Journal of Selected Topics in Applied Earth Observations and Remote Sensing 8, 1753-1762.

Prati, C., Ferretti, A., Perissin, D., 2010. Recent advances on surface ground deformation measurement by means of repeated space-borne SAR observations. Journal of Geodynamics 49, 161-170.

Pritt, M.D., 1996. Phase unwrapping by means of multigrid techniques for interferometric SAR. IEEE Transactions on Geoscience and Remote Sensing 34, 728-738.

Pritt, M.D., Shipman, J.S., 1994. Least-squares two-dimensional phase unwrapping using FFT's. IEEE Transactions on Geoscience and Remote Sensing 32, 706-708.

Rödelsperger, S., 2011. Real-time processing of ground based synthetic aperture radar (GB-SAR) measurements. Technische Universität Darmstadt, Fachbereich Bauingenieurwesen und Geodäsie.

Rödelsperger, S., Becker, M., Gerstenecker, C., Läufer, G., Schilling, K., Steineck, D., 2010. Digital elevation model with the ground-based SAR IBIS-L as basis for volcanic deformation monitoring. Journal of Geodynamics 49, 241-246.

Rödelsperger, S., Coccia, A., Vicente, D., Meta, A., 2012. Introduction to the new metasensing ground-based SAR: Technical description and data analysis, 2012 IEEE International Geoscience and Remote Sensing Symposium (IGARSS). IEEE, pp. 4790-4792.

Rödelsperger, S., Meta, A., 2014. MetaSensing's FastGBSAR: ground based radar for deformation monitoring, SAR Image Analysis, Modeling, and Techniques XIV. International Society for Optics and Photonics 9243(18), 1-8.

Reeves, B., Noon, D.A., Stickley, G.F., Longstaff, D., 2001. Slope stability radar for monitoring mine walls, Subsurface and Surface Sensing Technologies and Applications III. International Society for Optics and Photonics, pp. 57-68.

Reza, T., Zimmer, A., Blasco, J.M.D., Ghuman, P., Aasawat, T.K., Ripeanu, M., 2018. Accelerating persistent scatterer pixel selection for InSAR processing. IEEE Transactions on Parallel and Distributed Systems 29, 16-30.

Rice, D., 2014. Landslides cause about 25 deaths a year in the USA. Available at: https://eu.usatoday.com/story/weather/2014/03/25/landslide-mudslide-washington/6873693/ (Accessed: 12 October 2018)

Rich, P.M., Dubayah, R., Hetrick, W.A., Saving, S.C., 1994. Using Viewshed models to calculate intercepted solar radiation: applications in ecology. American Society for Photogrammetry and Remote Sensing Technical Papers, 524-529.

Riesen, P., Strozzi, T., Bauder, A., Wiesmann, A., Funk, M., 2011. Short-term surface ice motion variations measured with a ground-based portable real aperture radar interferometer. Journal of Glaciology 57, 53-60.

Rodriguez, E., Martin, J., 1992. Theory and design of interferometric synthetic aperture radars, IEE Proceedings F (Radar and Signal Processing). IET, pp. 147-159.

Rudolf, H., Leva, D., Tarchi, D., Sieber, A., 1999a. A mobile and versatile SAR system, Geoscience and Remote Sensing Symposium, 1999. IEEE 1999 International Geoscience and Remote Sensing Symposium. IGARSS'99. vol. 1, pp. 592-594.

Sagiya, T., Miyazaki, S.i., Tada, T., 2000. Continuous GPS array and present-day crustal deformation of Japan. Pure and applied Geophysics 157, 2303-2322.

Samiei-Esfahany, S., Martins, J.E., van Leijen, F., Hanssen, R.F., 2016. Phase estimation for distributed scatterers in InSAR stacks using integer least squares estimation. IEEE Transactions on Geoscience and Remote Sensing 54, 5671-5687.

Scaioni, M., 2015. Modern technologies for landslide monitoring and prediction. Springer.

Scaioni, M., Feng, T., Lu, P., Qiao, G., Tong, X., Li, R., Barazzetti, L., Previtali, M., Roncella, R., 2015. Close-range photogrammetric techniques for deformation measurement: Applications to landslides, Modern technologies for landslide monitoring and prediction. Springer, pp. 13-41.

Schmetz, J., Menzel, W.P., Velden, C., Wu, X., van de Berg, L., Nieman, S., Hayden, C., Holmlund, K., Geijo, C., 1995. Monthly mean large-scale analyses of upper-tropospheric humidity and wind field divergence derived from three geostationary satellites. Bulletin of the American Meteorological Society 76, 1578-1584.

Schroedel, J., 2002. Structural Deformation Surveying - Engineering and Design.

Schulz, W.H., Coe, J.A., Ricci, P.P., Smoczyk, G.M., Shurtleff, B.L., Panosky, J., 2017. Landslide kinematics and their potential controls from hourly to decadal timescales: Insights from integrating ground-based InSAR measurements with structural maps and long-term monitoring data. Geomorphology 285, 121-136.

Serkan, M., Musaoglu, N., Kirkici, H., Ormeci, C., 2008. Edge and fine detail preservation in SAR images through speckle reduction with an adaptive mean filter. International Journal of Remote Sensing 29, 6727-6738.

Serrano-Juan, A., Vázquez-Suñè, E., Monserrat, O., Crosetto, M., Hoffmann, C., Ledesma, A., Criollo, R., Pujades, E., Velasco, V., Garcia-Gil, A., Alcaraz, M., 2016. Gb-SAR interferometry displacement measurements during dewatering in construction works. Case of La Sagrera railway station in Barcelona, Spain. Engineering Geology 205, 104-115.

Settles, E., Göttle, A., Von Poschinger, A., 2008. Slope monitoring methods-a state of the art report. ClimChalp Interreg III B Alpine Space Work package 6.

Shanker, P., Casu, F., Zebker, H.A., Lanari, R., 2011. Comparison of persistent scatterers and small baseline time-series InSAR results: a case study of the San Francisco Bay Area. IEEE Geoscience and Remote Sensing Letters 8, 592-596.

Shirzaei, M., Walter, T.R., 2011. Estimating the effect of satellite orbital error using wavelet-based robust regression applied to InSAR deformation data. IEEE Transactions on Geoscience and Remote Sensing 49, 4600-4605.

Skolnik, M.I., 1962. Introduction to radar. Radar handbook 2.

Skolnik, M.I., 2008. Radar Handbook, Third Edition. McGraw-Hill Education.

Soumekh, M., 1999. Synthetic aperture radar signal processing. New York: Wiley.

Sousa, J.J., Hooper, A.J., Hanssen, R.F., Bastos, L.C., Ruiz, A.M., 2011. Persistent scatterer InSAR: a comparison of methodologies based on a model of temporal deformation vs. spatial correlation selection criteria. Remote Sensing of Environment 115, 2652-2663.

Spaans, K., Hooper, A., 2016. InSAR processing for volcano monitoring and other near‐real time applications. Journal of Geophysical Research: Solid Earth 121, 2947-2960.

Suri, S., Schwind, P., Uhl, J., Reinartz, P., 2010. Modifications in the SIFT operator for effective SAR image matching. International Journal of Image and Data Fusion 1, 243-256.

Takahashi, K., Matsumoto, M., Sato, M., 2013. Continuous observation of natural-disaster-affected areas using ground-based SAR interferometry. IEEE Journal of Selected Topics in Applied Earth Observations and Remote Sensing 6, 1286-1294.

Tapete, D., Casagli, N., Luzi, G., Fanti, R., Gigli, G., Leva, D., 2013. Integrating radar and laser-based remote sensing techniques for monitoring structural deformation of archaeological monuments. Journal of Archaeological Science 40, 176-189.

Tarchi, D., Antonello, G., Casagli, N., Farina, P., Fortuny-Guasch, J., Guerri, L., Leva, D., 2005. On the use of ground-based SAR interferometry for slope failure early warning: the Cortenova rock slide (Italy), Landslides. Springer, pp. 337-342.

Tarchi, D., Oliveri, F., Sammartino, P.F., 2013. MIMO radar and ground-based SAR imaging systems: equivalent approaches for remote sensing. Geoscience and Remote Sensing, IEEE Transactions on 51, 425-435.

Tarchi, D., Rudolf, H., Luzi, G., Chiarantini, L., Coppo, P., Sieber, A., 1999a. SAR interferometry for structural changes detection: A demonstration test on a dam, IEEE 1999 International Geoscience and Remote Sensing Symposium. IGARSS'99 Proceedings. IEEE, pp. 1522-1524.

Tarchi, D., Rudolf, H., Luzi, G., Chiarantini, L., Coppo, P., Sieber, A., 1999b. SAR interferometry for structural changes detection: a demonstration test on a dam, IEEE 1999 International Geoscience and Remote Sensing Symposium, IGARSS'99 Proceedings. IEEE, pp. 1522-1524.

Touzi, R., Lopes, A., Bruniquel, J., Vachon, P.W., 1999. Coherence estimation for SAR imagery. IEEE Transactions on Geoscience and Remote Sensing 37, 135-149.

Tribolet, J., 1977. A new phase unwrapping algorithm. IEEE Transactions on Acoustics Speech and Signal Processing 25, 170-177.

UNISDR, G., 2015. Global Assessment Report on Disaster Risk Reduction, Making Development Sustainable: The Future of Disaster Risk Management. Geneva: United Nations)(www. preventionweb. net/english/hyogo/gar/2015/en/gar-pdf/GAR2015_EN.pdf).

UNISDR, G., 2017. Annual Report 2017: 2016-17 Biennium Work Programme Final Report. Avalaible at: https://www.unisdr.org/we/inform/publications/58158 (Accessed: 10 August, 2018)

Usai, S., 2003. A least squares database approach for SAR interferometric data. IEEE Transactions on Geoscience and Remote Sensing 41, 753-760.

Van Trees, H.L., 2004. Optimum array processing: Part IV of detection, estimation, and modulation theory. John Wiley & Sons.

Van Westen, C.J., 2013. Remote sensing and GIS for natural hazards assessment and disaster risk management. Treatise on geomorphology 3, 259-298.

Vasile, G., Trouvé, E., Lee, J.-S., Buzuloiu, V., 2006. Intensity-driven adaptive-neighborhood technique for polarimetric and interferometric SAR parameters estimation. IEEE Transactions on Geoscience and Remote Sensing 44, 1609-1621.

Vigny, C., Socquet, A., Peyrat, S., Ruegg, J.-C., Métois, M., Madariaga, R., Morvan, S., Lancieri, M., Lacassin, R., Campos, J., 2011. The 2010 Mw 8.8 Maule megathrust earthquake of central Chile, monitored by GPS. Science 332, 1417-1421.

Wang, G., 2011. GPS landslide monitoring: single base vs. network solutions—a case study based on the Puerto Rico and Virgin Islands permanent GPS network. Journal of Geodetic Science 1, 191-203.

Wang, T., Jonsson, S., Hanssen, R.F., 2014. Improved SAR image coregistration using pixel-offset series. IEEE Geoscience and Remote Sensing Letters 11, 1465-1469.

Wang, Y., Zhu, X.X., 2015. Automatic feature-based geometric fusion of multi-view TomoSAR point clouds in urban area. IEEE Journal of Selected Topics in Applied Earth Observations and Remote Sensing 8, 953-965.

Wang, Y., Zhu, X.X., 2016. Robust estimators for multipass SAR interferometry. IEEE Transactions on Geoscience and Remote Sensing 54, 968-980.

Wang, Z., Mills, J., Xiao, W., Huang, R., Zheng, S., Li, Z., 2017. A Flexible, Generic Photogrammetric Approach to Zoom Lens Calibration. Remote Sensing 9, 244.

Werner, C., Wiesmann, A., Strozzi, T., Kos, A., Caduff, R., Wegmiuler, U., 2012. The GPRI multi-mode differential interferometric radar for ground-based observations, EUSAR 2012; 9th European Conference on Synthetic Aperture Radar. VDE, pp. 304-307.

Wilcoxon, F., 1945. Individual comparisons by ranking methods. Biometrics bulletin 1, 80-83.

Wolff, C., 2018. Radar Tutorial [online]. Available at: http://www.radartutorial.eu/index.en.html (Accessed: 20 October, 2018).

Wright, T.J., Parsons, B.E., Lu, Z., 2004. Toward mapping surface deformation in three dimensions using InSAR. Geophysical Research Letters 31.

Wujanz, D., Neitzel, F., Hebel, H., Linke, J., Busch, W., 2013. Terrestrial radar and laser scanning for deformation monitoring: first steps towards assisted radar scanning. ISPRS Annals of Photogrammetry, Remote Sensing and Spatial Information Sciences 2, 325-330.

Yang, J., 2017. Study on ground moving target indication and imaging iechnique of

airborne SAR. Springer.

Yi, T.-H., Li, H.-N., Gu, M., 2013. Experimental assessment of high-rate GPS receivers for deformation monitoring of bridge. Measurement 46, 420-432.

Yue, H., Lay, T., 2011. Inversion of high‐rate (1 sps) GPS data for rupture process of the 11 March 2011 Tohoku earthquake (Mw 9.1). Geophysical Research Letters 38.

Zebker, H.A., Lu, Y., 1998. Phase unwrapping algorithms for radar interferometry: residue-cut, least-squares, and synthesis algorithms. JOSA A 15, 586-598.

Zebker, H.A., Villasenor, J., 1992. Decorrelation in interferometric radar echoes. IEEE Transactions on geoscience and remote sensing 30, 950-959.

Zeng, T., Mao, C., Hu, C., Tian, W., 2016. Ground-based SAR wide view angle full-field imaging algorithm based on keystone formatting. IEEE Journal of Selected Topics in Applied Earth Observations and Remote Sensing 9, 2160-2170.

Zhang, F., Hu, C., Li, W., Hu, W., Li, H.-C., 2014. Accelerating time-domain SAR raw data simulation for large areas using multi-GPUs. IEEE Journal of Selected Topics in Applied Earth Observations and Remote Sensing 7, 3956-3966.

Zhang, L., Liao, M., Balz, T., Shi, X., Jiang, Y., 2015. Monitoring landslide activities in the three gorges area with multi-frequency satellite SAR data sets, Modern Technologies for Landslide Monitoring and Prediction. Springer, pp. 181-208.

Zhao, C., Zhang, Q., He, Y., Peng, J., Yang, C., Kang, Y., 2016. Small-scale loess landslide monitoring with small baseline subsets interferometric synthetic aperture radar technique—case study of Xingyuan landslide, Shaanxi, China. Journal of Applied Remote Sensing 10, 026030.

Zheng, S., Wang, Z., Huang, R., 2015. Zoom lens calibration with zoom-and focus-related intrinsic parameters applied to bundle adjustment. ISPRS Journal of Photogrammetry and Remote Sensing 102, 62-72.

Zhou, Y., Thomas, M.Y., Parsons, B., Walker, R.T., 2018. Time-dependent postseismic slip following the 1978 M w 7.3 Tabas-e-Golshan, Iran earthquake revealed by over 20 years of ESA InSAR observations. Earth and Planetary Science Letters 483, 64-75.

Zumberge J.F., Heflin M.B., Jefferson D.C., Watkins M.M., Webb F.H. (1997) Precise point positioning for the efficient and robust analysis of GPS data from large networks. Journal of Geophysical Research 102(B3), 5005–5017